Electrochemical synthesis of silicon-based materials and their evaluation as anodes for Lithium-ion Batteries (LiBs)

(Dissertation)

To be awarded the degree of
Doctor rerum naturalium (Dr. rer. nat.)

Adel Elsayed

May 2019

Electrochemical synthesis of silicon-based materials and their evaluation as anodes for Lithium-ion Batteries (LiBs)

Doctoral Thesis
(Dissertation)
To be awarded the degree
Doctor rerum naturalium (Dr. rer. nat.)

Submitted by
Adel Mohammed Abdellatif Elsayed
from Fayoum / Egypt

Approved by
The Faculty of Natural and Materials Science
Clausthal University of Technology

Date of Oral Examination

17. May 2019

Dean: **Prof. Dr.-Ing. Karl-Heinz Spitzer**

Chairperson of the Board of Examiners: **Prof. Dr. Sabine Beuermann**

Supervising tutor: **Prof. Dr. rer. nat. Frank Endres**
Reviewer: **apl. Prof. Dr.-Ing. Ulrich Kunz**

„Gedruckt mit Unterstützung des Deutschen Akademischen Austauschdienstes“

Electrochemical synthesis of silicon-based materials and their evaluation as anodes for Lithium-ion Batteries (LiBs)

Dissertation
Zur Erlangung des Grades eines Doktors
der Naturwissenschaften (Dr. rer. nat.)

vorgelegt von
Adel Mohammed Abdellatif Elsayed
aus Fayoum / Ägypten

genehmigt von der
Fakultät für Natur-und Materialwissenschaften
der Technischen Universität Clausthal

Tag der mündlichen Prüfung

17. May 2019

Dekan

Prof. Dr.-ing. Karl-Heinz Spitzer

Vorsitzende der Promotionskommission

Prof. Dr. Sabine Beuermann

Betreuer

Prof. Dr. rer. nat. Frank Endres

Gutachter

apl. Prof. Dr.-Ing. Ulrich Kunz

Acknowledgement

In the frame of the DAAD-GERLS 2014 under the supervision of Prof. Dr. Frank Endres in the Institute of Electrochemistry (IEC), Clausthal University of Technology, this doctoral work was carried out.

All praises to Allah the Almighty for giving me the blessing, the tolerance and the strength.

My greatest gratitude is dedicated to my supervisor Prof. Dr. rar. nat. Frank Endres for giving me the opportunity to pursue my Ph.D. degree under his supervision with a state of freedom in the work environment and a lot of support. Also, I gratefully appreciate his guidance and revision that helped me in research work and during the time of writing this thesis. I would like to direct my special thanks and appreciation to co-referent Prof. Dr.-Ing. Ulrich Kunz for his consideration and time during reviewing my thesis. Many thanks to all of our colleagues in the group for their help and warm feelings.

For the financial support in the frame of the German- Egyptian Research Long-term Scholarship (GERLS) program, I am very grateful and thankful for the German Academic Exchange Service (DAAD) and the Egyptian Ministry of Higher Education (MoHE). Many thanks also to the National Research Center (NRC) committees for their help and concern.

I am very grateful for my wife for her continuous support, encouragement, patience and concern for taking care of our daughter "Talya".

Adel Elsayed
Clausthal-Zellerfeld, May 2019

Electrochemical synthesis of silicon-based materials and their evaluation as anodes for Lithium-ion Batteries (LIBs)

Adel Elsayed

Abstract

Lithium-ion batteries (LIBs) are currently the most powerful energy supply for portable electronic devices. Silicon is a promising anode material for LIBs with theoretical capacities of up to 4200 mAh/g. However, the commercialization of silicon as an anode in LIBs is hindered by its poor cycling stability. The present thesis deals with the synthesis of Si-compounds (Si_xGe_{1-x}, $Si_xGe_{1-x}Al_y$) and Si-composite (Si-reduced graphene oxide, Si-rGO) thin films as anode materials that were prepared by pulsed-electrodeposition (PED). Bare Si films were prepared by potentiostatic pulsed-electrodeposition in [BMP]TFSI at different duty cycle values (50%, 25%, 16% and 6%). XPS analysis for the SEI formed on Si anodes in LiTFSI/[BMP]TFSI revealed stable inorganic compounds. Si_xGe_{1-x} compound-films (x= 0.3, 0.6, 0.7, 0.9) prepared by potentiostatic pulsed-electrodeposition in [EMIm]TFSI exhibited promising cycling stability and higher gravimetric capacity compared to bare Si anode-films, possibly due to the enhancement in both electrical conductivity and Li diffusion. $Si_{\mathbf{0.6}}Ge_{\mathbf{0.4}}$ leads to the highest gravimetric capacity with improved cycling stability. $Si_{\mathbf{0.7}}Ge_{\mathbf{0.3}}$ showed the highest areal capacity values of around 0.14 mAh/cm^2. $Si_{\mathbf{0.9}}Ge_{\mathbf{0.1}}$ displayed a cycling performance similar to silicon. For ~400 nm-thick $Si_{0.95}Ge_{0.05}$ anode-film, quite a good rate-capability with gravimetric capacity values of around 900 mAh/g when cycled at 41.5 C-rate (128.5 A/g) were obtained,

making it interesting for micro-battery applications. $Si_{0.35}Ge_{0.45}Al_{0.2}$ prepared by potentiostatic pulsed-electrodeposition in [BMP]TFSI, displayed a high areal capacity of about 0.4 mAh/cm^2 when cycled at a current density of 0.8 A/g with good cycling stability and good rate-capability compared to Si and Si_xGe_{1-x}. EIS studies suggest the activation and/or modification of $Si_xGe_{1-x}Al_y$ upon cycling. XPS analysis of the SEI formed on $Si_{0.35}Ge_{0.45}Al_{0.2}$ showed LiF in addition to AlO_x and $LiAlF_x$ which were reported to buffer, protect and improve the integrity of the interfacial layer. Si-reduced graphene oxide (Si-rGO), prepared by sequential pulsed-electrodeposition in [BMP]TFSI displayed a high electrochemical performance compared to other tested films, resulting in gravimetric capacities of above 1200 mAh/g with areal capacity values of around 0.25 mAh/cm^2 when cycled at a current density of 600 mA/g. EIS studies for Si-rGO suggest that the composite anode exhibits kinetic enhancement and activation/modification processes upon cycling. XPS analysis for the SEI indicated LiF, Li_2O, Li_2CO_3, CF_x, LiS, SiS and CF_3SO_2Li.

Kurzfassung

Lithium-Ionen-Batterien (LIBs) sind derzeit die leistungsstärkste Energieversorgung für tragbare elektronische Geräte. Silizium ist ein vielversprechendes Anodenmaterial für LIBs mit theoretischen Kapazitäten von bis zu 4200 mAh/g. Der Kommerzialisierung von Silizium als Anode in LIBs steht jedoch seine schlechte Zyklenstabilität entgegen. Die vorliegende Doktor-Arbeit beschäftigt sich mit der Synthese von Si-Verbindungen (Si_xGe_{1-x}, $Si_xGe_{1-x}Al_y$) und dünnen Schichten aus Si-Verbundstoffen (Si-reduziertem Graphenoxid, Si-rGO) als Anodenmaterialien, die durch gepulste-Elektroabscheidung (*pulsed electrodeposition*, PED) hergestellt wurden. Blanke Si-Filme wurden durch gepulste potentiostatische Elektroabscheidung in 1-Butyl-1-methyl-pyrrolidinium bis(trifluormethylsulfonyl)- imid ([BMP]TFSI), bei verschiedenen Werten des Arbeitszyklus (50%, 25%, 16% und 6%) hergestellt. Die XPS-Analyse der auf Si-Anoden gebildeten *Solid-electrolyte interface* (SEI) in LiTFSI/[BMP]TFSI zeigte stabile anorganische Verbindungen. Filme aus Si_xGe_{1-x}-Verbindungen (x = 0,3, 0,6, 0,7, 0,9), die durch gepulste potentiostatische Elektroabscheidung in 1-Ethyl-3-methyl-imidazolium bis (trifluormethylsulfonyl)imid ([EMIm]TFSI) hergestellt wurden, zeigten vielversprechende Zyklenstabilität und höhere gravimetrische Kapazität im Vergleich zu blanken Si-Anodenfilmen, möglicherweise aufgrund der Verstärkung sowohl der elektrischen Leitfähigkeit als auch der Li-Diffusion. $Si_{0,6}Ge_{0,4}$ führt zu der höchsten gravimetrischen Kapazität bei verbesserter Zyklenstabilität. $Si_{0,7}Ge_{0,3}$ zeigte die höchsten Flächenkapazitätswerte von etwa 0,14 mAh/cm². $Si_{0,9}Ge_{0,1}$ zeigte eine Zyklusleistung ähnlich wie Silizium. Für einen

~400 nm-dicken $Si_{0,95}Ge_{0,05}$-Anodenfilm wurde eine recht gute Zyklisierbarkeit mit gravimetrischen Kapazitätswerten von etwa 900 mAh/g bei einem Zyklus bei 41,5 C (128.5 A/g) erhalten, was es für Mikrobatterieanwendungen interessant macht. Durch gepulste potentiostatische Elektroabscheidung in [BMP]TFSI hergestelltes $Si_{0,35}Ge_{0,45}Al_{0,2}$ zeigte eine hohe Flächenkapazität von etwa 0,4 mAh/cm², wenn es bei einer Stromdichte von 0,8 A/g bei guter Zyklusstabilität und guter Zyklisierbarkeit mit Si und Si_xGe_{1-x} verglichen wurde. EIS-Untersuchungen legen die Aktivierung und/oder Modifikation von $Si_xGe_{1-x}Al_y$ beim Zyklisieren nahe. Die XPS-Analyse der auf $Si_{0.35}Ge_{0.45}Al_{0.2}$ gebildeten SEI zeigte LiF zusätzlich zu AlO_x und $LiAlF_x$, von denen berichtet wurde, dass sie die Integrität der Grenzflächenschicht schützen und verbessern. Si-reduziertes Graphenoxid (Si-rGO), das durch sequentielle, gepulste Elektroabscheidung in [BMP]TFSI hergestellt wurde, zeigte im Vergleich zu anderen getesteten Filmen eine hohe elektrochemische Leistung, was zu gravimetrischen Kapazitäten von über 1200 mAh/g mit Flächenkapazitätswerten von etwa 0,25 führte mAh/cm², bei einer Stromdichte von 600 mA/g. EIS-Untersuchungen für Si-rGO legen nahe, dass die Verbundanode beim Zyklisieren kinetische Verstärkungs-, Aktivierungs- und/oder Modifizierungsprozesse zeigt. Die XPS-Analyse für die SEI zeigte LiF, Li_2O, Li_2CO_3, CF_x, LiS, SiS und CF_3SO_2Li an.

Motivation

Silicon is an attractive anode material for Lithium-ion Batteries (LIBs) as it has the highest theoretical capacity (4200 mAh/g) which is ten times higher than the theoretical capacity of graphite anode, in addition to its low cost, its availability, and its safety. Even though, the deformation and cracking problems of Si during lithiation/delithiation processes deteriorate its cycling stability. Electrodeposition is a simple and versatile method that requires only a simple setup with low cost. Preparation of Si compounds and Si composite films was done by pulsed-electrodeposition as versatile and controllable method. The present thesis focuses on the pulsed-electrodeposition of Si_xGe_{1-x}, $Si_xGe_{1-x}Al_y$ compounds and Si-rGO composites films as promising anode materials that could improve the electrochemical performance of LIBs. Owing to its higher electrical conductivity, its superior ionic diffusivity and its limited volume changes during cycling, germanium is a favorable add-element to Si anodes. Al, either in the elemental form as electrochemically active add-element or in the oxide form as a protective and buffering coating layer, is a promising element for stabilizing the Si anode cyclability and improving its rate-capability as well. Hence, adding Al to Si-Ge compound films can further improve the rate capability and the cycling stability of $Si_xGe_{1-x}Al_y$ anodes. Graphene is a favorable material to optimize the electrochemical performance of Si in LIBs by enhancing both its electrical conductivity and its mechanical properties, demonstrated to elevate both the produced gravimetric and areal capacity along with enhancing the rate-capability of the composite anode in LIBs.

Content

1. Introduction

List of abbreviations

AAMs: Anodic Alumina Membranes

BE: Binding energy

BMP: 1-Butyl-1-Methyl-pyrrolidinium

CE: Counter Electrode

CE: Coulombic Efficiency (%)

CPE: Constant Phase Elements

C-rate: Cycling-rate

CV: Cyclic Voltammetry

CVD: Chemical Vapor Deposition

DMC: Di-methyl Carbonate

EC: Ethylene Carbonate

ECW: Electrochemical Window

EDX: Energy Dispersive X-ray

EIS: Electrochemical Impedance Spectroscopy

EMIm: 1-Ethyl-3-methyl-imidazolium

EVs: Electric Vehicles

FE-SEM: Field Emission-Scanning Electron Microscope

FIR: Far-Infrared

FTIR: Fourier Transform Infrared

FWHM: Full Width at Half-Maximum

GO: graphene oxide

ILs: Ionic Liquids

LIBs: Lithium-ion Batteries

Li-M-O: Lithium Metal Oxide

MID-IR: Mid Infrared

NHE: Normal Hydrogen Electrode

OCP: Open Circuit Potential

ppm: part per million

PTFE: Polytetrafluoroethylene

PED: Pulsed Electrodeposition

QRE: Quasi-reference Electrode

QCM: Quartz Crystal Microbalance

rGO: reduced graphene oxide

RE: Reference Electrode

RTILs: Room Temperature Ionic Liquids

SEI: Solid-Electrolyte Interface

SiNPs: Si Nanoparticles

SiNWs: Si Nanowires

SiNTs: Si Nanotubes

TFSI: bis(trifluoromethylsulfonyl)imide

UHV: Ultrahigh Vacuum

UPD: Under Potential Deposition

WE: Working Electrode

XPS: X-ray Photo-electron Spectroscopy

1. Introduction

1.1. Introduction to Lithium-ion Batteries (LIBs)

After the invention of the first electrochemical cell in the 1800s by Count Volta, several battery types have been developed and introduced for the commercial markets, including lead-acid, Alkaline, nickel-cadmium, nickel-metal hydride and lithium-ion batteries [1-3]. Nowadays, the advanced energy storage devices become the inherent driving force for modern life that revolutionized its communication and its transportation technologies. Lithium-ion Batteries are considered as the most attractive energy storage systems that have triggered the vast application scale of portable electronic devices which rapidly developed in the recent 25 years [4, 5].

Lithium-ion batteries were first developed in Japan by Asahi Kasei then later commercialized by Sony® in 1991 [6]. Lithium is considered as the lightest and most electropositive metal (-3.04 V vs. standard hydrogen electrode) which makes it an important element to expedite and enrich electrochemical storage processes in battery system [7, 8]. As introduced in table (1.1), LIB exhibits unique characteristics, in terms of its good energy density, high power density, good cycle life together with low self-discharge rate which lead to a rapid acceptance in the market [9, 10].

Tab. 1.1. *Cycling characteristics of different batteries compared to LIBs* ***[9, 10]***.

Battery type	Operational voltage (V)	Energy density ($WhKg^{-1}$)	Comments
Lead-acid	1.9	30	Commonly known as car-starter battery, low energy density.
Alkaline	1.5	50-80	Not rechargeable, high capacity for low-power devices.
Ni-Cadmium	1.2	50	Memory effect, low discharge density.
Ni-metal hydride	1.2	60	Lazy battery-effect, low energy density.
Lithium-ion	4.0	150	Light, high voltage, no-memory effect, high capacity, good charge retention, comparably expensive.

1.2. Electrochemical principles of a lithium-ion battery

Lithium-ion batteries generally consist of four main components; namely two working electrodes (anode and cathode), the separator and the Li-ion electrolyte. The working electrodes have to be insertion-active for lithium ions **[7]**. The anode materials used in LIBs are commonly based on graphite and lithium alloyed metals **[7]**. On the other hand, LIB-cathode materials customarily include transition metal oxides (Manganese Oxide, Cobalt Oxide, Nickel Oxide, Cobalt Oxide, Manganese spinel), Lithium transition metal oxides (Lithium Nickel, Lithium Cobalt oxide), Iron Phosphate ($LiFePO_4$) and Lithium-Nickel-Manganese-Cobalt ternary oxides (Li-NMC oxides) **[7]**. The separator is a film of an ionically conductive but electronically insulating material, placed between the two working electrodes. The Li-ion electrolyte -in the solution form- is composed of a lithium salt dissolved in a suitable solvent (usually organic carbonate solvent) [7]. During charging and discharging processes, lithium ions get inserted into/removed from the solid matrix of the employed electrodes while electrons are extracted instantaneously in the opposite direction [7, 11, 12]. Figure (1.1) shows the schematic diagram of commercial lithium- ion battery in which graphite and lithium metal oxide (Li-M-O) are employed as the anode and the cathode, respectively [13].

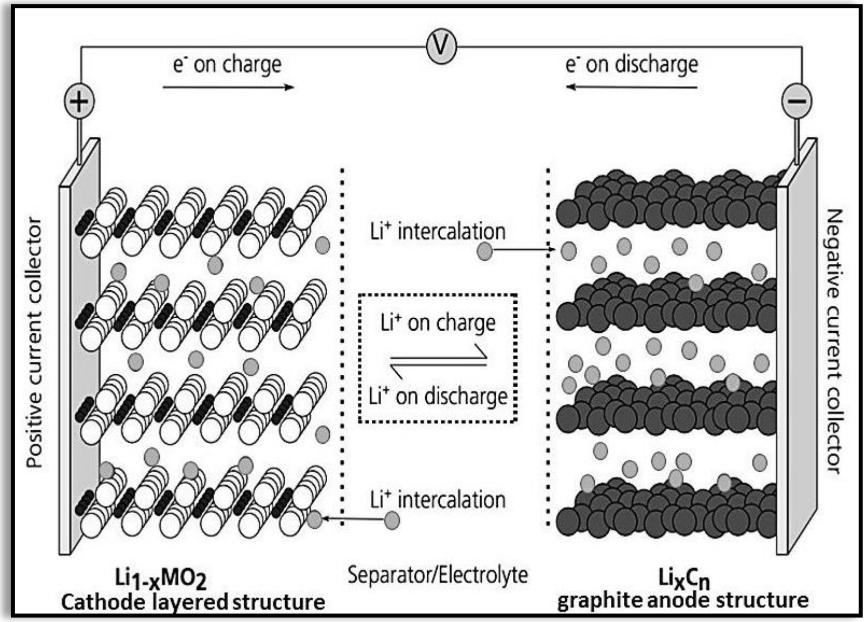

Fig. 1.1. *Schematic diagram for the charge/discharge process in a commercial LIB containing graphite anode and Lithium transition metal oxide as the cathode, adapted from Linden et al.* [13].

Upon charging, lithium ions get inserted in the graphite anode through an intercalation mechanism, resulting in a “reversible” oxidation of the cathode and a “reversible” reduction of the anode as well. The reverse process smoothly takes place during the discharging process ideally without the deformation of anode and cathode structure [13].

1.3. Challenges in lithium-ion batteries

Great efforts from both industry and academia have been dedicated to the development of Lithium-ion batteries that can not only retain higher gravimetric/volumetric capacities and greater energy densities but also can demonstrate sustainability and environmental compatibility [6, 7]. Commercial LIBs often employ traditional electrodes such as carbonaceous anodes (mostly graphite) and lithium transition metal oxide cathodes ($LiCoO_2$), whose theoretical capacities are ranged between 372 and 200 mAh/g. In order to realize LIBs with remarkably higher energy densities, the traditional electrode materials should be replaced by new more advanced materials that can produce much higher specific capacities [14-16]. Applications of Lithium-ion batteries have been devoted to more advanced energy avenues in electric vehicles (EVs) and other large-scale energy storage devices. However, LIBs are still not satisfactory for these applications that require at least 4-times higher energy density than that retained by the conventional LIBs to fulfill an 800 km-operation range of gasoline vehicles [16-19].

1.4. Advanced lithium-ion batteries electrodes

Figure (1.2) shows the gravimetric capacities values and the working potential ranges for different electrode materials [18]. The development of LIB-cathodes is mainly focusing on “Li-rich NMC” which comprise the beneficial combination of Ni, Co, and Mn, demonstrating higher capacities exceeding 280 mAh/g with open circuit potentials of around 4.5 V versus Li/Li^+ [20].

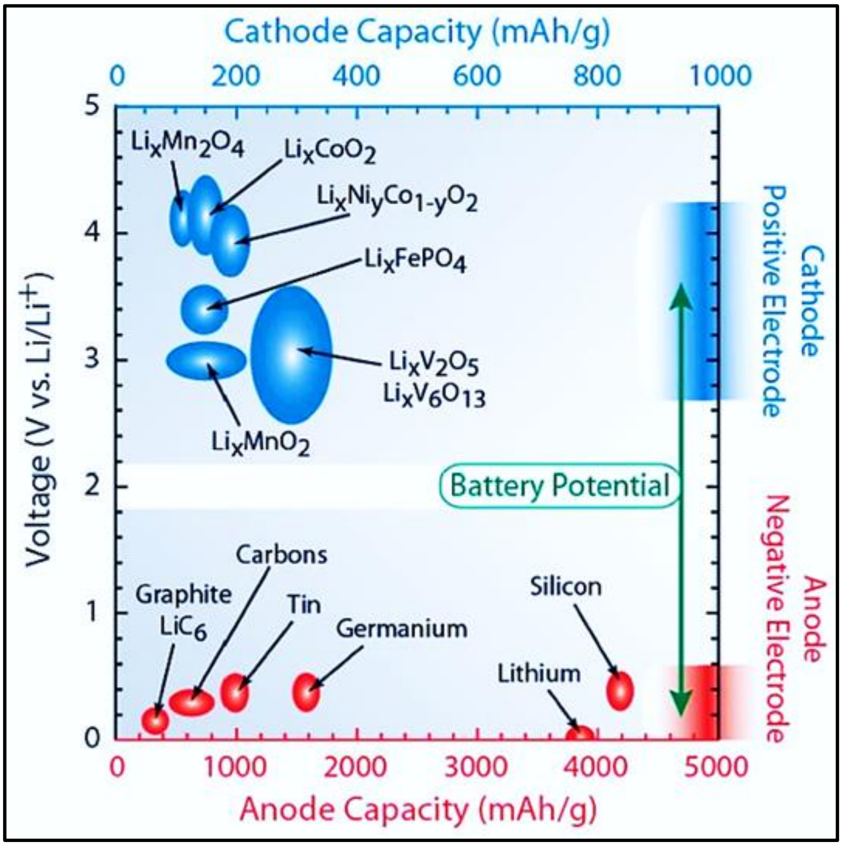

Fig. 1.2. *Theoretical capacity values and working potential ranges for different LIBs electrodes* [18].

For advanced anode materials, table (1.2) introduces a comparison between different anode materials in terms of their physical and electrochemical characters [19]. In terms of the capacity values, Si has the highest theoretical capacity (4200 mAh/g) which is higher than that of other alloy-type anodes (Sn, Sb, Al, and Mg). Compared to intercalation anode-type, the theoretical capacity of Si is ten-times higher than the theoretical capacity of graphite anode and twenty times higher than that of the $Li_4Ti_5O_{12}$ anode [19, 21].

Tab. 1.2. *Comparison between various anode-materials modified from reference (19).*

Anode material	Li	C	$Li_4Ti_5O_{12}$	Si	Sn	Sb	Al	Mg
Density (g/cm^2)	0.53	2.25	3.5	2.3	7.3	6.7	2.7	1.3
Lithiated-phase	Li	LiC_6	$Li_7Ti_5O_{12}$	$Li_{4.4}Si$	$Li_{4.4}Sn$	Li_3Sb	LiAl	Li_3Mg
Theoretical capacity (mAh/g)*	3862	372	175	4200	994	660	993	3350
Volume change (%)	100	12	1	420	260	200	96	100
Potential vs. Li/Li$^+$	0	0.05	1.6	0.4	0.6	0.9	0.3	0.1
Anode-type	**Ref.**	**Intercalation type**		**Alloy-type**				

**All capacity values are based on anode-materials in the de-lithiated state except Li.*

1.5. Si anode

1.5.1. Si as alloy-type anode

Replacing intercalation-anode materials (such as graphite) by alloy-anodes is required to obtain developed LIBs with higher energy densities **[22, 23]**. Alloy-type anode materials such as Si, Ge, Sn, Sb, and Pb can store lithium through the formation of Li-rich binary alloys producing high capacity values as shown in figure (1.3) **[22]**.

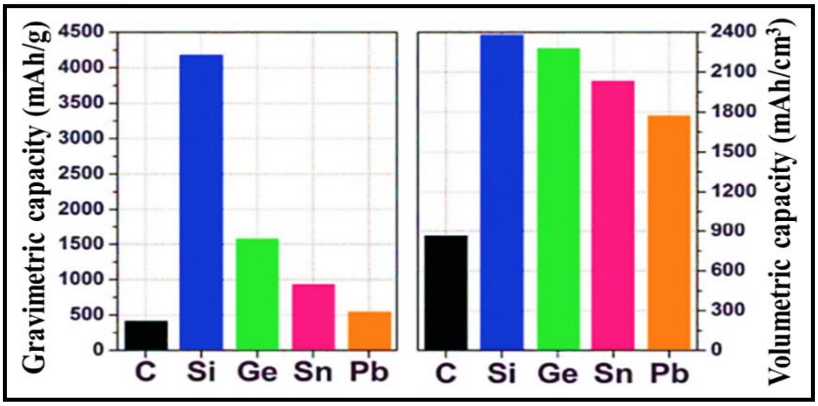

Fig. 1.3. *Gravimetric and volumetric capacities of Si compared to graphite anode and other Li-alloy anodes (Ge, Sn, Pb). The capacity values were calculated based on the maximum alloyed phases ($Li_{4.4}Si$, $Li_{4.25}Ge$, $Li_{4.25}Sn$, and $Li_{4.25}Pb$)* **[22]**.

Among Li-alloy anodes, silicon has the highest gravimetric capacity of 4200 mAh/g through alloying with lithium in the form of $Li_{22}Si_5$ at high temperature according to equation (1.1) **[24]**.

$22Li + 5Si \rightarrow Li_{22}Si_5$ ……………………….....…Equ. 1.1.

X-ray diffraction studies by Obrovac and Christensen **[25]** suggested that the alloying reaction of Li with Si at room temperature undergoes a lower level of lithiation ($Li_{15}Si_4$) according to equation (1.2). Thus, the theoretical capacity of Si at maximum Li-alloying is equal to 3589 mAh/g **[26, 27]**.

$15Li + 4Si \rightarrow Li_{15}Si_4$ ……………………….….…..…Equ. 1.2.

Silicon possesses other desirable properties as a promising anode material, such as its availability as the second most abundant element, its low cost and its safety margin compared to other anode materials **[28]**. Silicon exhibit also a low lithiation potential (0.4 - 0.05 V vs. Li/Li^+), which is a plus when it is coupled with Li-transition metal oxides (Li-TMOs) cathodes, where the full-cell voltage will be above 4V **[29, 30]**.

Despite these distinct advantages, the commercialization of silicon as anode matrix in LIBs is hindered by its poor cycling performance. Si-Li alloying process normally comes along with a noteworthy volume change (300%-420%) which results in disintegration and cracking of the Si anode integrity deteriorating its capacity **[27]**. This unfavorable mechanical deformation causes also delamination of the Si anode, disconnecting it from the current collector, which creates a severe fading in the anode capacity upon cycling **[31, 32]**. Besides, throughout this volume variation, the SEI layer is not stable, and the exposure of the cracked Si electrode to the electrolyte will lead to a growth of SEI, which results in reducing the capacity [33, 34]. The above mentioned mechanical deformations and chemical degradations of silicon-based materials, along with its low conductivity are the main drawbacks for its commercialization.

1.5.2. Strategies for enhancing the electrochemical performance of the Si anode

Improving the mechanical properties, increasing Si anode conductivity and enhancing the chemical stability of the electrode-electrolyte interphase are important to optimize the electrochemical performance of Si anodes in LIBs [35]. The majority of efforts in this direction were focusing on material design aspects, including the synthesis of nanostructures, porous or Si thin films, as well as other synthesis procedures such as coating or alloying of Si active material with other elements.

1.5.2.1. Si-nanostructures

Generally, nano-structured silicon can buffer its volume change during charging/discharging processes and thus -in principle- improve its cycle stability. For this reason, several methods have been devoted to design Si nanostructured-anodes including Si nanoparticles (SiNPs) [36-42], Si nanowires (SiNWs) [43-46] and Si nanotubes (SiHNTs) [47-49] using different synthesis strategies and techniques.

Silicon nanowires were first synthesized by C. K. Chan *et al.* [50]. Although it displayed astonishing capacities above 3000 mAh/g, the research group reported that the Si NWs anode exhibited a rapid drop in its retained capacity to zero after only 12 cycles at a low current density of 210 mA/g. Ramesh and Nagaraja [51] have also investigated Si nanowires at a markedly high current density (4200 mA/g). The produced high gravimetric capacity (1134 mAh/g) was found to drop quite fast. T. Song *et al.* have reported that the rapid drop in the capacity of a Si NW anode was confirmed to mainly arise from both the excessive SEI formation and the delamination of Si nanowires from the current collector **[52]**.

Inspired by Si-nanowire design, M. H. Park *et al.* **[53]** have synthesized Si-nanotubes, integrated with carbon as a protective coating layer which exhibited good electrochemical performance in LIBs. The high performance of SiNTs has been referred to the protective SiO_2 outer layer that can buffer the excessive deformation of the anode and limits the growth of thick SEI layers as well. As a comparison between Si nanowires and Si nanotubes anode types, H. Wu *et al.* **[54]** have studied the electrochemical performance of double-walled silicon nanotubes (DWSiNTs) at the same cycling rate which was applied for SiNWs anode by T. Song *et al.* **[52]**. The retained capacities of DW-SiNTs anode were found to be lower than that of SiNWs anode.

Indeed, a Si nanostructure-anode type within a critical size regime (diameter, length) can withstand the large volume variations by relieving the mechanical strain of the Si anode that causes its cracking **[55]**. Liu and Huang determined the critical size of Si nanoparticles to be 150 nm as the maximum **[56]**. For SiNWs anodes, Quiroga-Gonzalez *et al.* **[57]** have concluded that Si nanowires with 1 μm-length and 300 nm-diameters seem to be optimal to avoid structural deformation and delamination. However, the large surface area of nano-Si anodes increases side reactions and stimulates the overgrowth of the SEI, which is a critical issue limiting its cyclability **[35, 58]**.

1.5.2.2. Si porous structure

Porous structures of Si anodes can improve the electrochemical performance of Si anode by relieving the mechanical strain and providing space for the volume expansion which normally occurs during lithiation and de-lithiation processes. The pioneering synthesis method of micro-porous silicon by magnesio-thermic reduction of silica was first suggested by Bao *et al.* **[59]** then later replicated by Liu *et al.* **[60]**. The Si anode as microporous structure displayed a reversible gravimetric capacity of more than 2500 mAh/g at a cycling rate of 2100 mA/g for 200 cycles **[60]**.

Both nanostructured and mesoporous Si anodes have a shortcoming characteristic related to their density which is lower than the one of a raw silicon anode. As a result, the cycling stability and the pronounced gravimetric capacity values of nanostructured and mesoporous Si anodes are accompanied with low volumetric capacities which -in turn- limit the obtained energy density of the battery **[35]**.

1.5.2.3. Si thin films

A Si thin film is another promising design that has been reported to demonstrate very stable cycling performance and high gravimetric capacities in LIBs **[61-63]**. The positive effect of decreasing the thickness of the Si film on its cyclability has been studied with computational methods by Juchuan Li *et al.* **[64]**. The research group has confirmed that as the thickness of the Si film decreases, the average size of the cracked islands decreases. Takamura *et al.* **[65]** have studied the electrochemical performance of silicon thin films, synthesized by a vacuum deposition technique. The thin anode film with a thickness of 50 nm displayed excellent cycling stability with a reversible gravimetric capacity of above 2000 mAh/g when cycled at 30 C-rate for 1000 cycles. The group has also examined a 440 nm-thick Si film that produced a gravimetric capacity of above 2000 mAh/g at 1 C-rate. For avoiding cracking and irreversible morphological changes, it was reported that the thickness of the Si anode film should be limited to 100-200 nm [66].

Despite the outstanding performance of ultrathin Si films, the areal capacity is still a sever issue due to the low mass-loading of Si film at such small thickness. The low areal capacity for thin Si anodes compared to commercial graphite anodes is a point of weakness that should be overcome. At this end, the adjustment of Si film-thicknesses should demonstrate a trade-off between its areal and gravimetric capacities. Besides, the thickness/capacity impact should be rectified such that the associated mechanical degradation and resistance problems should be limited [67].

1.5.2.4. Si alloys

During the past decade, a lot of studies have been dedicated to the electrochemical performance of Si combined with other elements such as Cu [68-70], Mo [71], Fe [72, 73], Al [74], B [75], Y [76], Ti [77] and Ge [78-83] either in the form of composite or multilayer films. The incorporation of elements with Si participates not only in increasing the anode conductivity but also in improving the mechanical properties of a raw Si-anode that can endure greater cyclability at high cycling rates [84-87]. Germanium has been intensively investigated as add-element to Si, reported to enhance its performance in LIBs. Compared to Silicon, the limited volume changes of Germanium during cycling together with its higher electrical conductivity and its superior ionic diffusivity make it a favorable add-element for optimizing the cycling performance of Si anodes [78-83]. The enhanced cycling performance of silicon-germanium alloy anodes either in the layered or in the composites design was referred to the high conductivity and the superior diffusivity of Ge which can enhance the Li kinetics in the designed anode [83].

1.5.2.5. Si-carbon and Si-graphene films

The combination of silicon with carbon is a popular form as a modified Si anode. Carbon was demonstrated to improve the electrochemical performance of Si anodes in either multilayer structures [88] or in the composite form [89-91]. Several groups have studied the performance of Si/C composite films in LIBs [92-96]. They have reported that carbon not only increases the conductivity of the anode film but also contributes to improving the cycling stability of Si by buffering the volume changes during lithiation/de-lithiation processes.

Si-graphene is a promising combination that can improve the Si performance in LIBs. Graphene was reported to retain a capacity up to 1116 mAh/g upon lithiation corresponding to LiC_2, which is about three times higher than that of a conventional Graphite anode [97]. The combination of Si and graphene in a composite form is a promising anode-design to optimize Si anode performance in LIBs [98]. The incorporation of graphene with Si not only increases the anode conductivity but also enhance its cycling stability. Also, the SEI formed on a Si-graphene composite becomes more stable, hence dominating more cycling stability [94, 96, 97]. Si/graphene in multilayer structures is another anode type in which the integrated graphene as a flexible component can buffer the volume expansion of Si and isolate Si particles, sidestepping their aggregation upon cycling.

According to the following characteristics, graphene is a promising material to optimize the electrochemical performance of Si in LIBs [94-99]:

(i) As an excellent conductive item, reinforcing graphene with Si material can efficiently increase the electrical conductivity of the anode film.

(ii) Graphene sheets can act as a mechanical supporter for Si anode, maintaining its structural integrity.

(iii) As a fixable additive, graphene can beneficially mitigate and accommodate the deformation processes caused by the volume expansion/contraction of Si particles during the alloying/de-alloying processes.

(iv) Graphene layers can also isolate Si nanoparticles, circumventing its aggregation problem which expected to occur during cycling.

(v) Graphene was reported to improve the adhesion between the electrode materials and the current collector, preventing its delamination upon cycling [100].

1.5.3. Si electrodeposited-films

Silicon thin films can be deposited by several methods and techniques such as chemical vapor deposition (CVD) [101-103] and radio frequency magnetron techniques [104-105]. The significant limitations of these techniques are associated with the cost and the complexity of the used system together with the slow deposition rate on the large scale. Electrodeposition is a neat technique, demonstrated as a simple and versatile method that requires a simple setup with low cost [106]. It was widely performed in industry to synthesize thin films of various metals, alloys, and composites. Structure and thickness of the electrodeposited films can be modified by adapting the solutes concentrations and the applied deposition parameters (voltage, current density, deposition time, etc.) [107].

1.5.3.1. Electrodeposition of Si films

The electrodeposition of Si in the aqueous medium is not possible due to the high cathodic potential of Si at -0.83 V versus normal Hydrogen electrode (NHE), compared to water [108] which results in the hydrolysis of water and the immediate oxidation of Si [109]. For this reason, electrodeposition of Si was carried out in organic solvents or in high- temperature molten salts [110-119] before the widespread usage of ionic liquid electrolytes.

1.5.3.1.1. Electrodeposition of Si films in ionic liquids (ILs)

Electrodeposition of Si in organic media is usually associated with the oxidation of the Si deposits. Also, the need for a high temperature in case of using molten salt electrolytes makes it an unfavorable system. Therefore, electrodeposition methods of Silicon have been developed beyond these systems to other non-aqueous electrolytes, especially Room-Temperature Ionic Liquids (RTILs) [120-124]. Ionic liquids (ILs) are ionic salts that usually have a melting point lower than 100 °C [125]. The growing attention for Ionic liquids arises from their exceptional chemical, thermal, and electrochemical stability added to their negligible vapor pressure and their non-flammability properties [125, 126, 127]. Several studies have reported the electrodeposition of Si in ionic liquids either by potentiostatic or galvanostatic electrodeposition [121, 128 -131].

1, 3 di-alkyl- imidazolium bis (trifluoromethylsulfonyl) imide **“[C_nC_nIm]TFSI’’** and 1, 1 di-alkyl- pyrrolidinium bis (trifluoromethylsulfonyl) imide **“[$C_nC_nP_y$]TFSI’’** ionic liquids consist of a hydrophobic anion/cation combination which validates good viscosity and wide electrochemical stability [132]. In addition, its immiscibility with water and its low polarity are advantages [132-134] making them favorable electrolytes for Si electrodeposition from volatile and hydrophilic solutes.

1.5.3.1.2. Pulsed-Electrodeposition (PED) of Si films

The electrodeposition of Si using the pulsed technique is another modified method to prepare Si films with modified properties [135]. PED is an extension to conventional electrodeposition methods which has found much attention as being more versatile and controllable [136, 137]. This technique not only allows the preparation of deposits with high purity and low porosity, it was also reported to adjust grain size, grain size-distribution, crystallite-shape and morphology of the deposits [138, 139].

In Pulsed-electrodeposition, potential and/or current are/is alternated rapidly between two values within a series of square-wave pulses, equal in amplitude and duration [136, 138, 139]. Each pulse consists of an ON-Time (T_{ON}) interval during which potential and/or current density are/is applied, followed by an OFF-Time (T_{OFF}) interval during which the current passed through the electrodeposition solution adjusted to be zero. During the rest time (T_{OFF}) intervals, the analytes and electrolyte solution have a greater chance to diffuse from the bulk solution to the ionically-depleted region in cathode immediate vicinity through a convective diffusion process [138, 139]. Under such conditions, the nucleation rate usually improves and deposit's grain size is consequently reduced. Therefore, pulsed-electrodeposition can be adapted to produce uniform, dense Si films with smaller particle size [138, 139]. Besides, PED is a more efficient technique for controlling the composition and the thickness of Si anode films by controlling the pulse parameters (temporal parameters and pulse amplitudes) and the deposition time [135].

2. Experimental

2.1. Chemicals and solutions

2.1.1. Ionic liquids

The following ionic liquids, 1-Ethyl-3-methyl-imidazolium bis(trifluoromethylsulfonyl)imide **"[EMIm]TFSI"** and 1-Butyl-1-methyl-pyrrolidinium bis(trifluoromethylsulfonyl)imide **"[BMP]TFSI''** were employed as electrolytes for the electrochemical deposition of Si films, Si_xM_y compound films (M= Ge, Al) and Si-reduced graphene oxide (Si-rGO) composite film. Table (2.1) displays the structure and a few physical properties of these ionic liquids at room temperature [140-142]. The ionic liquids were purchased from Io-Li-Tec, Heilbronn, Germany. Before use, water from [EMIm]TFSI and [BMP]TFSI was reduced to values of below 2 ppm by drying at 100 °C under vacuum for 12 hours. The drying process was done in an Argon filled glove box (OMNI-LAB from Vacuum Atmospheres) with O_2 and H_2O below 2 ppm. The water content in the dried ionic liquids was evaluated using the karl-Fischer titration method.

Tab. 2.1. *Structure and some physical properties of [EMIm]TFSI and [BMP]TFSI at room temperature* [140-142].

Characteristics		**[EMIm]TFSI**	**[BMP]TFSI**
Structure	**Cation**	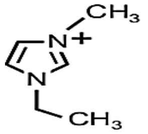	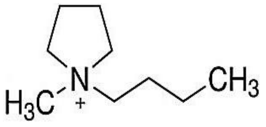
	Anion	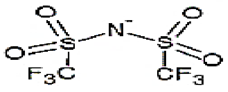	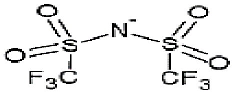
Molar mass (g/mol)		**391.31**	**422.41**
Density (g/ml)		**1.52-1.2** [141, 142]	**1.4**
Melting point (°C)		**-15 to -17** [141, 142]	**-50** [140]
Conductivity (mS/cm)		**8.8**	**2.2**
Viscosity (mm.s) [140]		**18**	**71**
Electrochemical window (ECW) /V		**4.1- 4.2** [141, 142]	**5.2-5.7** [141, 143]

2.1.2. Electrodeposition baths

The electrochemical baths used for the deposition of Si, Si_xGe_{1-x}, $Si_xGe_{1-x}Al_y$ and Si-rGO films are shown in table (2.2). $SiCl_4$ (99.99%) and $GeCl_4$ (99.99%) were purchased from Sigma-Aldrich in the highest quality. $AlCl_3$ (99.0%) was purchased from Fluka Analytica. Graphene oxide suspension in H_2O (4 mg/ml) was purchased from Sigma-Aldrich. Before using the GO suspension, it was dried at 60° C for 1 hour under air, and then the powder was collected and ground in a mortar. Subsequently, 5 g of GO powder was added to 10 ml of IL solutions inside of the glovebox then stirred overnight till the GO- IL suspension (0.5 mg/ml) become homogeneous. All electrodeposition solutions were prepared in the aforementioned glove box.

Tab. 2.2. *Electrochemical baths prepared for the electrodeposition of Si, Si_xGe_{1-x}, $Si_xGe_{1-x}Al_y$ and Si-rGO films.*

Electrodeposition baths		**Deposited anode-films**
IL- electrolytes	**Analytes**	
[BMP]TFSI	$SiCl_4$ (0.5 M)	Si films
[EMIm]TFSI	$SiCl_4$ (0.5 M) + $GeCl_4$ (0.25 M)	Si_xGe_{1-x} films
	$SiCl_4$ (0.5 M) + $GeCl_4$ (0.5 M)	
[BMP]TFSI	$SiCl_4$ (0.5 M) + $GeCl_4$ (0.25 M) + $AlCl_3$ (0.02 M)	$Si_xGe_{1-X}Al_y$ film
[BMP]TFSI	$SiCl_4$ (0.5 M)/graphene oxide (0.5 g/ml)	Si-rGO composite film

2.2. Electrodeposition equipment

2.2.1. Electrodeposition cell

The electrodeposition cell used in all experiments is made of Polytetrafluoroethylene (PTFE), clamped over a PTEF-covered Viton O-ring onto the substrate, yielding a geometric surface area of 0.33 cm^2. Before each electrodeposition experiment, PTFE cell and O-ring were washed in a mixture of concentrated H_2SO_4 and H_2O_2 (35%) in 50:50 vol. ratio, then followed by refluxing in distilled water, in order to remove any contaminants.

2.2.2. Electrodes

In all electrodeposition experiments, a Pt wire was used as a quasi-reference electrode (QRE) and a folded Pt wire was applied as a counter electrode. Immediately before each electrodeposition, the Pt quasi-reference and counter electrodes were cleaned in a H_2-flame, to ensure a complete removal of any organic contamination. A Cu substrate was used as the working electrode in all electrodeposition experiments. Before each deposition, the Cu sheet (12 mm x 12 mm) was polished with Silicon carbide paper to remove superficial oxide layers, then ultrasonically washed in Acetone and Isopropanol baths several times in order to remove any organic contaminants. Figure (2.1) shows a photo of the PTFE electrodeposition cell with the three cell electrodes which were used in the electrochemical deposition of Si, Si_xGe_{1-x}, $Si_xGe_{1-x}Al_y$ and Si-rGO film.

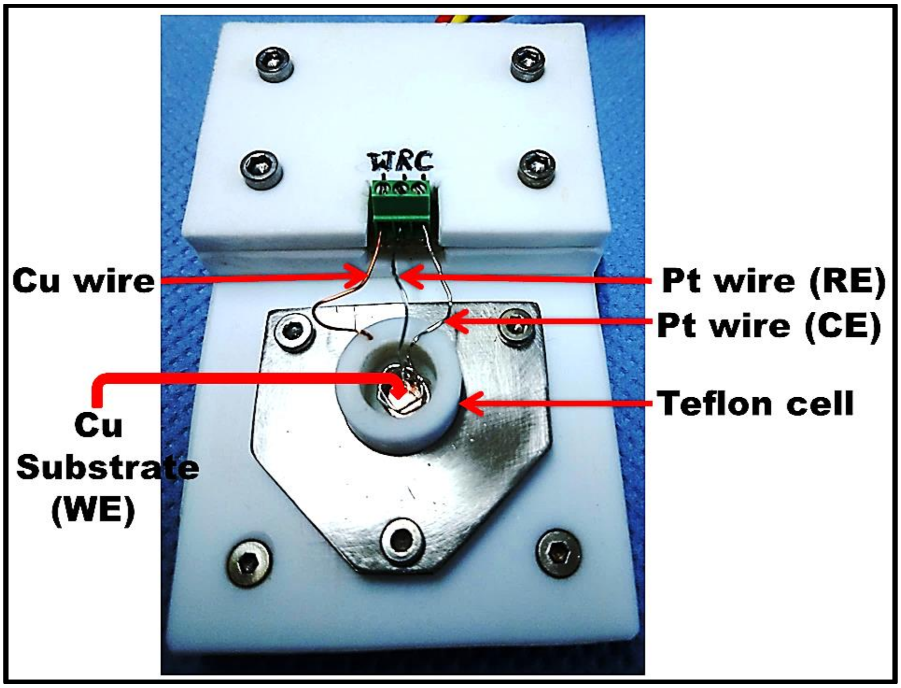

Fig. 2.1. *Photo of the electrodeposition cell with three electrodes used in all electrochemical deposition of Si,* Si_xGe_{1-x}*,* $Si_xGe_{1-x}Al_y$ *and Si-rGO films.*

2.3. Electrochemical methods of characterization

2.3.1. Cyclic Voltammetry (CV)

The cyclic voltammetry measurements were performed for both the neat ionic liquids and the prepared electrodeposition baths at a scanning rate of either 10 or 50 mV/s versus Pt QRE, using a VersaSTAT 3 (Princeton Applied Research) potentiostat/galvanostat, controlled by power-CV and power-step software.

2.3.1.1. Potentiostat operation

Figure (2.2) shows a scheme of a potentiostat with a three-electrode system (the working electrode, the counter electrode, and the reference electrode), customarily used in CV measurements **[143, 144]**. The potentiostat role is to regulate the potential difference between the reference and the working electrode, minimizing the iR drop between them without passing any Faradic current in the reference electrode. The role of the counter electrode is to pass all the current needed to balance the faradic current through the working electrode. The counter electrode often swings to extreme potentials in order to balance the faradic process at the working electrode in the opposite direction.

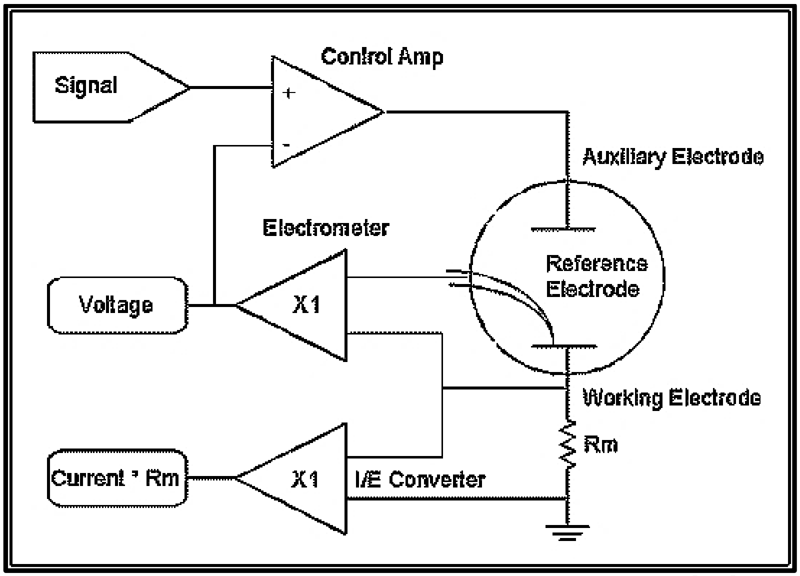

Fig. 2.2. *Simplified scheme of a three-electrode potentiostat* *[144]*.

2.3.1.2. Cyclic voltammetry operation

Cyclic voltammetry is a technique, extensively used for obtaining information about electrochemical reactions via a rapid identification of the characteristic red-ox potentials. In cyclic voltammetry, a triangular potential waveform is applied to the working electrode with time and the correlated current simultaneously measured as shown in figure (2.3.a) [143, 145]. The plot of current versus potential is termed as “the cyclic voltammogram” as shown in figure (2.3.b).

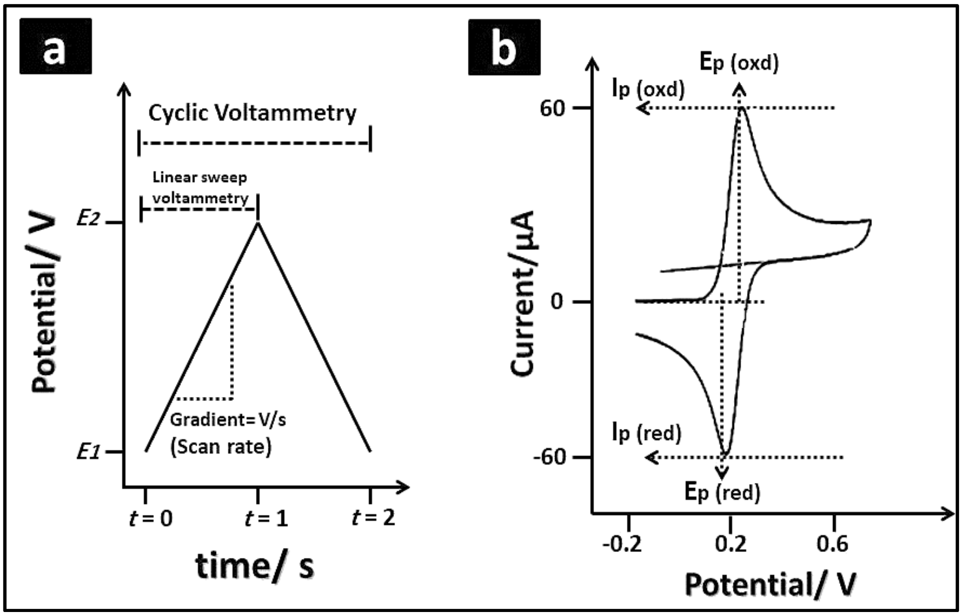

***Fig. 2.3. (a)** Potential-time profile used to perform linear sweep and cyclic voltammetry. **(b)** Typical cyclic voltammogram, representing the red-ox peak position (E_P) and red-ox peak height (I_P) [145].*

The scanning rate [dV/dt (V/s)] is the rate of the applied potential-change over time. In CV measurements, the potential is measured between the working electrode (WE) and the reference electrode (RE), while the current is measured between the working electrode and the counter electrode (CE). During the forward scan, the cathodic current increases at characteristic potentials (E_p red.), correlated to the reduction of the analytes at a maximum cathodic current (i_p red.). The cathodic current (i_p red.) decreases when the concentration of the reducible analytes is depleted. Upon the reverse scan at which an oxidizing potential is applied, the reduced analytes get oxidized at characteristic potentials (E_p oxd.). According to the red-ox peak position (E_P) and the red-ox peak height (I_P) values, CV data can provide information about the reduction/oxidation processes and the rates of electrochemical reactions regarding the electrodeposition of Si, Si_xGe_{1-x}, $Si_xGe_{1-x}Al_y$, and Si-rGO films.

2.3.1.3. Cyclic voltammetry of ionic liquids as electrolytes

[EMIm]TFSI and [BMP]TFSI ionic liquids were employed as the electrodeposition electrolytes without adding any further solvents. The electrodes are immobile without stirring the solutions during cyclic voltammetry, thus the cyclic voltammetry probes the diffusion-controlled red-ox peaks. Cyclic voltammetry measurements were performed for neat ionic liquids to measure their electrochemical window (ECW). Also it was performed for the electrodeposition baths to understand the electrochemical reactions regarding the electrodeposition of Si, Si_xGe_{1-x}, $Si_xGe_{1-x}Al_y$ and Si-rGO films.

2.3.2. Pulsed-Electrochemical Deposition (PED)

Si, Si_xGe_{1-x}, $Si_xGe_{1-x}Al_y$ and Si-rGO films were prepared by potentiostatic pulsed-electrodeposition technique in the aforementioned argon-filled glove box using VersaSTAT 3 (Princeton Applied Research) potentiostat / galvanostat controlled by power-CV and power-step software. In potentiostatic pulsed-electrodeposition, the potential is alternated between two values (P1 and P2) within a series of square-wave pulses, equal in amplitude and duration as shown in figure (2.4). The values of P1 and P2 are determined according to the CV. The first potential (P1) which has a more negative value is applied at the ON-TIME (T_{ON}) intervals, during which the electrodeposition process takes place. On the other hand, P2 is a characteristic potential at which the raised current in solution controlled to be around zero. This potential is normally chosen at a less negative value or zero and applied during the OFF-Time (T_{OFF}) so that no deposition takes place during these periods (the rest time). In the experiments of this thesis, P2 could not be set to zero as Cu substrate can be oxidized at this potential. Also, the ‘’Potentiostatic’’ pulsed method was chosen to avoid the damage of the ionic liquid that could arise in the case of a “galvanostatic” pulsed-technique. The pulse duty cycle can be calculated according to equation (2.1).

Duty cycle = T_{ON} / (T_{ON} + T_{OFF})……...………........……..............………...**Equ. 2.1.**

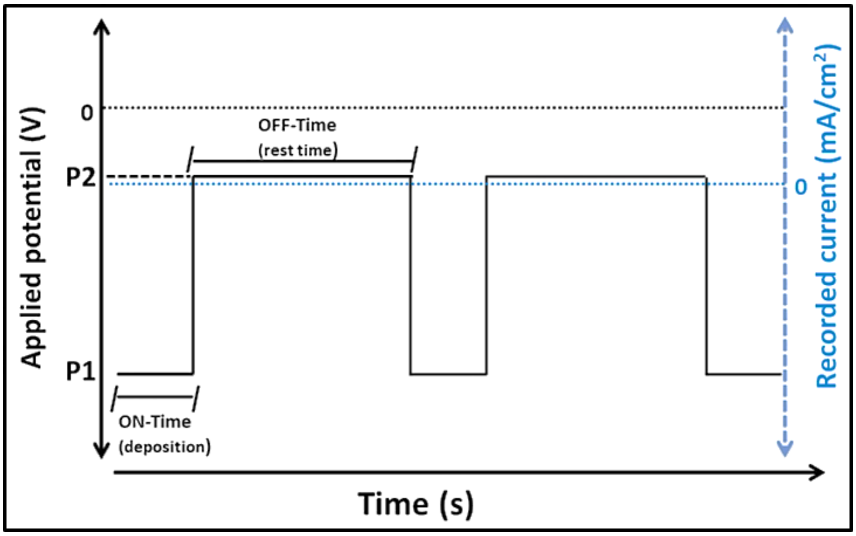

Fig. 2.4. *Typical pulsed-potential square waves applied in potentiostatic pulsed-electrodeposition with the correlated current density.*

2.4. Characterization techniques

2.4.1. Scanning Electron Microscopy (SEM)

A Field Emission-Scanning Electron Microscope (FE-SEM) from Joel Company was used as the standard technique to qualitatively characterize the topography and morphology of the deposited Si, Si_xGe_{1-x}, $Si_xGe_{1-x}Al_y$ and Si-rGO films. This technique is equipped with Energy Dispersive X-ray (EDX) spectroscopy to analyze the composition of the deposited films. After each deposition, all deposits were washed with Di-Methyl Carbonate (DMC) and dried inside of the glove box before transferring to a SEM (JOEL:JSM-7610F). The apparatus is provided by a Semi-in lens type OL which can create a strong magnetic field around the specimen, providing an ultra-high spatial resolution (1 kV 1.3 nm, 15 kV 1 nm). The dried films were taped on top of a flat SEM-holder for the top-view investigations or on the side of a 90°-vertical SEM holder for the cross-section view and film-thickness measurements.

In SEM investigations, images are produced by probing the sample with a primary electron beam with electron's energy up to 50 keV, generated by heating a metallic cathode whose emitted electrons are accelerated by high voltage and focused by several electromagnetic lenses. The electron beam scans the sample across a rectangular area and interacts with it in the form of elastic and inelastic interactions. The interaction between the electron beam and the sample surface results in the emission of high energy-backscattered electrons, low energy-secondary electrons, light emission, and X-ray emission as sketched in figure (2.5) **[146]**.

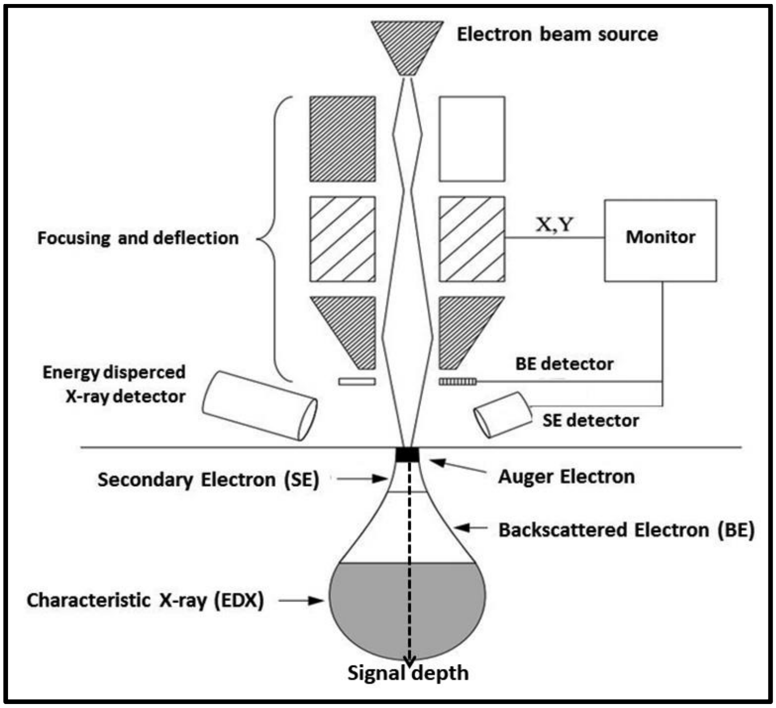

Fig. 2.5. *A schematic diagram of the Scanning Electron Microscope (SEM) principle (modified from H. Lüth et al.* [146]*).*

The backscattered electrons result from elastic interactions between the subjected beam and nuclei, while the secondary electron is induced from the inelastic interaction between the subjected beam and the nuclei [147]. In addition, these interactions may also induce Auger electrons. In SEM, the secondary and backscattered electrons are mostly used for imaging the topography and morphology of the examined spacemen.

2.4.2. Energy dispersive X-ray spectroscopy

Energy dispersive X-ray (EDX) spectroscopy is a technique integrated into the SEM device that can be used simultaneously during SEM analysis. In EDX, the emitted X-Ray which results from the interaction between the primary electron beam and the specimen surface is used for both the quantitative and the qualitative analysis of the tested material. When the primary electron beam hits the nuclei, electrons are ejected out from the atomic shells, leaving a hole which is further filled by another electron from higher shells. The energy difference between these two electrons results in the form of X-ray [146]. The X-ray spectra are characteristic for each element that can be used to analyze the composition of the films through not only direct analysis for specific areas, but also for mapping the element distribution in the film.

2.4.3. Fourier Transform Infrared Spectroscopy (FTIR)

The FT-IR measurements were performed on a Bruker VERTEX 70 FT-IR spectrometer which consists of a multilayer mylar beam splitter DLATGS detector with preamplifier and polyethylene (PE) windows for the internal optical path. The instrument was equipped with an extension for measurements in the far-IR region. The accessible spectral region for this configuration was between 30 and 3600 cm^{-1}.

2.4.4. Raman spectroscopy

The Raman spectroscopic measurements were carried out with a Raman module FRA 106 (Nd:YAG laser, 1064 nm) attached to a Bruker IFS 66V interferometer. The samples were sealed under an argon atmosphere in glass capillaries and the measurements were carried out at room temperature.

2.4.5. X-ray Photo-electron Spectroscopy (XPS)

The chemical compositions of the deposited and cycled Si, Si_xGe_{1-x}, $Si_xGe_{1-x}Al_y$ and Si-rGO films were analyzed using X-ray Photo-electron Spectroscopy (XPS). The deposits or the cycled anode films were washed gently with dimethyl carbonate for only 5 seconds to remove the electrolyte residuals, and then mounted on a hermetic XPS-transfer chamber to ensure no exposure to air.

2.4.5.1. XPS apparatus and measurements

The XPS measurements were performed using a monochromatic XPS device (XR50M with monochromator Focus 500, SPECS) under ultrahigh vacuum conditions using Al Kα line with photon energy of 1486.61 eV. The spectra were collected perpendicular to the sample surface by hemispherical electron energy analyzer (HSA) (Phoibos 150, SPECS), which was used in Medium Area Lens Mode with a pass energy (Epass) of 20 eV. The FWHM of the measured peaks was of up to ∼1.1 eV (for C 1s). In XPS measurements, the samples were irradiated using Al Kα line photon energy of a monochromatic X-ray source. The spectra were obtained using an ultrahigh vacuum (UHV) apparatus with a base pressure (UHV, basis pressure below 5×10^{-10} mbar). The emitted electrons were detected using a hemispherical analyzer (Omicron EA125) under an angle of 45° to the surface normal. All XPS spectra were displayed as a function of the binding energy with respect to the Fermi level. The survey scans were obtained within 1 mm x 1 mm spot size with 0.5 eV step for 40 minutes as total scan time. The narrow scans were obtained with 1 mm x 1 mm spot size with 0.25

eV step for 2-10 minutes as totals scan time. The etching was done with 2 keV Ar ions for different time ranging between 5-20 minutes, according to the desired depth-profile and the roughness of the analyzed layer.

2.4.5.2. XPS fitting

The fitting of XPS spectra was performed with Casa-XPS software (version 2.3.15, Casa Software Ltd.) to identify the atomic and chemical composition of the tested films at different sputtered layers. All samples were assumed to be electronically insulating and fitted with linear backgrounds. The spectra were corrected by an electron energy transmission curve, which was calibrated in several measurements of compounds with known chemical composition. The obtained figures present the spectra as a function of binding energy (BE) with respect to the Fermi level. Some spectra were shifted with respective to C 1s assigned at 284.8 eV to compensate for any offsets (occurring during the measurements) or shifts resulting from charging the film which is normally found in semiconductor films. The detail spectra are shown after background subtraction according to Shirley *et al.* **[148]**. The decomposition of experimental peaks was made by a superposition of Gaussian and Lorentzian functions. To get quantitative chemical composition, the calculated photo-electronic cross sections were taken into account according to Scofield *et al.* **[149]**, ranged between 5-20 minutes, according to the desired depth-profile and the roughness of the analyzed layer.

2.4.6. Electrochemical investigations in lithium-ion batteries

The Electrochemical performances of as-deposited Si, Si_xGe_{1-x}, $Si_xGe_{1-x}Al_y$, and Si-rGO films were tested as anode-films in LIBs. Cyclic Voltammetry (CV), galvanostatic charge/discharge and Electrochemical Impedance Spectroscopy (EIS) tests were performed for all of the deposited films in a “sandwich cell” inside the aforementioned glove box using VersaSTAT 3 (Princeton Applied Research) potentiostat/galvanostat controlled by power-CV and power-step software. After depositions, the deposits were removed and cleaned with DMC, subsequently investigated in Half-cell LIBs type in 0.5 M LiTFSI/[BMP]TFSI] electrolyte.

2.4.6.1. Half-cell design

i. Electrodes

The electrodeposited Si, Si_xGe_{1-x}, $Si_xGe_{1-x}Al_y$ and Si-rGO films were tested as anodes in a half-cell LIB in which the deposits were cycled versus a Li foil (Alfa Aesar 99%) as the reference and the counter electrode. Before using the Li foil, it was scratched gently with a spatula inside the glove box to remove the superficial oxidized layers.

ii. Separator

A separator is a porous membrane placed between the two electrodes that should be permeable for Li ions but electronically acting as an insulator that prevents the electric contact between the battery electrodes [150]. The separator must be electrochemically stable towards both the electrolyte and the electrode materials. Furthermore, it should be porous enough with good wettability and should have sufficient mechanical strength and a homogeneous pore-distribution [150, 151]. The deposited anode-films and the Li foil were separated in all electrochemical experiments of this thesis by a commercial porous polypropylene membrane (Celgard® 2400) of 25 µm-thickness.

iii. Li ion electrolyte

The role of the Li-ion electrolytes in LIBs is to act as an ionic conductor to accomplish the transportation process of lithium ions between the positive and the negative electrode during charging and discharging processes [151]. The choice of the battery electrolyte is very crucial to optimize the battery performance. The capacity of a cell and its lifetime are affected by the battery electrolytes and the reactions within the electrode-electrolyte interface as well [152]. LiTFSI (0.5 M) dissolved in [BMP]TFSI ionic liquid was the electrolyte of choice used to investigate the electrochemical performance of Si, Si_xGe_{1-x}, $Si_xGe_{1-x}Al_y$ and Si-rGO films. LiTFSI/ILs electrolytes have been intensively studied as an alternative batteries-electrolyte. These types of electrolytes gained particular interests due to its broad electrochemical window, its electrochemical stability, its safety and its relatively low viscosity [153, 154], compared to the conventional LIB electrolytes in which Li salts (such as $LiPF_6$) dissolved in carbonates-organic electrolytes.

iv. Current collectors

Al and Cu are often used as the current collector in LIBs. For Al, it is commonly used as the current collector for cathode materials, owing to its chemical stability at high voltages in the range of 3-5 V versus Li/Li^+. Copper is customarily used as the current collector for negative electrodes (anodes) due to its electrochemical stability in the potential range below 3 V versus Li/Li^+. As all Si, Si_xGe_{1-x}, $Si_xGe_{1-x}Al_y$ and Si-rGO films were deposited on Cu plate, a Cu substrate was also applied as the current collector in the designed cell. For Lithium reference/counter electrode, Cu was also used as its current collector as the OCP of half-cells is not exceeding 3 V versus Li^+/Li.

2.4.6.2. Electrochemical methods

2.4.6.2.1. Cyclic voltammetry

Cycling voltammetry of as-deposited Si, Si_xGe_{1-x}, $Si_xGe_{1-x}Al_y$ and Si-rGO films were performed against Li electrode in 0.5 M LiTFSI/[BMP]TFSI electrolyte, to test the alloying/de-alloying features of lithium in these anode films. All CV experiments were conducted using VersaSTAT 3 (Princeton Applied Research) potentiostat/galvanostat, controlled by power-CV and power-step software at a scanning rate of 1 mV/s.

2.4.6.2.2. Galvanostatic charge/discharge evaluations

Galvanostatic investigation is a chrono-potentiometry or a constant current technique, considered as the standard method to evaluate the cycling performance, by measuring the amount of charge stored and released by the tested electrode in LIBs. From this method, the specific capacity values, the voltage profiles, the cycling stability and the rate-capability of the tested electrode can be evaluated. The galvanostatic charge/discharge evaluations of as-deposited Si, Si_xGe_{1-x}, $Si_xGe_{1-x}Al_y$ and Si-rGO films were tested in the aforementioned glove box using VersaSTAT 3 (Princeton Applied Research) potentiostat/galvanostat, controlled by power-CV and power-step software.

i. The initial charging

The initial charging of the tested anodes should be performed at a low current density so that the SEI can be formed uniformly and smoothly. The initial charging of Si, Si_xGe_{1-x}, $Si_xGe_{1-x}Al_y$ and of Si-rGO films were often performed at a current density of 0.03 mA/cm^2.

ii. Calculation of the anode active-mass

For electrodes which are made by the casting procedure, the mass of the active material is known prior to the cycling according to the ratio of the active material to that of other additives (binder and conductive carbon). For electrodeposited films, the films contain other inactive elements, thus it is more equitable to calculate the mass of the active material in deposited films (Si, Ge, Al, and graphene) from the first charging time, taking into account that the anode produces a practical capacity close to their theoretical capacities upon initial charging.

iii. Calculation of the theoretical capacities

Generally, the theoretical capacities of alloy-type electrodes are calculated according to equation (2.2), where ξ is the molar concentration of Li at full lithiation, **n** is charge number carried by Li (1C) and **F** is Faraday constant (96500 C/mol= 26800 mAh/mol).

$$\textbf{Theoretical capacity (mAh/g)} = \frac{\xi.\mathrm{n.F}}{\textbf{Molar mass of the anode}} \textbf{..........Equ. 2.2.}$$

- For Si, its theoretical capacity was calculated according to equation (2.3) **[83]** taking into consideration that the fully alloyed-form of Si with Li is $Li_{15}Si_4$, so ξ, in this case, equals to 3.75 mols. Also, the molar mass of Si (M_{Si}) is 28 g/mol, thus the theoretica capacity for Si anodes is 3589 mAh/g.

$$\textbf{Si theoretical capacity (mAh/g)} = \frac{\xi.\mathrm{n.F}}{\textbf{Molar mass of Si}} \textbf{................Equ 2.3.}$$

- For Si_xGe_{1-x} alloys, the theoretical capacity was calculated according to equation (2.4), taking into consideration that the fully lithiated form of Ge is equal to that of Si ($Li_{15}Ge_4$) according to Baggetto *et al.* **[155]**. The value of Si_xGe_{1-x} capacities varied according to the stoichiometry of Si and Ge in the alloy film, taking into consideration that the molar mass of Ge (M_{Ge}) is 72.64 g/mol.

$$\mathbf{Si_xGe_{1-x}}\ \textbf{theoreitical capacity (mAh/g)} = \frac{\xi.\mathrm{n.F}}{\mathrm{x(MSi)+1-x\ (MGe)}} \textbf{............Equ. 2.4.}$$

- For $Si_xGe_{1-x}Al_y$ alloy, its theoretical capacity was calculated according to equation (2.5), where the value of ξ' in the case of Al is equals to 1.5 mol according to the Li-Al alloying phase of Li_3Al_2 **[156, 157]**, thus the theoretical capacity of Al is 1989 mAh/g.

$$\mathbf{Si_xGe_{1-x}Al_y}\ \textbf{theo. capacity (mAh/g)} = \frac{\xi.\mathrm{n.F}}{\mathrm{x(MSi)+1-x\ (MGe)}} + \frac{\xi'.\mathrm{n.F}}{\mathrm{y(MAl)}} \textbf{...Equ. 2.5.}$$

- For Si-rGO composite anode, the theoretical capacity of graphene was considered to be 1116 mAh/g. This value was estimated according to T.M. Paronyan *et al.* who reported that Li intercalates with graphene sheets in the lithiated-form of Li_NC_{2N} **[97]**. Consequently, the theoretical capacity of Si-rGO anode can be calculated according to equation (2.6), considering the value of ξ'related to graphene to be 0.5 mol.

$$\textbf{Si-rGO theo. capacity (mAh/g)} = \frac{\xi.n.F}{x(MSi)} + \frac{\xi'.n.F}{y(M\ Carbon)} \quad \text{………....Equ. 2.6.}$$

iv. Current density and cycling-rate

In galvanostatic cycling, the current density (expressed by mA/g), is the amount of charge at which the desired electrodes is cycled, calculated based on the mass of active material. According to the Electrochemical Dictionary **[158]**, the current density can also be expressed in terms of the cycling rate (C-rate), where 1 C is the amount of charge, inserted in or extracted from the investigated electrode in one hour, noted by ampere-hours (Ah). In case of thin film electrodes, it is more reasonable to quantize charge and discharge loading rates in mA/g, so that the active mass of electrodes can be compared and the areal capacity (mAh/cm^2) can be evaluated. Long cycling of as-deposited Si, Si_xGe_{1-x}, $Si_xGe_{1-x}Al_y$ and Si-rGO films was firstly performed at a constant C-rate to evaluate their cycling stability. Also, these anode films were cycled at higher C-rates to investigate their load capability (rate-capability). It should be taken into consideration that, as the cycling rate increases, the performance of the tested electrode usually decreases.

v. Coulombic Efficiency (CE)

Coulombic efficiency (CE) gives an indication of the cycling stability in terms of the reversibility of de-lithiation processes in tested electrodes. CE is given as a percentage (%), calculated by dividing the charge retained from de-lithiation process over the charge entered during the lithiation process. The first irreversible capacity loss is the inverse of the coulombic efficiency of the first cycle during which SEI is formed. After the first cycle, charge/discharge capacities are lower than the initial charging capacity, which -in turn- accounts for the largest amount of charge consumed in SEI formation.

vi. Capacity retention

Capacity retention is the specific capacity that the electrode is able to retain after a specific number of cycles, giving an indication of the cycling stability at a specific current rate. In alloy-type anode materials, capacity retention is an important factor that implies the chemical and mechanical stability of the electrode upon cycling.

2.4.6.3. Electrochemical Impedance Spectroscopy (EIS)

EIS has also been performed to distinguish not only the electrochemical reactions taking place in the surface and the bulk vicinity of Si, Si_xGe_{1-x}, $Si_xGe_{1-x}Al_y$ and Si-rGO films but also to evaluate the lithiation/delithiation kinetics inside of these films. EIS measurements have been investigated in the aforementioned glove box using VersaSTAT 3 (Princeton Applied Research) potentiostat/galvanost. The fresh and the cycled anode films were tested by EIS with an ac-amplitude of 10 mV within a frequency range of 100 KHz to 0.1 Hz. The measured spectra were fitted with Z-SimpWin software. The in-phase and out-of-phase components corresponding to the current response were fitted to equivalent circuits that model only the half-cell, excluding the EIS response of Li reference/counter electrode. The values of the capacitance (C_{dl}, C_{SEI}, $C_{ads/trab}$, etc.) are mainly frequency-dependent, considered as the most complex components of the battery circuit. Sometimes they had been replaced by the constant phase elements (CPE) as a proper alternative for fitting the depressed semicircles in Nyquist plots due to the non-uniformity of the interfacial-SEI layer and the microscopic characteristic of deposit particles.

3. Results and discussion

3.1. Silicon anode-films

3.1.1. Silicon film by pulsed-electrodeposition at a duty cycle of 50%

3.1.1.1. Cyclic voltammetry of $SiCl_4$/[BMP]TFSI electrodeposition bath

Cyclic voltammetry was firstly performed for the neat [BMP]TFSI ionic liquid to evaluate its electrochemical window (ECW) and to distinguish its electrochemical stability on Cu. Figure (3.1a) shows the cyclic voltammogram of neat [BMP]TFSI, recorded on a Cu substrate at a scan rate of 50 mV/s. The cathode potential was scanned from OCP to -4 V versus Pt as a quasi-reference electrode (QRE). The $[BMP]^+$ cation starts reduction after -2.75 V then the cathodic current sharply increases, indicating the full breakdown of the ionic liquid. Endres *et al.* have reported that [BMP]TFSI ionic liquid exhibits an electrochemical window of 5 V when cycled from 3 to -3 V (vs. Pt QR) on Au(111) **[159]**.

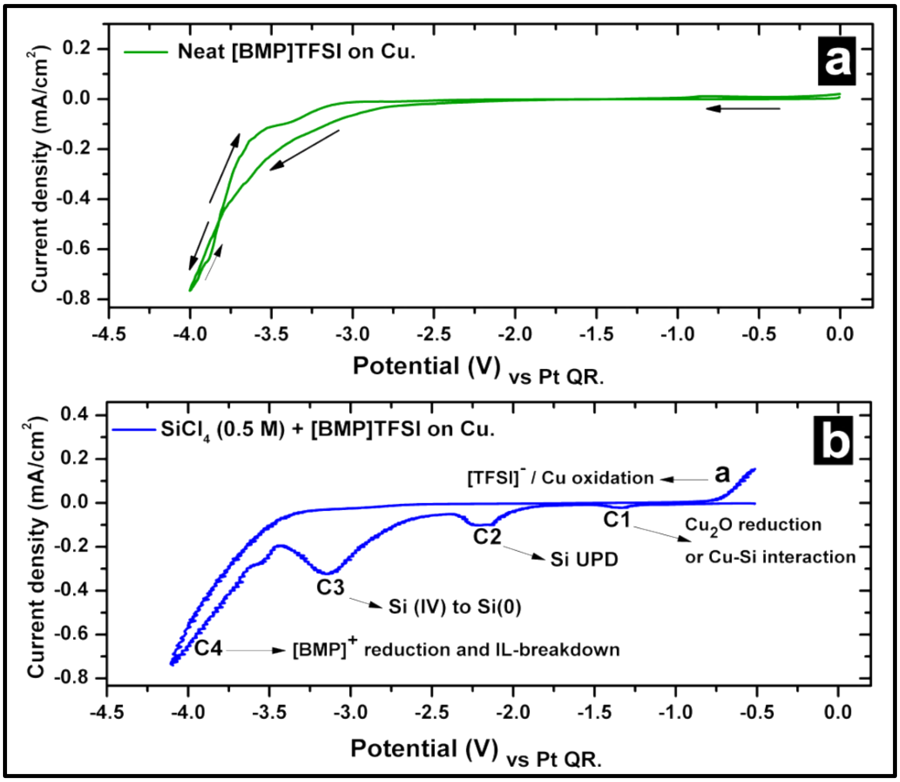

Fig. 3.1. (a) *Cyclic voltammogram of the neat [BMP]TFSI ionic liquid, recorded on Cu substrate from OCP to -4 V at a scan rate of 50 mV/s.* ***(b)*** *Cyclic voltammogram of $SiCl_4$ (0.5 M) in [BMP]TFSI on Cu from OCP to -4 V at a scan rate of 50 mV/s.*

Cyclic voltammetry was also used for $SiCl_4$/[BMP]TFSI electrodeposition bath to understand the electrochemical reactions regarding Si electrodeposition in the employed electrolyte. Figure (3.1b) represents the cyclic voltammogram for a solution of $SiCl_4$ (0.5 M) in [BMP]TFSI, recorded on a Cu substrate. The cathode potential was swept from OCP to -4 V versus Pt QRE at a scan rate of 50 mV/s. As labeled, the cathodic regime shows four reduction peaks. The foremost reduction peak (C1) can be attributed to the reduction of the superficial Cu-oxide layer, as reported by C. A. Vlaic *et al.* and supported by quartz crystal microbalance (QCM) technique **[160]**. This peak does not exist in the cyclic voltammogram of pure [BMP]TFSI on copper, so it is likely correlated to a type of reaction between $SiCl_4$ and Cu forming Cu-silicide compounds **[161]**. The second reduction peak (C2) at around -2.2 V can be indexed to under-potential deposition process of Si (Si UPD) on Cu substrate **[161]**. Also this peak could be correlated to the formation of oligochlorosilanes **[162]**. The third cathodic peak (C3) at around -3.15 V is correlated with bulk deposition of Si **[161, 162]**. On the more negative cathodic side, the rising current after -3.5 V is related to the reduction of the $[BMP]^+$ cation, after which the ionic liquid fully breaks down **[161, 162]**. On the other hand, the anodic part shows one oxidation peak before -0.75 V, which can be indexed to the oxidation of either the $[TFSI]^-$ anion and/or the Cu-substrate. The electrochemical stability of [BMP]TFSI makes it a suitable electrolyte for Si electrodeposition on Cu substrates. Its not too high viscosity, its good conductivity and its kinetic diffusivity provide a good environment for $SiCl_4$ reduction.

3.1.1.2. Potentiostatic pulsed-electrodeposition of Si film in [BMP]TFSI at a duty cycle of 50%

A Si film was prepared by the potentiostatic pulsed-electrodeposition technique as an extension of the conventional potentiostatic electrodeposition method, aimed to produce better Si deposit with improved physical and electrochemical properties **[135, 138-140]**. Figure (3.2a) shows the overall pulsed-potential waves along with the *j*/t curve for Si electrodeposition from 0.5 M $SiCl_4$/[BMP]TFSI. The electrodeposition was performed for three hours and the applied potential values were adjusted by a computer-controlled potentiostat. Figure (3.2b) shows a magnification of the applied potential waves with the associated current values at the pulses intervals. Each pulse was adapted for 10 seconds during which a more negative cathodic potential (P1) with a value of -3 V was applied during ON-TIME (T_{ON}) intervals for 5 seconds. Constantly, a less negative cathodic potential (P2) with the values of -0.7 V was applied for another 5 seconds during the OFF-TIME (T_{OFF}) intervals, so the pulse duty cycle was controlled to be 50%. The potential waves did not appear as square-waves only due to some limitations in the potentiostat. The potential values were selected according to the CV features shown in figure (3.1b) that P1 is the characteristic potential for the Si electrodeposition. Also, P2 was selected at such value (-0.7 V) that almost no current expected to arise through the deposition solution (the rest-time).

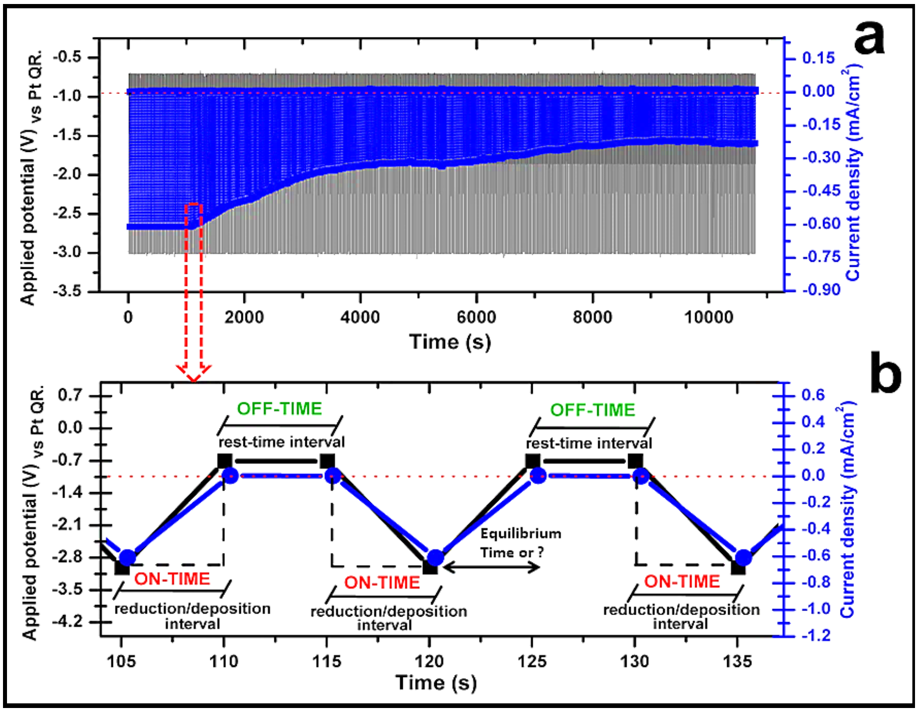

Fig. 3.2. *Potentiostatic pulsed-electrodeposition of Si in [BMP]TFSI at a duty cycle of 50%;* ***(a)*** *overall potentiostatic pulsed-electrodeposition curve along with the j/t curve for 3 hours,* ***(b)*** *close-up portion for the applied potential waves (black) along with the associated current density (blue). When applying P2 (-0.7 V) during* T_{OFF} *intervals, the values of the evolved current is almost zero.*

Applying the T_{OFF} (the rest–time intervals) is the significant difference between the continuous electrodeposition and the pulsed-electrodeposition procedure, which can provide a better chance for both the deposition interface to discharge and for the electrodeposition solution to diffuse, replenishing its concentration nearby the deposition vicinity. At these conditions, both the nucleation rate and the deposition efficiency can be improved, so that the obtained deposit is expected to be more compact, dense with smaller particles [135, 138, 164] which can reflect positively on the electrochemical performance of the deposited film when applied as an anode in LIBs.

3.1.1.3. Scanning Electron Microscopic investigations

FE-SEM images of the Si film deposited by potentiostatic pulsed-electrodeposition for three hours at a duty cycle of 50% is shown in figure (3.3a, b). From the macroscopic view, the morphology of Si film appears as less compact, consisting of cracked islands with a porous structure. The feature of the deposit regarding its non-compactness and its non-homogeneity features can be explained in terms of the pulses temporal parameters (T_{ON}, T_{OFF}). In the case of the pulsed electrodeposition of Si at a high duty cycle values with equal T_{ON} and T_{OFF} intervals (50% duty cycle), the timescale of T_{ON} intervals seems to be more satisfactory for the reduction of the analyte/electrolyte than for their diffusion. On the other hand, during T_{OFF} intervals, the timescale for discharging the deposition and for replenishing the analyte concentration at the deposition vicinity seems to be not long enough. Consequently, the accumulation of charges at the deposition interface is expected, which makes the diffusion from the bulk solution to the cathode surface more difficult with time, resulting in porous Si deposits with less compact feature [135, 164].

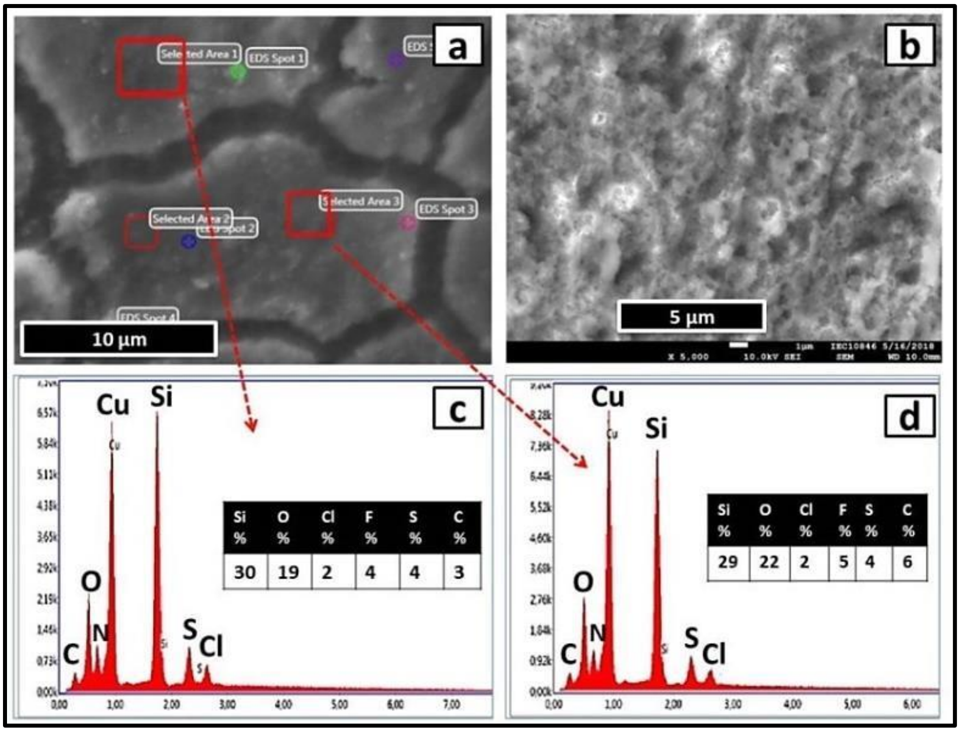

Si %	O %	Cl %	F %	S %	C %
30	19	2	4	4	3

Si %	O %	Cl %	F %	S %	C %
29	22	2	5	4	6

Fig. 3.3. *FE-SEM images of as-deposited Si film in [BMP]TFSI by potentiostatic pulsed-electrodeposition at 50% duty cycle* ***(a, b)****. EDX spectra of the deposited Si film at different scanned areas with the elemental atomic ratios* ***(c, d)****.*

Figure (3.3c, d) shows the EDS-spectra of as-deposited Si films at different scanned areas. The percent of oxygen in the EDS spectra partially arose from the deposit oxidation when the sample was transferred to SEM device under air. The C, S, N and F traces are IL-residuals which seem to be trapped in the deposits films. Indeed, [BMP]TFSI seemed to be exposed to a non-bulk decomposition, affected by a localized over-potential on the growth sites as reported by B. Gattu *et al.* **[135]**.

3.1.1.4. X-ray Photoelectron Spectroscopy of Si film

Ex-situ XPS analysis was performed for as-deposited Si films, to investigate the composition in different deposition layers. Figure (3.4a) shows the XPS survey spectra of the deposit before and after sputtering. The upper-most layer is mostly covered with decomposed products of [BMP]TFSI. After sputtering, the spectra of Si and other elements (Cl, C, S, N, O and F) are detected which were trapped in the bulk vicinity of the deposit **[135]**. Also, a large Cu peak can be detected after sputtering for 10 and 20 minutes, which may refer to the dissolution of Cu and its reaction with the electrolyte and $SiCl_4$ analyte.

The high resolution spectra of Si 2p, F 1s, O 1s, N 1s, C 1s and Cl 2p with their deconvolutions in different deposit layers are illustrated in figure (3.4b). Si 2p spectra indicate that the elemental Si is partially oxidized to SiO_2 which peak is evident at around 104 eV, supported by the SiO_2 peak at around 533 eV in O 1s spectra **[165]**. The deconvolution peak located at 101 eV in Si 2p could be indexed to either fluorinated Si (SiF_x) **[166]** or Cu-Si compounds **[167, 168]**. It seems that F ions might somehow reacted with Si particles by breaking the Si-Si bond forming SiF_x compound which could result in a shift in Si peaks position to higher binding energy at 101 eV, supported by the correlated SiF_x peak in F 1s spectra at around 685 eV **[169, 170]**. According to S. Yokoyama *et al.* **[166]**, as the full width at half-maximum (FWHM) of Si 2p is increased after sputtering, SiO_2 peak could be indexed to fluorinated-SiO_x, especially it is shifted to higher binding energy from 103 to 104 eV **[165]**. In Cl 2p spectra, the doublet peak at around 200 and 202 eV could be attributed to $CuCl_x$ compounds **[165]**, referring to the reaction of copper with the solutechloride ions. C 1s spectra show two peaks related to $[BMP]^+$ cation in either alkyl (C-C and C-H) or in Pyrrolidine form (C-N) which appears prominently in the upper layers [165]. Also, C-F_x peaks can be detected in the deeper layers at around 290 eV, supported by the corresponding peak in F 1s spectra at around 690 eV [165, 171]. The alkyl radicals which results from the reduction and decomposition of $[BMP]^+$ on deposit surface could attack the Si-Si bond through nucleophilic reactions forming Si-C bond [171-173], which peak can be detected in C 1s spectra at around 283 eV. The alkyl radicals could also attack the Si-O-Si bond forming new Si-O-C bond [172], which peak could occur at 104 eV in Si 2p spectra. Also, the energy shift of SiO_2 peak in O 1s spectra to a higher binding energy (584 eV) may suggest the formation of Si–O–C and/or Si–O–F bonds on the surface of Si particles [166]. Si–O–C compounds were reported to be a promising material that can improve the cycling stability of a Si anode in LIBs [174]. Carbonates peak can be also detected in C 1s spectra at around 288 eV which could be overlapped with –C=O peaks [165]. In N 1s spectra, the intensities of N_{anion} and N_{cation} peaks are not equal in all investigated layers, which can refer to the decomposition of [BMP]TFSI in the upper deposit layer and in the bulk deposit as well [171, 175].

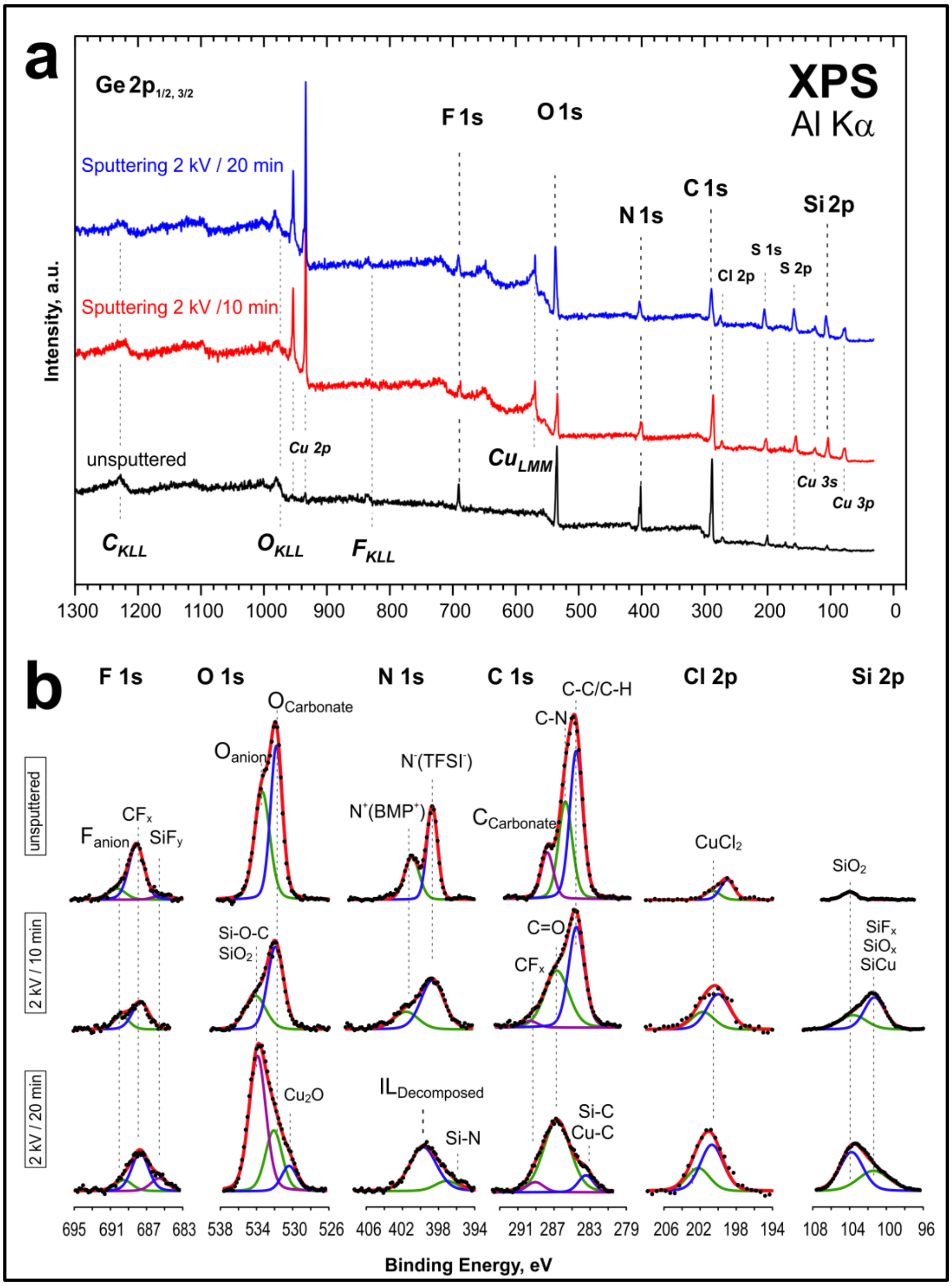

Fig. 3.4. *XPS analysis of as-deposited Si film prepared by potentiostatic pulsed- electrodeposition in [BMP]TFSI at a duty cycle of 50%;* ***(a)*** *overall XPS survey,* ***(b)*** *high resolution spectra of F 1s, O 1s, N 1s, C 1s, Cl 2p and Si 2p with their deconvolutions in upper-most and two sputtered layers.*

Figure (3.5) shows the atomic ratios of F 1s, O 1s, N 1s, C 1s, Cl 2p and Si 2p obtained by XPS analysis. The atomic percent of Si compounds increases deeper in the film. C-compounds have the most prominent ratios, contributing to the film composition by ~30%. The majority of C-compounds results from the decomposed $[BMP]^+$ cations. The reduction/decomposition process of $[BMP]^+$ cation during deposition could be explained as reported by C. Nguyen *et al.* as follow. During the electrodeposition process of Si, electrons are swept to the Si@Cu cathode which becomes negatively charged, so the Pyrrolidine ring is adsorbed and reduced on the deposit surface. The reduction of $[BMP]^+$ cations results in the decomposition of the alkyl group attached with the Pyrrolidine ring producing alkyl radicals **[171-173]**.

The inserted table illustrates the concentration of the decomposition-components of the ionic liquid-cation (C_{alkyl}, C_{hetero}, carbonates/-C=O, N_{cation}) and the ionic liquid-anion (CF_x, N_{anion}), in addition to $CuCl_2$ concentrations in the investigated deposit layers. The pure [BMP]TFSI contain single N atom in both the anion and the cation, so the concentration of N_{anion} and N_{cation} should to be equal in case of non-decomposed [BMP]TFSI electrolyte **[175]**. The ratios of N_{anion}/N_{cation} in the upper-most and in the 1st-sputtered layer are less than 1, which can indicate that the electrolyte is partially decomposed. In the 2nd-sputtered layer (bulk deposit), it seems that the electrolyte is fully decomposed. $CuCl_2$ concentration is evident in deeper deposit layers, referring to the reaction of the solute-chlorides and the cupper substrate. It seems that the pulsed electrodeposition at high duty cycle values could results in robust reduction of the electrolyte especially at short T_{OFF} intervals which are not sufficient to refresh the electrolyte concentration nearby the deposition area [163].

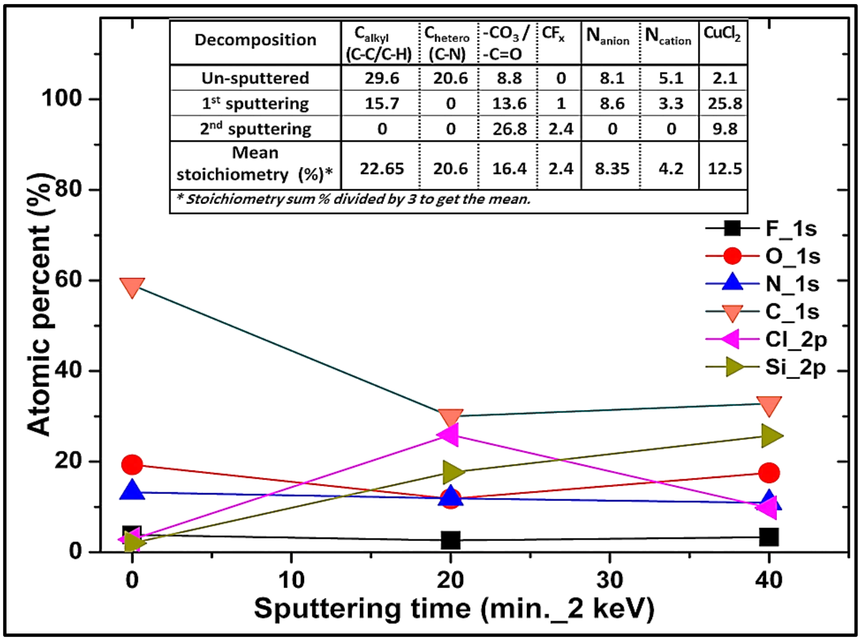

Decomposition	C_{alkyl} (C-C/C-H)	C_{hetero} (C-N)	$-CO_3$ / -C=O	CF_x	N_{anion}	N_{cation}	$CuCl_2$
Un-sputtered	29.6	20.6	8.8	0	8.1	5.1	2.1
1st sputtering	15.7	0	13.6	1	8.6	3.3	25.8
2nd sputtering	0	0	26.8	2.4	0	0	9.8
Mean stoichiometry (%)*	22.65	20.6	16.4	2.4	8.35	4.2	12.5

** Stoichiometry sum % divided by 3 to get the mean.*

Fig. 3.5. *Relative atomic percent of F 1s, O1s, N 1s, C 1s, Cl 2p and Si 2p calculated from XPS spectra at the uppermost and two sputtered layers of Si film prepared by potentiostatic pulsed-electrodeposition in [BMP]TFSI at a duty cycle of 50%. The inserted table illustrates the stoichiometric data of the electrolyte decomposition-components, in addition to* $CuCl_2$ *concentrations in all investigated deposit layers.*

3.1.1.5. Electrochemical performance in LIB

3.1.1.5.1. Cyclic voltammetry in LIB

To test the lithium alloying/de-alloying features in as-deposited Si films, cyclic voltammetry was performed for this film in half cell against Li (counter and reference electrode) in 0.5 M LiTFSI/[BMP]TFSI electrolyte. The cyclic voltammetry measurements shown in figure (3.6) were tested at a scanning rate of 1 mV/s. The potential was scanned in the range of 0.01 V and $OCP_{LIB\text{-}cell}$ for ten cycles. Generally, the silicon anode film exhibited two lithiation (alloying) processes and a single de-lithiation (de-alloying) process. In the cathodic part, the first cathodic peak centered at 1.4 V is related to SEI formation [176]. This peak exists only in the first cycle, indicating that this interfacial layer stops growing after the initial lithiation. The Li-Si alloying peak starts beyond 0.7 V as a broad peak which disappears after the 5th cycle. The second alloying peak starts at around 0.2 V till 0.01 V, correlated to the Si full lithiation forming $Li_{15}Si_4$ [177]. In the stripping/de-lithiation part, a broad de-lithiation peak at around 0.5 V can be detected in all cycles. It is worth noting that the intensity of de-lithiation peaks increase upon cycling, suggesting a kinetic enhancement in the Si anode film, which was also observed in Si anodes cycled in both $LiPF_6$/fluorinated-EC/DEC and LiFSI/[EMIm]FSI electrolytes [178]. The CV features of as-tested Si film are in good agreements with other Si anode films produced by pulsed-electrodeposition in [BMP]TFSI [135].

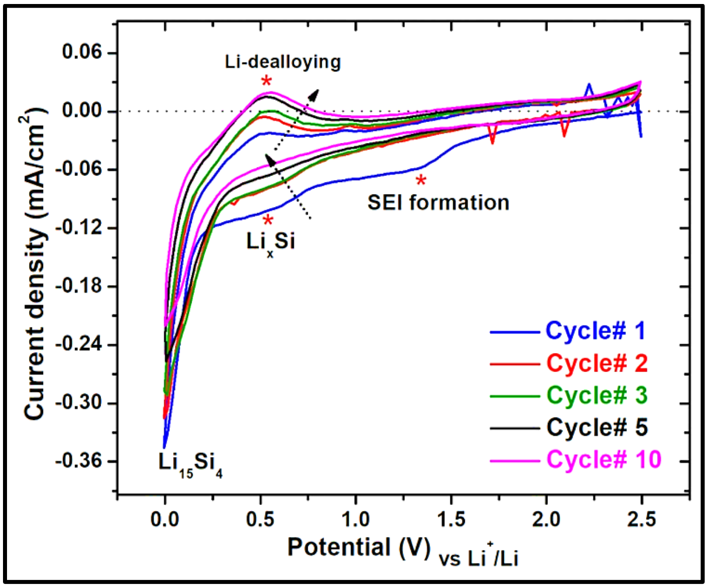

Fig. 3.6. *Consecutive cyclic voltammograms of Si anode films prepared by potentiostatic pulsed-electrodeposition in [BMP]TFSI at a duty cycle value of 50%. The CV measurements were performed at a scanning rate of 1 mV/s in 0.5 M LiTFSI/[BMP]TFSI in half cell-battery against Li (counter and reference electrode).*

3.1.1.5.2. Galvanostatic cycling evaluation in LIB

To evaluate the charge/discharge capacity values and the cycling stability of as-deposited Si films, it was galvanostatically cycled in half cell-LIB versus Li in 0.5 M LiTFSI/[BMP]TFSI electrolyte. Figure (3.7a) shows the potential plateau of the initial charging/discharging cycle at a low current density (0.03 mA/cm^2). The voltage profile is similar to that of Si anodes prepared by different techniques and methods **[176, 177]**. It was essential to perform the first lithiation process at such low current density (less than 0.1 C) so that the SEI can be created smoothly and homogeneously. At the initial charging process, the Si anode film is supposed to electrochemically behave ideally, as the measured capacity is equivalent to the theoretical value of Si (3589 mAh/g). However, the active mass of Si in the deposited film was calculated, found to be 0.0001 g/cm^2. The first capacity loss calculated from the first cycle is very high (84%) which mostly results from the amount of charge consumed in SEI-formation and cannot be retained in the first de-lithiation process or in the subsequent cycles.

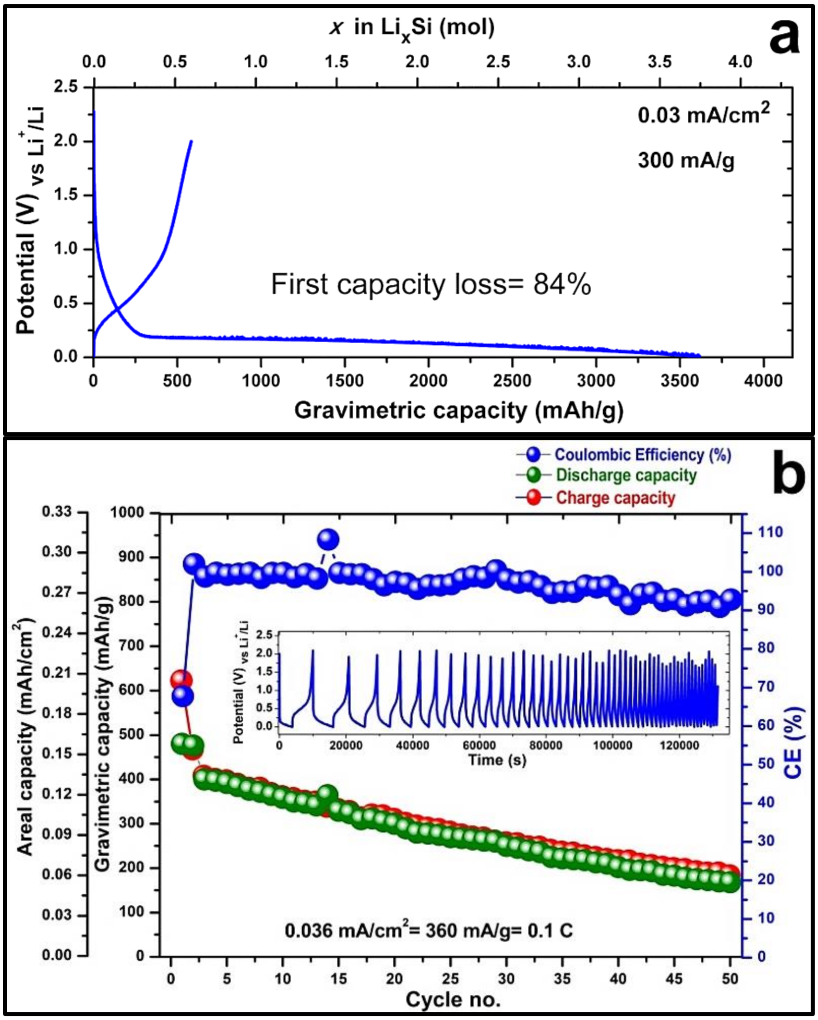

Fig. 3.7. *Galvanostatic cycling performance of as-deposited Si, deposited by potentiostatic pulsed-electrodeposition at a duty cycle of 50%;* ***(a)*** *voltage profile of the initial cycle at a current density of 0.03 mA/g,* ***(b)*** *long charge/discharge cycling at 360 mA/g (0.1 C-rate).*

Figure (3.7b) introduces the galvanostatic cycling performance of as-deposited Si anode for 50 cycles at a current density of 300 mA/g, which is equivalent to 0.1 C-rate. Upon cycling, the anode film displayed good coulombic efficiency of around 95%, which reflects the feasibility of the reversible de-alloying processes in the film. Even though, the cycled anode-film shows a continuous decrease in capacity. The capacity retention after 50 cycles is only 35% of that retained in the initial discharge. The areal capacities are less than 0.2 mAh/cm^2 due to the low values of the produced capacities, added to the low mass loading of the Si film, compared to other Si electrodes made by casting procedures. The poor cycling performance could be explained in terms of the weak compactness feature of the deposit. The cracked Si deposit seemed to interrupt the diffusion of Li^+-ions, which deteriorates the cycling stability. Also, the structural deformation of the Si anode and the over growth of SEI upon long cycling are the expected drawbacks that participate in the capacity fading, deteriorating the cycling stability of Si anode-film.

3.1.1.6. Electrochemical Impedance Spectroscopy (EIS)

Electrochemical Impedance Spectroscopy (EIS) is a distinguishing tool for investigating the Li^+ ion kinetics at the electrolyte/electrode interface and in the bulk electrode, owing to its advantage of separating the diffusion processes from other electrochemical processes in a wide frequency range. Figure (3.8) shows the EIS-Nyquist plots of Si anode films over 50 cycles at 0.1 C-rate by applying an ac-amplitude of 20 mV in the frequency range 10^5-0.1 Hz. The inset shows a magnification of the Nyquist plots in the high-to-medium frequency range. The intercept with *x*-axis signifies the equivalent series element of the ohmic resistances (R_0), interrelated to the reciprocal of ionic conductivity of the electrolyte solution and the contact resistance of the cell hardware (the separator contact resistance and the current collector resistance) **[179]**. It can be noticed that R_0 resistance values increase with cycling especially after the 30th and the 50th cycles, which can refer to the delamination of Si film from the Cu-current collector added to the increased electrolyte resistance over long cycling **[180]**.

All Nyquist plots exhibit one semicircle in the high-to-middle frequency region as shown in the magnification inset inside figure (3.8), followed by one Warburg-diffusion line in the low-frequency range. The slope of the Warburg line at high-to-medium frequencies has angle values more than 45°, which seems to be a contribution of a pseudo-capacitive behavior. The absence of the first semicircle in the high-frequency range which resembles the impedance contribution on SEI (Z_{SEI}) implies that the resistance through this interfacial layer is negligible and can be comparable with the ultra-thin SEI film formed in $LiPF_6$/fluorinated-EC electrolytes **[181]**. The single semicircle is correlated to the Faradic impedance response of Li ions intake in the bulk anode-film which shares the contribution of the mass transfer resistance and the doubl-layer capacitor denoted by R_{ct}, C_{dl}. The values of this Faradic impedance increase with cycling due to the deformation of the anode, hindering the lithium kinetics inside of the Si film. A Warburg tail can be used to qualitatively evaluate the lithium kinetics in the bulk anode film, where its value is inversely proportional to the length of the imaginary impedance (Z_{im}) **[182]**. Accordingly, the Warburg tail after the second charging/discharging cycle becomes longer, suggesting lower accessibility (decreased Li^+ diffusivity) of Li ions during the successive cycles.

The best fitting equivalent circuit (shown inside figure 3.8) exhibits an extension of the conventional equivalent circuit customarily used in LIB-EIS studies. It includes a contribution of a non-Faradic impedance related to an adsorption/trapping process (R_{ads}/C_{ads}) existing in parallel to the mass transfer impedance, which can be indexed to the impedance response of a partially covered electrode **[183]**. $C_{alloying}$ and $R_{alloying}$ denote to the impedance contribution by alloying and de-alloying processes. This circuit could arise some question concerning adsorption/trapping processes that need further investigations on different Si anodes and in different LiTFS-ILs electrolytes, which could not be accomplished due to the time-limitation. As C_{SEI}, C_{dl} and $C_{ads.}$ are mainly frequency-dependent as the most complex components of the battery circuit, they were sometimes replaced by constant phase elements (CPE) as a proper alternative to fit the depressed semicircles in Nyquist plots, as a consequent of the non-uniformity of the interfacial-SEI layer, in addition of the porosity and the microscopic characteristic of the deposited particles **[180]**. J. R. MacDonald has introduced a similar circuit network (ladder network) that proposes simulating adsorption, which can be applied for electrode systems **[184]**. The diffusion-trapping impedance has been studied by C. Montella *et al.* postulating its kinetic model which is also valid for the ion insertion in host electrode materials **[185]**. J. Bisquert has reported that the ion-trapping process contributes Faradaic impedance with capacitive and resistive EIS components in the low frequency region **[186]**. At this end, the Si anode may exhibit adsorption/desorption processes which refers to its complicated interactions not only with lithium but also with other electrolyte-elements during cycling. Fluorine may play a role in the reduction of SEI thickness which should reflect positively on the cycling performance of the Si anode. Even though, EIS-Nyquist plots indicated that the cycled anode-film exhibited cracking and delamination from the current collector. These mechanical problems seem to be dominating factors that deteriorate the cycling stability of Si anode-films.

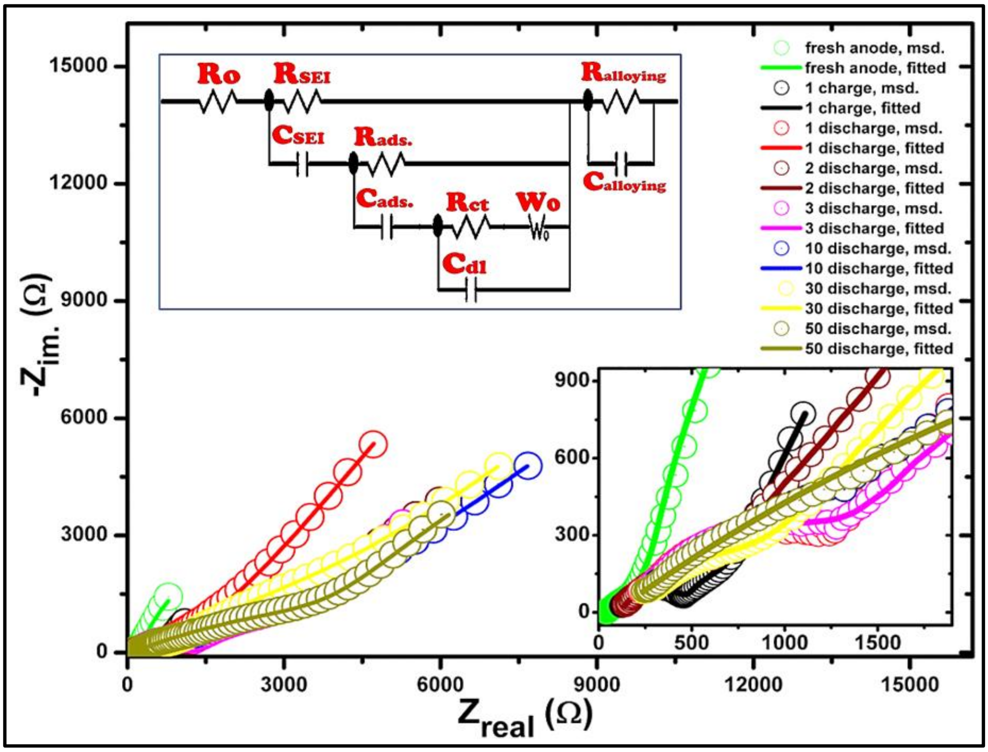

Fig. 3.8. *EIS-Nyquist plots of Si anode films throughout 50 cycles at 0.1 C-rate in LiTFSI/[BMP]TFSI electrolyte. The inset shows a magnification of the Nyquist plots in the high-to-middle frequency region. The best fitting equivalent circuit is also shown.*

To further elucidate electrochemical reactions at the interface and the bulk electrode, in addition to the diffusion dynamics of the Li ion in Si anode upon cycling, the Bode plots were analyzed. Figure (3.9a, b) depicts the Bode plots of Si anode over 50 cycles at 0.1 C-rate. As shown in figure (3.9a), Bode magnitude plots exhibited distinct difference in impedance values which increase upon cycling at all frequency ranges, representing slower kinetics of electrochemical reactions occurring during the successive cycling of the Si anode **[180, 187]**. In the low-to-high frequency region, the impedance values are correlated to charge transfer phenomena (charge transfer resistance in the bulk anode and/or in the SEI) **[180, 187, 188]**. The R_{ct} values in this frequency range increase upon cycling correlated with the decrease in the charge transfer rate, which could result from the deformation and the cracking of Si anode upon cycling. The impedance values in the low frequency region from 1 to 0.1 Hz (< log 1 Hz) represent the Warburg behavior of a semi-infinite solid state diffusion of Li^+-ions in the bulk active material **[180, 187]**. The values of the impedance modulus increase after the second discharging process in this frequency range, reflecting a limitation of the Li diffusion rate in the bulk anode upon cycling **[187, 188]**.

Figure (3.9b) displays Bode-phase plots of Si anode over 50 cycles corresponding to the phase shift between the imposed potential and the resulting current. The single semicircle observed in the Nyquist plots in figure (3.8) are more evident in this half Bode plot as a single peak in all phase-shift curves in the mid-frequency region from log 5Hz to log 3Hz (100 kHz-1000 Hz). This phase shift is associated with the charge transfer in the bulk anode and/or in the SEI separating the active anode material and the electrolyte **[180, 187]**. It can be observed that the peak intensities in this frequency region increase upon cycling, indicating a correlated increase in the charge transfer impedance **[180, 187]**. The charge transfer frequency is almost invariant till the 30th cycle, while the charge transfer resistance increase, which may suggest that the electrochemically active mass of the cycled anode is decreasing upon cycling **[187, 188]**. After long cycling (50 cycles), the phase shift associated with the charge transfer starts at a higher frequency at around 10 kHz (log 4 Hz) which can correlate with the progressive wetting of the anode active surface after long cycling **[187]**. The Bode diagrams exhibit a relaxation in the mid-to-low frequency region at around log 2 Hz. This relaxation may be attributed to the reduction of the initial SiO_x layer formed on Si particles after initial cycling [188]. Another interpretation for this relaxation could be related to the electro-adsorption process of Li^+-ions or other species onto the anode surface [189, 190].

The Bode phase plots display short plateaus in low-frequency region from 1 to 0.1 Hz, corresponding to the solid state diffusion of Li ions. It is worth noting that this diffusion region starts at a higher frequency after the 10th cycle, which generally could refer to an activation of the cycled anode [187]. The phase shifts reflected at lower phase angle values upon cycling (θ= 60° and 42° after the 1st charging and the 50th discharging process, respectively), indicating the decrease of pseudo-capacitance processes with cycling. The decrease of capacitance values can be explained in terms of the decrease of the active electrochemical surface [187], resulting in the decrease of lithium diffusion into the anode pores and into the bulk of the particles as well [191, 192].

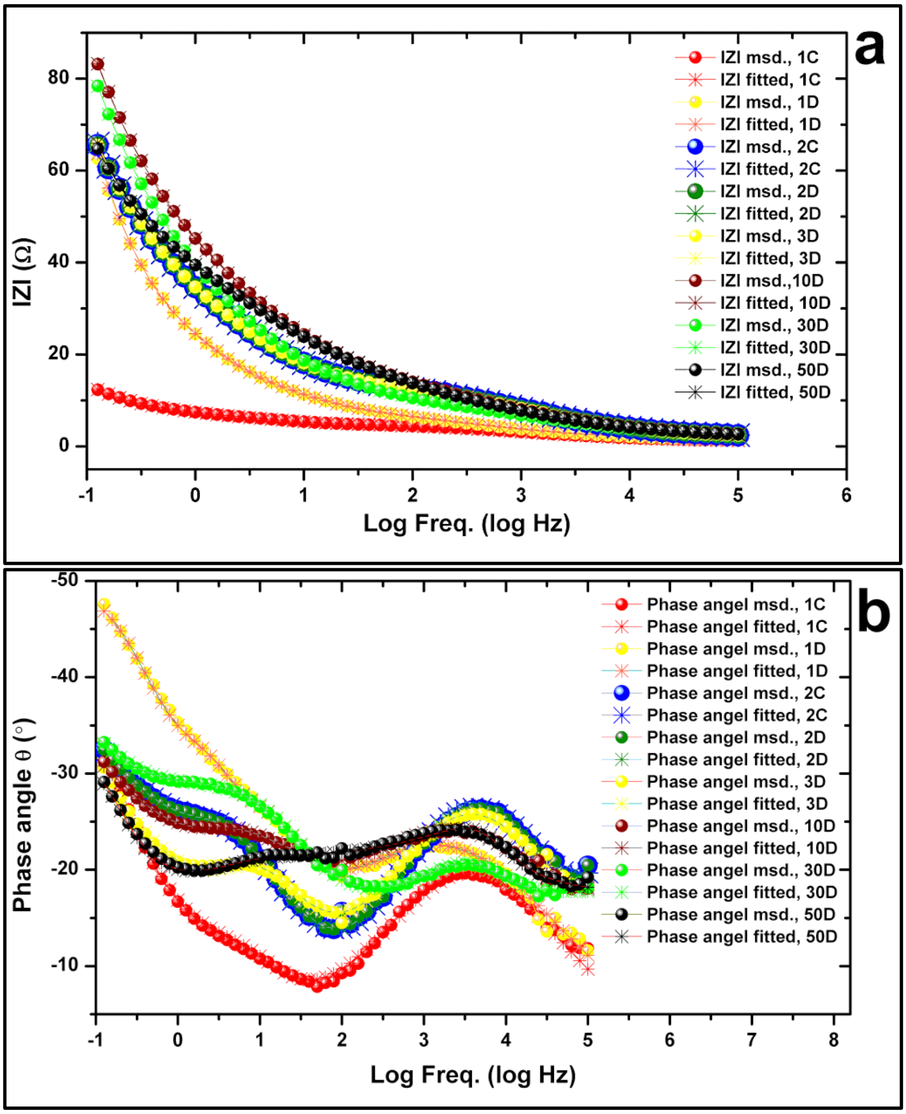

Fig. 3.9. *Bode plots of Si anode film over 50 cycles at 0.1 C-rate in LiTFSI/[BMP]TFSI electrolyte; Bode amplitude plots which represent the total impedance magnitude* ***(a)****, Bode phase-shift plots of the cells upon cycling* ***(b).***

3.1.1.7. X-ray Photoelectron Spectroscopy of SEI layers formed on Si film after 1-charge

The majority of studies that investigated the SEI formed on cycled electrodes by XPS technique were often conducted at different states of charge (SOC) exploring only the upper SEI layers without investigating the deeper layers. The uppermost SEI layer likely contains residuals of the bulk electrolyte and other surface contamination that can hide some spectroscopic signals, thus the interpretation of the de-convoluted spectra in this case becomes debatable **[193]**. The deep SEI layer near the electrode often consists of insoluble and more passivating inorganic components such as LiF and Li_2CO_3 **[193, 194]**. On the other hand, the upper SEI layers, especially the outermost one near the electrolyte are mostly composed of metastable and poorly passivating organic products such as $ROCO_2Li$ and ROLi (R=CH_2, CH_3, CH_2CH_2, CH_2CH_3, $CH_2CH_2CH_3$ depending on the electrolyte solvent) **[193, 195-198]**. C. Nguyen *et al.* **[172, 199]** have extensively studied the SEI composition formed on a cycled Si-Cu anode in LiTFSI/[$Py_{1,3}$]TFSI electrolyte by ex-situ XPS technique.

Herewith, the composition of SEI-layers formed on as-cycled Si electrode was analyzed using ex-situ XPS after initial charging at a current density of 300 mA/g till 0.01 V in LiTFSI/[BMP]TFSI electrolyte, exploring its composition in the uppermost, the buried and the 2nd-sputtered layer. Figure (3.10a) shows the XPS survey for SEI layers before and after sputtering. In the upper-most SEI layer, both Si 2p and Li 1s spectra can hardly be detected as the surface of the cycled anode is mostly covered with electrolyte residuals (pure LiTFSI/[BMP]TFSI).

The high resolution spectra of F 1s, O 1s, N 1s, C 1s, S 2p, Si 2p, and Li 1s with their deconvolutions are illustrated in figure (3.10b). In Si 2p spectra, it can be detected that the elemental Si is mainly oxidized to SiO_x, supported by the SiO_2 peak at around 533 eV in O 1s spectra [165]. The deconvolutions of Si 2p spectra include two peaks at around 103 and 104 eV which can be correlated to Li_ySiO_2 [200] and SiO_xF_y, respectively [166]. The second deconvolution peak could also be allocated to Si-O-C compounds [172-174]. As mentioned before, the reduction and decomposition process of $[BMP]^+$ cation could result in the production of negatively charged Alkyl radicals which, in turn, could split the Si-Si or Si-O-Si bonds through a nucleophilic attack resulting in the formation of Si-C or Si-O-C bonds [172]. Also, the F ion from the LiTFSI salts or TFSI anion could react with Si or SiO_x surface forming Si-F or Si-O-F bonds [171-173]. The formation of Si-O-F and Si-O-C bonds may cause the shift in SiO_2 peak from 103.5 eV to 104.5 eV. In details, the substitution of oxygen in SiO_2 by more electronegative fluorine or carbon decreases the negative charge on Si oxide surface, which results in reducing the tendency of the charge transfers from Si to O causing the shift of SiO_2 peak to a higher binding energy [201, 202]. Li_ySi alloying peak barely can be detected at the deeper layer at around 99 eV [170]. In the F 1s spectra, LiF peaks at around 685.8 eV are more intense in deeper layers, confirmed by its corresponding peak in Li 1s spectra at around 57 eV which can be detected only after sputtering [170]. Also, F 1s spectra show CF_3 peaks at around 690 eV, confirmed by the CF_3 peak in C 1s spectra at around 293 eV [165]. The formation of LiF and Si-F_x species are reported to begin by the breakdown of C-F bond in $TFSI^-$ anions, which could result in the production of CF_3SO_2Li salt [172].

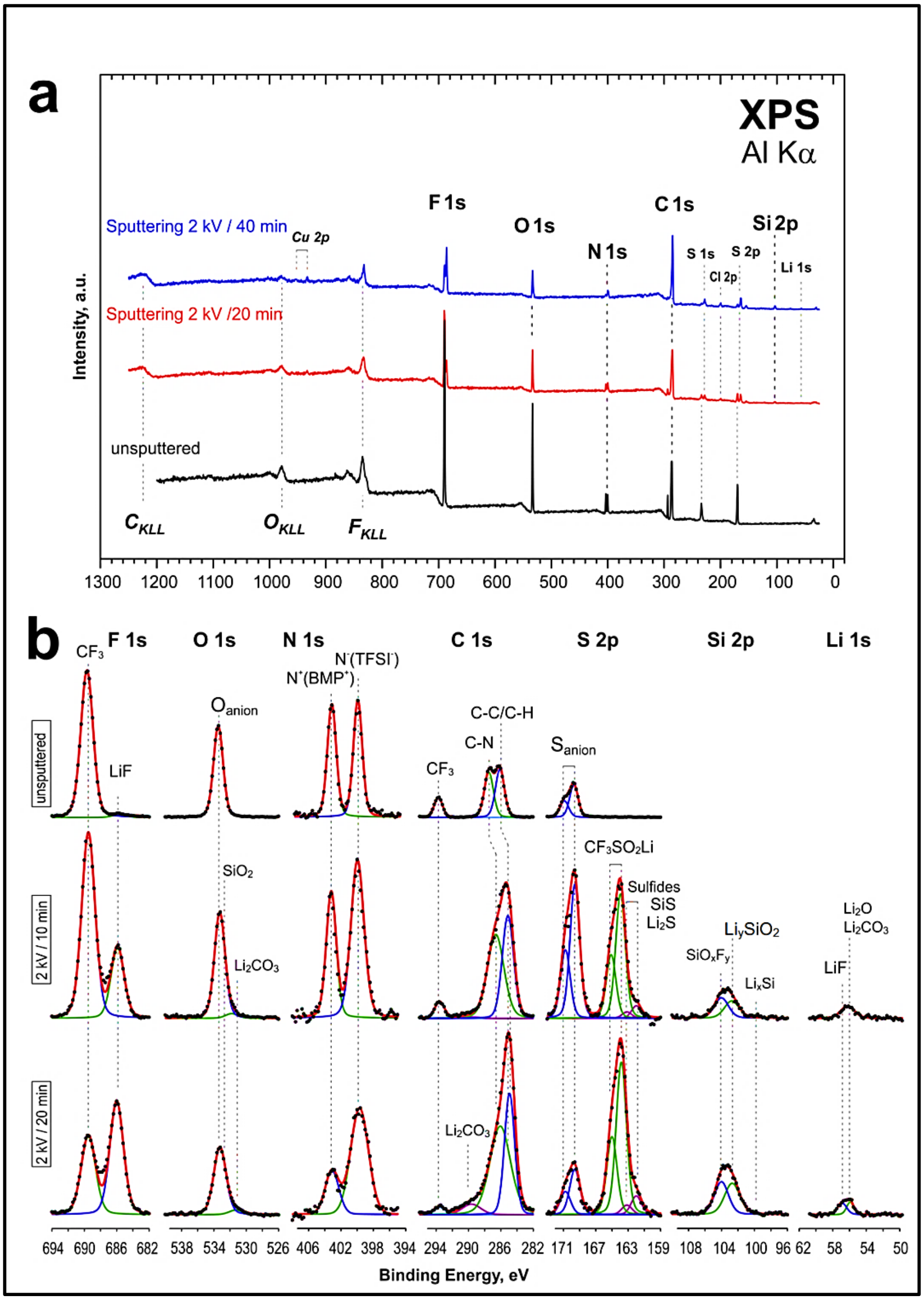

Fig. 3.10. *XPS analysis of the SEI formed on Si film after initial charging in 0.5 M LiTFSI/[BMP]TFSI till 0.01 V;* ***(a)*** *the overall XPS survey for the uppermost and two deeper SEI layers,* ***(b)*** *the detailed spectra of F 1s, O 1s, N 1s, C 1s, S 2p, Si 2p, and Li 1s with their deconvolution.*

As shown in S 2p spectra, the decomposed anion could produce Lithium sulfates salts in the chemical form of CF_3SO_2Li at around 164 eV [172, 203]. Sulfides doublet peak (Li_2S/SiS) can be detected at around 160 eV [165, 203, 204]. The peak at around 171 eV can be indexed to S-anion [175]. In N 1s spectra, the peak at around 399.4 eV is possibly correlated to some N^--containing compounds [171, 175]. The intensities of N_{anion} and N_{cation} peaks which are not equal in deeper SEI layers could give an indication for the decomposition of the electrolyte [171, 175]. The feature of S 2P and N 1s spectra could support the decomposition mechanism of $TFSI^-$ anion according to equation (3.1) [172].

$CF_3SO_2NSO_2CF_3^- + e \rightarrow F^- + {}^{\bullet}CF_2SO_2NSO_2CF_3^-$ .... Equ. 3.1.

In C 1s spectra, both carbon-alkyl peaks (C-C, C-H peak) and carbon–hetero peak (C-N) can be found at around 285 eV and 287 eV, respectively. The C-O-C peak (not easily distinguishable) may overlap with the C-N peak at around 286.5 eV [197, 201, 204]. Lithium carbonate (Li_2CO_3) peak can be detected in the deeper layers around 299 eV [165]. The SEI structure is in good agreements with that reported by P. C. Howlett *et al.* [203].

Si composite anodes in Si–O–C and Li-Si-O-C forms were reported to exhibit better cycling performance compared to bare Si films [174]. The improvement in the electrochemical performance of these composite anodes was referred to the formation of Li_2O during the initial lithiation which can stabilize both the film integrity and the SEI layer as well [174]. In our case, the analyzed SEI layer formed on as-cycled Si electrodeposits could contain Si–O–C and Li-Si-O-C compounds, in addition to other stabilizing and passivating SEI compartments (LiF, Li_2CO_3, Li_2O, LiOH) [193, 194]. The detailed XPS studies of the SEI layer formed after several cycles are required to elucidate the role of these SEI compounds on the cycling stability of Si anode films which could not be accomplished due to the time-limitation of this thesis.

Figure (3.11) shows the atomic ratios of F 1s, O 1s, N 1s, C1s, S 2p, Si 2p, and Li 1s calculated from XPS peaks intensities. The atomic percent of carbon is very dominant, mostly coming from the decomposed $[BMP]^+$ cation. The relative concentration of Li_2O, Li_2CO_3, LiF, CF_3SO_2Li and LiS/SiS in SEI layers are introduced in the inserted table. These compounds are insoluble and more passivating compounds **[193, 194]** sharing a ratio of approximately 17.25% of the composition of investigated SEI layers which could improve its stability over cycling. Even though, it seems that the large volume change of the Si anode (300-420%) and its consequent cracking and delamination become dominating and robust drawbacks after several cycles. These mechanical deformation problems result in a poor cycling stability of Si anodes.

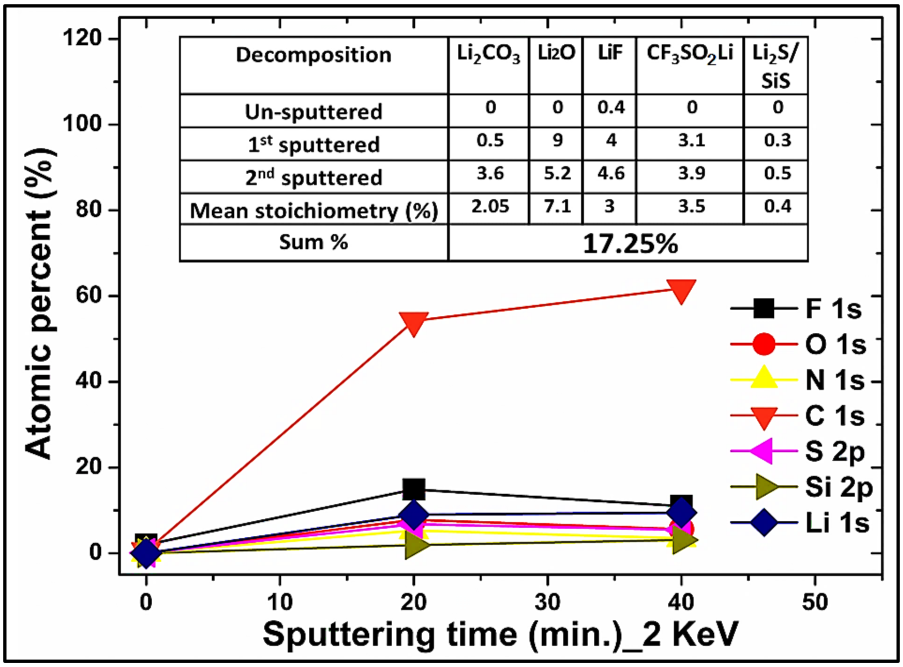

Decomposition	Li_2CO_3	Li_2O	LiF	CF_3SO_2Li	$Li_2S/$ SiS
Un-sputtered	0	0	0.4	0	0
1st sputtered	0.5	9	4	3.1	0.3
2nd sputtered	3.6	5.2	4.6	3.9	0.5
Mean stoichiometry (%)	2.05	7.1	3	3.5	0.4
Sum %	17.25%				

Fig. 3.11. *Relative atomic percent of F 1s, O 1s, N 1s, C 1s, Cl 2p and Si 2p compounds, calculated from XPS spectra of the SEI at the uppermost and two sputtered layers of the Si film. The inserted table illustrates the stoichiometry data of* Li_2O, Li_2CO_3, *LiF,* CF_3SO_2Li *and LiS/SiS in SEI-investigated layers.*

3.1.1.8. FTIR and Raman spectroscopy for LiTFSI/[BMP]TFSI electrolyte

To investigate the chemical stability of LiTFSI-[BMP]TFSI electrolyte, it was analyzed by both FTIR and Raman spectroscopy before cycling (neat electrolyte) and after 50 cycles at 360 mA/g as shown in figure (3.12a, b). Both the IR and the Raman spectra indicated that the electrolyte was not subjected to bulk reduction or decomposition which confirms its stability over cycling in LIBs. In IR spectra (inset a), CF_3H peak (belongs to C–F stretching) at around 1152 cm^{-1} does not exist which could indicate that the TFSI anion is not exposed to bulk reduction and decomposition. The formation of CF_3H peak is probable if the reduction of the TFSI anion takes place through the cleavage of C–S bond which was postulated by E. Markevich *et al.* **[205]** according to equation (3.2) in which CF_3^- further deprotonates the $[BMP]^+$ cation forming CF_3H molecules.

$$\mathbf{N(SO_2CF_3)_2^- + e^- \rightarrow N(SO_2CF_3)_2^{2-\bullet} \rightarrow \bullet SO_2NSO_2CF_3^- + CF_3^{-\cdot}} \textbf{....Equ. 3.2.}$$

In Raman spectra (inset b), the symmetric deformation peak of CF_3 [$\delta_s(CF_3)$] at around 740 cm^{-1} which refers to the “free” TFSI anion **[206]** does not exhibit any changes in its position or intensity after long cycling. Also, the position and the intensities of the C-H stretching peaks located in the frequency range of 2850-2997 cm^{-1} did not change after long cycling which confirms that the $[BMP]^+$ cation was not subject to excessive reduction in the bulk electrolyte after long cycling. Andrea Balducci have reported that the [BMP]TFSI electrolyte displays better stability as battery electrolyte compared to [BMP]FSI by FTIR studies **[207]**.

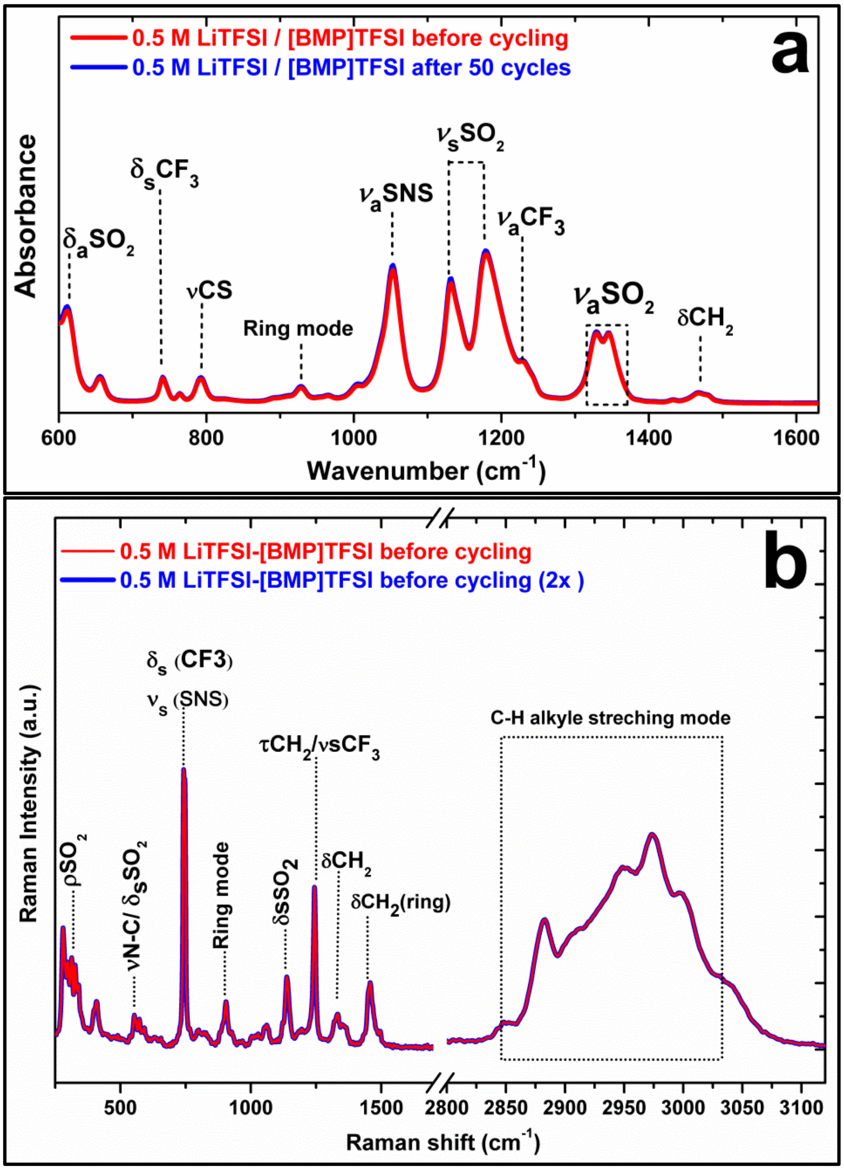

Fig. 3.12. *FT-IR spectra **(a)** and Raman spectra **(b)** of 0.5 M LiTFSI-[BMP]TFSI electrolyte before cycling (blue) and after 50 cycles (red) at a current density of 360 mA/g.*

3.1.2. Silicon anode film by pulsed-electrodeposition at a duty cycle of 25%

A Si anode film has been electrodeposited at different pulsed potentials, different temporal parameters (T_{ON}, T_{OFF}) and shorter electrodeposition time, to evaluate the effect of changing the pulsed-electrodeposition procedure on its physical and electrochemical properties.

3.1.2.1. Potentiostatic pulsed-electrodeposition of Si at a duty cycle of 25%

Figure (3.13a) shows the overall pulsed-potential waves along with the *j*/t curve for Si electrodeposition from 0.5 M $SiCl_4$ in [BMP]TFSI. The electrodeposition was performed at a lower duty cycle (25%) and much shorter deposition time (20 minutes). Figure (3.13b) shows a magnification for the applied potential waves and the associated current values at each pulse interval. The values of the applied potentials were adjusted to equal -3 V and -0.5 V for P1 and P2, respectively. The deposition-pulse interval (T_{ON}) was adopted at a concise time (0.5 second) at which P1 was applied, followed by the rest-half pulse at which P2 is applied for 1.5 seconds. It can be detected that when applying P2 at -0.5 V versus Pt, even the anodic current jumps to high current values, it drops rapidly to zero. Also, adjusting T_{OFF} intervals to be longer than that of T_{ON} can provide a better chance for the deposition interface to discharge and for the electrolyte to diffuse, which is expected to produce more compact Si film with better physical and electrochemical properties **[135]**.

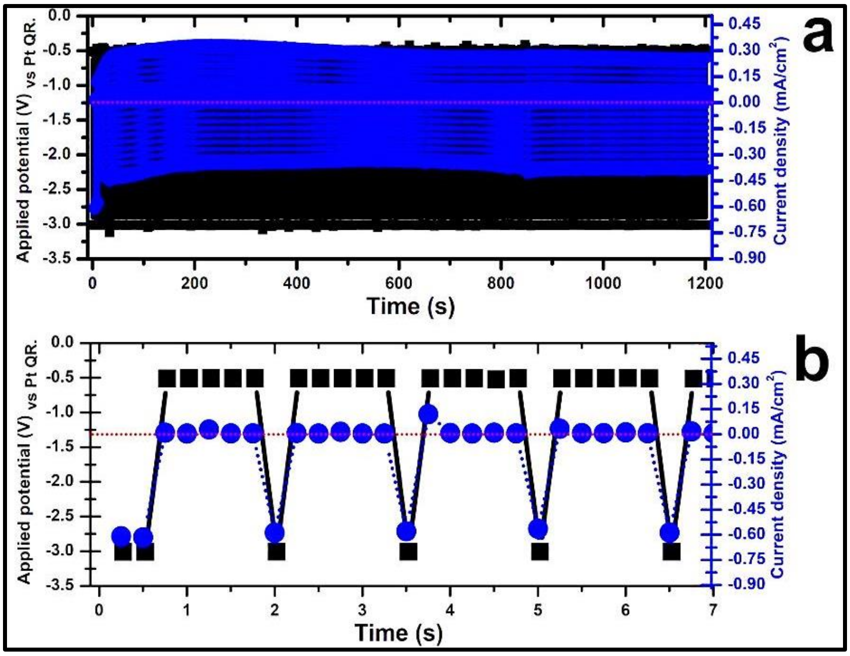

Fig. 3.13. *Potentiostatic pulsed-electrodeposition of Si in [BMP]TFSI ionic liquid at a duty cycle of 25% for 20 minutes;* ***(a)*** *overall pulsed-potentials waves with the j/t* curve, ***(b)*** *a close-up portion showing the applied potential waves (black) and their correlated current density (blue).*

3.1.2.2. Scanning Electron Microscopic investigations

FE-SEM images of the Si film obtained by pulsed electrodeposition at a duty cycle of 25% are shown in figure (3.14a, b). From the macroscopic view, it can be detected that the Si deposit is more compact with finer particles, compared to a Si film which was deposited at a duty cycle of 50%. At longer T_{OFF}, the electrodeposit seems to have a better chance to discharge, and the electrolyte had enough time to replenish its concentration in the electrodeposition vicinity which can reflect positively on the film homogeneity and compactness. Figure (3.14c, d) illustrate the EDS spectra of the Si deposit in different areas. C, F, S, and Cl elements refer to the decomposed components of the ionic liquid and of $SiCl_4$ **[135]**.

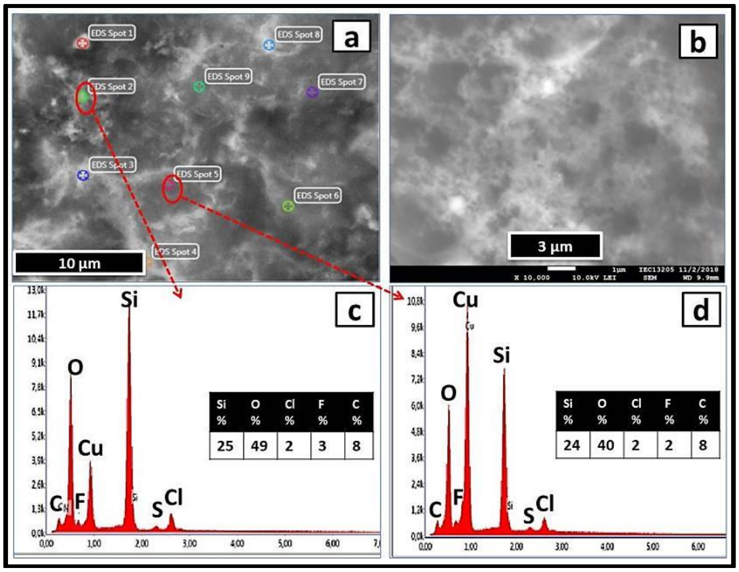

Si %	O %	Cl %	F %	C %
25	49	2	3	8

Si %	O %	Cl %	F %	C %
24	40	2	2	8

Fig. 3.14. *FE-SEM images* ***(a, b)*** *and EDX spectra* ***(c, d)*** *for Si film deposited by pulsed-electrodeposition at 25% duty cycle in [BMP]TFSI for 20 minutes.*

3.1.2.3 Galvanostatic cycling evaluation in LIB

The as-deposited Si-film was applied as an anode in LIBs to evaluate its electrochemical performance in half-cell battery type using 0.5 M LiTFSI/[BMP]TFSI as the battery electrolyte. Figure (3.15a) shows the potential plateau of the initial charge/discharge cycle at 0.03 mA/cm^2 (681 mA/g). The silicon-anode film shows an ideal lithiation plateau of Si-anode material **[176-178]**. The initial discharge plateau curve shows one pseudo-plateau in the potential range of 0.2-0.5 V versus Li$^+$/Li, correlated with the Li extraction. The calculated active mass of Si in the deposit-film is only 44 µg/cm^2. This Si anode film shows a first "irreversible" capacity loss equal to 90% which is mainly caused by SEI forming. This value is higher than that of the less compact Si film, which might be referred to the higher activity of Si particles in such small size, stimulating the formation of a thicker SEI layer **[35, 58]**.

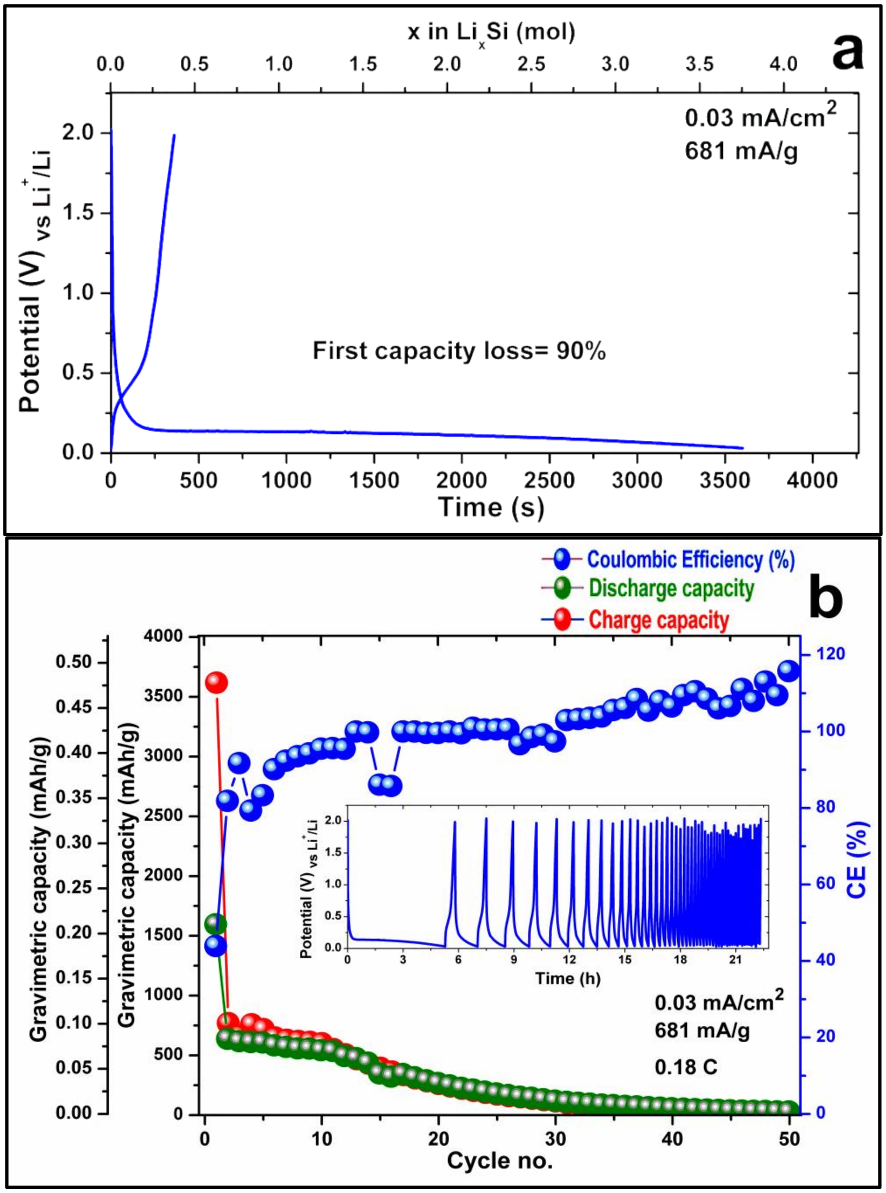

Fig. 3.15. *Galvanostatic cycling performance of Si film, deposited by potentiostatic pulsed-electrodeposition at a duty cycle of 25%;* ***(a)*** *potential plateau of the initial charge/discharge cycle at a current density of 681 mA/g (0.18 C-rate),* ***(b)*** *50 charge/discharge cycles at the same current density.*

Figure (3.15b) shows the long galvanostatic cycling of the Si anode film at a current density of 680 mA/g, equivalent to 0.18 C-rate. The cycled anode film shows a stable cycling performance in the first

10 cycles with discharge capacity values over 480 mAh/g, then decreasing continuously during the next cycles. The coulombic efficiency values gradually increase, which can reflect the improvement in the de-alloying process upon cycling. It seems that the compact feature of this Si anode helps it to withstand for the volume expansion during the first ten cycles. After ten cycles, the excessive structure deformation of the Si anode and its expected delamination from Cu-substrate seemed to become dominant, causing such deterioration in the retained capacity. The capacity retention after 50 cycles is very low, equal to 3.6 % of that retained in the initial discharge. In conclusion, this Si film showed a limited cycling improvement when cycled at a current density 2 times higher than that at which the first Si film (prepared at a duty cycle value of 50%) was cycled.

3.1.3. Si anode film by pulsed-electrodeposition at a duty cycle of 16%

3.1.3.1. Potentiostatic pulsed-electrodeposition of Si film at a duty cycle of 16%

This Si deposit was also synthesized using the potentiostatic pulsed-electrodeposition technique but at much lower duty cycle value (16%) for 45 minutes. The applied potentials were also adjusted at more appropriate values, aimed to avoid the excessive decomposition of the electrolyte and the dissolution of the Cu substrate. Figure (3.16a) shows the overall pulsed-potential waves along with the *j*/t curve of the Si film in 0.5 M $SiCl_4$/[BMP]TFSI for 45 minutes. Figure (3.16b) shows a magnification for the potential waves and the associated current values at each pulse interval. The values of the applied potentials were -3 V and -1 for P1 and P2, respectively. Concerning the pulse-temporal parameters, T_{ON} and T_{OFF} intervals were adopted to be 1 second and 5 seconds, respectively, so the duty cycle equals 16%. When applying P2 at -1 V, the anodic current drops back rapidly to zero. Adapting T_{OFF} intervals to be much longer than that of T_{ON} (5-times longer) expected to provide a superior chance for the deposition interface layer to discharge, and for the electrolyte to diffuse to the reduction/deposition vicinity. Consequently, the pulsed electrodeposition at these potential values and temporal parameters were anticipated to producing more compact Si films with less porous structure and better physical and electrochemical properties.

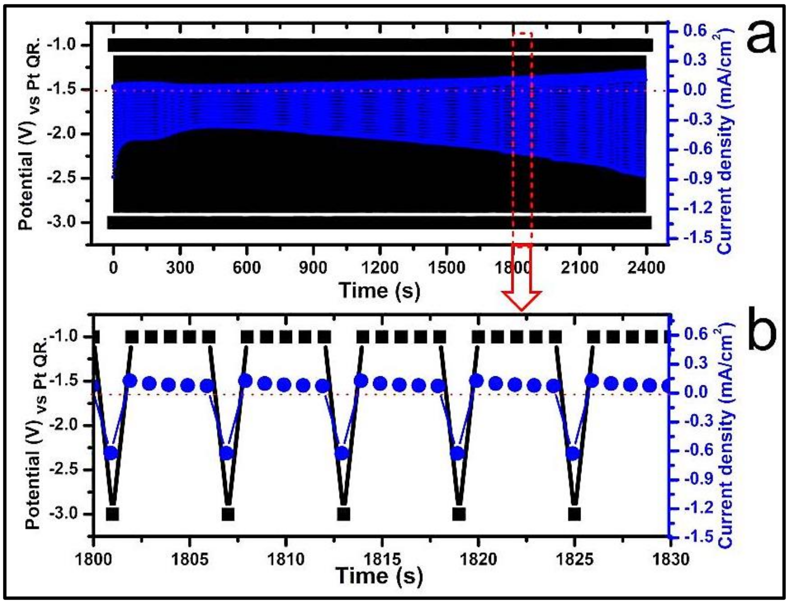

Fig. 3.16. *Potentiostatic pulsed-electrodeposition of Si in [BMP]TFSI at a duty cycle of 16% for 45 minutes;* ***(a)*** *overall pulsed-potentials waves with the j/t* curve, ***(b)*** *a close-up portion showing the applied potential waves (black) and its correlated current density (blue) at each pulse interval.*

3.1.3.2. Scanning Electron Microscopic investigations

FE-SEM images of Si film obtained by the potentiostatic pulsed-electrodeposition at a duty cycle of 16% is shown in figure (3.17a, b). It seems that the electrodeposition of this Si film at much lower duty cycle (16%) with much longer T_{OFF} provides sufficient long time for the electrodeposition solution to replenish its concentration near the cathode, increasing the electrodeposition efficiency which reflects positively on the compactness of the deposit [135, 163, 164]. Also, the high cathodic current produced during T_{ON} intervals seems to improve the nucleation of Si particles [135, 138-140]. These electrodeposition parameters seem to reflect positively on the Si film integrity and compactness that it appears as a dense film with non-porous structure. Even though, the deposit appears to be cracked somewhere within the macroscopic scale which could not be easily discussed in terms of the applied electrodeposition parameters. Figure (3.17c, d) illustrates EDS spectra of the Si deposit. Also, some traces of ionic liquid and $SiCl_4$ residuals such as C, F, S and Cl elements are found with higher oxygen percent.

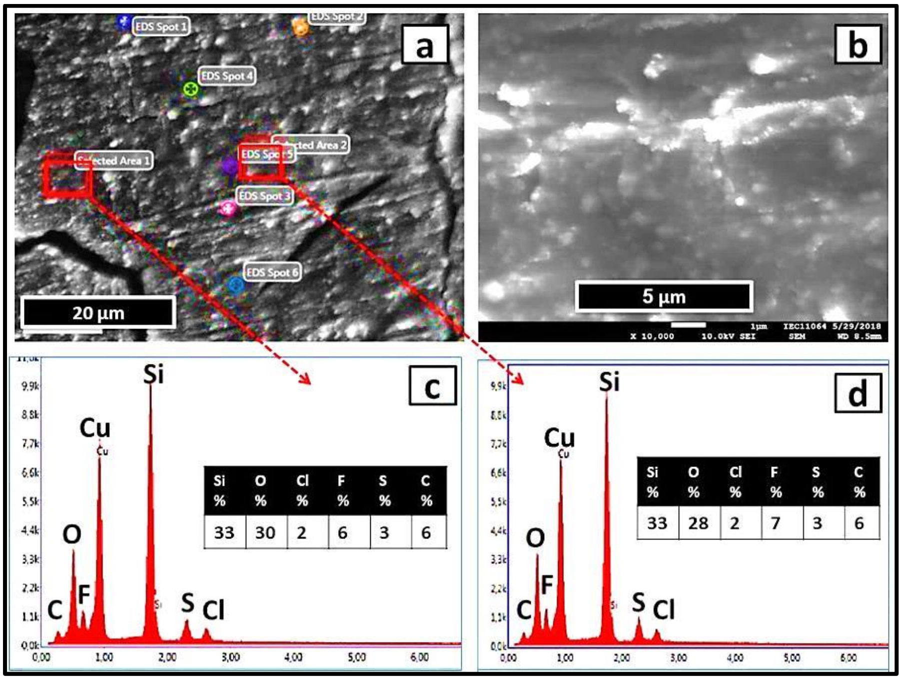

Si %	O %	Cl %	F %	S %	C %
33	30	2	6	3	6

Si %	O %	Cl %	F %	S %	C %
33	28	2	7	3	6

Fig. 3.17. *FE-SEM images* ***(a, b****), and EDX spectra* ***(c, d)*** *of as-deposited Si film which was prepared by pulsed electrodeposition in [BMP]TFSI at a duty cycle of 16% for 45 minutes.*

3.1.3.3. Galvanostatic cycling evaluation in LIB

Figure (3.18a) shows the initial charge and discharge cycle of the deposited Si film at 0.03 mA/cm^2 (0.9 mA/g, 0.25 C-rate). The active mass of Si in the deposit equals 33 µg/cm^2. The first capacity loss upon the initial cycle is 48% which is much lower than that of other Si-film deposited at duty cycle values of 50 and 25%. This could be explained in terms of the compactness of the deposit that may prevent the growth of a thick SEI.

Figure (3.18b) shows the galvanostatic cycling of this Si film for 50 cycles at 0.25 C-rate. This anode film exhibited high capacity values over 25 cycles when cycled at such high current density (900 mA/g) compared to the retained capacity values of other Si-anode although were cycled at lower current density values (360 and 680 mA/g). The cycled anode also shows a capacity fading, but with lower level compared to other Si films tested before. Even though, the capacity retention after 50 cycles is very low, equal to 8.7% of that retained in the initial discharge. In conclusion, the anode film displayed a partial improvement in its electrochemical performance regarding the high gravimetric capacity values retained during the first 25 cycles, in addition to the lower trend in its capacity fading compared to other Si deposits. Even though, the anode-film still shares the same cycling drawback of all tested Si films that the capacity retention and the cycling stability is limited.

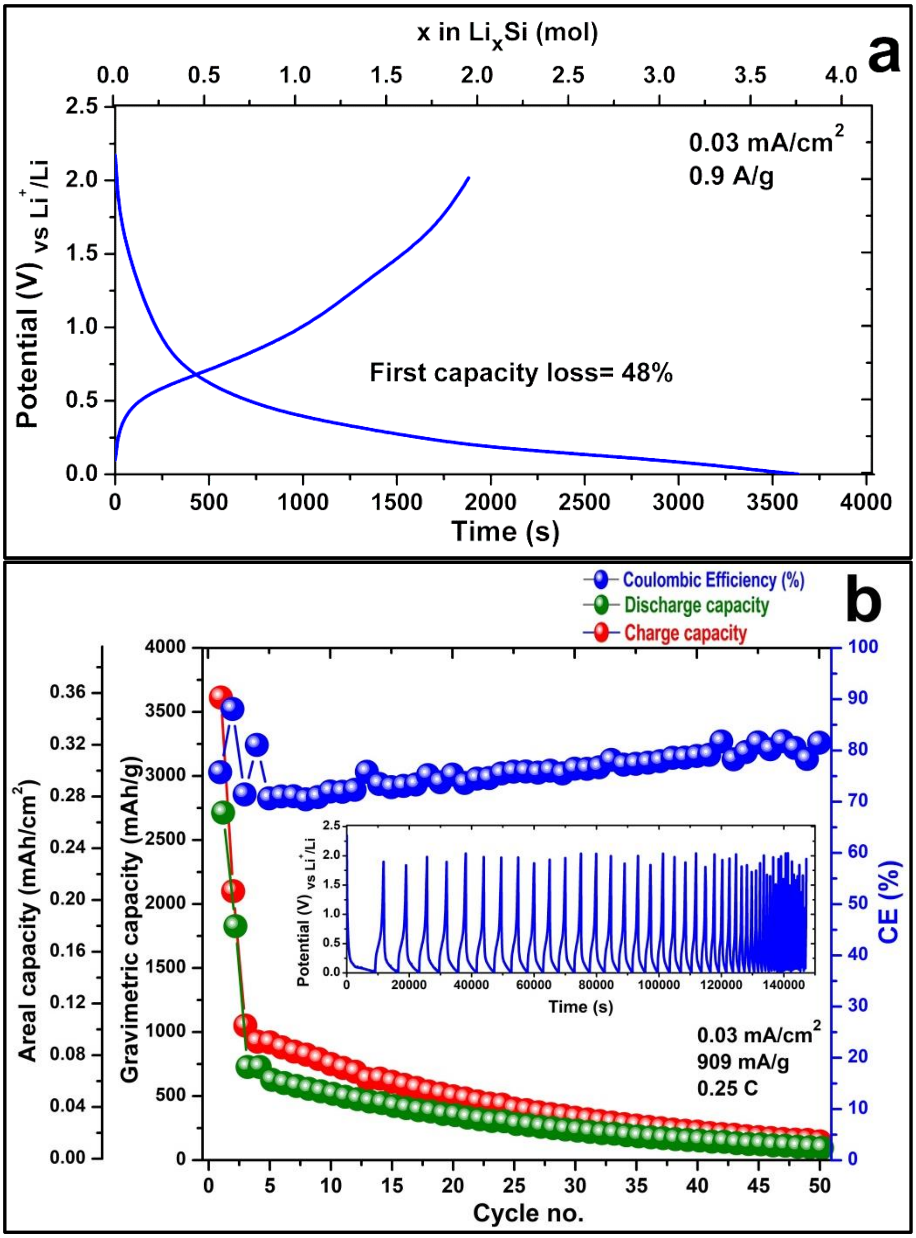

Fig. 3.18. *Galvanostatic cycling performance of Si film, deposited by the potentiostatic pulsed-electrodeposition at a duty cycle of 16%;* ***(a)*** *voltage profile of the initial charge/discharge cycle at a current density of 0.9 A/g,* ***(b)*** *long charge/discharge cycling at 0.9 A/g (0.25 C-rate).*

3.1.4. Raman spectroscopy of $SiCl_4$/[BMP]TFSI electrodeposition baths

To evaluate the effect of deposition parameters on $SiCl_4$/[BMP]TFSI electrodeposition bath in terms of its decomposition, a Raman analysis was performed before and after pulsed-electrodeposition processes of Si films at two different duty cycle values (50% and 16%) as shown in figure (3.19a, b). As shown in inset a, the corresponding peak of free TFSI anion which appears at around 742 cm^{-1} (including the symmetric streching of S-N-S bond and the symmetric deformation of CF_3 bond) **[206]** can give an indication of the rate of the electrolyte decomposition. The intensity of this peak decreases as the value of the duty cycle increases, which indicates that the pulsed electrodeposition at 50% duty cycle results in decomposition of TFSI anion in higher ratio compared to that at 16% duty cycle.

Also, as shown in inset b, the same trend can also be detected for TFSI peaks in the frequency range of 1136-1244 cm^{-1} corresponding to the symmetric streching of SO_2 and CF_3, repectively **[206]**. Furthermore, the intensities of $[BMP]^+$ peaks corresponding to the streching mode of alkyl groups attached to the pyrolidine ring in the frequency range of 2890-3000 cm^{-1} shows also the same trend **[207]**, decreasing as the duty cycle value of the pulsed electrodepostion increases. This indicates that the reduction of $[BMP]^+$ cation increase as the duty cycle values of pulsed-electrodeposition increase.

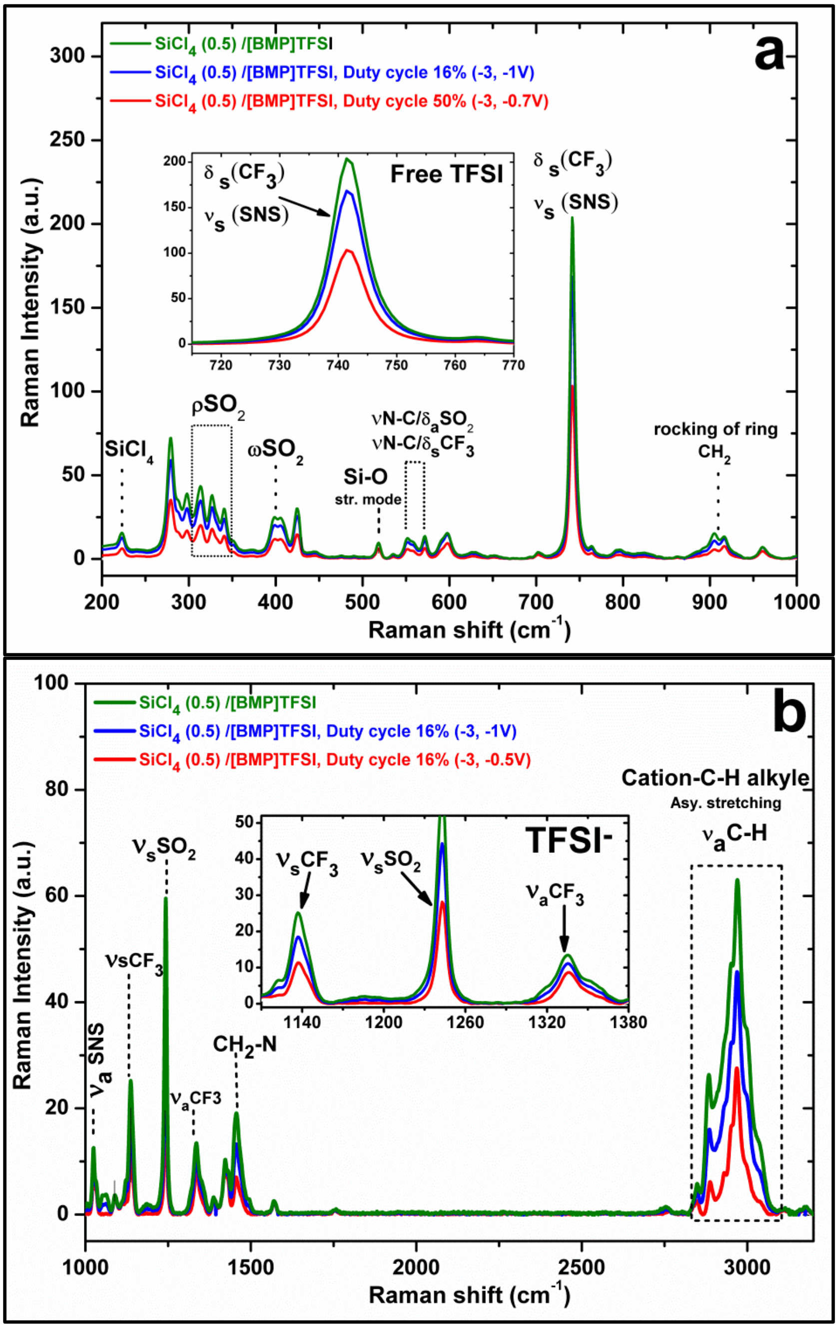

Fig. 3.19. *Raman spectra in the frequency regions of 200-1000* ***(a)*** *and 1000-3200 cm*$^{-1}$ ***(b)***, *for 0.5 M SiCl*$_4$*/[BMP]TFSI electrodeposition bath before pulsed-electrodeposition (green), and after pulsed-electrodeposition at duty cycle of 50% (bleu) and 16% (red).*

In conclusion, the pulsed-electrodeposition at longer T_{OFF} (in the case of PED at 16% duty cycle) appears to limit the excessive decomposition of the deposition electrolyte. As mentioned before, at longer rest time (T_{OFF}), the deposition area can be efficiently discharged and the electrolyte can replinsh its concentration at this area, which limts its localized decomposition on the deposition sites [135, 138, 163]. Thus, the pulsed-electrodeposition at lower duty cycle seems to be beneficial not only for the deposit film but also for the electrodeposition bath, limiting its decomposition.

Conclusion on Si as anode material in LIBs

Pulsed electrodeposition of Si films is a feasible and rather controllable method as the deposition rate and the ions concentration near the deposition interface can be controlled. Interrupting the deposition process by longer rest-time intervals (T_{OFF} intervals) provides a good chance for discharging the electrodeposition vicinity and for elevating the concentration of the deposition solution near the cathode. Also, adjusting the deposition pulses (T_{ON} intervals) at concise intervals may result in evolving high current values that can improve the nucleation process **[138]**. The variations of these parameters give the chance to produce Si deposits with well-tolerated features (compact film with small particle size and decent loading density). The pulsed-electrodeposition of Si film at a duty cycle of 50% produced a cracked film with less compact feature compared to that which was prepared at a duty cycle of 25%. The pulsed-electrodeposition of the Si film at a duty cycle of 16% produced a compact Si film without porous structure. Si deposits were found to contain a high percentage of carbon, in addition to other IL- decomposed items such as S, F, C and N. The detected carbon could result from the adsorption/reduction of $[BMP]^+$ producing negatively-charged Alkyl radicals. These decomposed alkyl radicals could react with either Si or SiO_x on the surface of Si particles forming Si-C or Si-O-C bonds which was reported to improve the electrochemical performance of Si anode and stabilize the SEI formed during cycling.

Cyclic voltammetry measurements for Si deposited-films obtained by pulsed electrodeposition show lithation and de-lithiation features categorized to Si anode materials prepared by other methodes. The CV feature exhibited an increase in the intensities of the de-lithiation peaks over cycling which can be explained in terms of a kinetic enhancement in the cycled anode **[177]**. This kinetic enhancement during de-lithiation processes of Si results in increasing the value of the coulombic efficiency (CE) more than 100% at some cycles. Si anode film deposited at a 25% duty cycle shows a limited improvement in its cycling stability during the first ten cycles when cycled at 680 mA/g, compared to the Si films deposited at a duty cycle of 50%. For Si anode film deposited at 16% duty cycle, it shows the lowest first capacity loss. Also, it produces higher capacity values when cycled at higher current density values (0.9 A/g). Even though, all Si films exhibit poor cycling stability over 50 cycles due to the structural deformation and the delamination of Si films out from the Cu current collector which was supported by the EIS study.

Si deposit was also synthesized using the potentiostatic pulsed-electrodeposition at much lower duty cycle value (6%), anticipated to produce a Si deposit with much improved physical and electrochemical properties to investigate its rate-capability in LIB. The Si anode film shows poor cycling stability and low rate-capability where the gravimetric and areal capacity values drop to around zero when the anode was cycled at 0.6 C-rate. These results are introduced in the appendix part (sections 5.1.2, 5.1.3, and 5.1.4).

EIS studied for Si anode upon 50 cycles indicated that R_{ct} values increase accompanied with a decrease in $D_{Li}{}^{+}$ upon cycling which could result from structure deformations and cracking of the anode. Also, Si anode seems to exhibit adsorption/desorption processes during cycling which refers to its complicated interactions not only with lithium but also with other electrolyte-elements during cycling. The fitting circuit introduced in EIS-study could arise some question about adsorption/trapping processes. To elucidate that, it needs further investigations on different Si anodes to be cycled in different LiTFS-ILs electrolytes, which could not be accomplished due to the time-limitation of the thesis study.

The XPS analysis indicated that the SEI formed on Si anode-films in LiTFSI/[BMP]TFSI electrolyte contains stabilizing compounds such as Li_2O, LiF, CF_3SO_2Li, SiS, Li_2S and Li_2CO_3 salts that can improve its mechanical stability. The detailed XPS studies of the SEI layer formed on Si anode after several cycles are required to elucidate the role of these SEI compounds on the cycling stability of Si anode films which could not be accomplished due to the time-limitation of this thesis. Even though, it seems that the volume expansion of Si anode and its consequent cracking and delamination are robust and dominating problems that limit its cycling stability. Handling these drawbacks by preparing Si alloys and composite films might improve its mechanical stability. Also, it can elevate the electrical conductivity and the kinetics of the anode during cycling, aimed to improve its cycling stability and rate-capability.

3.2. Si$_x$Ge$_{1-x}$ anode-films

Si$_x$Ge$_{1-x}$ alloy-films were prepared by potentiostatic pulsed-electrodeposition to be investigated as modified anodes in half-cell LIBs. Ge is a promising add-element for Si anode, expected to improve the electrochemical performance by increasing the conductivity, limiting the volume changes and improving the Li-kinetics in the Si anode film.

3.2.1. Si$_x$Ge$_{1-x}$ electrodeposition in [EMIm]TFSI

3.2.1.1. Cyclic voltammetry of SiCl /GeCl$_4$/[EMIm]TFSI baths

Cyclic voltammetry measurements of the neat [EMIm]TFSI and SiCl$_4$/GeCl$_4$/[EMIm]TFSI electrodeposition baths have been recorded on Cu at a scanning rate of 10 mV/s to investigate the electrochemical reactions regarding Ge-Si co-deposition in [EMIm]TFSI. The cyclic voltammetry of neat [EMIm]TFSI ionic liquid is shown in figure (3.20a) starting from OCP to -4 V versus Pt QRE. [EMIm]TFSI starts decomposition at around -2.7 V, so its cathodic stability regime is about 2.7 V vs. Pt QRE.

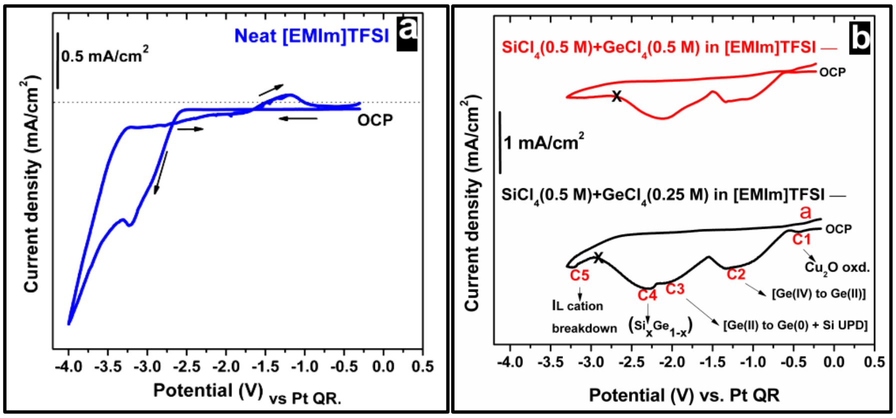

***Fig. 3.20. (a)** Cyclic voltammogram of neat [EMIm]TFSI. **(b)** Cyclic voltammograms of two SiCl$_4$/GeCl$_4$/[EMIm]TFSI solutions with SiCl$_4$:GeCl$_4$ molar ratio of 2:1 (black) and 1:1 (red). All voltammetry measurements were recorded on Cu at a scan rate of 10 mV/s starting from OCP to the negative direction.*

Figure (3.20b) illustrates the cyclic voltammograms of $SiCl_4$/$GeCl_4$/[EMIm]TFSI solutions with different molar concentrations of $GeCl_4$ (0.5 and 0.25 M). As labeled in the black voltammogram of $SiCl_4$ (0.5 M)/$GeCl_4$ (0.25 M)/[EMIm]TFSI solution in the cathodic regime, the foremost reduction peak (C1) could be correlated to Cu_2O reduction **[160]**. The second reduction peak (C2) at around -1.2 V can be indexed to the reduction of Ge^{IV} ions to Ge^{II}, as reported by Endres *et al.* **[120]**. After that, a shoulder (C3) at around -2 V can be detected, contributed with the full reduction of Ge^{II} to Ge along with Si UPD **[120, 161]**. This reduction peak is constantly followed by C4 peak at -2.25 V which can be indexed to the Si-Ge co-deposition, forming Si_xGe_{1-x} alloy **[120]**. The rising current after -2.8 V is related to the reduction of $[EMIm]^+$ cation, after which the ionic liquid breaks down at C5. In the anodic stripping, a single oxidation peak can be detected before -0.5 V, related to the oxidation of $[TFSI]^-$ anion and Cu-substrate as well **[120]**. The voltammogram of $SiCl_4$ (0.5 M)/$GeCl_4$ (0.5 M)/[EMIm]TFSI solution is very similar to the voltammogram of the electrodeposition solution saturated with lower molar ratio of $GeCl_4$ (red voltammogram). It worth noting that in $SiCl_4$ (0.5 M)/$GeCl_4$ (0.5 M)/[EMIm]TFSI solution, the $[EMIm]^+$ cation starts decomposition at a lower potential value which could be referred to the higher viscosity of this electrodeposition bath which is saturated with a higher molar ratio of $GeCl_4$ **[209]**.

3.2.1.2. Potentiostatic pulsed-electrodeposition of Si_xGe_{1-x} films

Si_xGe_{1-x} compounds were prepared by the potentiostatic pulsed-electrodeposition in a single bath containing both $SiCl_4$ and $GeCl_4$ analytes in [EMIm]TFSI. All Si_xGe_{1-x} films were produced via alternating the same potential values (P1= -2.7 V and P2 = -0.5 V) for

30 minutes. T_{OFF} intervals were changed between two values of 0.5 second and 2.5 seconds, adjusting the pulse duty cycle values to be 50% and 16%, respectively. In principle, for the electrodeposition of two metals or semiconductors in one electrodeposition bath, the concentration of the analytes should be balanced towards the less-noble element (Si in our case). In case of $SiCl_4$ (0.5 M)/$GeCl_4$ (0. 5 M)/[EMIm]TFSI bath, the co-deposition effect of $GeCl_4$ on Si electrodeposition in equal concentration to $SiCl_4$ was aimed to be investigated. Table (3.1) shows the pulses temporal parameters and the potential values applied for the potentiostatic pulsed-electrodeposition of Si_xGe_{1-x} films in [EMIm]TFSI ionic liquid.

Tab. 3.1. *Electrolytic bath concentrations and pulsed-electrodeposition parameters for Si_xGe_{1-x} electrodeposition in [EMIm]TFSI.*

Sample ID*	**$SiCl_4$:$GeCl_4$ M/M%**	**PED potentials**		**Temporal parameters**		**Duty cycle**
		P1	**P2**	**T_{ON}**	**T_{OFF}**	
$SG_{21}DC_{50}$	2:1	-2.7 V	-0.5 V	0.5 s	0.5 s	50%
$SG_{21}DC_{16}$	2:1	-2.7 V	-0.5 V	0.5 s	2.5 s	16%
$SG_{11}DC_{50}$	1:1	-2.7 V	-0.5 V	0.5 s	0.5 s	50%
$SG_{11}DC_{16}$	1:1	-2.7 V	-0.5 V	0.5 s	2.5 s	16%
**DC refers to "duty cycle" which equal to $T_{ON}/(T_{ON} + T_{OFF})$*						

Figure (3.21, insets a-d) shows the overall pulsed-electrodeposition curves of Si_xGe_{1-x} deposits along with their *j*/t curves. The insets (a′-d′) show a magnification portion for the potential-square waves with the evolved current values at each pulse interval.

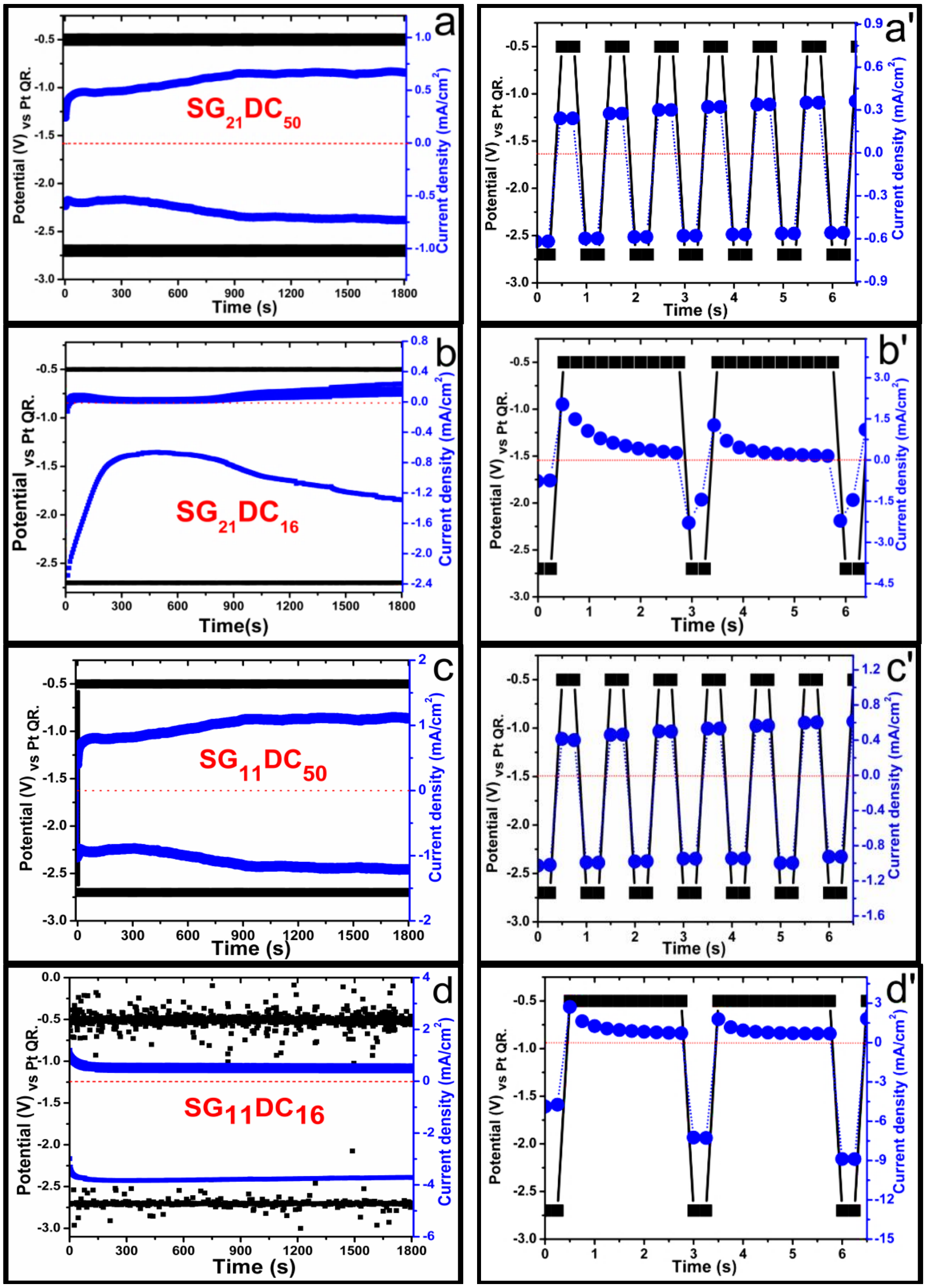

Fig. 3.21. *Overall potentiostatic pulsed-electrodeposition curves of* Si_xGe_{1-x} *samples;* $SG_{21}DC_{50}$ ***(a)****,* $SG_{21}DC_{16}$ ***(b)****,* $SG_{11}DC_{50}$ ***(c),*** *and* $SG_{11}DC_{16}$ ***(d)*** *for 30 minutes. Close- up portions showing the potential square-waves (black) and the correlated current (blue) for each* Si_xGe_{1-x} *deposits at pulse intervals;* $SG_{21}DC_{50}$ ***(a′)****,* $SG_{21}DC_{16}$ ***(b′)****,* $SG_{11}DC_{50}$ ***(c′),*** *and* $SG_{11}DC_{16}$ *samples* ***(d′)****.*

Adapting longer rest-time (T_{OFF}) in case of $SG_{21}DC_{16}$ and $SG_{11}DC_{16}$ samples provides a better chance for the current density to drop to zero, compared to other samples ($SG_{21}DC_{50}$ and $SG_{11}DC_{50}$), which helps in discharging the deposition-interface. Also, at longer T_{OFF} intervals, the species have enough time to diffuse, enriching their concentration in the reduction/deposition area which is expected to improve the deposition rate. On the other hand, adjusting T_{ON} intervals to be much shorter than T_{OFF} in these samples could produce higher current values, compared to other samples ($SG_{21}DC_{50}$ and $SG_{11}DC_{50}$) that can improve the nucleation efficiency, producing smaller Si_xGe_{1-x} grains.

X. Dou *et al.* have reported the electrodeposition of $Bi_{1-x}Sb_x$ nanowire-alloys in anodic alumina membranes (AAMs) using the potentiostatic pulsed-deposition technique by adjusting the value of the second potential (P2) to zero volt **[210]**. In the present experiments, the reason for adjusting the second potential applied during the rest-time at such value (-0.5 V) was to avoid the oxidation of $TFSI^-$ anion and Cu substrate. D. Pullini and D. Busquets-Mataix have also reported the pulsed electrodeposition of Co/Cu multilayer nanowires in a single electrodeposition bath through alternating individual pulses for Cu and Co **[211]**. In our case, the electrodeposition of Si in individual pulses can produce layered Si-Ge deposits in which Si and Ge are not well-alloyed. It is worth noting that the pulsed electrodeposition of Si_xGe_{1-x} by adjusting the value of P1 at -2.4 V produced Ge-rich Si_xGe_{1-x} deposits with low Si percent (less than 3%).

3.2.2. Scanning Electron Microscopic investigations

FE-SEM images of Si_xGe_{1-x} deposits with the EDS spectra are shown in figure (3.22, insets a-d). From the macroscopic view, we can detect the difference in the morphology of Si_xGe_{1-x} films deposited at different pulse parameters. $SG_{21}DC_{50}$ and $SG_{11}DC_{50}$ samples which were deposited at 50% duty cycle appear as less compact deposits with larger particle size as shown in insets a and c. On the other hand, $SG_{21}PP_{16}$ and $SG_{11}PP_{16}$ samples which were deposited at 16% duty cycle appear as more compact deposits with smaller particles as shown in insets b and d. These results are in a good agreement with other studies that introduced similar morphology-changes by changing the pulse duty cycle values **[135]**. The variation in the morphology and the particle size of Si_xGe_{1-x} deposits can be explained in terms of the applied duty cycle values. In the case of $SG_{21}DC_{50}$ and $SG_{11}DC_{50}$ samples which were deposited at high duty cycle values (50%) with equal T_{ON} and T_{OFF} intervals, the timescale of T_{ON} intervals seems to be more suitable for Si^{IV}/Ge^{IV} reduction **[135, 138]**. On the other hand, the diffusion process during T_{OFF} intervals seems to be not satisfactory. It seems that the accumulated charge in the deposition interface, in addition to the limited diffusion of the electrodeposition solution during the short T_{OFF} intervals (0.5 second) could result in such deposits with low density and less compact features **[135, 138]**. However, by adapting the T_{OFF} intervals to be much longer than T_{ON} intervals (5 times longer) in case of $SG_{21}DC_{16}$, $SG_{11}DC_{16}$ samples, the diffusion time becomes more adequate, so that the interfacial reduction/deposition zone becomes sufficiently discharged and replenished with fresh analytes, which result in more compact deposits. At these conditions, Ge also seemed to have a better influence in promoting Si reduction which results in Si-rich Si_xGe_{1-x} deposits.

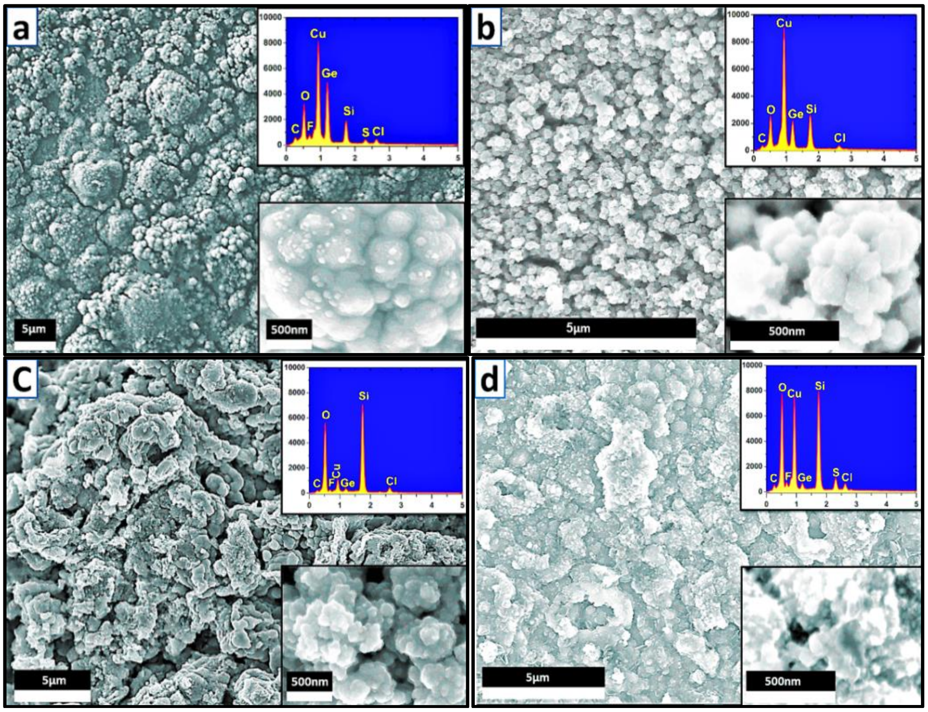

Fig. 3.22. *SEM images with the EDS spectra of Si_xGe_{1-x} films produced by potentiostatic pulsed-electrodeposition; $SG_{21}DC_{50}$* ***(a)****, $SG_{21}DC_{16}$* ***(b)****, $SG_{11}DC_{50}$* ***(c)****, and $SG_{11}DC_{16}$* ***(d)*** *samples.*

Table (3.2) shows the relation between the duty cycle values applied in the pulsed-deposition and the atomic percent of Si and Ge in each Si_xGe_{1-x} films. Also, it represents the effect of $GeCl_4$ concentration on the stoichiometry of Si_xGe_{1-x} deposits. The pulses temporal parameters and the concentration of $GeCl_4$ seem to have a dual effect on the Si-Ge co-deposition in [EMIm]TFSI electrolyte. The Si/Ge atomic ratio in each deposit was calculated from the EDX analysis which is customarily used as an adequate method by obtaining the mean atomic ratios over several scanned areas **[212]**.

Tab. 3.2. *Si and Ge atomic ratio in each Si_xGe_{1-x} deposit, calculated from the EDX analysis over more than 15 scanned points and areas.*

Sample ID	**Duty cycle**	**Si_xGe_{1-x} stoichiometry***
$SG_{21}DC_{50}$	50%	$Si_{0.3}Ge_{0.7}$
$SG_{21}DC_{16}$	16%	$Si_{0.6}Ge_{0.4}$
$SG_{11}DC_{50}$	50%	$Si_{0.7}Ge_{0.3}$
$SG_{11}DC_{16}$	16%	$Si_{0.9}Ge_{0.1}$
**x ± 0.03-0.05*		

Figure (3.23, insets a-d) illustrates the EDS-elemental mapping of as-deposited Si_xGe_{1-x} films. The insets show the distribution of Si and Ge in each deposit. The elemental mapping of $SG_{21}DC_{50}$ deposit (inset a) confirms that the deposit is cracked and composed of separated islands. The prominent percent of oxygen in all deposits mostly arises from the oxidation during transferring the samples to SEM device under the air. The C, S, N and F traces are ILs-residuals, trapped in the deposit films which also can be seen in EDS spectra in figure (3.22).

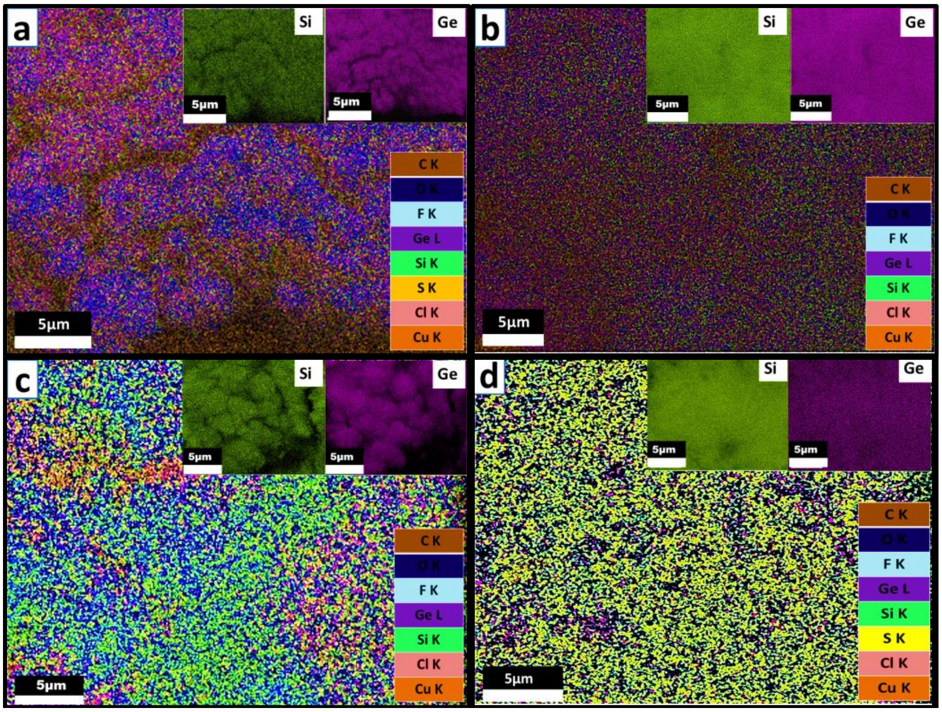

Fig. 3.23. *EDS micro-mapping of Si_xGe_{1-x} deposits; $SG_{21}DC_{50}$* ***(a)****, $SG_{21}DC_{16}$* ***(b)****, $SG_{11}DC_{50}$* ***(c)****, and $SG_{11}DC_{16}$ samples* ***(d)*** *with Si and Ge overall mapping (insides).*

Figure (3.24, insets a-d) shows the thickness measurements of Si_xGe_{1-x} films by FE-SEM. The pulsed-electrodeposition parameters seem to have an effect on the thicknesses of Si_xGe_{1-x} deposits. The measurements of the deposit thickness was not completely accurate owing to the non-uniformity of most of Si_xGe_{1-x} deposits, especially $SG_{21}DC_{50}$ and $SG_{11}DC_{50}$ deposits which were deposited at higher duty cycle values with shorter T_{OFF} intervals. Nevertheless, it can be concluded that the pulsed-electrodeposition at 16% duty cycle can produce thinner and more compact Si_xGe_{1-x} films compared to that films deposited at 50% duty cycle.

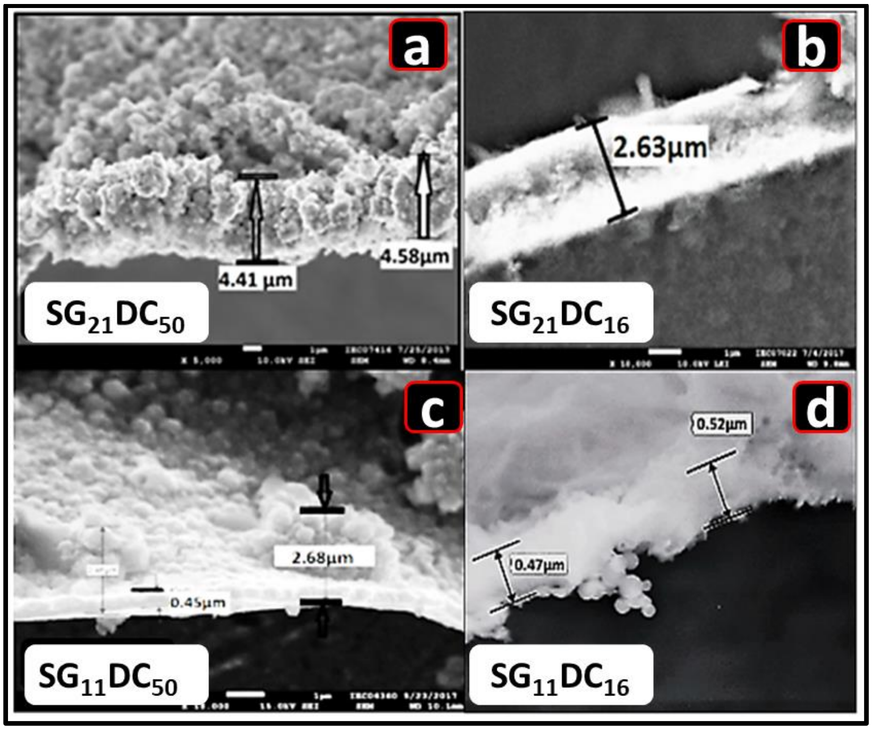

Fig. 3.24. *SEM thickness-measurements of Si_xGe_{1-x} films produced by potentiostatic pulsed-electrodeposition; $SG_{21}DC_{50}$* ***(a)****, $SG_{21}DC_{16}$* ***(b)****, $SG_{11}DC_{50}$* ***(c)****, and $SG_{11}DC_{16}$ samples* ***(d)****.*

3.2.3. FT-IR spectroscopic analysis of Si_xGe_{1-x} films

Si_xGe_{1-x} deposits were analyzed by FT-IR to detect the bonding configuration of Si-Ge from the infrared absorption in the MID-IR range of 600-1100 cm^{-1} as shown in figure (3.25). The first peak at around 620 cm^{-1} is assigned to the Si-Si stretching mode in $Si_{0.6}Ge_{0.4}$, $Si_{0.7}Ge_{0.3}$, and $Si_{0.9}Ge_{0.1}$ deposits **[213, 214]**. Another two sharp peaks detected at around 795 and 1060 cm^{-1} can be correlated to bending and stretching vibration modes of the Si–O bonding, respectively **[215]**. N. S. Rao *et al.* **[214]** have assigned the peak at around 740 cm^{-1} to the Ge-Ge mode. In our case, this peak could be also indexed to both the asymmetric stretching of S-N-S and the symmetric deformation of CF_3 groups as decomposition compounds of TFSI anion which were trapped in the bulk deposits. Si–O–Ge vibrational mode was also reported to occur in the frequency range of 995 and 1030 cm^{-1} [215, 216]. The intensities of the above mentioned peaks at 620, 795, and 1060 cm^{-1} can signify the atomic ratios of Si in Si_xGe_{1-x} films which increase as the Si percent in these films increases.

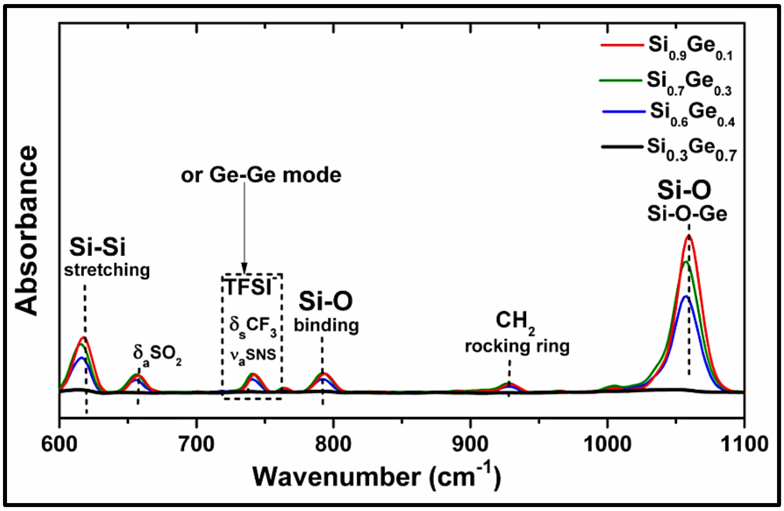

Fig. 3. 25. FT-IR spectra of Si_xGe_{1-x} films in the MID-IR range from 1100 to 600 cm^{-1}.

3.2.4. Electrochemical performance in LIB

3.2.4.1. Cyclic voltammetry in LIB

Cycling voltammograms of as-deposited Si_xGe_{1-x} films from OCP to 0.01 V vs. Li/Li^+ using LiTFSI/[BMP]TFSI electrolyte are shown in figure (26, insets a-d). The cycling voltammetry measurements were performed in half-cells to test the lithium alloying/de-alloying features in each deposit against Li as reference and counter electrode. Generally, the Li alloying peaks in all Si_xGe_{1-x} anode films start at around 0.5 V, followed by an increase in the negative current, correlated with their full-lithiation phases, forming $Li_{15}[Si_xGe_{1-x}]_4$ alloys [83]. In case of the Ge-rich $Si_{0.3}Ge_{0.7}$ anode-film (shown in inset a), its alloying peak is quite weak, possibly due to its large particles and the non-compact feature of this deposit, taking into consideration that the high Ge content (60%) shares low capacity values compared to Si. This anode also shows a significant peak at around 1.15 V, related to the reductive decomposition of Li^+-electrolyte and the formation of SEI-interfacial layer **[83]**. In $Si_{0.6}Ge_{0.4}$ and $Si_{0.7}Ge_{0.3}$ deposits (insets b and c), their SEI peaks at around 1.6 and 1 V, respectively, are less evident, which may indicate that their SEI layer is thinner compared to that formed on Ge-rich Si_xGe_{1-x}. In addition, the SEI correlated peak is not evident in $Si_{0.9}Ge_{0.1}$ anode-film in inset d. It worth noting that SEI peaks become not evident after the first cycle in all Si_xGe_{1-x} anode-films, indicating that this interfacial layer stops growing. The foremost peaks before 2 V in $Si_{0.6}Ge_{0.4}$ and $Si_{0.7}Ge_{0.3}$ anode-films (insets b and C) are correlated to Li under-potential deposition (Li-UPD) **[217, 218]**.

In the stripping/de-lithiation part, all Si_xGe_{1-x} anode-films show only one broad de-alloying peak around 0.65 V. It can be concluded that the germanium-rich $Si_{0.3}Ge_{0.7}$ anode-films show a single lithium insertion peak and also a single Li-extraction peak, similar to the cycling performance of Ge electrodes **[83]**. On the other hand, the silicon-rich anode films ($Si_{\mathbf{0.6}}Ge_{\mathbf{0.4}}$, $Si_{\mathbf{0.7}}Ge_{\mathbf{0.3}}$, and $Si_{\mathbf{0.9}}Ge_{\mathbf{0.1}}$ deposits) show two lithiation peaks and one broad de-lithiation peak, which can be categorized to the cycling performance of Si-like electrodes **[83]**. It worth mentioning that the current values of de-lithiation peaks in all silicon-rich anode films ($Si_{\mathbf{0.6}}Ge_{\mathbf{0.4}}$, $Si_{\mathbf{0.7}}Ge_{\mathbf{0.3}}$, and $Si_{\mathbf{0.9}}Ge_{\mathbf{0.1}}$ deposits) increase with cycling which can refer to a kinetic-modification in these anode-films **[178]**, similar to the cycling performance of Si-films that were discussed before in section 3.1.1. Also, the appearance of several lithiation peaks in $Si_{0.7}Ge_{0.3}$ might indicate that the Si and Ge in this film are not mixed on an atomic scale [83].

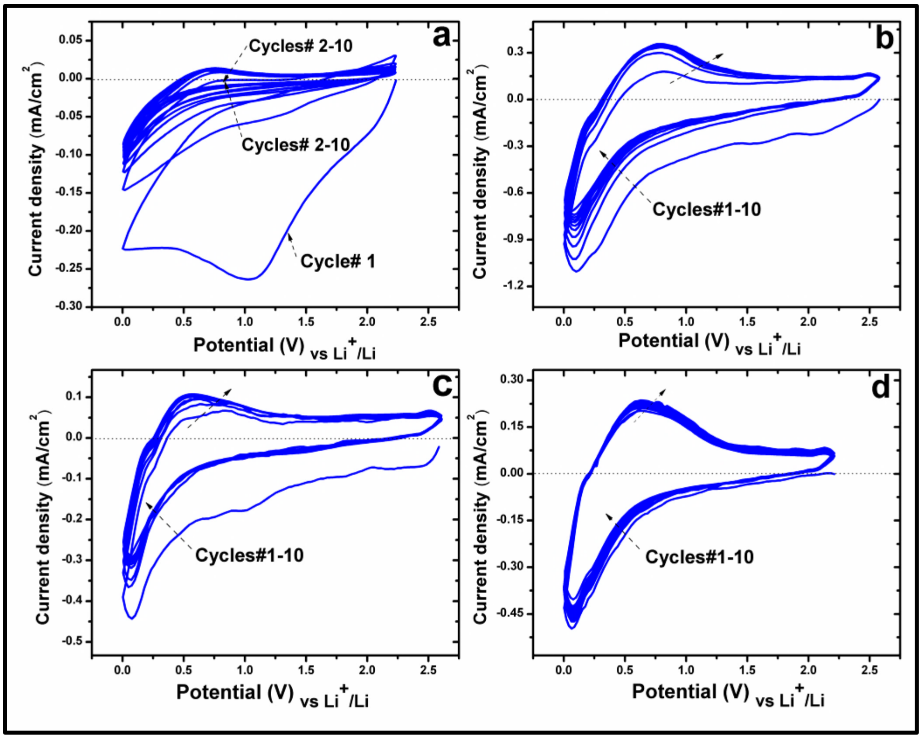

Fig. 3.26. *Cyclic voltammograms of Si_xGe_{1-x} anode-films; $Si_{0.3}Ge_{0.7}$* ***(a)****, $Si_{0.6}Ge_{0.4}$* ***(b)****, $Si_{0.7}Ge_{0.3}$* ***(c)*** *and $Si_{0.9}Ge_{0.1}$* ***(d)*** *at a scanning rate of 1 mV/s using 0.5 M LiTFSI/[BMP]TFSI as the battery electrolyte.*

3.2.4.2 Galvanostatic cycling evaluation in LIB

Figure (3.27, insets a-d) illustrates the voltage profiles of the dc-cycled Si_xGe_{1-x} anode-films at 0.75 C-rate. The insets inside show the first charge/discharge plateaus when the anodes were cycled at 0.01 mA/cm^2. The values of the first capacity loss are 60%, 56%, 73% and 88% for $Si_{0.3}Ge_{0.7}$, $Si_{0.6}Ge_{0.4}$, $Si_{0.7}Ge_{0.3}$ and $Si_{0.9}Ge_{0.1}$ anodes, respectively.

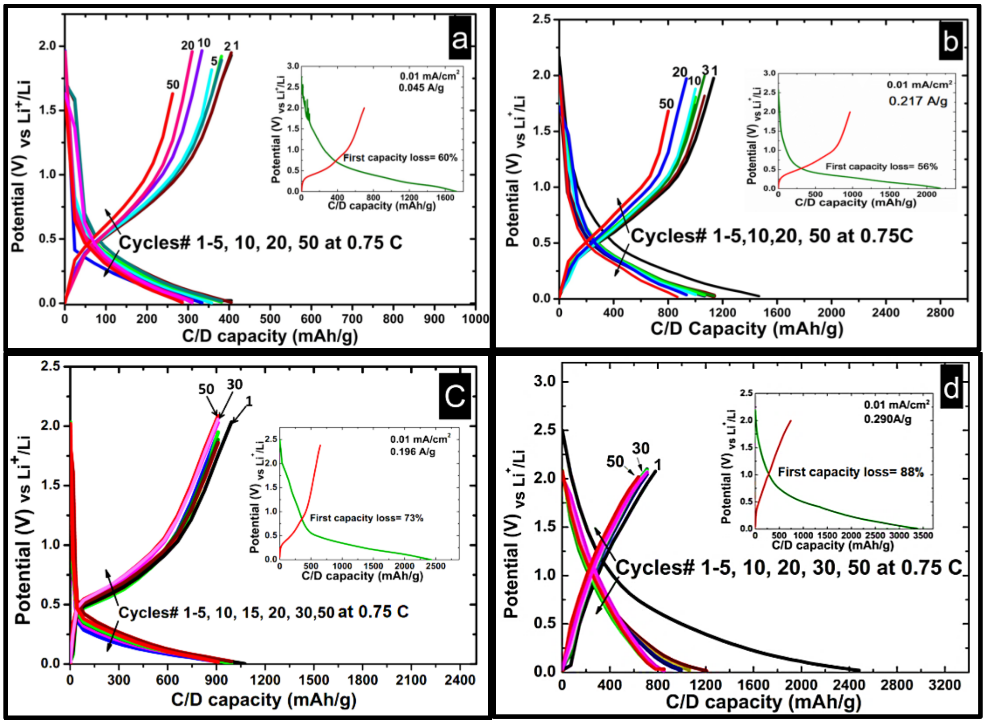

Fig. 3.27. *Voltage profiles of* $Si_{0.3}Ge_{0.7}$ ***(a)****,* $Si_{0.6}Ge_{0.4}$ ***(b)****,* $Si_{0.7}Ge_{0.3}$ ***(c),*** *and* $Si_{0.9}Ge_{0.1}$ *anodes* ***(d)*** *when cycled at 0.75 C-rate. The voltage profiles of these anode films upon initial charge/discharge cycles at a current density of 0.01* mA/cm^2 *with their first irreversible capacity loss values are shown inside.*

The galvanostatic charge/discharge performances of as-deposited Si_xGe_{1-x} anode films at C-rates of 0.75 C and 1.5 C are shown in figure (3.28, insets a-d) with their chrono-potentiograms. The cycling performances of Si_xGe_{1-x} anode films can be split into three categories [83]. For $Si_{0.3}Ge_{0.7}$ anode film (inset a), its cycling performance is similar to Ge anode material with good cycling stability and high coulombic efficiency of around 95%. Even this anode-film shows quite low gravimetric capacity, its cycling stability can be attributed to its high electronic and ionic conductivity due to the high Germanium content [83]. $Si_{0.6}Ge_{0.4}$ and $Si_{0.7}Ge_{0.3}$ anode-films exhibit intermediate cycling performance between Si and Ge anode materials as shown in insets b and c [83]. $Si_{0.6}Ge_{0.4}$ anode-film shows high gravimetric capacity with a coulombic efficiency value around 98%, correlated to its small particle size and its compactness feature. For $Si_{0.7}Ge_{0.3}$, the capacity values and the coulombic efficiency show some fluctuation, which could confirm that, the Si_xGe_{1-x} film is not homogeneously mixed in the atomic scale which was noticeable in its voltammogram. $Si_{0.9}Ge_{0.1}$ anode-film (incest d) shows cycling performance similar to silicon-like materials **[83]** with poor coulombic efficiency, which improved when this anode film was cycled at higher cycling rate equal to 1.5 C.

The areal capacity values of all Si_xGe_{1-x} anode films are shown in figure (3.28e). These values are quite low due to the low mass loading of Si_xGe_{1-x} films. Taeseup Song *et al.*, have reported that Si/Ge double-layered nanotubes electrode retained 2 fold higher areal capacities compared to that of Si nanotubes electrodes **[82]** which is in good agreement with the results of the present thesis.

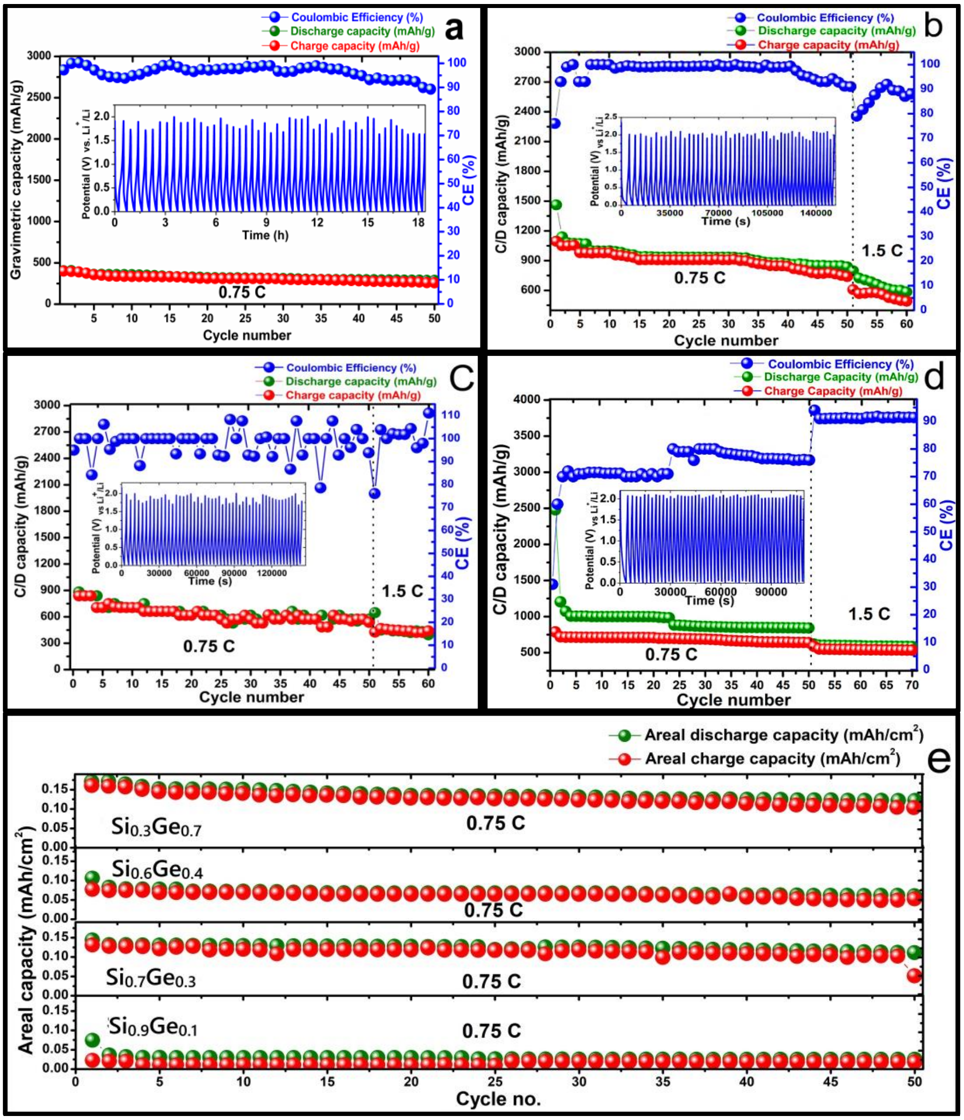

Fig. 3.28. *Galvanostatic charge/discharge performance for* Si_xGe_{1-x} *anode-films;* $Si_{0.3}Ge_{0.7}$ ***(a)****,* $Si_{0.6}Ge_{0.4}$ ***(b)****,* $Si_{0.7}Ge_{0.3}$ ***(c)****, and* $Si_{0.9}Ge_{0.1}$ ***(d)*** *at 0.75 and 1.5 C-rates with their chrono- potentiograms. Inset* ***(e)*** *shows the areal capacities of each* Si_xGe_{1-x} *anode-film at 0.75 C-rate.*

3.2.4.3 Galvanostatic cycling evaluation of ultrathin Si_xGe_{1-x} film in LIB

Figure (3.29a, b) shows the galvanostatic charge/discharge cycling performance of ultrathin Si_xGe_{1-x} anode. This anode films was deposited by the same potentiostatic pulsed-deposition procedure of

$SG_{11}DC_{16}$ sample at 16% duty cycle but for only 15 minutes in $SiCl_4$ (0.5 M)/$GeCl_4$ (0.5 M)/[EMIm]TFSI bath. The thickness of this Si_xGe_{1-x} anode is approximately predictable to be less than 400 nm. The stoichiometry of this Si_xGe_{1-x} calculated from EDX spectra was $Si_{0.95}Ge_{0.05}$.

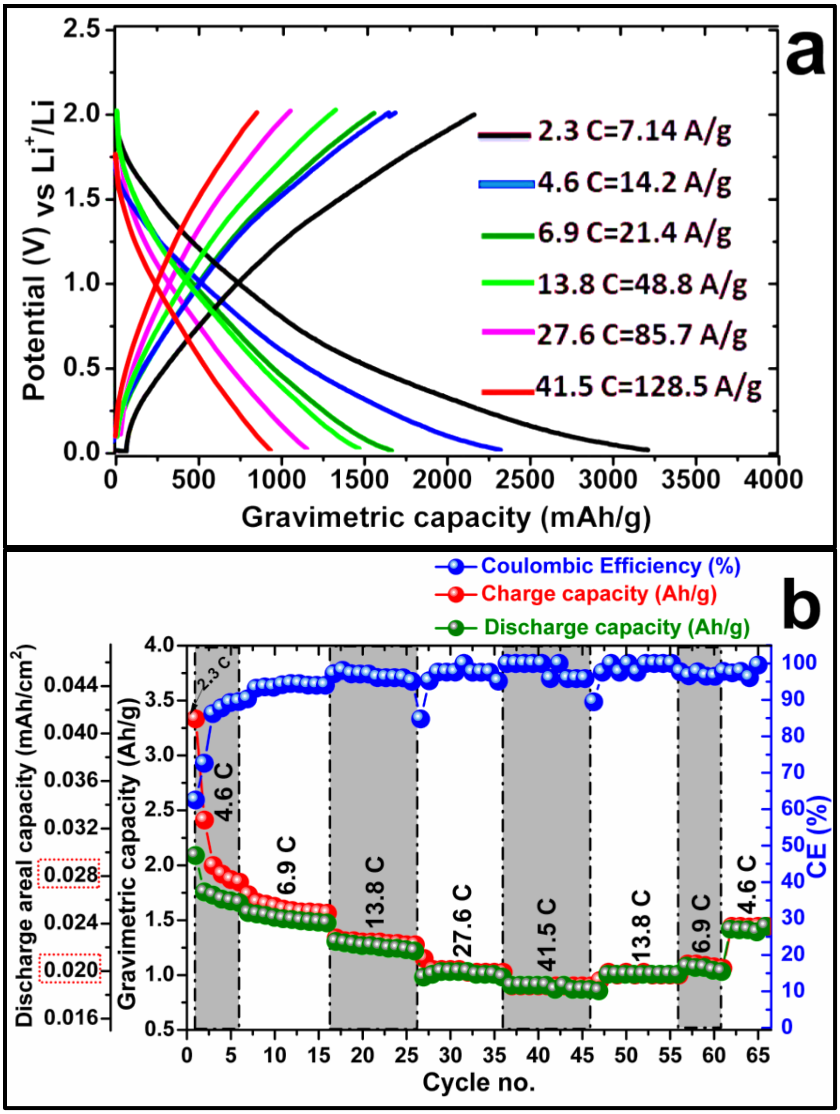

***Fig. 2.29**. Voltage plateaus **(a)** and galvanostatic charge/discharge performance at different cycling rates **(b)** of ultrathin $Si_{0.95}Ge_{0.05}$ anode film deposited by PED in $SiCl_4$ (0.5 M)/$GeCl_4$ (0. 5 M)/[EMIm]TFSI bath at 16% duty cycle for 15 minutes.*

The electrochemical performance of the ultrathin $Si_{0.95}Ge_{0.05}$ deposit displays high gravimetric capacity and promising high rate capability (~2000 mAh/g at 4.6 C-rate and ~900 mAh/g at 41.5 C-rate). Even though, the areal capacity values are very low (more than 30 μAh/cm^2 at 4.6 C-rate and more than 20 μAh/cm^2 at 41.5 C-rate). Takamura *et al.* **[65]** have reported similar results concerning the electrochemical performance of 50 nm-thick silicon films which produced a reversible gravimetric capacity of above 2000 mAh/g when cycled at 30 C-rate. The group has also reported that a 440 nm-thick Si film produced a gravimetric capacity of above 2000 mAh/g at 1C-rate. Nevertheless, the authors did not declared the values of the retained areal capacities, which are expected to be too low. Thus, even ultrathin Si_xGe_{1-x} anode can produce higher gravimetric capacity values and better cycling capability than ultrathin Si films reported in reference 65, the low areal capacity and energy density produced by such ultrathin anode films are not satisfying for the application in high-drain energy suppliers, but can be applied in micro-batteries.

3.2.5. Electrochemical Impedance Spectroscopy (EIS)

Figure (3.30) shows EIS-Nyquist plots of Si_xGe_{1-x} anodes after 50 cycles at 0.75 C-rate in the de-lithiated state. It can be seen that the Nyquist plots for all cycled anodes exhibit one semicircle in the high-to-middle frequency region, followed by one Warburg-diffusion slope in the low-frequency range. The Warburg tail is shorter in the case of $Si_{0.3}Ge_{0.7}$ and $Si_{0.6}Ge_{0.4}$ cycled anodes, suggesting higher accessibility of Li-ions in these alloy films compared to $Si_{0.7}Ge_{0.3}$ and $Si_{0.9}Ge_{0.1}$ anodes **[182]**, thanks to the high electronic conductivity and the greater diffusivity in Ge. The absence of the SEI-semicircle in all Si_xGe_{1-x} anode films (which may also exist as a very small semicircle overlapped with the next one) implies that the resistance through their SEI is negligible, which is consistent with the ultra-thin SEI formed in LiPF$_6$ in a florinated-EC electrolyte, where its Z$_{SEI}$ was reported also as negligible [181, 219]. Thus, it seems that TFSI-fluorine plays a role in reducing the thickness of SEI formed on Si$_x$Ge$_{1-x}$ anode-films.

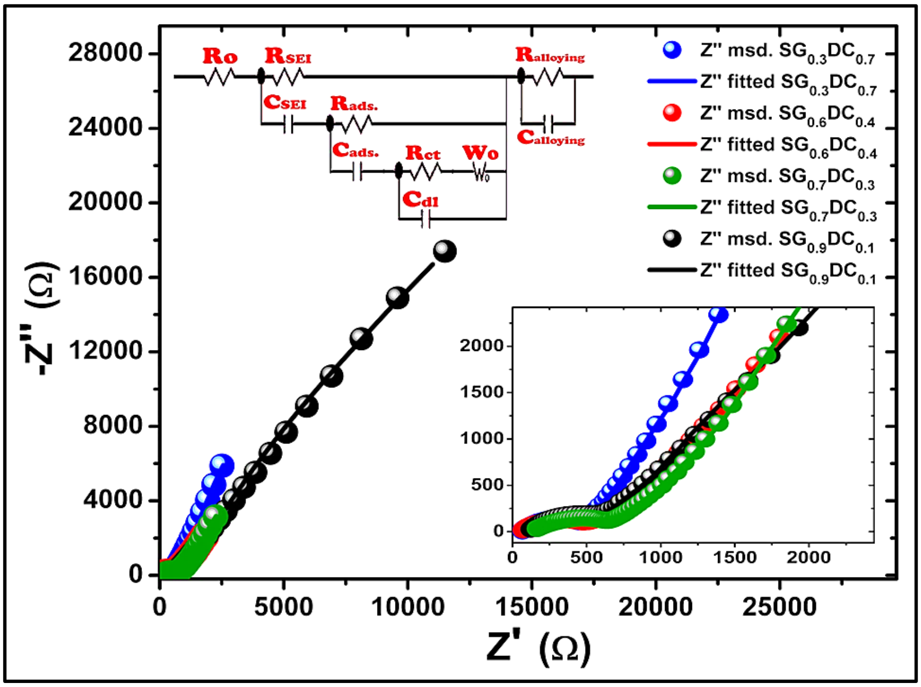

Fig. 3.30. *EIS-Nyquist plots of Si$_x$Ge$_{1-x}$ anode films after 50 cycles at 0.75 C-rate in the de-lithiation state. The inset shows a magnification of the Nyquist plots in the high-to-middle frequency region. The best fitting equivalent circuit is shown inside.*

Si$_x$Ge$_{1-x}$ anodes may exhibit adsorption/desorption process like Si anodes suggested by the fitting circuit which may indicate the complicated interactions of Si-Ge anodes not only with lithium but also with other electrolyte-elements trapped in the deposits. The inserted inset displays a magnification of Nyquist plots in the high-to-medium frequency range. The intercept with *x*-axis signifies the equivalent series of ohmic resistance (R$_0$), interrelated to the ionic conductivity of electrolyte solution and electronic contact resistance of cell hardware such as the separator contact-resistance and the current collector resistance. This ohmic resistance seems to increase as Si stoichiometry increase in Si_xGe_{1-x} anode, which could refer to the delamination of Si-rich Si_xGe_{1-x} anodes after long cycling [178]. The EIS-Bode plots of Si_xGe_{1-x} anodes after 50 cycles at 0.75 C-rate in the de-lithiated state are introduced in section 5.3.1 in the appendix part of this thesis.

3.2.6. X-ray Photoelectron Spectroscopy of SEI layers formed on Ge-rich and Si-rich Si_xGe_{1-x} anode-films after 1-charge

Ex-situ XPS investigations were performed to analyze the composition of SEI layers formed on cycled Ge-rich $Si_{0.3}Ge_{0.7}$ and Si-rich $Si_{0.9}Ge_{0.1}$ anode films after the first charging.

Figure (3.31a) shows XPS survey spectra of SEI layers formed on $Si_{0.3}Ge_{0.7}$ anode after the initial charging at a current density of 45 mA/g. The upper SEI layer seem to contain residuals of LiTFSI/[BMP]TFSI electrolyte. Figure (3.31b) shows the detailed spectra of Ge 2p, C 1s, O 1s, F 1s, Si 2p and Li 1s in different SEI layers formed on the Ge-rich $Si_{0.3}Ge_{0.7}$ anode after the first charge at a current density of 45 mA/g. Si 2p and Ge 2p deconvolution spectra show that the elemental Si and Ge are mainly oxidized after charging into SiO_x and GeO_x which peaks can be found at around 103 eV and 1220 eV in Si 2p and Ge 2p spectra, respectively [165]. This result is supported by the peak at 533 eV in O 1s spectrum related to the Li_ySiO_x/Li_yGeO_x compounds [200]. In F 1s detailed spectra, LiF peaks at around 685 eV are very dominant especially in deeper SEI layers, confirmed by the LiF peak at around 57 eV in Li 1s spectra. In C 1s spectra, Li_2CO_3 peaks can be detected at around 289 eV which intensities are dominant in upper SEI layers. On the other hand, Li_2O

peaks can be detected in deeper (2nd and 3rd-sputtered) SEI layers. LiF and Li_2CO_3, in addition to CF_3 compounds are expected to stabilize SEI as stable and more passivating compounds [193, 194], which can reflect positively in the electrochemical performance of $Si_{0.3}Ge_{0.7}$ anode.

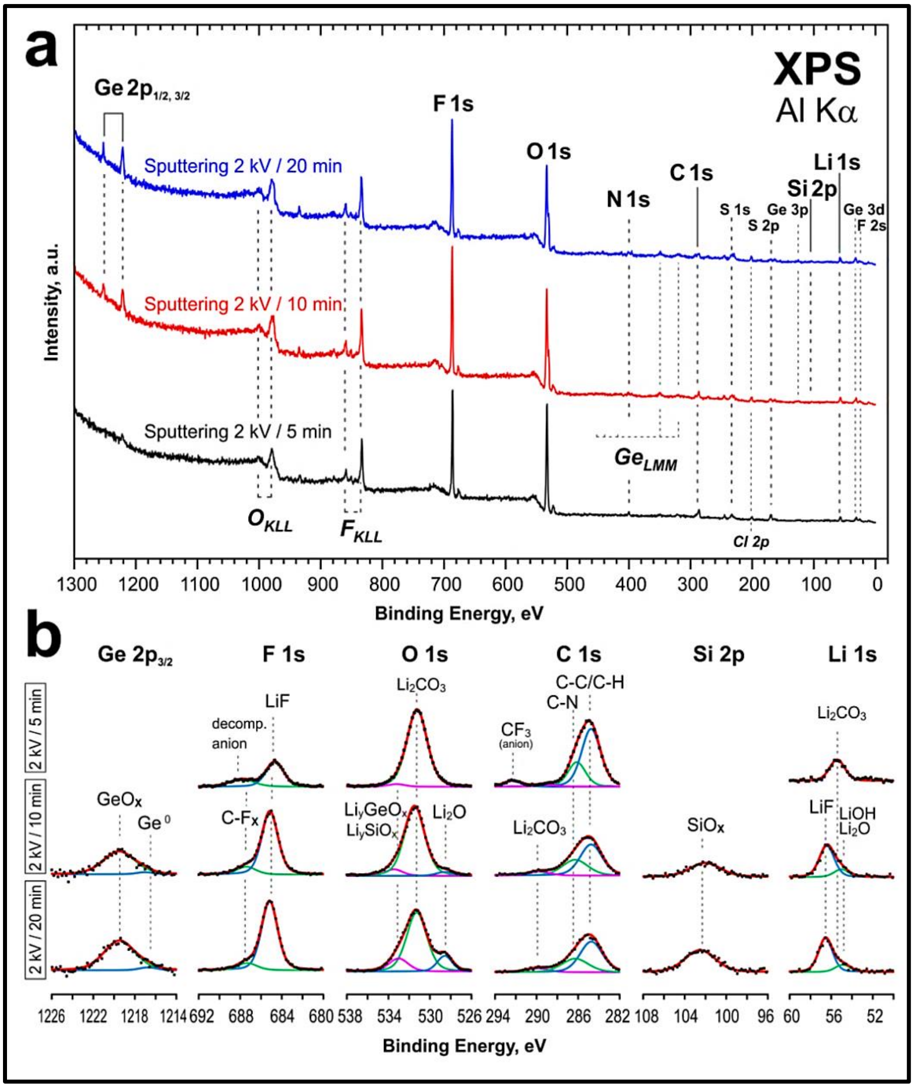

Fig. 3.31. *Ex-situ XPS analysis of SEI layers formed on Ge-rich* $Si_{0.3}Ge_{0.7}$ *deposit after the first charge at a current density of 45 mA/g in LiTFSI/[BMP]TFSI;* ***(a)*** *XPS survey spectra,* ***(b)*** *detailed spectra of Ge 2p, F 1s, O 1s, C 1s, Si 2p and Li 1s in different SEI layers.*

Figure (3.32a, b) shows the overall survey of SEI layers formed on Si-rich $Si_{0.9}Ge_{0.1}$ anode and the detailed spectra of Ge 2p, F 1s, O 1s, C 1s, Si 2p and Li 1s after full charging at a current density of 290 mA/g.

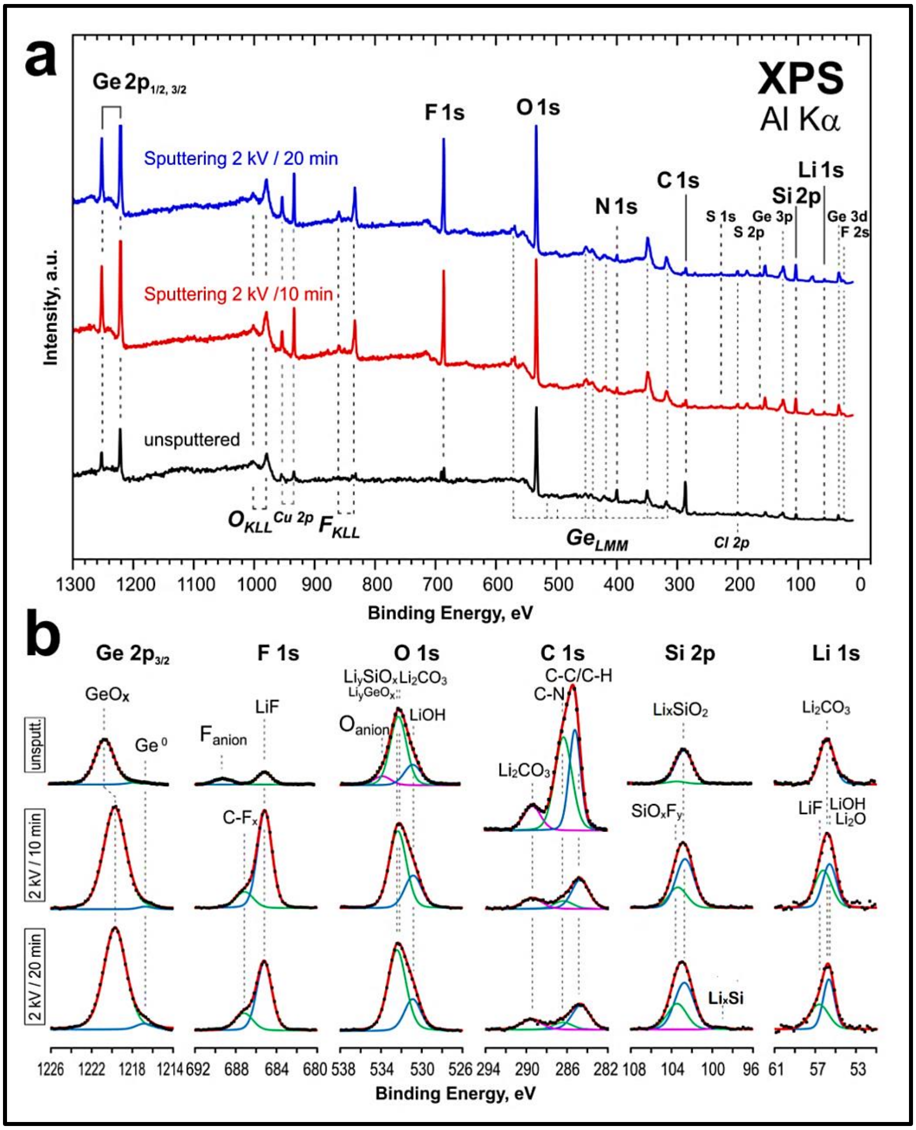

Fig. 3.32. *Ex-situ XPS analysis of SEI layers formed on Si-rich $Si_{0.9}Ge_{0.1}$ deposit after the first charge at a current density of 290 mA/g in LiTFSI/[BMP]TFSI;* ***(a)*** *XPS survey spectra,* ***(b)*** *the detailed spectra of Ge 2p, F 1s, O 1s, C 1s, Si 2p and Li 1s at different SEI layers.*

The deconvolutions of Si 2p spectra include two peaks at around 103 and 104 eV which could be correlated to Li_ySiO_2 **[200]** and SiO_xF_y, respectively **[166]**. F ions from the electrolyte could react with SiO_x surface forming Si-O-F bonds **[171-173]** causing a shift in SiO_2 peak from 103 eV to 104 eV. Li_ySi alloying peak can be detected at the deeper layer at around 98.5 eV **[170]**. LiF and Li_2CO_3 peaks are evident in all SEI investigated layers.

Figure (3.33) shows the atomic percent of Ge 2p, F 1s, O 1s, C 1s, Si 2p and Li 1s in SEI formed on Ge-rich $Si_{0.3}Ge_{0.7}$ anode (inset a) and Si-rich anode $Si_{0.9}Ge_{0.1}$ (inset b) after the first charge, calculated from the XPS data. SEI formed on $Si_{0.3}Ge_{0.7}$ anode has high percent of Li 1s, compared to the one formed on $Si_{0.9}Ge_{0.1}$ cycled anode. The inserted tables illustrate the concentration of some SEI decomposition-compound (LiF, Li_2O, Li_2CO_3 and CF_x) which were calculated from the intensities of deconvolution peaks of Li 1s and F 1s spectra. These inorganic compounds are stable and more passivating compared to other organic-SEI compounds **[193, 194]**, which could stabilize the SEI upon cycling. The concentration of these compounds in the SEI formed on $Si_{0.3}Ge_{0.7}$ anode is higher than that in SEI formed on $Si_{0.9}Ge_{0.1}$ anode, which could explain the cycling stability of the Ge-rich $Si_{0.9}Ge_{0.1}$ anode, compared to $Si_{0.9}Ge_{0.1}$ anode. The detailed XPS studies of the SEI layer formed after several cycles are required to elucidate the role of these SEI compounds on the cycling stability of Si anode films which could not be accomplished due to the time-limitation of this thesis.

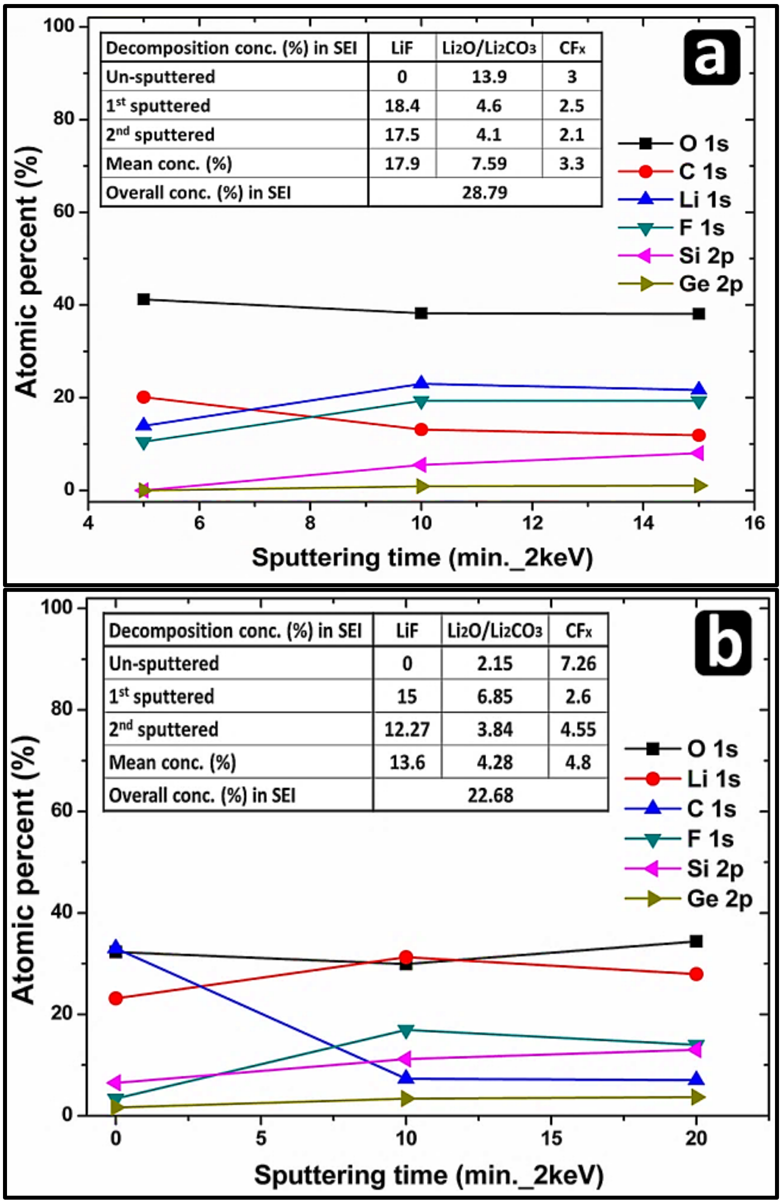

Decomposition conc. (%) in SEI	LiF	Li2O/Li2CO3	CFx
Un-sputtered	0	13.9	3
1st sputtered	18.4	4.6	2.5
2nd sputtered	17.5	4.1	2.1
Mean conc. (%)	17.9	7.59	3.3
Overall conc. (%) in SEI	28.79		

Decomposition conc. (%) in SEI	LiF	Li2O/Li2CO3	CFx
Un-sputtered	0	2.15	7.26
1st sputtered	15	6.85	2.6
2nd sputtered	12.27	3.84	4.55
Mean conc. (%)	13.6	4.28	4.8
Overall conc. (%) in SEI	22.68		

Fig. 3.33. *The atomic percent of Si 2p, Ge 2p, F 1s, O 1s, C 1s, and Li 1s calculated from the XPS data of SEI formed on* $Si_{0.3}Ge_{0.7}$ ***(a),*** *and* $Si_{0.9}Ge_{0.1}$ *anode films* ***(b)****. The inserted tables show the concentration of LiF,* Li_2O*,* Li_2CO_3 *and* CF_x *in SEI formed on each cycled anode.*

Conclusion on Si_xGe_{1-x} as anode material in LIBs

Si_xGe_{1-x} alloy-films were electrodeposited in [EMIm]TFSI ionic liquid by potentiostatic pulsed-electrodeposition. Changing PED-temporal parameters and $GeCl_4$ molar ratio result in Si_xGe_{1-x} deposits with different stoichiometry, morphology, and compactness features.

Si_xGe_{1-x} anode-films show variation in cycling performance in Lithium-ion batteries. For $Si_{0.3}Ge_{0.7}$ anode film, its cycling performance is similar to Ge anode material with good cycling stability and high coulombic efficiency of around 95%. Even this anode-film shows quite low gravimetric capacity, its cycling stability can be attributed to its high electronic and ionic conductivity due to its high Germanium content. $Si_{0.6}Ge_{0.4}$ anode-film produced a high gravimetric capacity with a superior coulombic efficiency. $Si_{0.7}Ge_{0.3}$ anode showed higher areal capacity values (of around 0.14 mAh/cm^2) compared to other Si-rich Si_xGe_{1-x} anode-films. Also, this anode showed a fluctuated coulombic efficiency as Si and Ge in these alloy-films seem to be not well-alloyed within the atomic scale. Si-rich $Si_{0.9}Ge_{0.1}$ anode exhibited poor cycling stability with lower capacity retention similar to Si-like materials. Even though, it's cycling stability improved when cycled at higher C-rates. Ultrathin $Si_{0.9}Ge_{0.1}$ anode with thickness estimated to be less than 400 nm produced high gravimetric capacity with extraordinary rate capability (~900 mAh/g at 41.5 C-rate/128.5 A/g). Even though, the areal capacity values produced by this anode were less than 20 μAh/cm^2. The low areal capacity retained by such ultrathin $Si_{0.09}Ge_{0.05}$ anode film makes it a more suitable for micro-batteries applications than for high-drain energy storage devices.

EIS studies for long cycled Si_xGe_{1-x} showed that the impedance contributions by SEI layers formed on all Si_xGe_{1-x} anodes after 50 cycles are entirely negligible, similar to an ultra-thin SEI formed in $LiPF_6$/fluorinated-EC electrolytes. Also, the non-faradic adsorption impedance was detected in Si_xGe_{1-x} anodes in the low-frequency region which refers to the complicated interactions of Si_xGe_{1-x} during cycling not only with lithium but also with other elements from the electrolyte.

Ex-situ XPS analysis showed that the SEI formed on Ge-rich $Si_{0.3}Ge_{0.7}$ anode is more stable than that formed on the Si-rich $Si_{0.9}Ge_{0.1}$ as it contain higher concentration of LiF, Li_2O, Li_2CO_3 and CF_x as SEI-stabilizing compounds which could explain the cycling stability in case of the Ge-rich Si_xGe_{1-x} compared to the poor cycling performance of Si-rich Si_xGe_{1-x} anode-films.

Compared to bare Si anode films, Si_xGe_{1-x} exhibited better cycling stability and higher retained gravimetric capacity values. The improvement in the electrochemical performance of Si_xGe_{1-x} films results from the enhanced electrical conductivity and Li-kinetics by alloying Ge with Si. Even though, the areal capacity of all Si_xGe_{1-x} anode films is still not satisfactory.

3.3. $Si_xGe_{1-x}Al_y$ anode-film

$Si_xGe_{1-x}Al_y$ ternary alloy-films were prepared by potentiostatic pulsed-electrodeposition to be investigated as modified anodes in half-cell LIB. The integration of Al to Si-Ge alloy could improve the mechanical problems of Si and Ge during cycling. Furthermore, Al was reported to limit the agglomeration of Si particles over cycling which could increase its cycling stability **[220]**, as well as both electrical conductivity and Li-kinetics in the anode, which is expected to reflect positively on its rate capability.

3.3.1. Cyclic voltammetry of $SiCl_4/GeCl_4/AlCl_3$/[BMP]TFSI electrodeposition bath

Cyclic voltammetry was used for $SiCl_4/GeCl_4/AlCl_3$/[BMP]TFSI bath in order to distinguish the electrochemical reaction regarding $Si_xGe_{1-x}Al_y$ electrodeposition on Cu. Figure (3.34) illustrates a representative voltammogram of the electrodeposition solution [0.5 M $SiCl_4$ + 0.25 M $GeCl_4$ + 0.02 M $AlCl_3$ in [BMP]TFSI], recorded on a Cu-substrate at a scanning rate of 50 mV/s. The cathode potential was scanned from OCP to -4 V versus Pt as a quasi-reference electrode (QRE). The cyclic voltammetry is such complex that distinguishing the exact reduction peaks for each analytes ($SiCl_4$, $GeCl_4$, and $AlCl_3$) in [BMP]TFSI is difficult. As labeled in figure (3.34), the cathodic regime shows four reduction peaks, together with another peak related to the decomposition of the employed IL. The reduction peak (C1) and the shoulder at C2 can be indexed to Al electrodeposition. Endres *et al.,* have reported that the cyclic voltammetry of $AlCl_3$ in [BMP]TFSI exhibits two small cathodic peaks at -0.9 and -1.3 V (vs. Al), presumably correlated to the bulk electrodeposition of Al **[221, 222]**. The followed cathodic peak (C3) at around -2.2 V is correlated to the reduction of Ge^{VI} to Ge^{II} **[120]**. C4 peak can be indexed to the bulk deposition of $Si_xGe_{1-x}Al_y$ ternary alloy. On the extreme cathodic side, the rising current after -3.2 V is related to the reduction of $[BMP]^+$ cation, after which the ionic liquid starts to decompose at C5. The anodic stripping regime shows two oxidation peaks at around -1.2 and -0.5 V, which can be allocated to the stripping of aluminum **[221]** and the oxidation of the $[TFSI]^-$ anion, respectively.

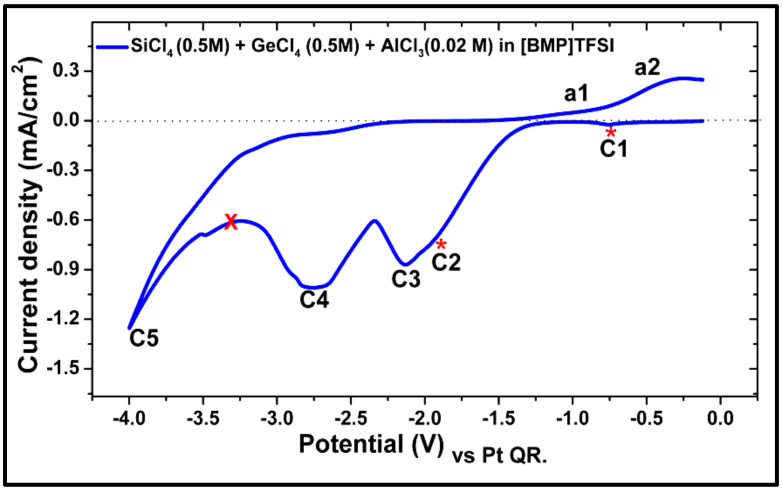

Fig. 3.34. *Cyclic voltammogram of the electrodeposition bath composed of $SiCl_4$ (0.5 M) + $GeCl_4$ (0.5 M) + $AlCl_3$ (0.02 M) in [BMP]TFSI ionic liquid, recorded on Cu from OCP to -4 V vs. Pt (QRE) at a scanning rate of 50 mV/s.*

3.3.2. Potentiostatic pulsed-electrodeposition of the $Si_xGe_{1-x}Al_y$ film

A $Si_xGe_{1-x}Al_y$ alloy film was electrodeposited by potentiostatic pulsed- electrodeposition at a duty cycle of 16%. Figure (3.35a) shows the overall pulsed-potential waves along with *j*/t curve of $Si_xGe_{1-x}Al_y$ electrodeposition for 30 minutes in $SiCl_4$ (0.5 M) + $GeCl_4$ (0.5 M) + $AlCl_3$ (0.02 M) in [BMP]TFSI ionic liquid. The analytes concentrations in this sole electrodeposition bath were unbalanced toward the less noble element (Si) so that the atomic percent of Al (as a more noble element) is expected to be lower than that of Si and Ge in the deposited $Si_xGe_{1-x}Al_y$ alloy-film.

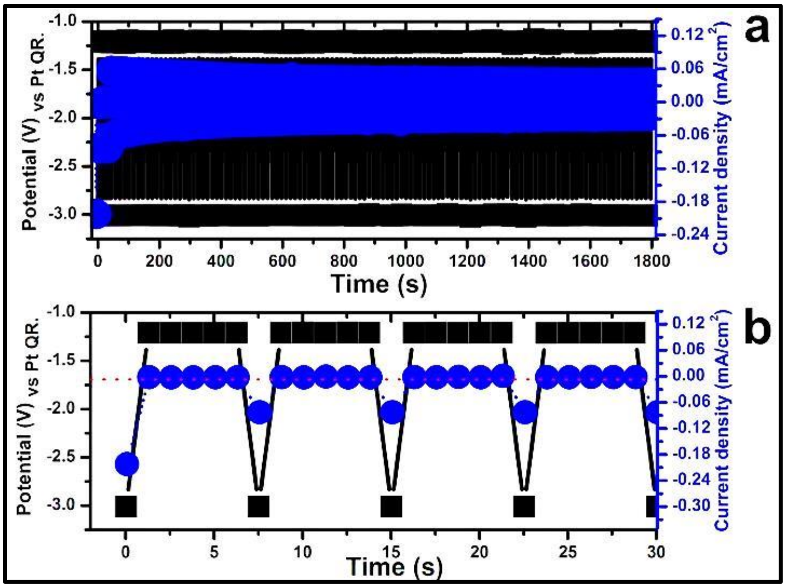

Fig. 3.35. *Potentiostatic pulsed-electrodeposition of* $Si_xGe_{1-x}Al_y$ *in* $SiCl_4$ *(0.5 M) +* $GeCl_4$ *(0.5 M) +* $AlCl_3$ *(0.02 M) in [BMP]TFSI at a duty cycle of 16% for 30 minutes.* ***(a)*** *Overall pulsed-potential waves with the j/t curve.* ***(b)*** *A close-up portion showing the applied potential waves (black) and its correlated current density (blue).*

Figure (3.35b) shows a magnification of the potential waves with the correlated current values at each pulse interval. Each pulse was adjusted for 6 seconds during which a more negative electrodeposition potential (P1= -3V) was applied during T_{ON} intervals for 1 second. Constantly, a less negative cathodic potential (P2= -1.2 V) was applied for 5 seconds during T_{OFF} intervals, so that the pulses duty cycle was controlled to be 16%. The value of P2 was chosen to be -1.2 V that almost no current was expected to arise through the deposition solution according to the cyclic voltammetry to avoid both the stripping of aluminum [221] and the oxidation of $[TFSI]^-$ anion. During the rest–time intervals (T_{OFF}) especially when it is much longer than T_{ON} (5 times longer in this case), the deposition-interface layer can be comfortably discharged and the electrolyte concentration expected to be sufficiently replenished around the deposition area [135, 138, 163]. Consequently, it is expected that both the nucleation process and the deposition rate will be improved at these deposition procedure, producing a compact, dense $Si_xGe_{1-x}Al_y$ deposit with smaller particles and low porosity.

3.3.3. Scanning Electron Microscopic investigations

FE-SEM images of a $Si_xGe_{1-x}Al_y$ film deposited by potentiostatic pulsed-electrodeposition for 30 minutes at a duty cycle of 16% are shown in figure (3.36a, b). The morphology of $Si_xGe_{1-x}Al_y$ deposits appears as a compact film with a limited porous feature. As well, the deposit consists of small particles as shown in inset b. The feature of the deposit in terms of its compactness and homogeneity can be explained through the pulse parameters. Pulsed-electrodeposition of $Si_xGe_{1-x}Al_y$ deposit at much longer T_{OFF} seems to provide enough time for the electrodeposition solution to replenish its concentration near the cathode [138, 163]. At these conditions, the nucleation process and the electrodeposition rate are expected to improve which results in a compact $Si_xGe_{1-x}Al_y$ deposit with small particle size. EDS-spectra of as-deposited $Si_xGe_{1-x}Al_y$ films in figure (3.36c, d) show some ILs-residuals and analytes, trapped in the deposits films.

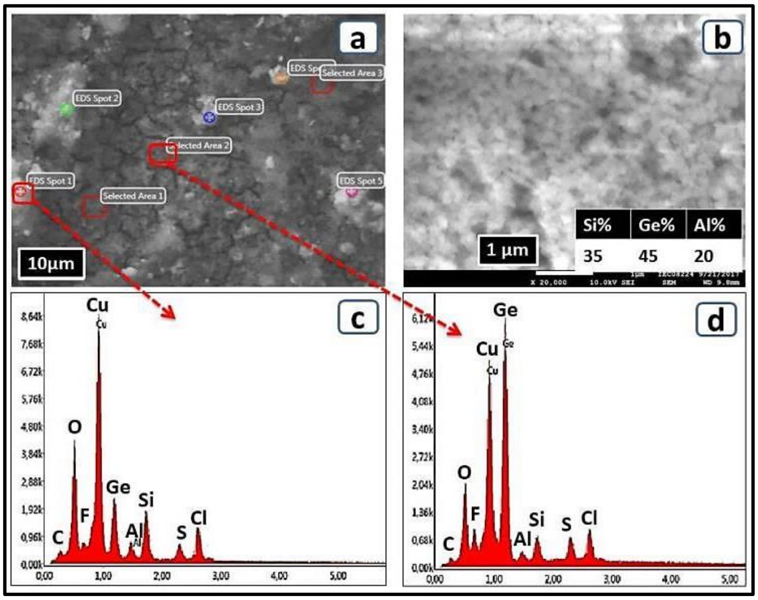

Fig. 3.36. *FE-SEM images (**a, b**), and EDX spectra **(c, d)** of as-deposited $Si_xGe_{1-x}Al_y$ which was prepared by pulsed-electrodeposition in a single bath [$SiCl_4$ (0.5 M) + $GeCl_4$ (0.5 M) + $AlCl_3$ (0.02 M) in [BMP]TFSI] at duty cycle of 16% for 30 minutes.*

Figure (3.37a) shows the overall elemental mapping for all elements contributing in $Si_xGe_{1-x}Al_y$ deposit. It seems that Cu is dissolved by $AlCl_3$ (as a Lewis acid) and redeposited on the surface. The elemental mapping of Ge, Si, and Al are shown in insets (b, c and d) respectively. $Si_xGe_{1-x}Al_y$ stoichiometry was calculated from EDX mapping and spectra by obtaining the mean atomic ratios over more than 20 scanned-spots and areas **[212]**, found to be $Si_{0.35}Ge_{0.45}Al_{0.2}$.

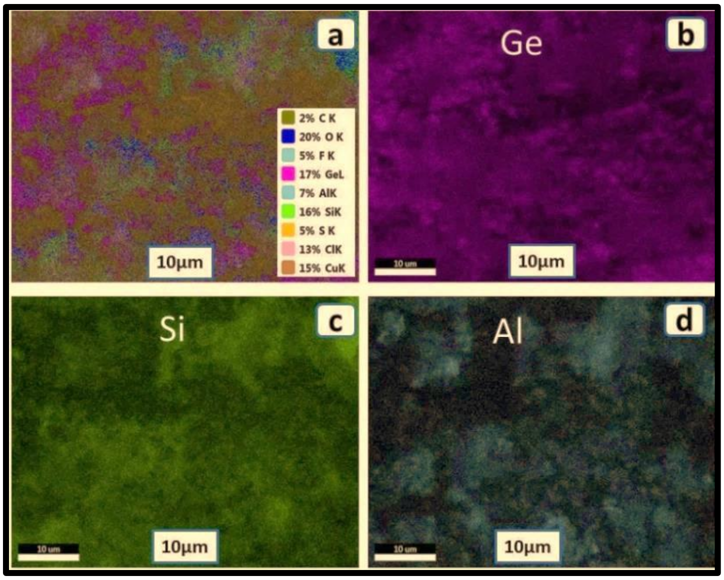

Fig. 3.37. *EDX-elemental mapping of as-deposited* $Si_xGe_{1-x}Al_y$ *film which was prepared by pulsed-electrodeposition in a single bath that contains* $SiCl_4$ *(0.5 M) +* $GeCl_4$ *(0.5 M) +* $AlCl_3$ *(0.02 M) in [BMP]TFSI at a duty cycle of 16% for 30 minutes. Overall mapping of all elements contributing in the film with their atomic ratios* ***(a)****, Elemental mapping of Ge* ***(b)****, Si* ***(c)*** *and Al* ***(d)****.*

3.3.4. Electrochemical performance in LIB

3.3.4.1. Cyclic Voltammetry in LIB

To test the lithium alloying/de-alloying features in as-deposited $Si_xGe_{1-x}Al_y$ film, cyclic voltammetry was performed for this alloy-film in a half-cell LIB in 0.5 M LiTFSI/[BMP]TFSI electrolyte. The cyclic voltammetry measurements shown in figure (3.38) were recorded at a scanning rate of 1 mV/s, starting from OCP to 0.01 V vs. Li/Li^+. The CV feature is quite different to the other voltammograms measured for Si and Si_xGe_{1-x} anode films. In the cathodic part, a broad SEI peak at 1.4 V is found in all cycles which indicate its frequent formation upon cycling. Also, the anode film exhibits one prolonged lithiation peak below 1 V till full lithiation at 0.01 V. In the anodic part, a single de-lithiation peak at around 1.1 V can be found as a broad peak. It can be concluded that the variation in cyclic voltammetry feature in this anode film compared to other Si and Si_xGe_{1-x} films gives the indication that Al is well alloyed with Si and Ge and well-mixed in the film within the atomic scale. Al appears to be an electrochemically active element, sharing some lithiation/de-lithiation processes. Also it seems to participate in the growth or the modification of the SEI.

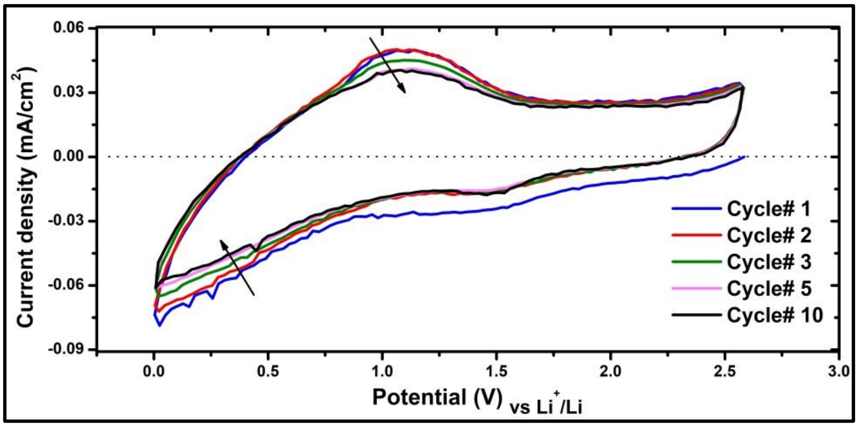

Fig. 3.38. *Consecutive cyclic voltammograms of $Si_xGe_{1-x}Al_y$ anode-films in a half-cell LIB in 0.5 M LiTFS/[BMP]TFSI electrolyte from OCP to 0.01 V at a scanning rate of 1 m V/s.*

3.3.4.2. Galvanostatic cycling evaluation in LIB

A $Si_xGe_{1-x}Al_y$ film was galvanostatically cycled in half-cell LIB at different current densities to evaluate its capacity output, its rate capability and its cycling stability. Figure (3.39a) shows the potential plateau of the $Si_xGe_{1-x}Al_y$ film upon initial charging/discharging at a low current density of 0.03 mA/cm^2 (equivalent to 100 mA/g). The anode film exhibit one pseudo-plateau around 1.75 V which can be related to the lithiation and/or the reduction of the superficial Cu or Cu-oxide layer on $Si_xGe_{1-x}Al_y$ anode film **[223]**. These pseudo-plateau is followed by a flat plateau before 0.5 V at which the lithiation processes of Si, Ge and Al take place. The active mass of $Si_xGe_{1-x}Al_y$

in the film was calculated from the initial charging, found to be 0.3 mg/cm^2, taking into consideration that the theoretical capacity of Al was considered as 1489 mAh/g corresponding to full lithiation of Li_3Al_2 [156, 157]. Also, the theoretical capacities of Si and Ge corresponding to the full-lithiation of $Li_{15}(Si_xGe_{1-x})_4$ are equal to 3589 and 1600 mAh/g, respectively, thus the theoretical capacity of $Si_{0.35}Ge_{0.45}Al_{0.2}$ anode-film equals 2377 mAh/g. The first capacity loss is 65% which presumbaly refers to the formation of a thick SEI layer.

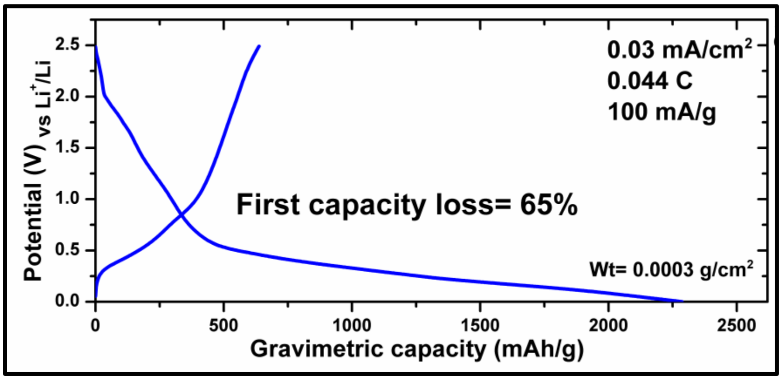

Fig. 3.39. *The voltage profile of the initial charge/discharge cycle of $Si_{0.35}Ge_{0.45}Al_{0.2}$ anode-film at a constant current density of 100 mA/g.*

Figure (3.40) introduces the galvanostatic cycling performance of $Si_{0.35}Ge_{0.45}Al_{0.2}$ anode film at different current density values. The anode film delivers high areal capacity values more than 0.5 mAh/cm^2 and gravimetric capacity values above 550 mAh/g when cycled at a current density of 800 mA/g (0.35 C-rate). Furthermore, the anode-film shows a good rate-capability and good cycling stability when cycled at higher current density values (1600 mA/g), producing areal capacity values at around 0.2 mAh/cm^2. The coulombic efficiency upon cycling is rather satisfying, fluctuating at higher cycling rates, which could be explained in terms of activation/modification processes in the $Si_xGe_{1-x}Al_y$ anode at some cycles.

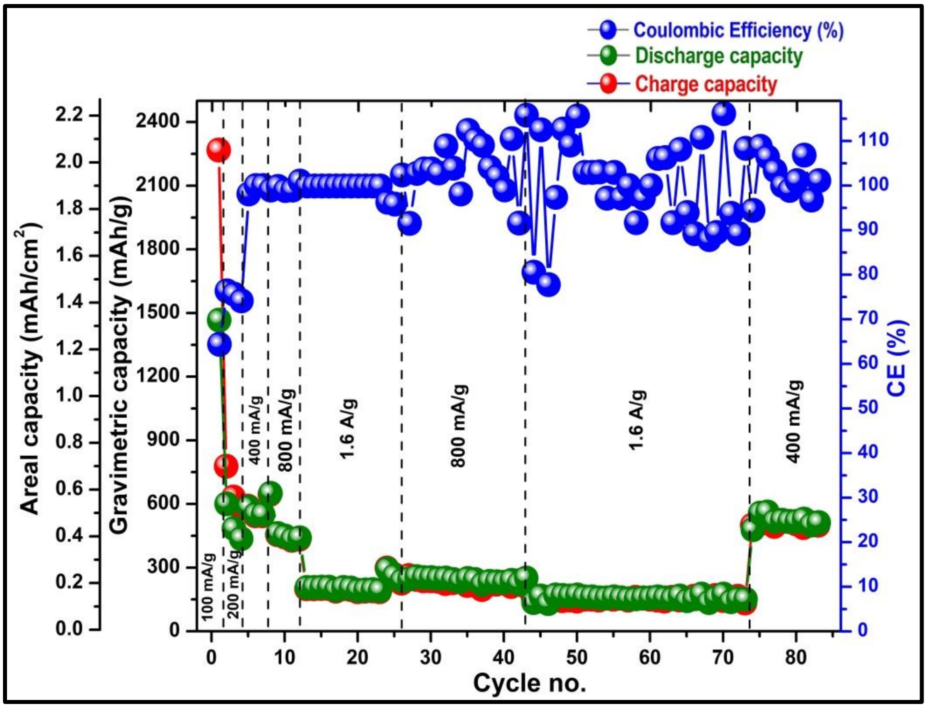

Fig. 3.40. *Galvanostatic cycling performance at current densities of 100, 200, 400, 800 and 1600 mA/g of as-deposited* $Si_{0.35}Ge_{0.45}Al_{0.2}$ *film which was synthesized by potentiostatic pulsed-electrodeposition at a duty cycle of 16% for 30 minutes.*

Figure (3.41) shows the potential plateaus of $Si_{0.35}Ge_{0.45}Al_{0.2}$ anode at different current densities of 200, 400, 800, and 1600 mA/g, equivalent to 0.044, 0.178, 0.35 and 0.7 C-rate, respectively. It is worth noting that the pseudo-plateaus at around 1.75 V does not exist after the initial charging/discharging cycles which indicates that the superficial Cu-oxide layer is electrochemically not effective after the first cycle. Also, the charge capacity values when $Si_{0.35}Ge_{0.45}Al_{0.2}$ was cycled at 200 and 400 mA/g are almost equal. As well, both the initial charge and discharge capacities when cycling the anode film at 800 and 1600 mA/g are identical, which signifies the promising rate-capability of this anode-film.

L.B. Chen *et al.*, have studied the electrochemical performance of Si–Al thin film in LIBs [224]. The atomic ratio of Si/Al in the tested film was 1:0.18, which is similar to the Si/Al ratio in as-deposited $Si_{0.35}Ge_{0.45}Al_{0.2}$ film. The Si–Al thin film showed greater rate-capability and better cycling performance than a bare Si anode film [224]. These results are in good agreements with the results obtained by $Si_{0.35}Ge_{0.45}Al_{0.2}$ anode-film. Other studies have investigated the role of Al_2O_3 as a coating layer on Si anode films. J. Shin and E. Cho have studied the electrochemical performance of Si anode film coated with an in-active Al_2O_3 layer which was found to prevent the agglomeration of Si particles and to improve the Si anode cyclability [220]. Also, they found that Al_2O_3 reacted with the fluoride species (HF which result from the decomposition of $LiPF_6$ salt) forming a protective layer which can buffer the volume expansion of the cycled anode and prevent its cracking [220]. Gaeun Hwang *et al.*, have also investigated the electrochemical performance of Si-Al alloy films coated with an Al_2O_3 layer. The coating film was found to suppress the volume expansion upon cycling. The anode also exhibited promising cycling stability and good rate-capability [225]. These studies have confirmed the role of Al either in the elemental form (as electrochemically active add-element) or in the oxide forms (as a buffering, coating layer) in stabilizing the Si anode cyclability.

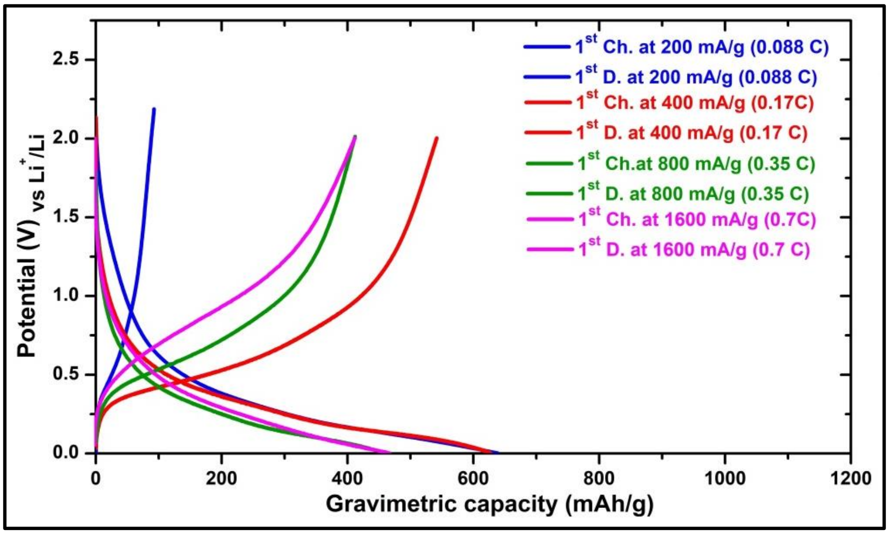

Fig. 3.41. *Potential plateaus of the initial charge/discharge cycles when $Si_{0.35}Ge_{0.45}Al_{0.2}$ film was cycled at current densities of 200, 400, 800 and 1600 mA/g (equivalent to 0.044, 0.178, 0.35, and 0.7 C-rates).*

3.3.5. Electrochemical Impedance Spectroscopy (EIS)

Figure (3.42) shows EIS-Nyquist plots of a $Si_{0.35}Ge_{0.45}Al_{0.2}$ anode film upon cycling. It can be seen that Nyquist plots for the anode film after the initial charging and the initial discharging process are almost identical, exhibiting one semicircle in the high-to-middle frequency region correlated to the faradic charge transfer impedance contribution in the bulk electrode (Z_{ct}) **[180]**. The absence of the SEI semicircle implies that the resistance through SEI is negligible **[181]**. The Nyquist plot after long cycling (83 cycles at different C-rates) shows two semicircles correlated to the contributed impedance by the SEI layer in addition to that of the mass transfer contributed impedance in the bulk anode. It is worth noting that, the Nyquist plot after long cycling has shorter Warburg tail compared to that after the first cycle, suggesting a higher accessibility of Li-ions after 83 cycles at higher C-rates **[182]**. The ohmic resistance (R_0) correlated to both the electrolyte solution and electronic contact resistance of the cell hardware [179] is less than 70 Ω. The value of this resistance did not change after long cycling, which could imply that the anode film did not exhibit delamination from the current collector. The EIS-Bode plots of $Si_{0.35}Ge_{0.45}Al_{0.2}$ anode film after cycling at different C-rates are introduced in section 5.3.2 in the appendix part of this thesis.

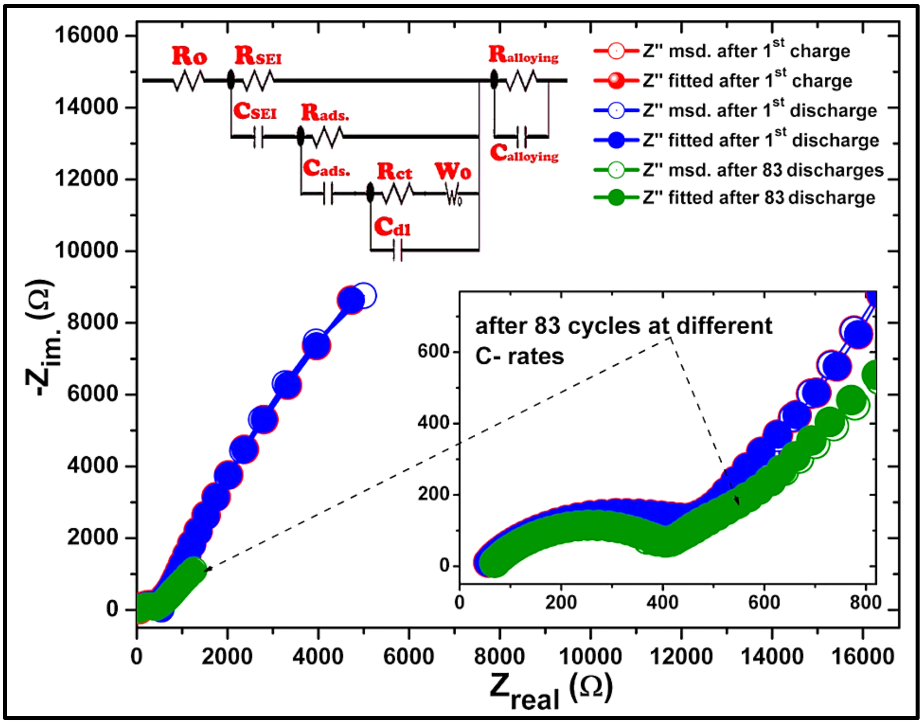

Fig. 3.42. EIS-Nyquist plots of $Si_{0.35}Ge_{0.45}Al_{0.2}$ anode film during cycling. The inset shows a magnification of the Nyquist plots in the high-to-middle frequency region. The best fitting equivalent circuit is shown inside.

3.3.6. X-ray Photoelectron Spectroscopy of SEI layers formed on $Si_{0.35}Ge_{0.45}Al_{0.2}$ anode after 1-charge

The composition of the SEI layers formed on $Si_{0.35}Ge_{0.45}Al_{0.2}$ anode after the initial charging in 0.5 M LiTFSI/[BMP]TFSI at 100 mA/g was analyzed using ex-situ XPS, investigating its composition in the upper-most, the buried and the deep layers. The detailed XPS spectra of Ge 2p, F 1s, O 1s, N 1s, C 1s, S 2p, Si 2p, Al 2p and Li 1s are illustrated in figure (3.43). Si 2p and Ge 2p spectra indicated that Si and Ge are mainly oxidized to SiO_x and GeO_x in SEI layers, supported by Li_ySiO_x/Li_yGeO_x peaks in O 1s spectra at around 533 eV **[165, 200]**. SiO_xF_y peaks at around 104.5 eV in Si 2p are very prominent in deeper SEI layers **[166]**. In Al 2p spectra, Al oxide peak exists in the uppermost SEI layer at around 74 eV **[165]**. Also, the peak at around 88 eV could be located to $LiAlF_x$ compounds **[165]**. LiF peaks in F1s (at around 686 eV) and in Li 1s (at around 56 eV) are prominent in deeper layers which also was reported in XPS analysis of the SEI formed on Al_2O_3@Si anode by J. Shin and E. Cho **[220]**. In N 1s spectra, N^+(BMP^+) peak becomes not evident in deeper SEI layer, which could refer to the robust decomposition of $[BMP]^+$ cation in bulk SEI **[171, 175]**. Also, the intensities of carbon-alkyl peaks (C-H/C-C) at around 285 eV and C-hetero peaks (C-N) at around 287 eV in C 1s spectra, related to decomposed $[BMP]^+$ cation decrease in deeper layers **[175]**. In S 2p spectra, the sulfides doublet peak at around 162 and 164 eV is the most dominant peak after sputtering, compared to other sulfur peaks related to CF_3SO_2Li and S_{anion} peaks.

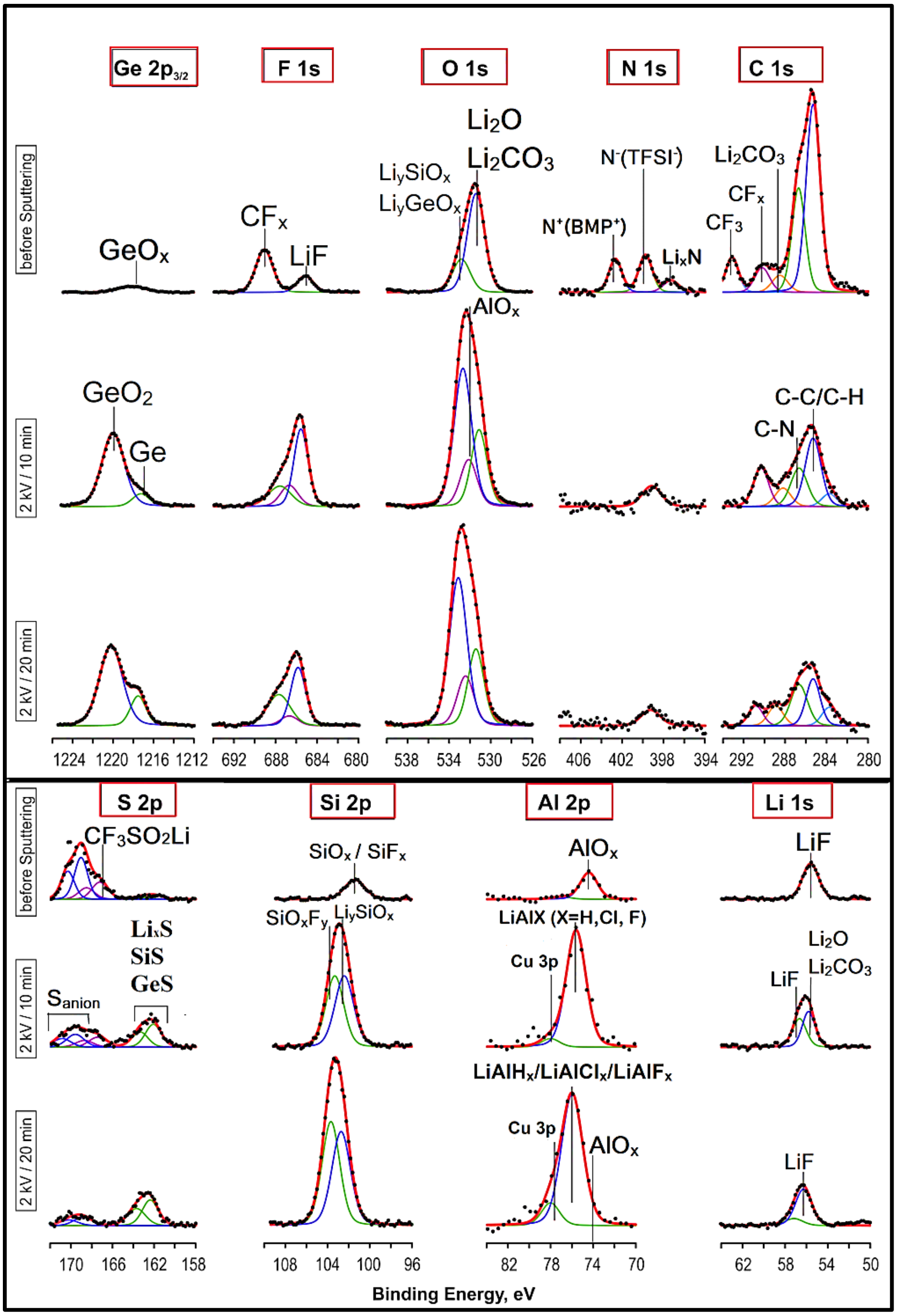

Fig. 3.43. *XPS detailed spectra of Ge 2p, F1s, O1s, N 1s, C 1s, S 2p, Si 2p, Al 2p and Li 1s with their deconvolutions of SEI layers formed on* $Si_{0.35}Ge_{0.45}Al_{0.2}$ *anode after the initial charging in 0.5 M LiTFSI/[BMP]TFSI at 100 mA/g.*

Figure (3.44) shows the atomic percent of Ge 2p, F 1s, O 1s, N 1s, C 1s, Cl 2p, S 2p, Si 2p, Al 2p and Li 1s calculated from XPS analysis. Li contributes by 27.6% to SEI composition as the highest ratio. This high concentration of Li in SEI could reflect that Al was electrochemically active, consuming a high percent of Li in addition to Si and Ge during the initial charging of $Si_{0.35}Ge_{0.45}Al_{0.2}$ anode. The inserted table illustrates the relative concentration of Li_2O, Li_2CO_3, LiF, AlO_x and $LiAlF_x$ in the investigated SEI layers. Al mostly exists in the form of $LiAlF_x$ with a concentration of around 4.79%. Al oxide on the SEI surface could react with fluoride species forming AlF_x which could act as protective and buffering layers as reported by J. Shin and E. Cho **[220]**. Also, the concentration of LiF in all SEI layers is higher than other SEI compounds**,** which could improve the mechanical properties of SEI as more stable and passivating compound. At this end, the SEI formed on $Si_{0.35}Ge_{0.45}Al_{0.2}$ anode contains stabilizing and protective compounds which can reflect positively on the cycling performance of this anode in LIBs. The detailed XPS studies of the SEI formed on $Si_{0.35}Ge_{0.45}Al_{0.2}$ anode after several cycles are required to elucidate the role of these SEI-compounds on the cycling stability of the anode films, which could not be accomplished due to the time-limitation of this thesis-study.

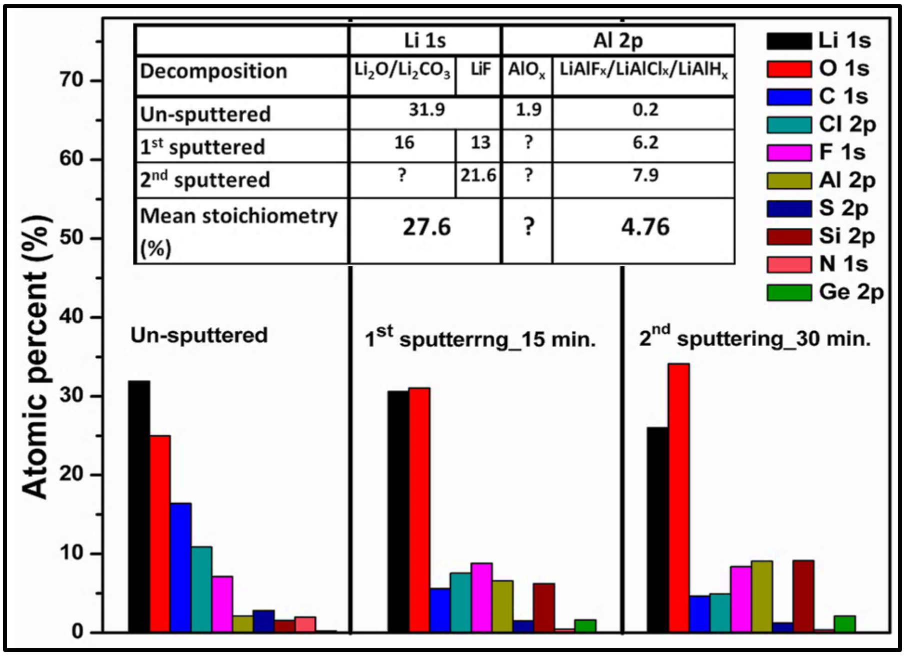

	Li 1s		Al 2p	
Decomposition	Li_2O/Li_2CO_3	LiF	AlO_x	$LiAlF_x/LiAlCl_x/LiAlH_x$
Un-sputtered	31.9		1.9	0.2
1st sputtered	16	13	?	6.2
2nd sputtered	?	21.6	?	7.9
Mean stoichiometry (%)	27.6		?	4.76

Fig. 3.44. *Relative atomic percent of Ge 2p, F1s, O 1s, N 1s, C 1s, Cl 2p, S 2p, Si 2p, Al 2p and Li 1s calculated from XPS spectra at the uppermost and two sputtered layers of SEI formed on* $Si_{0.35}Ge_{0.45}Al_{0.2}$. *The inserted table illustrates the relative concentration of* Li_2O, Li_2CO_3, *LiF,* AlO_x, *and* $LiAlF_x$ *in SEI layers.*

Conclusion on $Si_xGe_{1-x}Al_y$ as anode material in LIBs

$Si_xGe_{1-x}Al_y$ alloy films were electrodeposited by potentiostatic pulsed- electrodeposition at a duty cycle of 16% for 30 minutes in $SiCl_4$ (0.5 M) + $GeCl_4$ (0.5 M) + $AlCl_3$ (0.02 M) in [BMP]TFSI. The obtained $Si_xGe_{1-x}Al_y$ deposit-film was compact with the stoichiometry of $Si_{0.35}Ge_{0.45}Al_{0.2}$. $Si_xGe_{1-x}Al_y$ anode shows a comparably high gravimetric and areal capacity with good rate capability when investigated as an anode in LIB. The anode film retained an areal capacity of 0.4 mAh/cm^2 when cycled at a current density of 800 mA/g. Also, it shows better cycling stability and promising rate-capability compared to either Si or Si_xGe_{1-x} anode films.

EIS-Nyquest plots suggest an improvement in the chrage-transfere resistance and the Li-kinetics in this ternary alloy anode upon cycling, reflecting a structure-improvement of the anode (activation/modification processes) with cycling. Also, the value of the ohmic resistance (R_0) correlated to both the electrolyte solution and electronic contact resistance of cell hardware did not change after 83 cycles, which can indicate that the $Si_xGe_{1-x}Al_y$ anode film did not exhibit delamination from the current collector after long cycling. The composition of SEI formed on $Si_{0.35}Ge_{0.45}Al_{0.2}$ anode after the initial charging at 100 mA/g were performed by ex-situ XPS analysis, found to contain high concentration of LiF in all SEI layers which can improve its integrity as more stable and passivating inorganic compound. Also, Al mostly exists in the form of AlO_x in uppermost SEI which seems to react with fluoride forming protective and buffering layers of $LiAlF_x$ **[220]**.

It can be concluded that adding Al to Si-Ge alloy film seems to improve both the kinetics and the electrical conductivity of this anode which reflects positively on the rate-capability and the cycling stability of $Si_xGe_{1-x}Al_y$ anode in LIBs. Also, it is expected that Al can buffer the volume changes of the $Si_xGe_{1-x}Al_y$ anode during cycling that prevents the cracking of the anode, improving its cycling stability. At this end, this work and other literature **[220, 223-225]** demonstrated that Al, either in the elemental form (as electrochemically active add-element) or in the oxide form (as a protective, buffering coating layer), is a promising element for stabilizing the Si anode cyclability and for improving its rate capability as well.

3.4. Si-reduced graphene oxide (Si-rGO) composite anode

3.4.1. Cyclic voltammetry of graphene oxide in [BMP]TFSI ionic liquid

In order to investigate the electrochemical reduction of graphene oxide in [BMP]TFSI ionic liquid, cyclic voltammetry has been performed for a solution containing graphene oxide (1 g/ml) in [BMP]TFSI on Cu as shown in figure (3.45). The scan rate was adjusted to 10 mV/s from OCP to -3 V versus Pt (QRE). The voltammograms show several peaks at different potentials in the cathodic regime, attributed to the reduction of the surface-oxygen groups in the graphene oxide **[226]**. It seems that graphene oxide is gradually reduced at different potential values in [BMP]TFSI as it contains several O-groups such as carboxyl, epoxy or hydroxide groups. Also TFSI$^-$ was reported to be adsorbed on GO-surface, replacing some O-groups **[227]**.

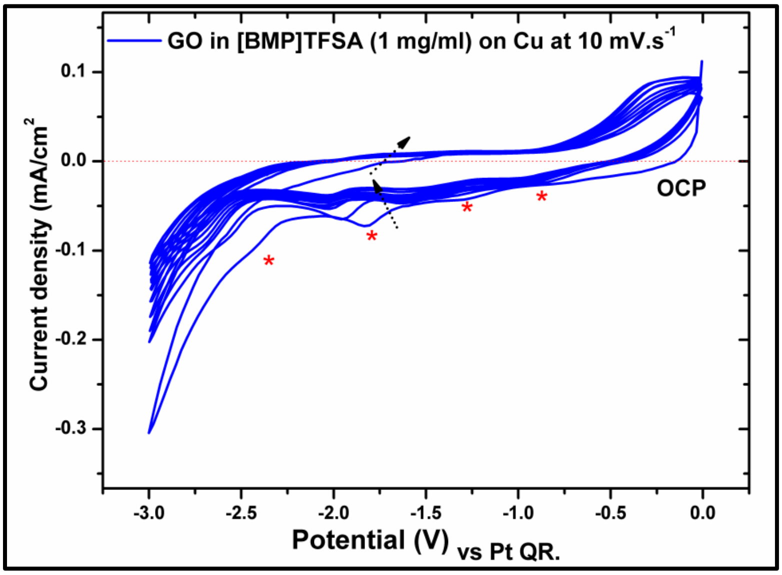

Fig. 3.45. *Cyclic voltammograms of 1 mg/ml graphene oxide (GO) in [BMP]TFSI recorded on Cu at a scan rate of 10 mV/s.*

3.4.2. Cyclic voltammetry of $SiCl_4$/GO/[BMP]TFSI solution

Cyclic voltammetry has also been performed for $SiCl_4$ /GO/[BMP]TFSI solution to investigate the electrochemical reaction regarding the Si-rGO composite electrodeposition. Figure (3.46) represents the cyclic voltammetry of the electrodeposition solution containing $SiCl_4$ (0.5 M) and GO (0.5 mg/ml) in [BMP]TFSI recorded on Cu at a scan rate of 10 mV/s. The first reduction peak (C1) possibly related to the reduction of the superficial copper oxide layer **[160]**. The subsequent three reduction peaks (C2, C3, and C4) can be indexed to the gradual reduction of graphene oxide **[228]**. The next reduction peaks (C5 and C6) are correlated to Si UPD and the reduction of Si^{IV} to Si, respectively **[161, 162]**, which might also share the associated reduction of graphene oxide at these potential values. The anodic stripping regime shows two anodic oxidation peaks (a1 and a2) correlated to the oxidation of IL-anion and the reduced-graphene oxide. The CV feature seems to be complicated, as several reduction peaks can share reduction processes of both graphene oxide and $SiCl_4$ which cannot be easily elucidated.

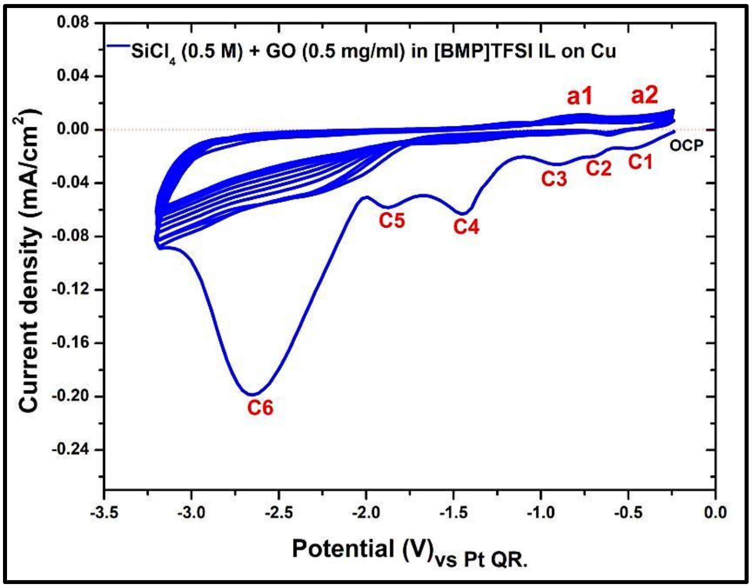

Fig. 3.46. *Cyclic voltammograms of $SiCl_4$ (0.5 M) and graphene oxide (0.5 g/ml) in [BMP]TFSI, recorded on Cu. The scan rate was 10 mV/s from OCP to -3 V versus Pt as QRE.*

3.4.3. Sequential pulsed-electrodeposition of Si-rGO composite

A Si-rGO composite film was prepared by the sequential pulsed-electrodeposition method in [BMP]TFSI. Figure (3.47) shows the sequential pulses for the alternative electrodeposition of Si/rGO in [BMP]TFSI for 30 minutes. Si and rGO were electrodeposited in a sole bath by applying proper potential values for Si electrodeposition in a single pulse for 14 seconds. Constantly, this pulse is followed by another pulse for 2 seconds at different potential values anticipated for the electrochemical reduction of graphene oxide. In the case of Si, the values of the applied potentials were -2.7 V as the deposition potential applied during T_{ON} intervals for 2s, and -0.5 V applied during the rest time (T_{OFF} intervals) for 12 seconds. For GO, the reduction potential was regulated at -1.5 V for 2 seconds (T_{ON}), followed by applying a lower potential (-0.5 V) during the rest time (T_{OFF}) for 12 seconds. Thus, the duty cycle values for Si and rGO alternative pulses are the same (14.3%). This deposition procedure is expected to produce a homogeneous and a well-distributed composite film where Si particles are integrated into the layers of the reduced-graphene oxide. Also, the electrodeposition procedure at such long T_{OFF} is expected to enable uniform deposit. Furthermore, it provides enough time for the electrolyte to diffuse to the deposition-interface region which can reflect positively on electrodeposition rate, producing a compact deposit **[135, 138, 163]**.

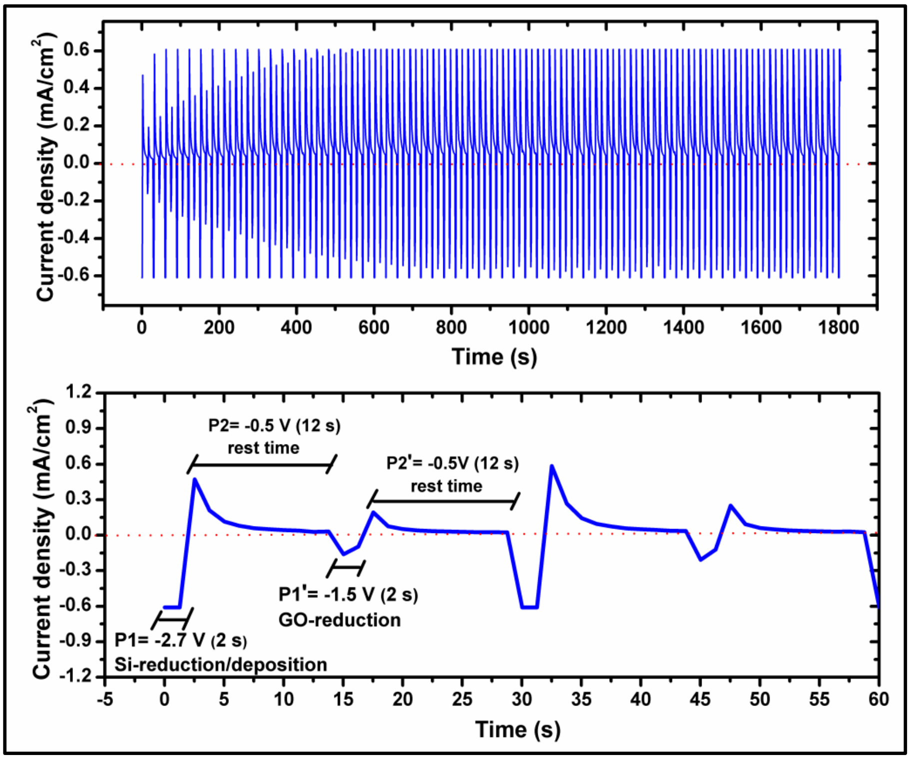

***Fig. 3.47. (a)** Sequential pulsed-electrodeposition of Si-rGO composite film for 30 minutes at 14.3% duty cycle in a single electrodeposition bath composed of* $SiCl_4$ *(0.5 M) and GO (0.5 g/ml) in [BMP]TFSI ionic liquid. **(b)** A magnification segment displaying the alternated individual pulses for Si electrodeposition separated by GO reduction pulses.*

3.4.4. Scanning Electron Microscopic investigations

FE-SEM images of as-electrodeposited Si-rGO composite-film are shown in figure (3.48 a, b). It can be seen that the morphology of this composite film is compact without cracks or pores. Furthermore, this pulsed-electrodeposition procedure seemed to provide a good opportunity for the deposition of Si particles to be homogeneously distributed between the graphene layers. Besides, the pulsed electrodeposition at longer rest time (12 seconds) allows the electrodeposit to discharge and also for the electrolyte to enrich its concentration near the cathode. Under these conditions, the deposition rate likely improved producing a compact and uniform deposit [135, 138, 163].

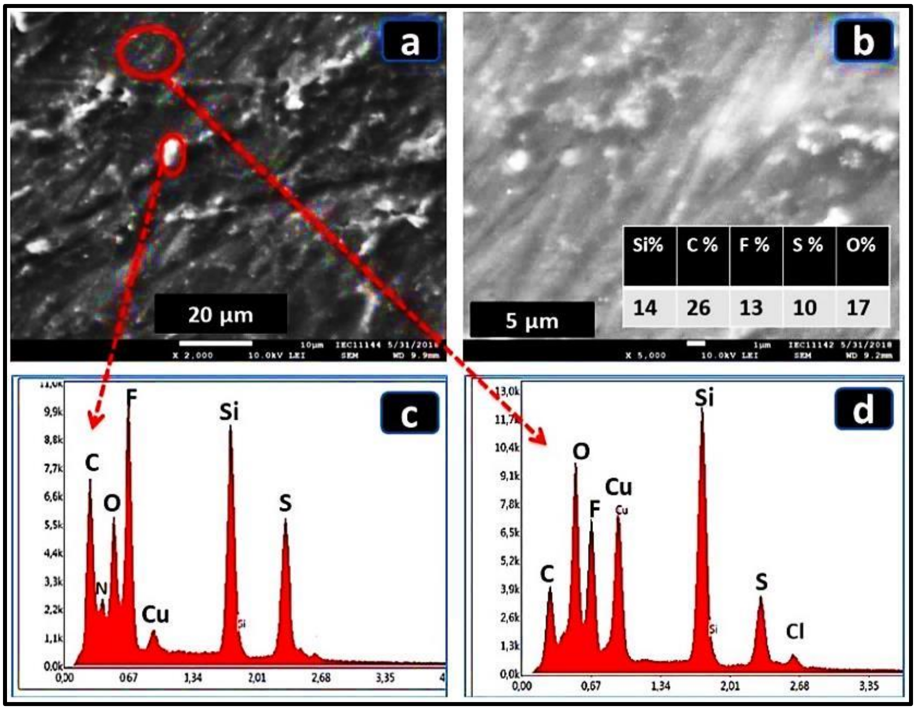

Si%	C %	F %	S %	O%
14	26	13	10	17

Fig. 3.48: *FE-SEM images* ***(a, b)*** *and EDX spectra* ***(c, d)*** *for Si-rGO composite obtained by sequential pulsed-electrodeposition in [BMP]TFSI ionic liquid at 14.3% duty cycle for 30 minutes.*

Figure (3.48 c, d) illustrates the EDS spectra of the Si-rGO composite film with the atomic percent of Si, C, F, S and O. The atomic ratios also were calculated from the EDX data over several investigated points to take the mean ratio [212]. It is expected that S, N and F atoms (with such high atomic percent) could be adsorbed on the graphene oxide, replacing some O atoms [227]. The atomic percent of Si to carbon in the deposit is approximately 1:1.85, thus the stoichiometry of Si-rGO$_x$ composite is estimated to be $Si_{0.35}C_{0.65}O_x$.

3.4.5. Electrochemical performance in LIB

3.4.5.1. Cyclic voltammetry in LIB

Cycling voltammogram of as-deposited Si-rGO composite-film versus Li in LiTFSI (0.5 M)/[BMP]TFSI at a scanning rate of 1 mV/s is shown in figure (3.49). The composite anode film shows a significant peak at around 1.4 V in the first cycle, normally correlated to the formation of SEI due to the reductive decomposition of Li^+-electrolyte [228]. This peak is not evident in the consecutive cycles, indicating that this interfacial layer stops growing. The first cycle also shows a weak and broad peak at around 0.6 V vs. Li/Li^+ correlated to the initial Li_xSi alloying phase, followed by a prominent peak around 0.1 V. This peak likely represents the lithiation process of both Si and rGO in this composite anode [228]. In the successive cycles, the first lithiation peak is replaced by another peak at around 0.35 V which has been reported in another Si-graphene composite material [228]. On the other hand, the stripping regime shows a broad de-lithiation peak at around 0.5 V, extended by a second small peak at 1 V. The two anodic processes are correlated to the de-lithiation of Si and graphene [228-230]. It is worth noting that the increase of the de-lithiation peak intensities after the second cycle suggests a kinetic enhancement in the composite anode, which was also reported in literature [228, 230].

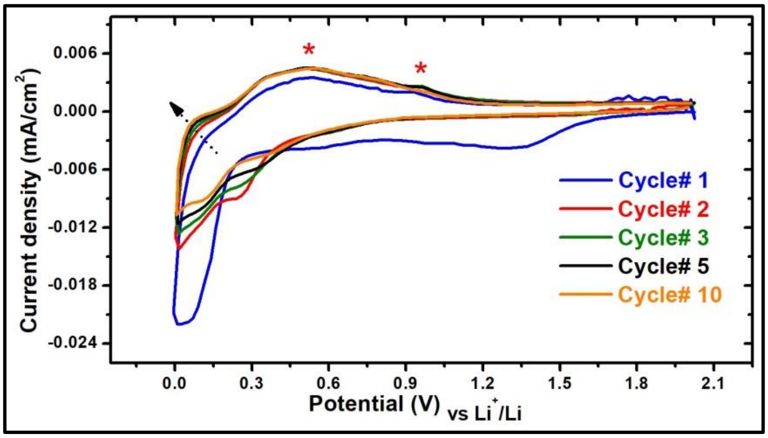

***Fig. 3.49.** Consecutive cyclic voltammograms of Si-rGO composite films at a scan rate of 1 mV/s versus Li/Li^+ in LiTFSI (0.5 M)/[BMP]TFSI electrolyte.*

3.4.5.2. Galvanostatic cycling evaluation in LIB

Figure (3.50a) shows a potential plateau of the initial charge/ discharge cycle of Si-rGO composite film at 0.03 mA/cm^2 (600 mA/g). At the initial charging, both Si and graphene active material suppose to behave ideally in LIB, such that the produced capacity is equivalent to their theoretical value (3589 mAh/g for Si and 1211 mAh/g for graphene) [97]. So the theoretical capacity of Si-rGO composite with the stoichiometry of $Si_{0.35}C_{0.65}$ is equivalent to 1985 mAh/g. The active mass of Si-rGO in the anode film was calculated from the first charge, found to be 50 μg/cm^2. Even a significant SEI peak appears in the CV, the first capacity loss for Si-rGO anode film is 49% which reflects the role of graphene in improving the de-lithiation process, compared to Si, Si_xGe_{1-x} and $Si_xGe_{1-x}Al_y$ anode-films.

Figure (3.50b) represents the galvanostatic cycling of the Si-rGO composite anode at a current density of 0.03 mA/cm^2 (600 mA/g). The cycled electrode displayed a good coulombic efficiency of around 95%, which sometimes apparently jumps to higher values.

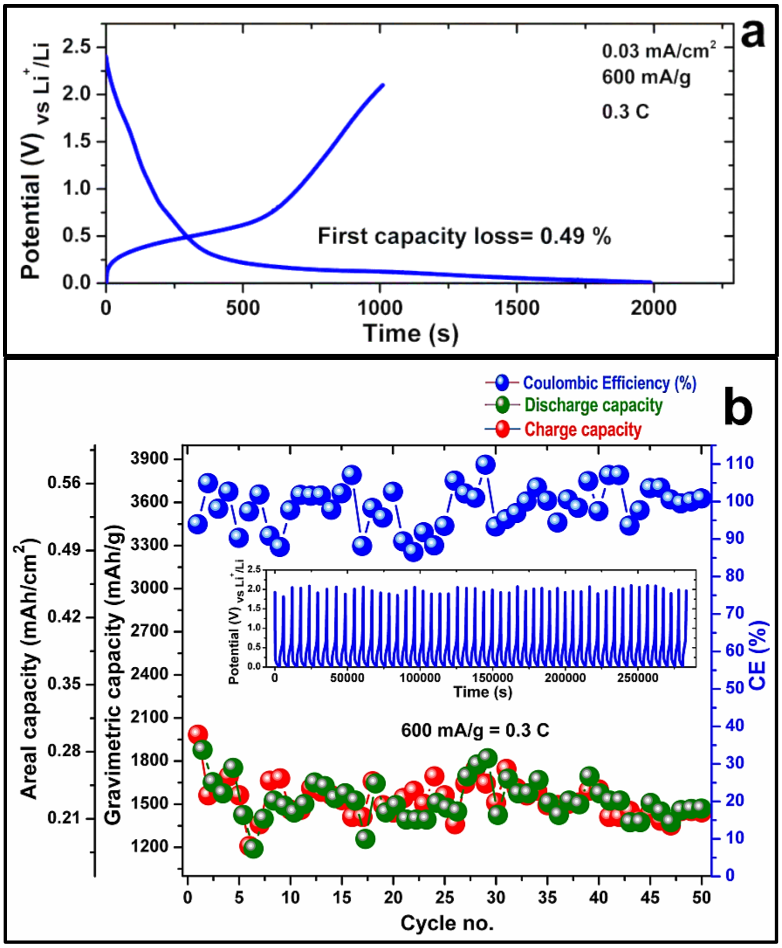

***Fig. 3.50**. Voltage profile of the initial charge/discharge cycle **(a)**, and galvanostatic charge/discharge cycling at 0.3 C-rate (600 mA/g) for 50 cycles **(b)** for Si-rGO composite film in LiTFSI (0.5 M)-[BMP]TFSI electrolyte.*

The improvement in the coulombic efficiency and the capacity retention values could be explained in terms of a kinetic improvement of the cycled anode [230] which appears in good agreement with the CV results in figure (3.49). A Si-rGO film exhibits a high gravimetric capacity greater than 1200 mAh/g with areal capacity values of around 0.25 mAh/cm^2 when cycled at 600 mA/g (0.3 C-rate). The discharge capacity retention over 50 cycles is 75% which confirms the significant improvement in the cycling stability of this anode film compared to Si, Si_xGe_{1-x} and $Si_xGe_{1-x}Al_y$ films.

Figure (3.51) shows the cycling evaluation of Si-rGO anode at different C-rates of 0.6, 0.9, 1.5 and 3 C-rates (equivalent to 1.2, 1.8, 3 and 6 A/g, respectively) to investigate its rate-capability. The composite anode film shows improved cycling stability and good rate capability. It retained gravimetric and areal capacity values of around 700 mAh/g and 0.11 mAh/cm^2, respectively, when cycled at a current density of 1200 mA/g. The improved cycling performance can be explained in terms of the high conductivity of the composite anode. Also, its compact feature seemed to be an influential factor that provides a non-interrupted pathway for the diffusion of Li$^+$ ions.

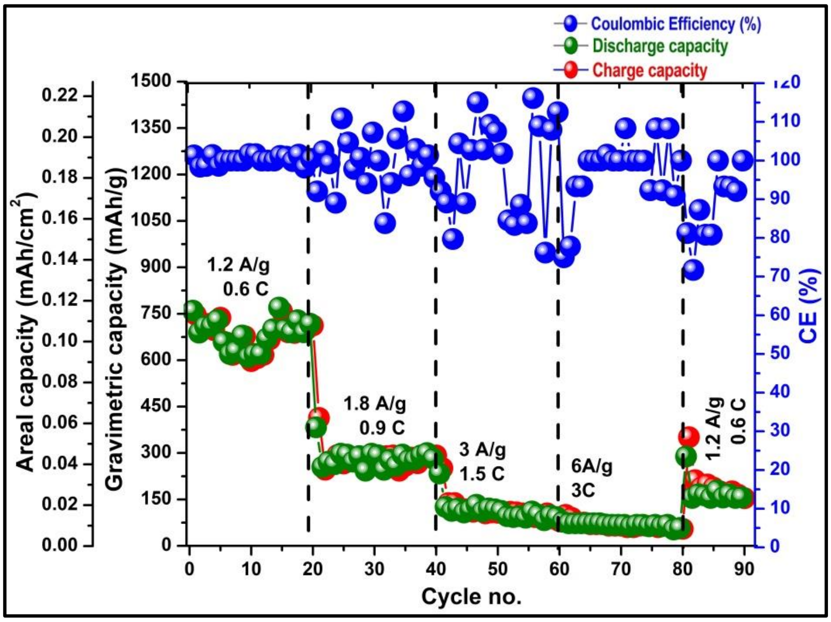

Fig. 3.51. *Galvanostaic cycling evaluation of Si-rGO composite-anode at 0.6, 0.9, 1.5 and 3 C-rates, equivallent to 1.2, 1.8, 3 and 6 A/g, respectively.*

3.4.6. Electrochemical Impedance Spectroscopy (EIS)

Figure (3.52) shows the EIS-Nyquist plots for Si-rGO composite anode after the initial charge, the initial discharge, the 10-discharge, the 30-discharge and the 50-discharge cycles at 0.3 C-rate. The inserted inset displays a magnification of the Nyquist plots in the high-to-medium frequency range. It can be seen that the Nyquist plot after the initial charging displays two overlapped semicircles. The first semicircle in the high-frequency range usually represents the contributed-impedance by the SEI film [170, 231]. The second semicircle in the mid-frequency region corresponds to the charge transfer impedance of Li ions in the bulk anode [170]. This second semicircle is reduced after the first discharging. Also, it disappears entirely after 50 cycles, indicating that the charge transfer resistance is so much reduced, which could be explained in terms of the activation and modification of this composite anode during cycling [230]. The activation/modification of a Si-graphene composite anode over cycling was reported in literature, confirming that adding graphene to silicone anode material can improve its charge-transfer impedance over long cycling [228, 230]. The EIS-Bode plots of Si-rGO composite anode upon 50 cycles are introduced in section 5.3.3 in the appendix part of this thesis. The fitting circuit does not include adsorption/trapping elements which indicates that this composite anode may not exhibit pseudo-capacitance process upon cycling.

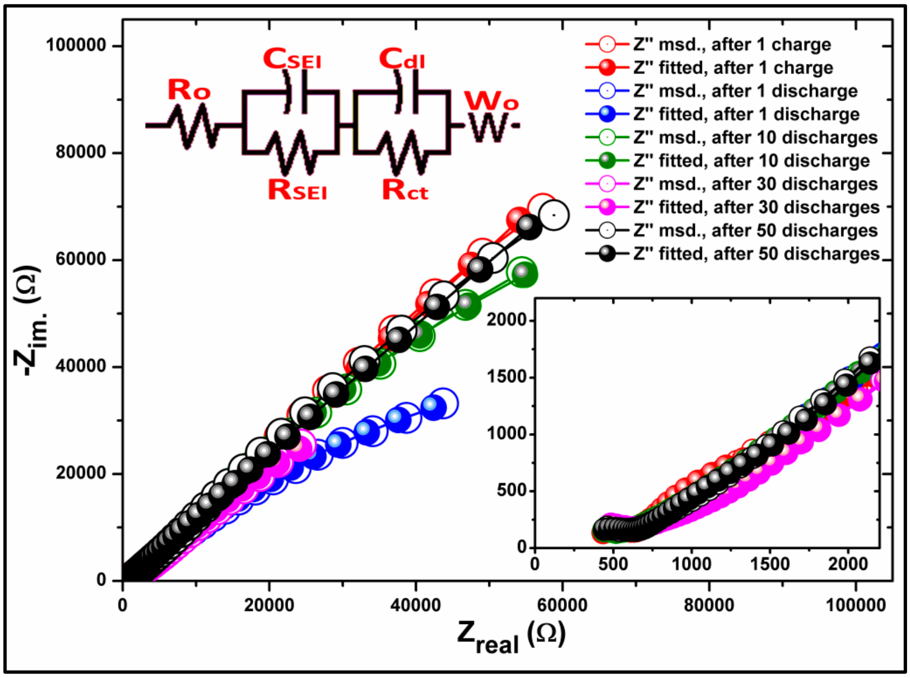

Fig. 3.52. *EIS-Nyquist plots of Si-rGO composite after the initial charge, initial discharge, the 10th discharge, the 30th discharge and the 50th discharge cycles at 0.3 C-rate. The inset shows a magnification of the Nyquist plots in the high-to-middle frequency region. The most fitting-equivalent circuit is shown inside.*

3.4.7. X-ray Photoelectron Spectroscopy of SEI layers formed on Si-rGO anode film after 1-charge

The composition of the SEI layers was analyzed using ex-situ XPS after the initial charging of Si-rGO anode film in 0.5 M LiTFSI/[BMP]TFSI, investigating its composition in the upper-most, the buried and the deep layers**.** Figure (3.53a) shows the overall XPS spectra for the SEI before and after sputtering. Si 2p and Li 1s spectra can hardly be detected in the un-sputtered layer as it is mostly covered with decomposed products of the electrolyte (supported by the relative intensities of N 1s peaks in inset b). The detailed spectra of F 1s, O 1s, N 1s, C 1s, S 2p, Si 2p and Li 1s are illustrated in figure (3.53b). In Si 2p spectra, the peak at around 104.5 eV can be indexed to SiO_xF_y **[166]**.

In F 1s spectra, the deeper SEI layers mostly contain LiF which peaks exist at around 685.2 eV. In Li 1s spectra, LiF peak at around 57 eV could also refers to Lithiated-carbon peak (LiC_x) **[231]**. In C 1s spectra, carbon-alkyl peak (C-H/C-C) can be detected at around 285 eV as intense and dominant peak in the deeper layer, which may refer to the presence of graphitic carbon **[231**. The intensity of Lithium carbonate (Li_2CO_3) peak at 290 eV is evident in the 2nd-sputtered SEI layer. In N 1s spectra, the peak at around 401.7 eV in deeper layer could be assigned to graphitic-N **[231]**. The uppermost SEI layer is mostly covered by decomposed electrolyte-residuals as indicated by the intensities of N^+ and N^- peaks **[171, 175]**. In S 2p spectra, the sulfides doublet-peak at around 160 and 162 eV is the most dominant after sputtering, compared to other peaks related to CF_3SO_2Li and decomposed S_{anion}.

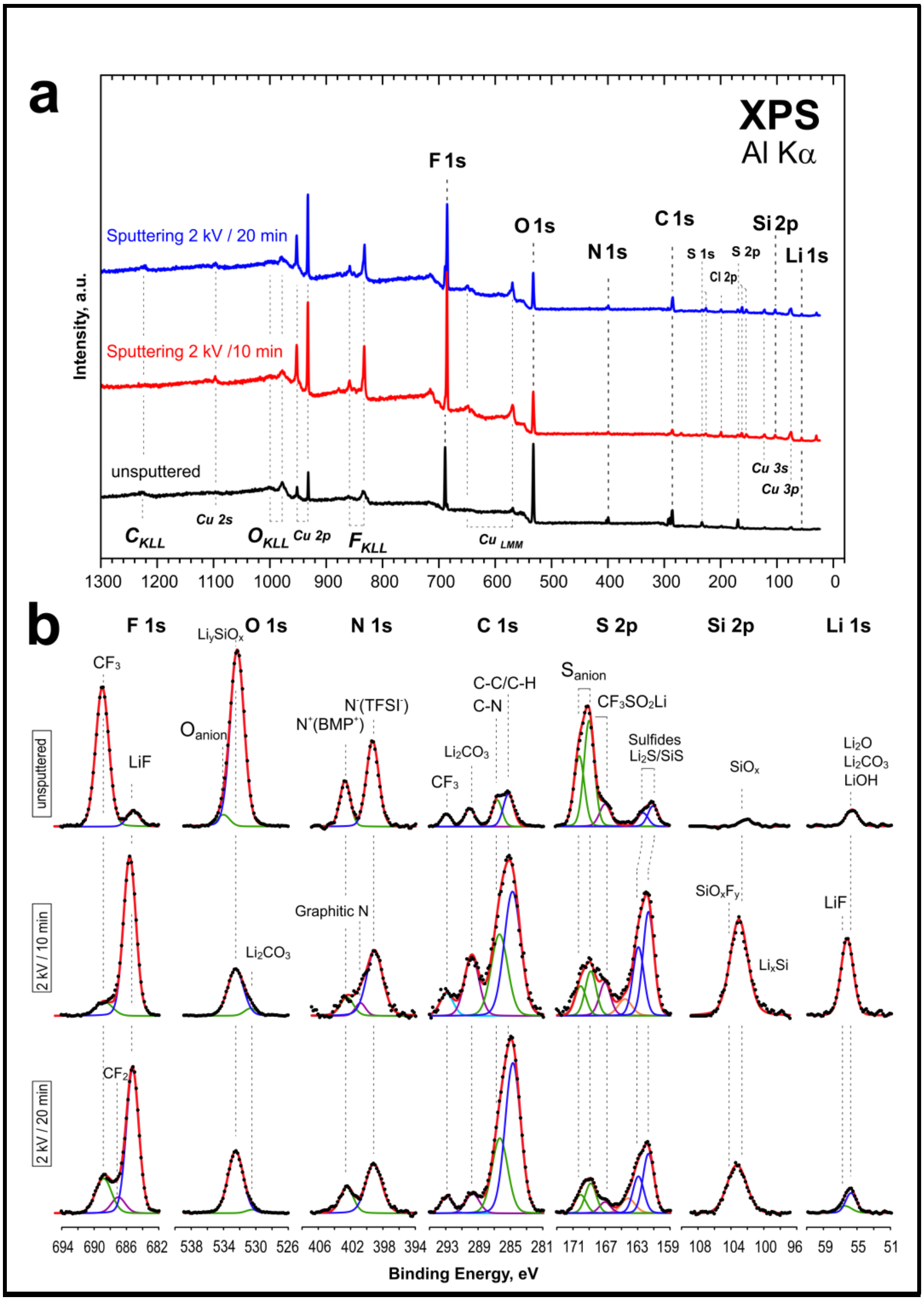

Fig. 3.53. *XPS analysis of SEI formed on Si-rGO composite film after the initial charging in 0.5 M LiTFSI/[BMP]TFSI till 0.01 V;* ***(a)*** *the overall XPS survey for uppermost and two sputtered SEI layers,* ***(b)*** *the detailed spectra and deconvolutions of F 1s, O 1s, N 1s, C 1s, S 2p, Si 2p, and Li 1s.*

Figure (3.54) shows the atomic ratios of F, O, N, C, S, Si, and Li calculated from XPS analysis. Li contributes by 34.7% to SEI composition which can reflect that the initial charging of Si-rGO anode is a lithiation-rich process where the graphene was electrochemically active. The inserted table illustrates the relative concentration of Li_2O, Li_2CO_3, LiF, CF_3SO_2Li, LiS and SiS in SEI layers. These compounds are less insoluble and more passivating compounds sharing a ratio of approximately 59.93% of SEI composition, expected to improve the stability of SEI upon cycling **[193, 194]**. In conclusion, the SEI formed on Si-rGO is Li-rich layers which could confirm the role of graphene in enriching electrochemical-lithation processes efficiently. Also, LiF, Li_2O, Li_2CO_3, CF_x, LiS, SiS in addition to CF_3SOLi contribute by ~60% of SEI composition which could improve its mechanical properties as more stable and passivating components. At this end, the SEI layers formed on Si-rGO can reflect the improved cycling stability and the high capacity output. The detailed XPS studies of the SEI formed on Si-rGO composite-anode after several cycles are required to elucidate the role of graphene and SEI-compounds on the cycling stability of the anode films, which could not be accomplished due to the time-limitation of this thesis-study.

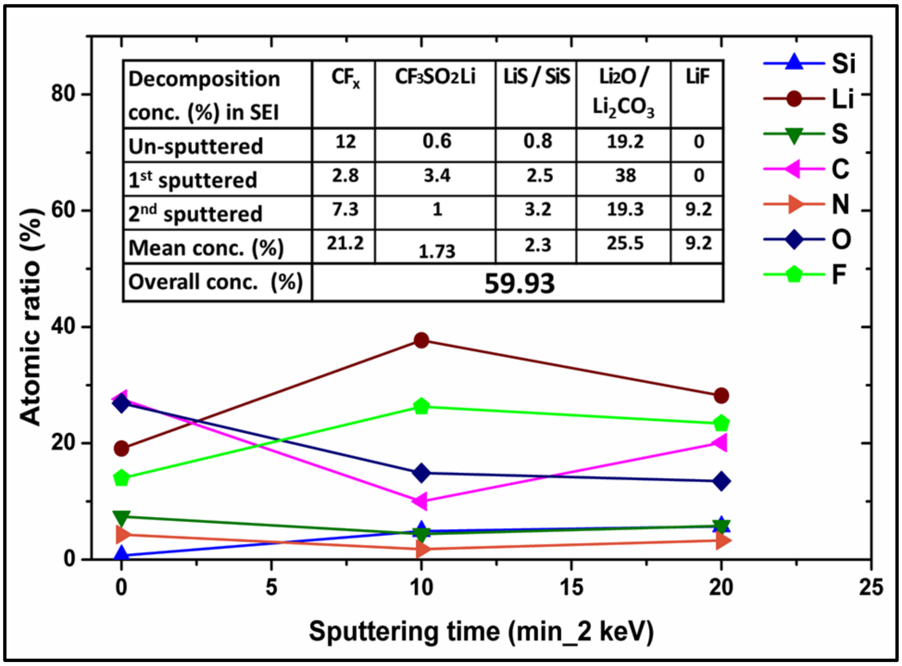

Decomposition conc. (%) in SEI	CF_x	CF_3SO_2Li	LiS / SiS	Li_2O / Li_2CO_3	LiF
Un-sputtered	12	0.6	0.8	19.2	0
1st sputtered	2.8	3.4	2.5	38	0
2nd sputtered	7.3	1	3.2	19.3	9.2
Mean conc. (%)	21.2	1.73	2.3	25.5	9.2
Overall conc. (%)	59.93				

Fig. 3.54. *Relative atomic percent of F, O, N, C, S, Si, and Li calculated from XPS spectra at the uppermost and two sputtered SEI layers formed on Si-rGO composite anode after the initial charging in 0.5 M LiTFSI/[BMP]TFSI. The inserted table illustrates the relative concentration of* Li_2O, Li_2CO_3, *LiF*, CF_x, CF_3SO_2Li, *LiS and SiS in SEI investigated layers.*

Conclusion on Si-rGO composite as anode material in LIBs

Si-rGO composite was prepared by the sequential pulsed-electrodeposition method in one electrodeposition bath composed of $SiCl_4$ (0.5 M) and graphene oxide (0.5 g/ml) in [BMP]TFSI for 30 minutes at a duty cycle of 14.3 %. The sequential electrodeposition of Si and rGO was performed by applying individual pulses with different potential values and equal intervals for Si electrodeposition and GO electrochemical reduction which produced a compact and uniform Si-rGO composite film with non-porous structure. This method provides a good opportunity for Si particles to be homogeneously distributed between the graphene layers. Si-rGO anode film showed better electrochemical performance compared to other tested films. The first irreversible capacity loss of Si-rGO anode film (49%) reflects the significant role of graphene in improving the initial de-lithiation process. Also, Si-rGO anode produced a high gravimetric capacity greater than 1200 mAh/g with areal capacity values of around 0.25 mAh/cm^2 when cycled at 600 mA/g during 50 cycles. As well, the capacity retention after 50 cycles was 75% which confirms the pronounced improvement in the gravimetric capacity, the areal capacity and cycling-stability of this composite anode film compared to Si, Si_xGe_{1-x} and $Si_xGe_{1-x}Al_y$ anodes. EIS-Nyquest plots indicated that the Si-graphene composite-anode displays a reduction in the charge-transfer impedance after the first de-lithiation process. The reduction of charge transfer contributed impedance could be explained in terms of the activation and modification of the composite anode upon cycling which also was reported in literature **[228, 230]**.

XPS analysis of the SEI formed on Si-rGO indicated that Li contributes by 34.7% in the SEI composition (mostly in the form of Li_2O and Li_2CO_3) reflecting the role of graphene in enriching the lithiation process. Also, Li_2O, Li_2CO_3, LiF, CF_x, CF_3SO_2Li, LiS and SiS compounds exist in this interfacial layer in higher percent (60%) compared to other SEI formed on Si, Si_xGe_{1-X} and $Si_xGe_{1-X}Al_y$ anode films. These inorganic compounds are more stable and more passivating, which could stabilize SEI and improve its mechanical properties. Hence, the characteristics of SEI layers formed on Si-rGO composite film can reflect the improved cycling stability, the high capacity retention and the improved rate-capability of the anode over cycling in LIBs.

4. Summary

- **On the pulsed-electrodeposition of Si, Si_xGe_{1-x}, $Si_xGe_{1-x}Al_y$ and Si-rGO films**

Pulsed-electrodeposition of Si, Si_xGe_{1-x}, $Si_xGe_{1-x}Al_y$ and Si-rGO films is a feasible and controllable technique, where the deposition rate and the ion concentration near the deposition interface can be controlled. The PED technique enables adjusting the pulses temporal parameters (T_{ON} und T_{OFF}) and the pulses amplitude so that compact deposits with fine particles, high density and low porosity can be obtained.

The pulsed-electrodeposition of Si film at a duty cycle of 50% produced a less compact film compared to the Si deposit which was prepared at a duty cycle of 25%. The pulsed-electrodeposition of the Si film at a duty cycle of 16% produced a non-porous Si film with a compact feature. Si_xGe_{1-x} alloys were prepared by the potentiostatic pulsed-electrodeposition in single baths containing both $SiCl_4$ and $GeCl_4$ solutes in [EMIm]TFSI with different $GeCl_4$ molar ratio (0.25 and 0.5 M). Changing the duty cycle values (50% and 16%) along with changing the $GeCl_4$ concentration in the deposition baths demonstrated dual influence in the Si-Ge co-deposition, producing Si_xGe_{1-x} films in different stoichiometry. Si_xGe_{1-x} films which were deposited at a duty cycle of 16% produced Si-rich Si_xGe_{1-x} deposits with more compact feature compared to Si_xGe_{1-x} films which were deposited at a duty cycle of 50% and lower $GeCl_4$ concentration. $Si_xGe_{1-X}Al_y$ was deposited by pulsed-electrodeposition at a duty cycle of 16% which produced a compact and uniform deposit with low porosity. Pulsed-electrodeposition of Si-reduced graphene oxide (Si-rGO) composite through sequential pulses alternated for the deposition of Si in individual pulses and separated by specific pulses for the electrochemical reduction of graphene oxide results in compact deposits where Si is well-distributed into the graphene layers homogeneously. All deposited films were found to contain IL-decomposed components such as C, S, F, and N which were trapped in the bulk deposits. FT-IR and Raman spectroscopic analysis of $SiCl_4$/[BMP]TFSI baths indicated that the pulsed-electrodeposition at lower duty cycle values seems to limit the decomposition of the electrolyte than the pulsed-electrodeposition at higher duty cycles values.

- **On the electrochemical performance of Si, Si_xGe_{1-x}, $Si_xGe_{1-x}Al_y$ and Si-rGO anodes in LIBs**

Si anode-films displayed lithiation and de-lithiation features categorized to Si anode materials prepared by other methods. The cyclic voltammetry features indicated that Si anode shows a kinetic enhancement over cycling during de-lithiation processes which result in increasing the coulombic efficiency (CE) values to more than 100% at some cycles. Si anode films deposited at 25% duty cycle showed a limited cycling improvement during the first ten cycles compared to Si film deposited at a duty cycle of 50%. Nevertheless, Si anode films deposited at 16% duty cycle produced higher capacity values even at a higher current density (0.9 mA/g) compared to other Si films deposited at 50 and 25% duty cycles. Even though, all Si films exhibited poor cycling stability over long cycling due to the structural deformation and the delamination of Si films out from the Cu current collector. The EIS study of Si anode during 50 cycles indicated that the anode film exhibit adsorption/desorption processes during cycling which denotes its complicated interactions with other elements during cycling. The

XPS analysis elucidated that the SEI formed on Si after the initial charging in LiTFSI/[BMP]TFSI contains SEI-stabilizing compounds such as Li_2O, LiF, CF_x, Li-sulfides and Li_2CO_3 that could improve its mechanical stability. Even though, the cracking and delamination of Si anodes upon cycling seem to be the dominant factors deteriorating their cycling stability.

Si_xGe_{1-x} films with different Si/Ge atomic ratio show variation in their cycling performance in LIBs. The cycling performance $Si_{\mathbf{0.3}}Ge_{\mathbf{0.7}}$ anode is similar to Ge-anode material with good cycling stability but with low gravimetric capacity values (of around 400 mAh/g). $Si_{\mathbf{0.6}}Ge_{\mathbf{0.4}}$ anode produced the highest gravimetric capacity compared to other Si-rich Si_xGe_{1-x} films with a coulombic efficiency value around 98%. For $Si_{\mathbf{0.7}}Ge_{\mathbf{0.3}}$, it displayed the highest areal capacities (around 0.14 mAh/cm^2) compared to other Si-rich Si_xGe_{1-x} films. $Si_{\mathbf{0.9}}Ge_{\mathbf{0.1}}$ anode-film displayed cycling performance similar to silicon-like materials with coulombic efficiency and capacity retention values lower than that of other Si_xGe_{1-x} anode films. Ultrathin $Si_{0.95}Ge_{0.05}$ anode with a thickness less than 400 nm displayed high rate-capability with gravimetric capacity values of around 900 mAh/g when cycled at 41.5 C-rate (128.5 A/g), but the discharge areal capacity values were less than 20 μAh/cm^2 which make it more satisfying for the application in micro-batteries. Compared to bare Si anode films, Si_xGe_{1-x} exhibited superior cycling stability and higher retained gravimetric capacity. EIS-Nyquist plots studies for Si_xGe_{1-x} anode after 50 cycles in the de-lithiation state indicated that D_{Li+} values in $Si_{\mathbf{0.3}}Ge_{\mathbf{0.7}}$ and $Si_{\mathbf{0.6}}Ge_{\mathbf{0.4}}$ anode films is higher than other Si_xGe_{1-x} films. Ex-situ XPS analysis showed that SEI layers formed on $Si_{0.3}Ge_{0.7}$ anode after initial charging contain a higher concentration of

SEI-stabilizing compounds (LiF, Li_2O, Li_2CO_3 and CF_x) than that formed on $Si_{0.9}Ge_{0.1}$ anode, which could clarify its improved cycling stability compared to the poor cycling performance of $Si_{0.9}Ge_{0.1}$anode.

$Si_{0.35}Ge_{0.45}Al_{0.2}$ anode produced high gravimetric and areal capacities with superior rate-capability compared to Si and Si_xGe_{1-x} anode films. The ternary alloy anode film retained an areal capacity of around 0.4 mAh/cm^2 when cycled at a current density of 800 mA/g. EIS-Nyquist plots of $Si_{0.35}Ge_{0.45}Al_{0.2}$ anode film confirmed the improvement of Li-kinetics in $Si_{0.35}Ge_{0.45}Al_{0.2}$ anode upon cycling. Ex-situ XPS analysis of SEI formed on $Si_{0.35}Ge_{0.45}Al_{0.2}$ anode after the initial charging indicated a high concentration of LiF and $LiAlF_x$ compounds which could protect and improve the integrity of the SEI upon cycling.

A Si-rGO composite anode-film showed superior electrochemical performance compared to Si, Si_xGe_{1-x}, $Si_xGe_{1-x}Al_y$ anodes. This composite anode produced high gravimetric capacity greater than 1200 mAh/g with areal capacity values of around 0.25 mAh/cm^2 when cycled at a current density of 600 mA/g for 50 cycles. As well, the capacity retention after 50 cycles was found to be 75% which confirms the pronounced improvement in the cycling-stability of this anode compared to Si, Si_xGe_{1-x} and $Si_xGe_{1-x}Al_y$ films. EIS tests indicated that Si-graphene anode displayed an improvement in the charge-transfer impedance upon cycling which reflects its promising cycling performance. XPS analysis of the SEI formed on Si-rGO after the initial charging indicated that this interfacial layer is rich with Li (28%) which can indicate the role of graphene in enriching the lithiation process. Also, LiF, Li_2O, Li_2CO_3, in addition to CF_3SO_2Li compounds exist in high concentrations equals 60% of the SEI composition. These inorganic salts are SEI-stabilizing components which can improve its mechanical properties as more stable and passivating components. The characteristics of SEI layers formed on Si-rGO could explain the superior cycling stability and the high capacity retention of this anode film compared to Si, Si_xGe_{1-x} and $Si_xGe_{1-x}Al_y$ films.

5. Appendix (Supportive Results, SR)

5.1. Si anode film by pulsed-electrodeposition at a duty cycle of 6%

5.1.1. Cyclic voltammetry of $SiCl_4$ (0.5 M) in [BMP]TFSI

Figure (SR1) illustrates the cyclic voltammogram of $SiCl_4$ (0.5 M) in [BMP]TFSI recorded on Cu substrate at a scanning rate of 50 mV/s versus Pt QRE. The cathodic regime shows several reduction peaks (C1, C2, C3, C4) which seem to correspond to alloy-deposition processes (may be Si-Cu alloying) and/or different under potential deposition of Si in addition the formation of oligochlorosilanes compounds, as reported by Endres *et al.* **[162]**. The peak (C5) is corresponding to the reduction of $SiCl_4$ to Si **[162]**. The anodic stripping regime shows a reduction process (C*) which means that a further Si deposition can start in the anodic regime, revealing that the decomposition of $[BMP]^+$ cation might passivate the Si surface **[159, 162]**.

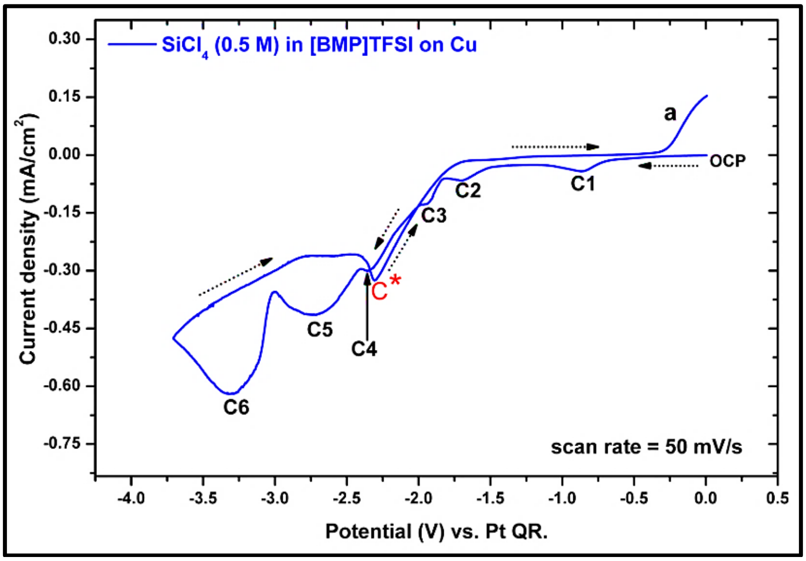

Fig. SR1. *Cyclic voltammogram of $SiCl_4$ (0.5 M) in [BMP]TFSI on Cu from OCP to -3.75 V at a scan rate of 50 mV/s.*

5.1.2. Potentiostatic pulsed-electrodeposition of Si film at a duty cycle of 6%

This Si film was synthesized using the potentiostatic pulsed-electrodeposition at much lower duty cycle value (6%). Figure (SR2a) shows the overall pulsed-potential waves along with the *j*/t curve of the Si film in 0.5 M $SiCl_4$/[BMP]TFSI for 30 minutes. Figure (SR2b) shows a magnification for the potential waves and current values at each pulse interval. The values of the applied potentials were -3 V as P1, applied for 1 second, followed by the second electrodeposition potential (P2, -0.5 V) which was applied for 14 seconds, so the duty cycle equals 6%. The electrodeposition of this Si film at such low duty cycle was anticipated to produce a deposit with much better physical and electrochemical properties to evaluate its rate-capability in LIB.

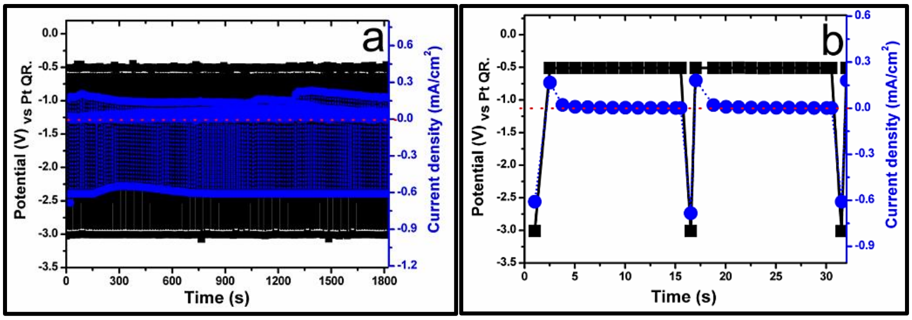

Fig. SR2. *Potentiostatic pulsed-electrodeposition of Si in [BMP]TFSI at a duty cycle of 6 % for 30 minutes;* ***(a)*** *overall potentiostatic pulsed-electrodeposition curve along with the j/t curve,* ***(b)*** *close-up portion for the applied potential waves (black) along with the associated current density (blue).*

5.1.3. Scanning Electron Microscopic investigations

FE-SEM images of the Si film deposited by potentiostatic pulsed-electrodepositions for 30 minutes at a duty cycle of 6 % are shown in figure (SR3a, b). The Si deposit has a porous structure with small particle size similar to that of the Si film deposited at 25%, where the value of P2 was also adapted at -0.5 V which might indicate that pulsed electrodeposition at P2=-0.5 V results in porous Si films. Figure (SR3c, d) illustrates the EDS-spectra of as-deposited Si films at different scanned areas. Nevertheless, the atomic percent of C, S, N and F trapped inside the deposit is comparably low.

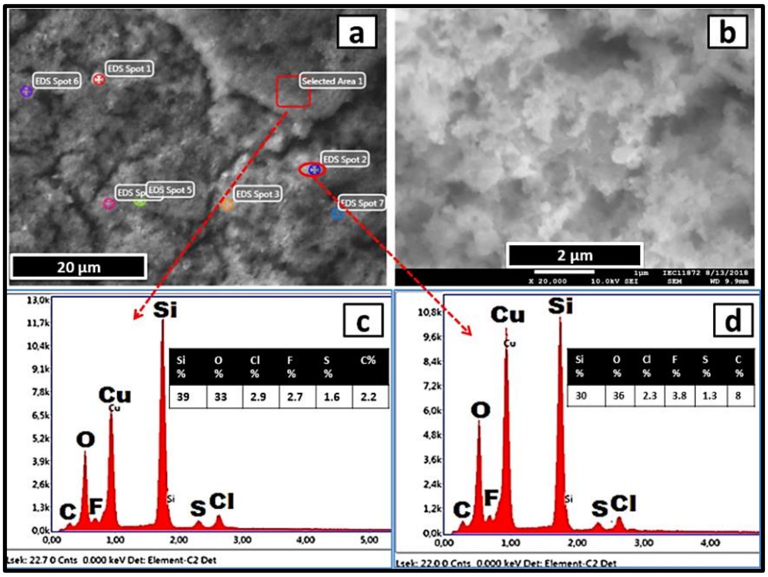

Fig. SR3. *FE-SEM images (**a, b**), and EDX spectra **(c, d)** of Si film which was prepared by pulsed-electrodeposition in [BMP]TFSI at a duty cycle of 6% for 30 minutes.*

5.1.4. Galvanostatic cycling and rate-capability investigations

Figure (SR4) shows the cycling evaluation of Si anode at different rates (0.2, 0.4 and 0.6 C-rates) to investigate its rate capability. The Si anode film shows poor cycling stability and low rate-capability. The gravimetric and areal capacity values drop to around zero when the anode was cycled at 0.6 C-rate. It seems that the structural deformation of Si films results from the volum expansion upon cycling, in addition to the film delamination out from the Cu current collector are dominating drawbacks that deteriorates the cycling performance of Si anode films over long cycling at constant current (as introduced before in section 3.1) and during cycling at different cycling rate as shown in figure (SR4).

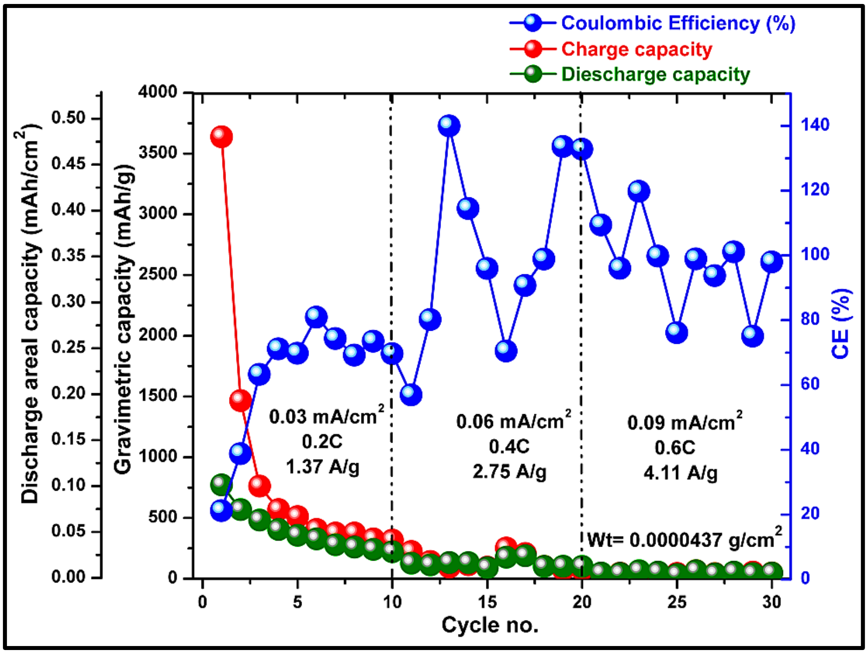

Fig. SR4. *Galvanostatic cycling performance at different cycling rates (0.2, 0.4 and 0.6 C) of Si-film, deposited by potentiostatic pulsed-electrodeposition at a duty cycle of 6%.*

5.2. Si_xGe_{1-x} electrodeposited in [BMP]TFSI by pulsed-electrodeposition

5.2.1. Cyclic voltammetry of $SiCl_4$/$GeCl_4$/[BMP]TFSI bath on Cu and Au substrates

Figure (SR5) shows the cyclic voltammograms of $SiCl_4$ (0.5 M)/$GeCl_4$ (0.5 M)/[BMP]TFSI bath on Cu (red voltammogram) and on gold substrates (orange voltammogram) at a scanning rate of 50 mV/s versus Pt QRE. The red voltammogram@Cu is similar to that of $SiCl_4$ (0.5 M)/$GeCl_4$ (0.5 M)/[EMIm]TFSI bath shown in figure (3.20) in section 3.2.1.1, taking into consideration that [BMP]TFSI start decomposition at more negative potential value of around 3 V versus Pt QRE. The first reduction peak appears in the voltammogram@Cu cannot be detected in the voltammogram@Au. This foremost peak can be attributed to either the reduction of the superficial Cu-oxide layer **[160]** or to a type of reaction between $SiCl_4$ and Cu **[161, 162]**. Thus, taking into consideration that Au is more noble (less reactive) than Cu, so these two postulation are still likely. The second reduction peak (C2) at around -1.25 V can be indexed to the reduction of Ge^{IV} ions to Ge^{II} **[120]**. After that, a shoulder (C3) at around -2 V can be detected only in the voltammogram@Cu, contributed with the full reduction of Ge^{II} to Ge along with Si UPD **[120, 161]**. C4 peak at -2.25 V can be indexed to the Si-Ge co-deposition, forming Si_xGe_{1-x} alloy **[120]**. The rising current after -3 V is related to the reduction of $[BMP]^+$ cation, after which the ionic liquid breaks down at C5. In the anodic stripping, a single oxidation peak can be detected before -1 V, related to the oxidation of $[TFSI]^-$ anion and Cu-substrate as well **[120]**.

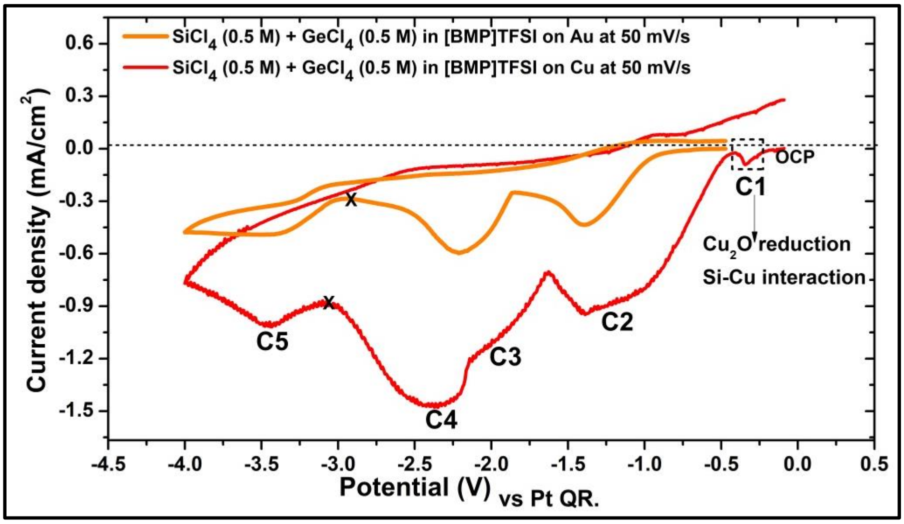

Fig. SR5. *Cyclic voltammograms of $SiCl_4$ (0.5 M)/$GeCl_4$ (0.5 M)/[BMP]TFSI bath on Cu (red) and on Au (orang). The voltammetry measurement was recorded at a scan rate of 50 mV/s starting from OCP to the negative direction.*

5.2.2. Scanning Electron Microscopic investigations

FE-SEM images of the Si_xGe_{1-x} film deposited by potentiostatic pulsed- electrodeposition in [BMP]TFSI at a duty cycle of 16% for 30 minutes is shown in figure (SR6a, b). The Si_xGe_{1-x} deposit has a porous structure, similar to that of Si_xGe_{1-x} film which was deposited in $SiCl_4$ (0.5 M)/$GeCl_4$ (0.5 M)/[EMIm]TFSI bath by pulsed-electrodeposition but a duty cycle of 50%. Figure (SR6c, d) illustrates the EDS spectra of as-deposited Si_xGe_{1-x} films at different scanned areas. Si/Ge stoichiometry was calculated from the EDX analysis by obtaining the mean atomic ratios over several scanned areas **[212]**, found to be $Si_{0.5}Ge_{0.5}$.

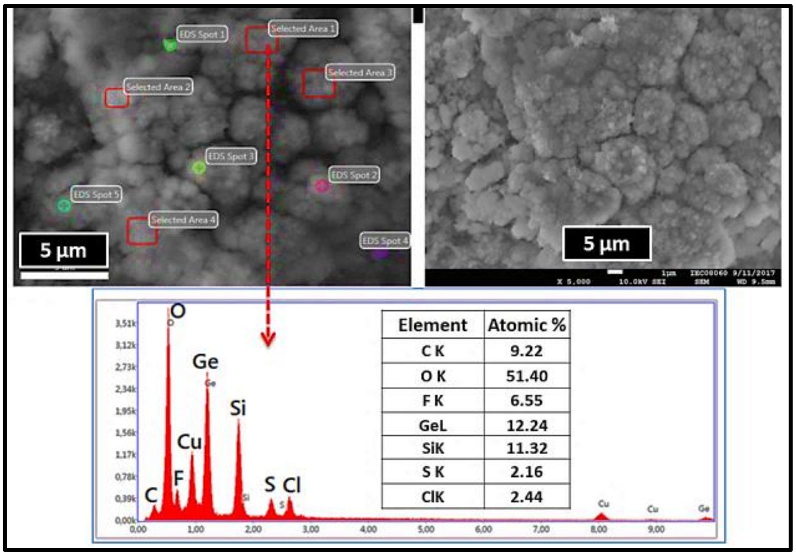

Element	Atomic %
C K	9.22
O K	51.40
F K	6.55
GeL	12.24
SiK	11.32
S K	2.16
ClK	2.44

Fig. SR6. *SEM images with the EDS spectra of $Si_{0.5}Ge_{0.5}$ films produced by potentiostatic pulsed-electrodeposition in [BMP]TFSI at a duty cycle of 16% for 30 minutes.*

5.2.3.Galvanostatic cycling evaluation in LIB

Figure (SR7a) illustrates the first charge/discharge plateaus of the dc-cycled Si_xGe_{1-x} anode-film at 0.75 C-rate. The values of the first irreversible capacity loss are 61.4%. The active mass of Si_xGe_{1-x} in the deposited film was calculated from the first charge, found to be 75 µg/cm^2. Figure (SR7b) presents the galvanostatic cycling performance of as-deposited Si_xGe_{1-x} anode-films for 50 cycles at a current density of 1.72 A/g, which is equivalent to 0.75 C-rate. The anode film displayed good cycling stability with gravimetric capacity values of around 400 mAh/g and discharge areal capacities at around 0.1 mAh/cm^2. The capacity retention after 50 cycles was 68%. The coulombic efficiency values was flactuated at some cycles to reach values more than 100 %, which could be related to activation/modification processes in the cycled anode. $Si_{0.5}Ge_{0.5}$ anode-film displayed cycling performance similar to that one of $Si_{0.3}Ge_{0.7}$ which was deposited in $SiCl_4$ (0.5 M)/$GeCl_4$ (0.5 M)/[BMP]TFSI bath by pulsed-electrodeposition at 50 duty cycle. The low capacity values could be interrelated with the non-compactness feature of the deposit which could result in the formation of thick SEI upon cycling **[33, 34]**.

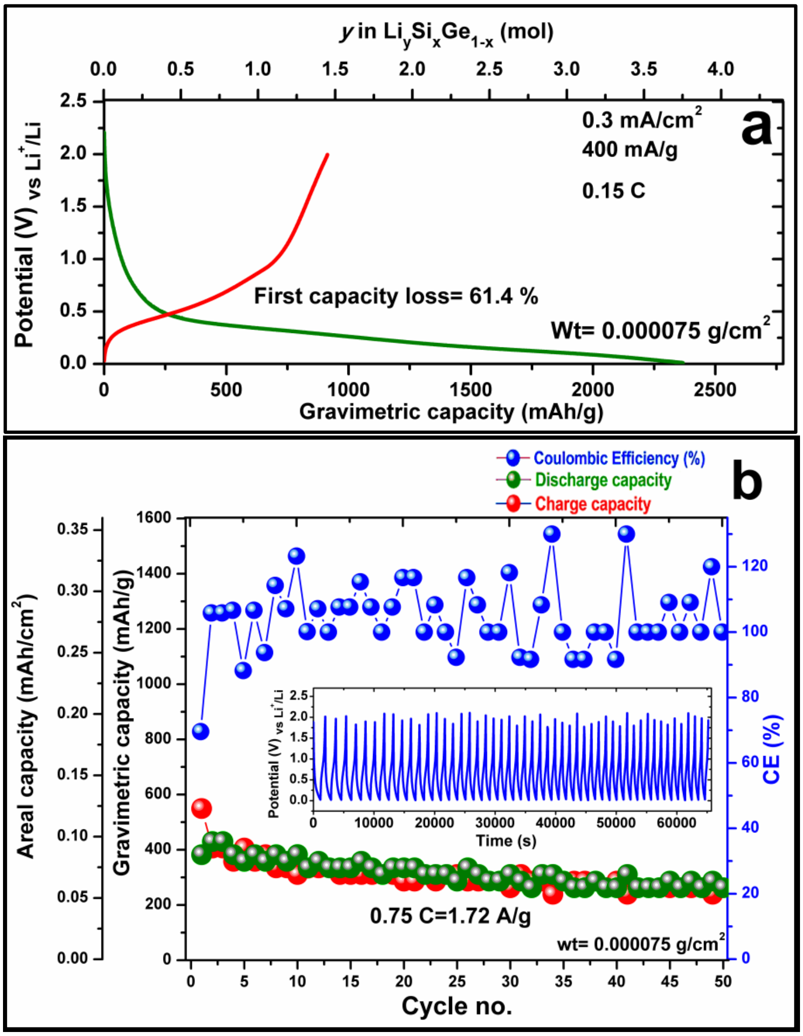

Fig. SR7. *Potential plateue of the initial charge/discharge cycle* ***(a)****, and galvanostatic charge/discharge cycling at 0.75 C-rate (1.72 A/g) for* $Si_{0.5}Ge_{0.5}$ *films produced by potentiostatic pulsed-electrodeposition in [BMP]TFSI at a duty cycle of 16% for 30 min.* ***(b)****.*

5.3. EIS-Bode plots of Si_xGe_{1-x}, $Si_xGe_{1-x}Al_y$ and Si-rGO anodes

5.3.1. EIS-Bode plots of Si_xGe_{1-x} anodes after 50 cycles

Figure (SR8a, b) represents Bode plots for Si_xGe_{1-x} anodes after 50 cycles at 0.7 C-rate in the de-lithiation state. As shown in figure (SR8a), Bode magnitude plots show variation in the impedance values for Si_xGe_{1-x} anodes especially in low frequency region from (< log 1 Hz) which characterize the diffusion rate of lithium ions in the bulk anodes [180, 186]. The values of impedance modulus increase as the percent of Si in Si_xGe_{1-x} anodes increase, reflecting slower kinetics of electrochemical reactions in Si-rich Si_xGe_{1-x} anodes, compared to $Si_{0.3}Ge_{0.7}$ anode. The impedance values in the high-to-mid frequency region (correlated with the charge transfer phenomena) [180, 187, 188] for $Si_{0.9}Ge_{0.1}$ anode shows the highest values, owing to the low Ge content in this film. Moreover, the Bode magnitude plots of this anode film are similar to that of bare Si anode shown in figure (3.8) in section 3.1.1.6.

Figure (SR8b) displays the Bode-phase plots of Si_xGe_{1-x} anodes after 50 cycles at 0.75 C-rate in the de-lithiation state. The phase shift curve of $Si_{0.3}Ge_{0.7}$ anode does not reflect evident peak in the high-to-mid frequency region, indicating that its mass transfer processes are not evident as a limiting steps after long cycling. For $Si_{0.6}Ge_{0.4}$ and $Si_{0.7}Ge_{0.3}$ anodes, their phase shift curves reflected two overlapped broad peaks in high-to-mid frequency ranges (100 kHz-10 Hz). This correlates with higher R_{ct} values in these anode films compared to $Si_{0.3}Ge_{0.7}$ anode [180, 187, 188]. The Bode phase plot of $Si_{0.7}Ge_{0.3}$ anode display short plateau in low-frequency region from 1 to 0.1 Hz, corresponding to the semi-infinite diffusion of Li^+-ions and reflecting a phase angle less than 45° equal to that of $Si_{0.3}Ge_{0.7}$ anode, which could indicate a higher rate of Li^+ ions diffusion, restricted to Warburg diffusion [191]. On the other hand, the phase shifts of $Si_{0.6}Ge_{0.4}$ and $Si_{0.9}Ge_{0.1}$ anodes reflected at higher angles (more than 60°) indicating pseudo-capacitance phenomena correlated with ion adsorption in these anode films [191, 192]. In conclusion, the Bode phase plots of Si_xGe_{1-x} anodes are more complex than that of bare Si anodes, but the Bode magnitude plots clarify that the diffusion of lithium ions in the interfacial SEI layer and into the bulk anodes slows down as the Si percent increase in Si_xGe_{1-x} anodes.

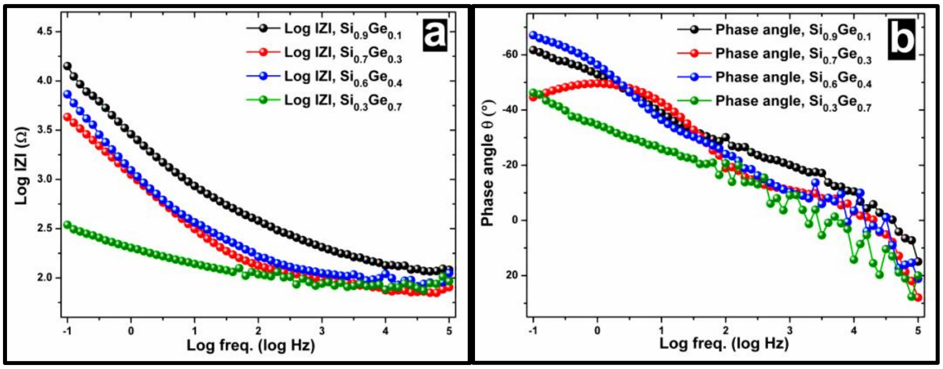

***Fig.* SR8.** *Bode plots of Si_xGe_{1-x} anodes after 50 cycles at 0.75 C-rate in the de-lithiation state; Bode magnitude plots **(a)**, Bode phase-shift plots **(b)**.*

5.3.2. EIS-Bode plots of $Si_xGe_{1-x}Al_y$ anodes upon cycling at different current densities

Figure (SR9a, b) depicts the Bode plots of $Si_{0.35}Ge_{0.45}Al_{0.2}$ anode film before and after cycling at different current densities (100, 200, 400, 800, and 1600 mA/g). As shown in figure (SR9a), Bode magnitude plots exhibited high impedance values at low frequencies which could be attributed to the oxide layer formed on the anode film [232]. This layer seems to get reduced when the anode was lithiated, resulting in the decrease of impedance values after cycling at 100 mA/g. The values of impedance modulus in all frequency regions increase after cycling the anode at 200 mA/g, then decrease when the anode was cycled at 400 mA/g, which could indicate the activation/modification processes of the anode upon cycling. Furthermore, the impedance values of the cycled anode at 800 and

1600 mA/g shows the same trend, displaying lower impedance values at all frequency regions, compared to that of the cycled anode after 200 mA/g. The feature of the Bode magnitude plots of $Si_{0.35}Ge_{0.45}Al_{0.2}$ indicates its good rate-capability which could be explained in terms of the activation/modification of the anode with cycling, even at higher current density.

Figure (SR9b) displays the Bode phase plots of $Si_{0.35}Ge_{0.45}Al_{0.2}$ anode film before and after cycling at different current densities (100, 200, 400, 800, and 1600 mA/g), corresponding to the phase shift between the imposed potential and the resulting current. Before cycling, the oxide layer on the anode film reflects a broad peak at low frequency regions **[232]**. The angle-shift plots after cycling at 200 mA/g shows a peak in the high-to-mid frequency range with higher intensity, compared to that after cycling the anode at 200, 400, 800, and 1600 mAh/g, which reflects the improvement in the charge transfer resistance in the anode upon cycling **[179, 187]**. This could correlates with the improvement in the anode structure (activation/modification) with cycling, reflecting its good cyclability and its great rate-capability. The phase-shift curve of $Si_{0.35}Ge_{0.45}Al_{0.2}$ anode in the low frequency region after cycling at 100, 1600 and after long cycling for 83 cycles show a phase angles higher than 45° (of around 65°) similar to the phase shift feature of pseudo-capacitors **[190, 191]**. This could indicate that the electrochemical processes in $Si_{0.35}Ge_{0.45}Al_{0.2}$ anode during cycling not only include Faradic processes but also share ions-adsorption processes (pseudo-capacitance phenomena) **[191, 192]**.

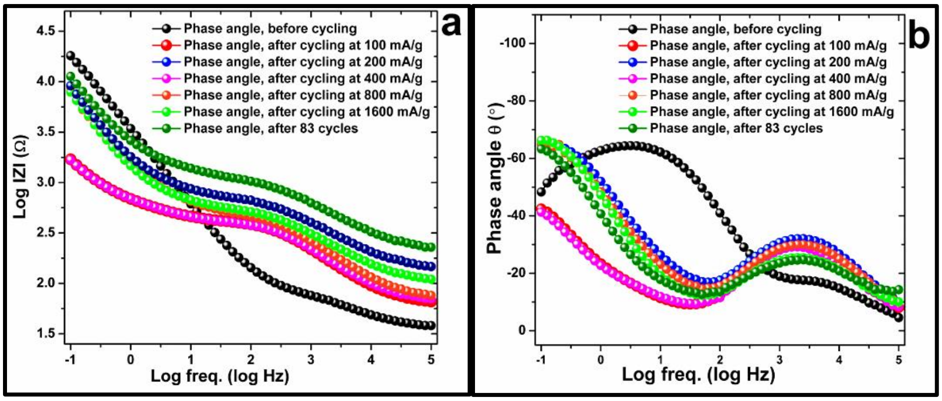

Fig. SR9. *Bode plots of $Si_{0.35}Ge_{0.45}Al_{0.2}$ anode film over cycling at different current densities (100, 200, 400, 800, and 1600 mA/g); Bode amplitude plots **(a)**, Bode phase-shift plots **(b).***

5.3.3. EIS-Bode plots of Si-rGO anodes upon cycling

Figure (SR10a, b) represents the Bode plots for Si-rGO composite anodes over 50 cycles at 0.3 C-rate (600 mA/g). As shown in figure (SR10a), Bode magnitude plots did not show a significant variation in impedance values in high-to-mid frequency regions, which can indicate the stability of the charge transfer impedance in the composite anode upon cycling [170, 233]. In the low frequency region, the composite anode exhibited an improvement in the D_{Li+} after the 2nd-discharge, 3rd-discharge and after the 3rd-discharge, showing lower impedance-modulus values, compared to that imposed after the initial charge/discharge and after the 2nd-charge process. This can be explained in terms of the activation and modification of the anode upon cycling [234].

Figure (SR10b) displays Bode phase plots of Si-rGO composite anodes over 50 cycles at 0.3 C-rate (600 mA/g). The phase-shift curve of Si-rGO composite anodes shows a peak with high intensity after the 1st charge process which becomes not evident after the subsequent cycles, reflecting the enhancement in the charge transfers processes in the composite anode upon cycling. In the low frequency region, the composite anode show less significant pseudo-capacitance features compared to other Si, Si_xGe_{1-x} and $Si_xGe_{1-x}Al_y$ anodes [191, 192] where the angle values of the phase shifts are less than 50°. The fitting circuit shown in figure (3.53) also does not introduce adsorption components correlated with the pseudo-capacitance processes. The Bode shift plots in the high frequency region from 100 kHz to 10 kHz exhibited high impedance values attributed to the contact impedance [234], which did not change upon cycling, indicating that the composite anode did not exhibit a delamination from the current collector over 50 cycles.

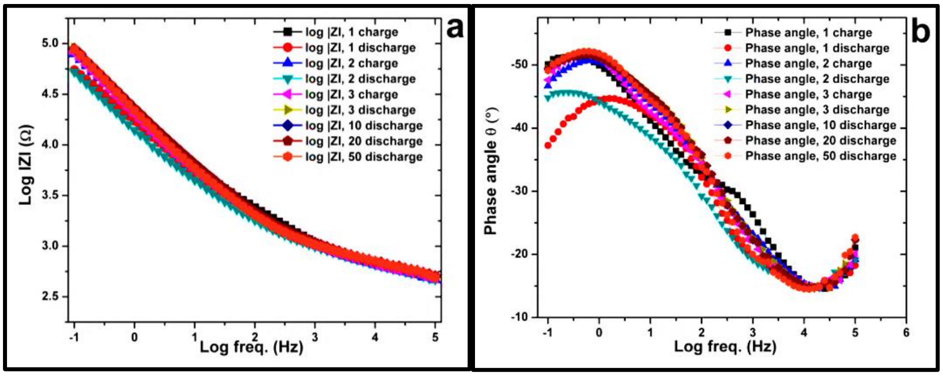

Fig. SR10. *Bode plots of Si-rGO composite anodes over 50 cycles at 0.3 C-rate (600 mA/g; Bode amplitude plots* ***(a)****, Bode phase-shift plots* ***(b).***

5.4. Electrochemical reduction of graphene oxide in ILs

5.4.1. Cyclic voltammetry of graphene oxide in different ionic liquids

Figure (SR11, insets a-d) represents the cyclic voltammetry of 1 mg/ml graphene oxide (GO) suspensions in [BMP]TFSI, [EMIm]TFSI, [BMP]TFO and [EMIm]TFO recorded on Cu at a scanning rate of 1 mV/s. The reduction peaks of GO in [BMP]TFSI, [EMIm]TFSI and [EMIm]TFO can be indexed to the gradual reduction of graphene oxide [220]. The anodic stripping regime in the cyclic voltammogram of GO in [EMIm]TFSI shows two anodic oxidation peaks which could correlates with the oxidation of IL-anion and/or Cu in addition to the oxidation of rGO.

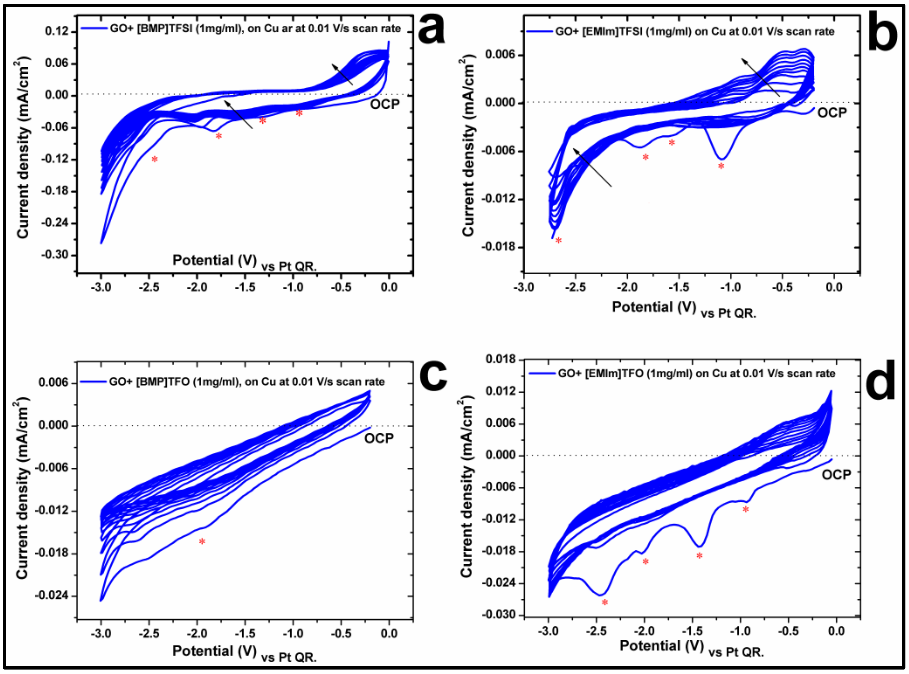

Fig. SR11. *Cyclic voltammograms of 1 mg/ml graphene oxide (GO) suspensions in [BMP]TFSI* ***(a)****, [EMIm]TFSI* ***(b)****, [BMP]TFO* ***(c)*** *and [EMIm]TFO* ***(d)****, recorded on Cu at a scanning rate of 1 mV/s.*

5.4.2. Scanning Electron Microscopy investigations of GO and rGO

Figure (SR12) shows FE-SEM image and EDX spectra of graphene oxide. The atomic ratio of C/O is 1.35. The detected Mn and S spectra in EDX comes from the Sulfuric acid and the permanganates which were used in the preparation of graphene from Graphite by Hummer’s method.

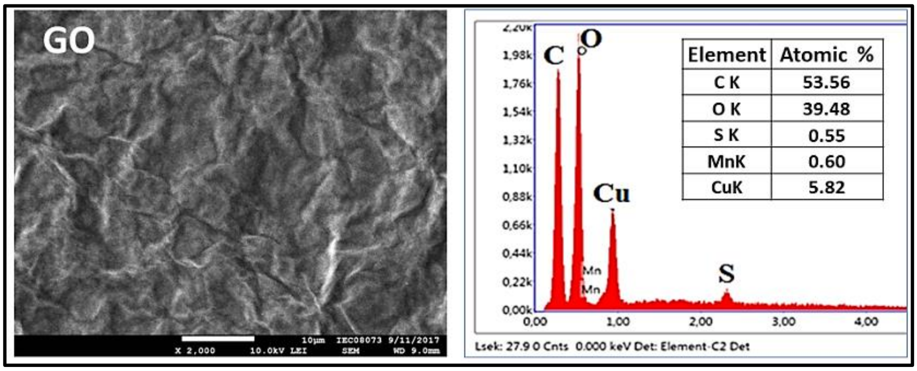

Element	Atomic %
C K	53.56
O K	39.48
S K	0.55
MnK	0.60
CuK	5.82

Figure SR12. *FE-SEM images and EDX spectra of graphene oxide flacks.*

Figure (SR13) shows FE-SEM image and EDX spectra of reduced graphene oxide in [BMP]TFSI at -1.7 V for 1 hours. The large sheets of graphene oxide are reduced to small fragments after reduction in [BMP]TFSI, which was reported also in other literature **[226]**. The atomic ratio of C/O is 3.6. It can be detected that the S, F and N (with such high atomic ratios) might somehow get attached to or adsorbed on rGO which may replace some oxygen atoms in GO **[227]**.

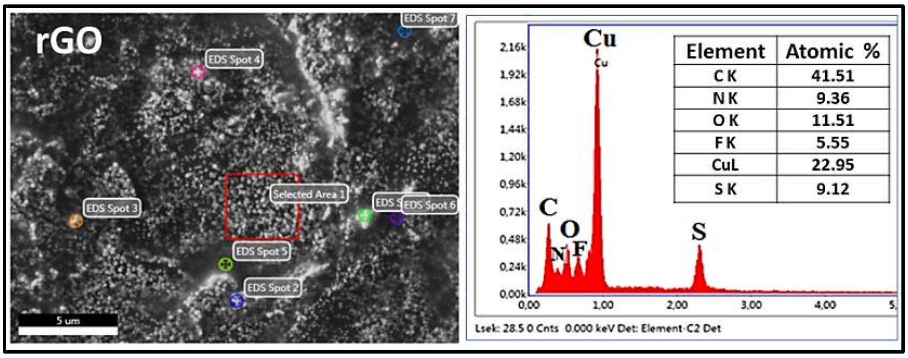

Element	Atomic %
C K	41.51
N K	9.36
O K	11.51
F K	5.55
CuL	22.95
S K	9.12

Fig. SR13. *FE-SEM images and EDX spectra for graphene oxide flacks after reduction in [BMP]TFSI for 1 hours at -1.7 V.*

5.4.3. X-ray diffraction (XRD) of GO and rGO

Figure (SR14) shows the XRD measurement of rGO which was reduced in [BMP]TFSI for 1 hours at -1.7 V, compared to that of GO. When GO is reduced to rGO, an XRD peak appears at 2θ of around 22°, indicating that the majority of the functional oxygen groups in graphene oxide are removal **[234]**.

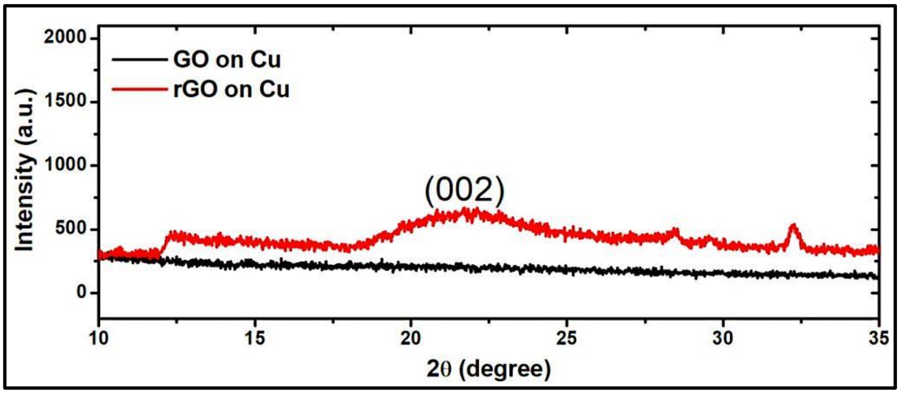

Fig. SR14. *XRD measurement of GO (black) and rGO (red) which was electrochemically reduced in [BMP]TFSI at -1.7 V for 1 hours.*

5.4.4. Rama spectroscopy of partially reduced graphene (rGO) in IL

Figure (SR15) shows the Raman spectra of rGO reduced in [BMP]TFSI for 1 hours at -1.7 V. ID/IG ratio reflect the degree of covalent binding in GO as a result of the stretching of C-C bond in sp^2 carbon form **[235]**. The G-band can be seen at around 1590 cm^{-1} and the D band at 1360 cm^{-1} **[236]**. The ID/IG for Graphite is 0.7 which increase after oxidation to 1.03 in case of GO **[237]**. After the reduction of GO, ID/IG become 0.85 (rGO) which indicates that most of the oxygen-containing groups were removal.

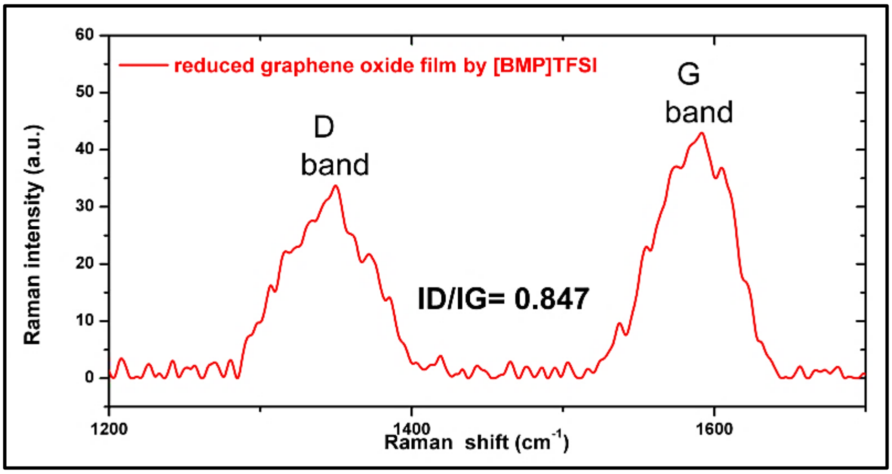

Fig. 15. *Raman spectra in the frequency regions of 1200-1800 cm^{-1} for rGO which was electrochemically reduced in [BMP]TFSI four 1 hour at a constant potential of -1.7 V.*

6. Prospective work

1- XPS studies for SEI layers on Si, Si_xGe_{1-x}, $Si_xGe_{1-x}Al_y$ and Si-rGO anodes after several cycles to elucidate the role of SEI-compounds on their cycling performance in LIBs.

2- FT-IR and Raman spectroscopic studies of SEI layers on Si, Si_xGe_{1-x} and $Si_xGe_{1-x}Al_y$ anodes to clarify the adsorption/desorption processes of IL-ions during cycling in LIBs which cause the pseudo-capacitance phenomena.

3- Synthesis and investigation of the electrochemical performance of Si_xAl_y-rGO composite anode which is expected to combine the advantages of Al and graphene, optimizing its cycling performance in LIBs.

This page intentionally left blank

7. References

1- B. Dunn, H. Kamath, J.-M. Tarascon; Electrical Energy Storage for the Grid: A Battery of Choices, Science, 2011, 334, 928-935.

2- E. C. Evarts; To the Limits of Lithium. Nature, 2015, 526 (4) S93-S95.

3- L. Grande, E. Paillard, J. Hassoun, J.-B. Park, Y.-J. Lee, Y.- K. Sun, S. Passerini, B. Scrosati; The Lithium/Air Battery: Still an Emerging System or a Practical Reality?, Adv. Mater., 2015, 27, 784- 800.

4- J. B. Goodenough; Electrochemical energy storage in a sustainable modern society, Energy Environ. Sci., 2014, 7, 14–18.

5- A. Fotouhi, D. J. Auger, K. Propp, S. Longo, M. Wild; A review on electric vehicle battery modelling: From Lithium-ion toward Lithium–Sulphur, Renewable Sustainable Energy Rev., 2016, 56, 1008–1021.

6- M. Armand, J.-M. Tarascon; Building Better Batteries. Nature, 2008, 451, 652-657.

7- Y. Mekonnen, A. Sundararajan, A. I. Sarwat; A review of cathode and anode materials for lithium-ion batteries, IEEE Southeast Con., 2016. DOI: 10.1109/SECON.2016.7506639.

8- J.-M. Tarascon, M. Armand; Issues and challenges facing rechargeable lithium batteries, Nature, 2011, 414 (6861), 359–367.

9- C. Daniel, J. O. Besenhard; Handbook of Battery Materials, Wiley-VCH, 2nd edition, (2011).

10- M. Winter, R. J. Brodd; What Are Batteries, Fuel Cells, and Supercapacitors?, Chem. Rev., 2004, 104 (10) 4245-4270.

11- T. Ohzuku, R. J. Brodd; An overview of positive-electrode materials for advanced lithium-ion batteries, J. Power Sources, 2007, 174 (2) 449–456.

12- B. Scrosati, J. Garche; Lithium batteries: Status, prospects and future, J. of Power Sources, 2010, 195 (9) 2419–2430.

13- D. Linden, T. B. Reddy, Handbook of Batteries. McGraw Hill, 3rd edition (1995).

14- Z. Yang, J. Zhang, M. C. W. Kintner-Meyer, X. Lu, X. D. Choi, J. P. Lemmon, J. Liu; Electrochemical Energy Storage for Green Grid, Chem. Rev., 2011, 111, 3577-3613.

15- A. Konarov, S.-T. Myung, Y.-K Sun; Cathode Materials for Future Electric Vehicles and Energy Storage Systems, ACS Energy Lett., 2017, 2, 703-708.

16- F. Lyu, Z. Sun, B. Nan, S. Yu, L. Cao, M. Yang, M. Li, W. Wang, S. Wu, S. Zeng, H. Liu, Z.-G. Lu; A Low-Cost and Novel Si Based Gel for Li-Ion Batteries, ACS Appl. Mater. Interfaces, 2017, 9, 10699-10707.

17- M. M. Thackeray, C. Wolverton, E. D. Isaacs; Electrical energy storage for transportation-approaching the limits of, and going beyond lithium-ion batteries, Energy Environ. Sci., 2012, 5, 7854-7863.

18- J. Dahn, G. M. Ehrlich; Chapter 29: Lithium-Ion Batteries, in: D. Linden, T.B. Reddy, (eds.) Handbook of Batteries, 2002, 3rd ed.

19- H. Wu, Y. Cui; Designing nanostructured Si anodes for high energy lithium ion batteries, Nano Today, 2012, 7, 414-429.

20- P. Rozier, J. M. Tarascon; Review-Li-rich layered oxide cathodes for next-generation Li-ion batteries: Chances and Challenges, J. Electrochem. Soc., 2015, 162 (14) A2490-2499.

21- L. Zhang, R. Rajagopalan, H. Guo, X. Hu, S. Dou, H. Liu; A green and facile way to prepare granadilla-like Silicon-based anode materials for Li-Ion Batteries, Adv. Funct. Mater., 2016, 26, 440-446.

22- C.-M. Park, J.-H. Kim, H. Kim, H.-J. Sohn; Li-alloy based anode materials for Li secondary batteries, Chem. Soc. Rev., 2010, 39, 3115-3141.

23- J. Song, M. Zhou, R. Yi, T. Xu, M. L. Gordin, D. Tang, Y. Yu, M. Regula, D. Wang; Interpenetrated Gel Polymer Binder for High-Performance Silicon Anodes in Lithium-Ion Batteries, Adv. Funct. Mater., 2014, 24, 5904-5910.

24- M. T. McDowell, I. Ryu, S. W. Lee, C. Wang, W. D. Nix, Y. Cui; Studying the Kinetics of Crystalline Silicon Nanoparticle Lithiation with in Situ Transmission Electron Microscopy, Adv. Mater., 2012, 24, 6034-6041.

25- M. N. Obrovac, M. N. L. Christensen; Structural Changes in Silicon Anodes during Lithium Insertion/Extraction, Electrochem. Solid-State Lett., 2004, 7, A93.

26- C. T. Lin, T. Y. Huang, J. J. Huang, N. L. Wu, M.-K. Leung; Multifunctional Co-Poly(Amic Acid): A New Binder for Si-Based Micro-Composite Anode of Lithium-Ion Battery, J. Power Sources, 2016, 330, 246-252.

27- T. M. Higgins, S. H. Park, P. J. King, C. Zhang, N. McEvoy, N. C. Berner, D. Daly, A. Shmeliov, U. Khan, G. Duesberg; A Commercial Conducting Polymer as Both Binder and Conductive Additive for Silicon Nanoparticle-Based Lithium-

Ion Battery Negative Electrodes, ACS Nano, 2016, 10, 3702-3713.

28- I. Kovalenko, B. Zdyrko, A. Magasinski, B. Hertzberg, Z. Milicev, R. Burtovyy, I. Luzinov, G. Yushin; Constituent of Brown Algae for Use in High-Capacity Li-Ion Batteries, Science, 2011, 334 (6052) 75-79.

29- B. Koo, H. Kim, Y. Cho, K. T. Lee, N. S. Choi, J. A. Cho; A highly Cross-Linked Polymeric Binder for High-Performance Silicon Negative Electrodes in Lithium Ion Batteries, Angew. Chem., Int. Ed. 2012, 51, 8762-8767.

30- R. Dash, S. Pannala; Theoretical Limits of Energy Density in Silicon-Carbon Composite Anode Based Lithium Ion Batteries, Sci. Rep. 2016, 6, 27449.

31- C. Chen, S. H. Lee, M. Cho, J. Kim, Y. Lee; Cross-Linked Chitosan as an Efficient Binder for Si Anode of Li-Ion Batteries, ACS Appl. Mater. Interfaces, 2016, 8, 2658-2665.

32- J.-Y. Choi, D. J. Lee, Y. M. Lee, Y.-G. Lee, K. M. Kim, J.-K. Park, K. Y. Cho; Silicon Nanofibrils on a Flexible Current Collector for Bendable Lithium-Ion Battery Anodes, Adv. Funct. Mater., 2013, 23, 2108–2114.

33- K. W. Schroder, H. Celio, L. J. Webb, K. J. Stevenson; Examining Solid Electrolyte Interphase Formation on Crystalline Silicon Electrodes: Influence of Electrochemical Preparation and Ambient Exposure Conditions, J. Phys. Chem. C, 2012, 116, 19737-19747.

34- Z.-H. Wu, J.-Y. Yang, B. Yu, B.-M. Shi, C.-R. Zhao, Z.-L. Yu; Self-Healing Alginate-Carboxymethyl Chitosan Porous Scaffold as an Effective Binder for Silicon Anodes in Lithium-Ion Batteries, Rare Met. 2016, DOI: 10.1007/s12598-016-0753-0.

35- A. F. Gonzalez, N.-H. Yang, R.-S. Liu; Silicon Anode Design for Lithium-Ion Batteries: Progress and Perspectives, J. Phys. Chem. C, 2017, 121, 27775-27787.

36- A. G. Kannan, S. H. Kim, H. S. Yang, D-W. Kim; Silicon nanoparticles grown on a reduced graphene oxide surface as high-performance anode materials for lithium-ion batteries, RSC Adv., 2016, 6, 25159-25166.

37- L. Wang, N. Lin, J. Zhou, Y. Zhu, Y. Qian; Silicon nanoparticles obtained via a low temperature chemical “metathesis” synthesis route and their lithium-ion battery properties, Chem. Commun., 2015, 51 (35) 2345-2348.

38- D. Lin, Z. Lu, P-C. Hsu, H. R. Lee, N. Liu, J. Zhao, H. Wang, C. Liu, Y. Cui; A high tap density secondary silicon particle anode fabricated by scalable mechanical pressing for lithium-ion batteries, Energy Environ. Sci., 2015, 8, 2371-2376.

39- D. Tang, R. Yi, M. L. Gordin, M. Melnyk, F. Dai, S. Chen, J. Song, D. Wang; Titanium nitride coating to enhance the performance of silicon nanoparticles as a lithium-ion battery anode, J. Mater. Chem. A, 2014, 2, 10375-10378.

40- R. Yi, F. Dai, M. L. Gordin, H. Sohn, D. Wang; Influence of Silicon nanoscale building blocks size and carbon coating on the performance of micro-sized Si-C composite Li-Ion anodes, Adv. Energy Mater., 2013, 3, 1507-1515.

41- J. Chang, X. Huang, G. Zhou, S. Cui, P. B. Hallac, J. Jiang, P. T. Hurley, J. Chen; Multilayered Si Nanoparticle/Reduced Graphene Oxide Hybrid as a High-Performance Lithium-Ion Battery Anode, Adv. Mater., 2014, 26, 758-764.

42- X. Chen, X. Li, F. Ding, W. Xu, J. Xiao, Y. Cao, P. Meduri, J. Liu, G.L. Graff, J. Zhang; Conductive rigid skeleton supported silicon as high-performance Li-Ion battery anodes, Nano Lett., 2012, 12, 4124-4130.

43- E. Peled, F. Patolsky, D. Golodnitsky, K. Freedman, G. Davidi, D. Schneier; Tissurelike silicon nanowires-based three-dimensional anodes for high-capacity Lithium Ion Batteries, Nano Lett., 2015, 15 (6) 3907-3916.

44- P. P. Prosini, C. Cento, F. Alessandrini, P. Gislon, A. Mancini, A. Rufoloni, F. Rondino, A. Santoni; Electrochemical characterization of silicon nanowires as an anode for lithium batteries, Solid State Ionics, 2014, 260, 49-54.

45- S. Sim, P. Oh, S. Park, J. Cho; Critical thickness of SiO_2 coating layer on core@shell bulk@nanowire Si anode materials for Li-Ion Batteries, Adv. Mater., 2013, 25, 4498-4503.

46- N. Liu, L. Hu, M. T. McDowell, A. Jackson, Y. Cui; Prelithiated Silicon nanowires as an anode for lithium ion batteries, ACS Nano, 2011, 5 (8) 6487-6493.

47- H. Wu, G. Chan, J. W. Choi, I. Ryu, Y. Yao, M. T. McDowell, S. W. Lee, A. Jackson, Y. Yang, L. Hu, Y. Cui; Stable cycling of double-walled silicon nanotube battery anodes through solid-electrolyte interphase control, Nature Nanotech., 2012, 7, 310-315.

48- L. F. Cui, R. Ruffo, C. K. Chan, H. L. Peng, Y. Cui; Crystalline–amorphous core–shell silicon nanowires for high capacity and high current battery electrodes; Nano Lett. 2009, 9, 491–495.

49- J.-H. Cho, S. T. Picraux; Enhanced Lithium Ion Battery Cycling of Silicon Nanowire Anodes by Template Growth to Eliminate Silicon Underlayer Islands, Nano Lett., 2013, 13, 5740-5747.

50- C. K. Chan, H. Peng, G. Liu, K. McIlwrath, X. F. Zhang, R. Huggins, Y. Cui; High Performance Lithium Battery Anodes Using Silicon Nanowires, Nature Nanotech., 2008, 3, 31-35.

51- M. Ramesh, H. S. Nagaraja; Effect of Current Density and Electrochemical Cycling on Physical Properties of Silicon Nanowires as Anode for Lithium Ion Battery, Mater. Charact., 2017, 129, 24-30.

52- T. Song, J. Xia, J.-H. Lee, D. H. Lee, M.-S. Kwon, J.-M. Choi, J. Wu, S. K. Doo, H. Chang, W. Park, D. S. Zang, H. Kim, Y. Huang, K.-C. Hwang, J. A. Rogers, U. Paik; Arrays of Sealed Silicon Nanotubes as Anodes for Lithium Ion Batteries, Nano Lett., 2010, 10, 1710-1716

53- M. H. Park, M. G. Kim, J. Joo, K. Kim, J. Kim, S. Ahn, Y. Cui, J. Cho; Silicon Nanotube Battery Anodes, Nano Lett., 2009, 9, 3844-3847.

54- H. Wu, G. Chan, J. W. Choi, I. Ryu, Y. Yao, M. T. McDowell, S. W. Lee, A. Jackson, Y. Yang, L. Hu; Stable Cycling of Double-Walled Silicon Nanotube Battery Anodes Through Solid- Electrolyte Interphase Control. Nat. Nanotech., 2012, 7, 310-315.

55- X. H. Liu, L. Zhong, S. Huang, S. X. Mao, T. Zhu, J. Y. Huang; Size-Dependent Fracture of Silicon Nanoparticles During Lithiation, ACS Nano, 2012, 6, 1522-1531.

56- X. H. Liu, J. Y. Huang; In Situ TEM Electrochemistry of Anode Materials in Lithium Ion Batteries, Energy Environ. Sci., 2011, 4, 3844.

57- E. Quiroga-Gonzȧlez, J. Carstensen, H. Föll; Good Cycling Performance of High-Density Arrays of Si Microwires as Anodes for Li Ion Batteries. Electrochim. Acta, 2013, 101, 93-98.

58- R. Jung, M. Metzger, D. Haering, S. Solchenbach, C. Marino, N. Tsiouvaras, C. Stinner, H. A. Gasteiger; Consumption of fluoroethylene carbonate (FEC) on Si-C composite electrodes for Li-Ion batteries, J. Electrochem. Soc., 2016, 163, A1705-A1716.

59- Z. Bao, M. R. Weatherspoon, S. Shian, Y. Cai, P. D. Graham, S. M. Allan, G. Ahmad, M. B. Dickerson, B. C. Church, Z. Kang; Chemical Reduction of Three-Dimensional Silica Micro-

Assemblies into Microporous Silicon Replicas, Nature, 2007, 446, 172-175.

60- N. Liu, K. Huo, M. T. McDowell, J. Zhao, Y. Cui; Rice Husks as a Sustainable Source of Nanostructured Silicon for High Performance Li-Ion Battery Anodes. Sci. Rep., 2013, 3, 1-7.

61- A. Mukanova, A. Jetybayeva, S.-T. Myung, S.-S. Kim, Z. Bakenov; A mini-review on the development of Si-based thin film anodes for Li-ion batteries, Materials Today Energy, 2018, 9, 49-66.

62- S. J. Lee, J. K. Lee, S. H. Chung, H. Y. Lee, S. M. Lee, H. K. Baik; Stress effect on cycle properties of the silicon thin-film anode, J. Power Sources, 2001, 97-98, 191-193.

63- H. Jung, M. Park, S. H. Han, H. Lim, S. K. Joo; Amorphous silicon thin-film negative electrode prepared by low pressure chemical vapor deposition for lithium-ion batteries, Solid State Commun., 2003, 125, 387-390.

64- J. Li, A. K. Dozier, Y. Li, F. Yang, Y.-T. Cheng; Crack pattern formation in thin film lithium-ion battery electrodes, J. Electrochem. Soc., 2011, 158, A689-A694.

65- T. Takamura, S. Ohara, M. Uehara, J. Suzuki, K. Sekine; A Vacuum Deposited Si Film Having a Li Extraction Capacity over 2000 mAh/g with a Long Cycle Life, J. Power Sources, 2004, 129, 96-100.

66- J. Li, A. K. Dozier, Y. Li, F. Yang, Y.-T. Cheng; Crack Pattern Formation in Thin Film Lithium-Ion Battery Electrodes. J. Electrochem. Soc., 2011, 158, A689.

67- S. Ohara, J. Suzuki, K. Sekine, T. J. Takamura; A thin film silicon anode for Li-ion batteries having a very large specific capacity and long cycle life, J. Power Sources, 2004, 136, 303–306.

68- J.O. Song, H.T. Shim, D. J. Byun, J. K. Lee; A study on the effect of structure and P-doping of Si thin film as an anode for lithium rechargeable batteries, Adv. Nanomater. Process, 2007, 124-126, 1063-1066.

69- H. J. Ahn, Y. S. Kim, W. B. Kim, Y. E. Sung, T. Y. Seong; Formation and characterization of Cu-Si nanocomposite electrodes for rechargeable Li batteries, J. Power Sources, 2006, 163, 211-214.

70- B. D. Polat, O. L. Eryilmaz, O. Keles, A. Erdemir, K. Amine; Compositionally graded SiCu thin film anode by magnetron sputtering for lithium ion battery, Thin Solid Films, 2015, 596, 190-197.

71- C. M. Hwang, C. H. Lim, J. H. Yang, J. W. Park; Electrochemical properties of negative $SiMo_x$ electrodes deposited on a roughened substrate for rechargeable lithium batteries, J. Power Sources, 2009, 194, 1061-1067.

72- J. B. Kim, H. Y. Lee, K. S. Lee, S. H. Lim, S. M. Lee; Fe/Si multi-layer thin film anodes for lithium rechargeable thin film batteries, Electrochem. Comm., 2003, 5, 544-548.

73- J. B. Kim, B. S. Jun, S. M. Lee; Improvement of capacity and cyclability of Fe/Si multilayer thin film anodes for lithium rechargeable batteries, Electrochim. Acta, 2005, 50, 3390-3394.

74- Q. Zhang, J. Liu, Z. Y. Wu, J. T. Li, L. Huang, S. G. Sun; 3D nanostructured multilayer Si/Al film with excellent cycle performance as anode material for lithium-ion battery, J. Alloy. Comp., 2016, 657, 559-564.

75- H. Liu, M. Zhu, Z. Du, M. N. Obrovac; The electrochemistry of amorphous Si-B thin film electrodes in Li cells, J. Electrochem. Soc., 2015, 163, A192-A196.

76- H. Li, H. Bai, Z. Tao, J. Chen; Si-Y multi-layer thin films as anode materials of high-capacity lithium-ion batteries, J. Power Sources, 2012, 217, 102-107.

77- S. Guo, H. Li, H. Bai, Z. Tao, J. Chen; Ti/Si/Ti sandwich-like thin film as the anode of lithium-ion batteries, J. Power Sources, 2014, 248, 1141-1148.

78- C.-M. Hwang, C.-H. Lim, J.-W. Park; Evaluation of Si/Ge Multi-layered Negative Film Electrodes Using Magnetron Sputtering for Rechargeable Lithium Ion Batteries, Thin Solid Films, 2011, 519, 2332–2338.

79- T. Song, H. Cheng, H. Choi, J.-H Lee, H. Han, D.H. Lee, D. S. Yoo, M.-S. Kwon, J.-M Choi, S.G. Doo; Si/Ge Double-Layered Nanotube Array as a Lithium Ion Battery Anode, ACS Nano, 2012, 6, 303–309.

80- H. Tian, F. Xin, X. Wang, W. He, W. Han; High capacity group-IV elements (Si, Ge, Sn) based anodes for lithium-ion batteries, J. Materiomics, 2015, 1, 153-169.

81- J. Wang, N. Du, H. Zhang, J. Yu, D. Yang; Cu-$Si_{1-x}Ge_x$ Core Shell Nanowire Arrays as Three-Dimensional Electrodes for High-Rate Capability Lithium-Ion Batteries, J. Power Sources, 2012, 208, 434–439.

82- T. Song, H. Cheng, H. Choi, J.-H. Lee, H. Han, D. H. Lee, D. S. Yoo, M.-S. Kwon, J.-M. Choi, S. G. Doo, H. Chang, J. Xiao, Y. Huang, W. Park, Y.-C. Chung, H. Kim, John A. Rogers, U. Paik;

Si/Ge double-layered nanotube array as a lithium ion battery anode, ACS Nano, 2012, 6 (1) 303–309.

83- P. R. Abel, A. M. Chockla, Y.-M. Lin, V. C. Holmberg, J. T. Harris, B. A. Korgel, A. Heller, C. B. Mullins; Nanostructured $Si_{(1-x)}Ge_x$ for Tunable Thin Film Lithium-Ion Battery Anodes, ACS Nano, 2013, 7 (3) 2249–2257.

84- J. Wang, T. Xu, X. Huang, H. Li, T. Ma; Recent Progress of Silicon Composites as Anode Materials for Secondary Batteries, RSC Adv. 2016, 6, 87778-87790.

85- J. K. Lee, C. Oh, N. Kim, J.-Y. Hwang, Y.-K. Sun; Rational Design of Silicon-Based Composites for High-Energy Storage Devices, J. Mater. Chem. A, 2016, 4, 5366-5384.

86- D. Ma, Z. Cao, A. Hu; Si-Based Anode Materials for Li-Ion Batteries: A Mini Review, Nano-Micro Lett., 2014, 6 (4) 347–358.

87- A. A. Arie, J. K. Lee; Electrochemical properties of P-Doped silicon thin film anodes of lithium ion batteries, Mater. Sci. Forum, 2013, 737, 80-84.

88- T. Mori, C.-J. Chen, T.-F. Hung, S. G. Mohamed, Y.-Q. Lin, H.-Z. Lin, J. C. Sung, S.-F. Hu, R.-S. Liu; High specific capacity retention of graphene/silicon nanosized sandwich structure fabricated by continuous electron beam evaporation as anode for lithium-ion batteries, Electrochim. Acta, 2015, 165, 166-172.

89- K. Kierzek, J. Machnikowski, F. Béguin; Toward the realistic silicon/carbon composite for Li-ion secondary battery anode, J. Appl. Electrochem., 2015, 45, 1-10.

90- J. Song, S. Chen, M. Zhou, T. Xu, D. Lv, M. L. Gordin, T. Long, M. Melnyk, D. Wang; Micro-sized silicon-carbon composites composed of carbon-coated sub-10 nm Si primary particles as high-performance anode materials for lithium-ion batteries, J. Mater. Chem. A, 2014, 2, 1257-1262.

91- R. Yi, J. Zai, F. Dai, M. L. Gordin, D. Wang; Dual conductive network-enabled graphene/Si-C composite anode with high areal capacity for lithium-ion batteries, Nano Energy, 2014, 6, 211-218.

92- A. A. Arie, J. O. Song, J. K. Lee; Structural and electrochemical properties of fullerene-coated silicon thin film as anode materials for lithium secondary batteries, Mater. Chem. Phys., 2009, 113 (1) 249-254.

93- K. F. Chiu, S. H. Su, H. J. Leu, C.Y. Wu; Silicon thin film anodes coated on micron carbon-fiber current collectors for lithium ion batteries, Surf. Coating. Technol., 2015, 267, 70-74.

94- U. Toçoglu, G. Hatipoglu, M. Alaf, F. Kayıs, H. Akbulut; Electrochemical characterization of silicon/graphene/MWCNT hybrid lithium-ion battery anodes produced via RF magnetron sputtering, Appl. Surf. Sci., 2016, 389, 507-513.

95- A. Mukanova, A. Nurpeissova, A. Urazbayev, S. Kim, M. Myronov, Z. Bakenov; Silicon thin film on graphene coated nickel foam as an anode for Li-ion batteries, Electrochim. Acta, 2017, 258, 800-806.

96- G. Radhakrishnan, P. M. Adams, B. Foran, M. V. Quinzio, M. J. Brodie; Pulsed laser deposited Si on multilayer graphene as anode material for lithium ion batteries, Apl. Mater., 2013, 1, 62103.

97- T. M. Paronyan, A. K. Thapa, A. Sherehiy, J. B. Jasinski, J. S. D. Jangam; Incommensurate graphene foam as a high capacity lithium intercalation anode, Sci. Rep., 2017, 7, 39944.

98- W. Sun, R. Hu, H. Liu, H. Zhang, J. Liu, L. Yang, H. Wang, M. Zhu; Silicon/Wolfram Carbide@Graphene composite: enhancing conductivity and structure stability in amorphous-silicon for high lithium storage performance, Electrochim. Acta, 2016, 191, 462-472.

99- Y. Chen, X. Zhang, Y. Tian, X. Zhao; Synthesis and Characterization of Silicon Nanoparticles Inserted into Graphene Sheets as High Performance Anode Material for Lithium Ion Batteries, J. Nanomaterials, 2014, Volum 2014, Article ID 734751, http://dx.doi.org/10.1155/2014/734751.

100- F. Sauvage, L. Laffont, J.-M. Tarascon, E. Baudrin; Factors affecting the electrochemical reactivity vs. lithium of carbon free $LiFePO_4$ thin films, J. Power Sources, 2001, 175 (1) 495–501.

101- G. Ferraresi, L. Czornomaz, C. Villevieille, P. Novák, M. El Kazzi; Elucidating the Surface Reactions of an Amorphous Si Thin Film as a Model Electrode for Li-Ion Batteries, ACS Appl. Mater. Interfaces, 2016, 8 (43) 29791-29798.

102- C. Pereira-Nabais, J. Światowska, M. Rosso, F. Ozanam, A. Seyeux, A. Gohier, P. Tran-Van, M. Cassir, P. Marcus; Effect of Lithiation Potential and Cycling on Chemical and Morphological Evolution of Si Thin Film Electrode Studied by ToF-SIMS, ACS Appl. Mater. Interfaces, 2014, 6 (15) 13023-13033.

103- P. Raghunath, M. C. Lin; Ab Initio Chemical Kinetics for SiH_2 + Si_2H_6 and SiH_3 + Si_2H_5 Reactions and the Related Unimolecular Decomposition of Si_3H_8 under a-Si/H CVD Conditions, J. Phys. Chem. A, 2013, 117 (42) 10811-10823.

104- X. Chen, K. Gerasopoulos, J. Guo, A. Brown, C. Wang, R. Ghodssi, J. N. Culver; A Patterned 3D Silicon Anode Fabricated by Electrodeposition on a Virus-Structured Current Collector, Adv. Funct. Mater., 2011, 21, 380–387

105- M. Daouahi, N. Rekik; Effect of Substrate Temperature on (Micro/Nano) Structure of a-SiC:H Thin Films Deposited by Radio-Frequency Magnetron Sputtering, J. Phys. Chem. C, 2012, 116 (39) 21018-21026.

106- R. K. Pandey, S. N. Sahu, S. Chandra; Handbook of Semiconductor Electrodeposition, Marcel Dekker: New York, 1996.

107- X. G. Zhang; Electrochemistry of Silicon and Its Oxide, Springer, 2001, ISBN: 0-306-46541-8.

108- A. J. Bard, R. Parsons, J. Jordan; Standard Potentials in Aqueous Solution, CRC Press, 1985; Vol. 6. ISBN: 9781351414746

109- A. Krishnamurthy, D. H. Rasmussen, I. I. Suni; Aqueous, Room Temperature Electrochemical Deposition of Compact Si Films, Electrochem. Solid-State Lett., 2011, 14 (9) D99-D101.

110- K. Yasuda, K. Maeda, T. Nohira, R. Hagiwara, T. Homma; Silicon Electrodeposition in Water-Soluble KF-KCl Molten Salt: Optimization of Electrolysis Conditions at 923 K, J. Electrochem. Soc., 2016, 163 (3) D95-D99.

111- J. Zhao, H. Yin, T. Lim, H. Xie, H.-Y Hsu, F. Forouzan, A. J. Bard; Electrodeposition of Photoactive Silicon Films for Low Cost Solar Cells, J. Electrochem. Soc., 2016, 163 (9) D506-D514.

112- Y. Nishimura, Y. Fukunaka, T. Nishida, T. Nohira, R. Hagiwara; Electrodeposition of Si Thin Film in a Hydrophobic Room Temperature Molten Salt, Electrochem, Solid-State Lett., 2008, 11 (9) D75-D79.

113- K. Stern, M. E. Mc-collum; Electrodeposition of silicon from molten salts, Thin Solid Films, 1985, 124, 129-134.

114- T. Munisamy, A. J. Bard; Electrodeposition of Si from organic solvents and studies related to initial stages of Si growth, Electrochim. Acta, 2010, 55 (11) 3797-3803.

115- X. L. Chen, K. Gerasopoulos, J. C. Guo, A. Brown, A. C. S. Wang, R. Ghodssi, J. N. A. Culver; A patterned 3D silicon anode fabricated by electrodeposition on a virus-structured current collector, Adv. Funct. Mater., 2011, 21, 380–387.

116- Y. Nishimura, Y. Fukunaka; Electrochemical reduction of silicon chloride in a non-aqueous solvent, Electrochim. Acta, 2007, 53, 111–116.

117- M. Schmuck, A. Balducci, B. Rupp, W. Kern, S. Passerini, M. Winter; Alloying of electrodeposited silicon with lithium- A principal study of applicability as anode material for lithium ion batteries, J. Solid State Electrochem., 2010, 14, 2203–2207.

118- R. Epur, M. Ramanathan, F. R. Beck, A. Manivannan, P.N. Kumta; Electrodeposition of amorphous silicon anode for lithium ion batteries. Mater. Sci. Eng. B, 2012, 177, 1157–1162.

119- Z. Zhao, J. Liu, C. Zhang; Preparation and Characterization of Electrochemically Deposited Silicon Films in Ionic Liquid from Polysilicon Byproduct $SiCl_4$, Int. J. Electrochem. Sci., 2018, 13, 8766–8774.

120- R. Al-Salman, S. Z. El-Abedin, F. Endres; Electrodeposition of Ge, Si and Si_xGe_{1-x} from an air- and water-stable ionic liquid, Phys. Chem. Chem. Phys., 2008, 10, 4650.

121- J. Mallet, M. Molinari, F. Martineau, F. Delavoie, P. Fricoteaux, M. Troyon; Growth of Silicon Nanowires of Controlled Diameters by Electrodeposition in Ionic Liquid at Room Temperature, Nano Letter, 2008, 8 (10) 3468-3474.

122- J. Zhang, S. Chen, H. Zhang, S. Zhang, X. Yao, Z. Shi; Electrodeposition of crystalline silicon directly from silicon tetrachloride in ionic liquid at low temperature, RSC Adv., 2016, 6 (15) 12061-12067.

123- M. Bechelany, J. Elias, P. Brodard, J. Michler, L. Philippe; Electrodeposition of amorphous silicon in non-oxygenated organic solvent, Thin Solid Films, 2012, 520, 1895.

124- N. K. Shah, R. K. Pati, Abhijit Ray, I. Mukhopadhyay; Electrodeposition of Si from an Ionic Liquid Bath at Room Temperature in the Presence of Water, Langmuir, 2017, 33, 1599−1604.

125- F. Endres, D. MacFarlane, A. Abbott; Electrodeposition from Ionic Liquids; John Wiley & Sons, 2008.

126- F. Bebensee, N. Borisenko, M. Frerichs, O. Hofft, W. Maus-Friedrichs, S. Z. El- Abedin, F. Endres; Surface Analysis of Nanoscale Aluminium and Silicon Films Made by Electrodeposition in Ionic Liquids, Zeitschrift für Physikalische Chemie, 2008, 222, 671.

127- F. Endres S. Zein El-Abedin; Air and water stable ionic liquids in physical chemistry, Phys. Chem. Chem. Phys., 2006, 8, 2101–2116.

128- J. Mallet, F. Martineau, K. Namura, M. Molinari; Electrodeposition of silicon nanotubes at room temperature using ionic liquid, Phys. Chem. Chem. Phys., 2013, 15 (39) 16446-16449.

129- S. Zein El-Abedin, N. Borissenko, F. Endres; Electrodeposition of nanoscale silicon in a room temperature ionic liquid. Electrochem. Commun., 2004, 6, 510–514.

130- G. Pulletikurthi, A. Lahiri, T. Carstens, N. Borisenko, S. Zein El-Abedin, F. Endres; Electrodeposition of silicon from three different ionic liquids: possible influence of the anion on the deposition process, J. Solid State Electrochem., 2013, 17 (11) 2823-2832.

131- Y. Tsuyuki, T. A. P. Huynh, J. Komadina, Y. Fukunaka, T. Homma; Electrochemical quartz crystal microbalance, X-ray photoelectron spectroscopy, and Raman spectroscopy analysis of $SiCl_4$ reduction in ionic liquids, Electrochim. Acta, 2015, 183, 49-55.

132- M. Galiński, A. Lewandowski, I. Stepniak; Ionic liquids as electrolytes, Electrochimica Acta, 2006, 51, 5567–5580.

133- P. Bonhôte, A.-P. Dias, N. Papageorgiou, K. Kalyanasundaram, M. Grätzel; Hydrophobic Highly Conductive Ambient-Temperature Molten Salts, Inorg. Chem., 1996, 35 (5) 1168-1178.

134- A. A. Miran Beigi, M. Abdouss, M. Yousefi, S. M. Pourmortazavi, A. Vahid; Investigation on physical and electrochemical properties of three imidazolium based ionic liquids (1-hexyl-3-methylimidazolium tetrafluoroborate, 1-ethyl-3-methylimidazolium bis(trifluoromethylsulfonyl) imide and 1-butyl-3-methylimidazolium methylsulfate), J. of Molecular Liquids, 2013, 177, 361–368.

135- B. Gattu , R. Epur, P. M. Shanti, P. H. Jampani, R. Kuruba, M. K. Datta, A. Manivannan, P. N. Kumta; Pulsed Current Electrodeposition of Silicon Thin Films Anodes for Lithium Ion Battery Applications, Inorganics, 2017, 5, 27.

136- M. Mallik, A. Mitra, S. Sengupta, K. Das, R. N. Ghosh, S. Das; Effect of Current Density on the Nucleation and Growth of Crystal Facets during Pulse Electrodeposition of Sn−Cu Lead-Free Solder, Cryst. Growth Des. 2014, 14, 6542−6549

137- N. Abl; Some theoretical Aspects of Pulse Electrolysis, Surface Technology, 1980, 10, 81-104.

138- M. S. Chandrasekar, M. Pushpavanam; Pulse and pulse reverse plating-Conceptual, advantages and applications, Electrochimica Acta, 2008, 53, 3313-3322.

139- M. Ghaemia, L. Binder; Effects of direct and pulse current on electrodeposition of manganese dioxide, J. Power Sources, 2002, 111, 248–254.

140- https://www.sigmaaldrich.com/catalog/ionic liquids.

141- M. Hayyan, F. S. Mjalli, M. A. Hashim, I. M. Al-Nashef, T. X. Mei; Investigating the electrochemical windows of ionic liquids, J. of Industrial and Engineering Chemistry, 2013, 19, 106–112.

142- N. Sánchez-Ramírez, B. D. Assresahegn, D. Bélanger, R. M. Torresi; A Comparison among Viscosity, Density, Conductivity, and Electrochemical Windows of N-n-Butyl-N-methylpyrrolidinium and Triethyl-n-pentylphosphonium Bis(fluorosulfonyl imide) Ionic Liquids and Their Analogues Containing Bis(trifluoromethylsulfonyl) Imide Anion, J. Chem. Eng. Data, 2017, 62, 3437-3444.

143- A. J. Bard, L. R. Faulkner; Electrochemical Methods: Fundamentals and Applications. John Wiley and Sons, New Jersey, 2001.

144- https://www.gamry.com/application-notes / instrumentation / potentiostat fundamentals.

145- C. H. Hamann, A. Hamnett, W. Vielstich; Electrochemistry. Wiley-VCH, 2nd edition, 2007.

146- H. Lüth; Solid Surfaces, Interfaces and Thin Films, Springer, 2010.

147- P. J. Goodhew, F. J. Humphreys; Elektronenmikroskopie. Grundlagen und Anwendung. McGraw-Hill Book Company, 2nd edition, 1998.

148- D. A. Shirley; High-Resolution X-Ray Photoemission Spectrum of the Valence Bands of Gold, Phys. Rev. B, 1972, 5, 4709-4714.

149- J. H. Scofield; Hartree-Slater Subshell Photoionization Cross-Sections at 1254 and 1487 eV. J. Electron Spectrosc. Relat. Phenom., 1976, 8, 129−137.

150- M. Yoshio, R. J. Brodd, A. Kozawa; Lithium-Ion Batteries. Springer, 1ST ed., 2009.

151- X. Huang, J. Hitt; Lithium ion battery separators: Development and performance characterization of a composite membrane, J. of Membrane Science, 2013, 425-426, 163-168.

152- A. Lewandowski, A. Swiderska-Mocek; Ionic liquids as electrolytes for Li-ion batteries-An overview of electrochemical studies, J. Power Sources, 2009, 194, 601–609.

153- C.-Y. Li, J. Patra, C.-H. Yang, C.-M. Tseng, S. B. Majumder, Q. Dong, J.-K. Chang; Electrolyte Optimization for Enhancing Electrochemical Performance of Antimony Sulfide/Graphene Anodes for Sodium-Ion Batteries–Carbonate-Based and Ionic Liquid Electrolytes, ACS Sustainable Chem. Eng., 2017, 5, 8269−8276.

154- L. Baggetto, P. H. L. Notten; Lithium-Ion (De)Insertion Reaction of Germanium Thin-Film Electrodes: An Electrochemical and in Situ XRD Study. J. Electrochem. Soc., 2009, 156, A169-A175.

155- M. Au, S. McWhorter, H. Ajo, T. Adams, Y. Zhao, J. Gibbs; Free standing aluminum nanostructures as anodes for Li-ion rechargeable batteries, J. Power Sources, 2010, 195, 3333–3337.

156- F. W. Gayle, J. B. Vander Sande, A. J. Mcalister; The Al-Li (aluminum-lithium) system, J. Phase Equilibria, 1984, 5, 21.

157- S. Li, J. Niu, Y.-C. Zhao, K. Pyo So, C. Wang, C. A. Wang, J. Li; High-rate aluminium yolk-shell nanoparticle anode for Li-ion battery with long cycle life and ultrahigh capacity, Nature Commun., 2015, 6, Article number: 7872.

158- A. J. Bard, G. Inzelt, F. Scholz; Electrochemical Dictionary, Springer Verlag, 1st edition (2008).

159- N. Borisenko, S. Zein El-Abedin, F. Endres; In Situ STM Investigation of Gold Reconstruction and of Silicon Electrodeposition on Au(111) in the Room Temperature Ionic Liquid 1 - Butyl - 1 - methylpyrrolidinium Bis (trifluoromethylsulfonyl)imide, J. Phys. Chem. B, 2006, 110, 6250-6256.

160- C. A. Vlaic, S. V. Ivanov, R. Peipmann, A. Eisenhardt, M. Himmerlich, S. Krischok, A. Bund; Electrochemical lithiation of thin silicon based layers potentiostatically deposited from ionic liquid, Electrochimica Acta, 2015, 168, 403–413.

161- G. Pulletikurthi, M. Olschewski, F. Endres; Electrodeposition of Lithium-Silicon Alloys from 1-butyl-1-methylpyrrolidinium bis(trifluoromethylsulfonyl)amide, J. Electrochem. Soc., 2018, 165 (16) D790-D795.

162- A. Willert, S. Zein El Abedin, F. Endres; Synthesis of Silicon and Germanium Nanowire Assemblies by Template-Assisted Electrodeposition from an Ionic Liquid, Australian Journal of Chemistry, 2014, 67 (6) 875-880.

163- V. Richoux, S. Diliberto, C. Boulanger, J. M. Lecuire; Pulsed electrodeposition of bismuth telluride films: Influence of pulse parameters over nucleation and morphology, Electrochim. Acta, 2007, 52, 3053–3060.

164- M. Rezaei-Sameti, S. Nadali, J. Rajabi, M. Rakhshi; The effects of pulse electrodeposition parameters on morphology, hardness and wear behavior of nano-structure Cr–WC composite coatings, J. Mol. Struct., 2012, 1020, 23–27.

165- J. F. Moulder, W. F. Stickle, P. E. Sobol, K. D. Bomben; Handbook of X-Ray Photoelectron Spectroscopy, Physical Electronics, Ed.: Eden Prairie, MN, 1995, ISBN: 0-9648124-1X.

166- S. Yokoyama, Y. Yamakage, M. Hirose; Laser-induced photochemical etching of SiO_2 studied by X-ray photoelectron spectroscopy, App. Phys. Lett., 1985, 47 (4) 15.

167- I. Kim, D. Byun, S. Lee, J. Lee; Electrochemical characteristics of copper silicide-coated graphite as an anode material of lithium secondary batteries, Electrochim. Acta, 2006, 52, 1532–1537.

168- H. Chen, Y. Xiao, L. Wang, Y. Yang; Silicon nanowires coated with copper layer as anode materials for lithium-ion batteries, J. Power Sources, 2011, 196, 6657–6662.

169- B. R. Weinberger, G. G. Peterson, T. C. Eschrich, H. A. Krasinski; Surface chemistry of HF passivated silicon: X-ray photoelectron and ion scatteringspectroscopy results, J. Appl. Phys., 1986, 60, 3232−3234.

170- D. E. Arreaga-Salas, A. K. Sra, K. Roodenko, Y. J. Chabal, C. L. Hinkle; Progression of Solid Electrolyte Interphase Formation on Hydrogenated Amorphous Silicon Anodes for Lithium-Ion Batteries, J. Phys. Chem. C, 2012, 116, 9072-9077.

171- N. Byrne, P. C. Howlett, D. R. MacFarlane, M. E. Smith, A. Howes, A. F. Hollenkamp, T. Bastow, P. Hale, M. Forsyth; Effect of zwitterion on the lithium solid electrolyte interphase in ionic liquid electrolytes, J. Power Sources, 2008, 184, 288-296.

172- C. Nguyen, S.-W. Woo, S.-W. Song; Understanding the Interfacial Processes at Silicon-Copper Electrodes in Ionic Liquid Battery Electrolyte, J. Phys. Chem. C, 2012, 116, 14764-14771.

173- M. Kroon, W. Buijs, C. J. Peters, G.-j. Witkamp; Decomposition of ionic liquids in electrochemical processing, Green Chem.; 2006, 8, 241-245.

174- T. Osaka, H. Nara, T. Momma, T. Yokoshima; New Si–O–C composite film anode materials for LIB by electrodeposition, J. Mater. Chem. A, 2014, 2, 883–896.

175- M. Olschewski, R. Gustus, O. Höfft, A. Lahiri, F. Endres; Monochromatic X-ray Photoelectron Spectroscopy Study of Three Different Ionic Liquids in Interaction with Lithium-Decorated Copper Surfaces, J. Phys. Chem. C, 2017, 121, 2675-2682.

176- S. Ivanov, C. A. Vlaic, S. Du, D. Wang and P. Schaaf, A. Bund; Electrochemical performance of nanoporous Si as anode for lithium ion batteries in alkyl carbonate and ionic liquid-based electrolytes, J. Appl Electrochem, 2014, 44, 159–168.

177- T. D. Hatchard, J. R. Dahn; In Situ XRD and Electrochemical Study of the Reaction of Lithium with Amorphous Silicon. J. Electrochem. Soc., 2004, 151, A838–A842.

178- H. Shobukawa, J. Shin, J. Alvarado, C. S. Rustomjia, Y. S. Meng; Electrochemical reaction and surface chemistry for performance enhancement of a Si composite anode using a bis(fuorosulfonyl)imide-based ionic liquid, J. Mater. Chem. A, 2016, 4, 15117.

179- W. Wang, Z. Favors, R. Ionescu, R. Ye, H. H. Bay, M. Ozkan, C. S. Ozkan; Monodisperse Porous Silicon Spheres as Anode Materials for Lithium Ion Batteries, Sci. Rep., 2015, 5, 8781.

180- S. Rodrigues, N. Munichandraiah, A. Shukla; AC impedance and state-of-charge analysis of a sealed lithium-ion rechargeable battery, J. Solid State Electrochem, 1999, 3 (7–8) 397–405.

181- Y. Lin, K. C. Klavetter, P. R. Abel, N. C. Davy, J. L. Snider, A. Heller, C. B. Mullins; High performance silicon nanoparticle anode in fluoroethylene carbonate-based electrolyte for Li-ion batteries, Chem. Commun., 2012, 48, 7268–7270.

182- M. Haro, T. Song, A. Guerrero, L. Bertoluzzi, J. Bisquert, U. Paik, G. Garcia-Belmonte; Germanium coating boosts lithium uptake in Si nanotube battery anodes, Phys. Chem. Chem. Phys., 2014, 16, 17930.

183- M.E. Orazem, B. Triboller; Electrochemical Impedance Spectroscopy, 2nd edition, 2017, P: 201. ISBN: 9781119340928.

184- J. R. MacDonald; Interface Effects In The Electrical Response Of Non-metallic Conducting Solids Ana Liquids, IEEE Transactions on Electrical Insulation, 1980, 15 (2) 65.

185- J.-P. Diard, C. Montella; Diffusion-trapping impedance under restricted linear diffusion conditions, J. Electroanalytical Chemistry, 2003, 557, 19-36.

186- J. Bisquert; Analysis of the kinetics of ion intercalation: Ion trapping approach to solid-state relaxation processes, Electrochim. Acta, 2002, 47, 2435.

187- Y. Oumellal, N. Delpuech, D. Mazouzi, N. Dupr, J. Gaubicher, P. Moreau, P. Soudan, B. Lestriez, D. Guyomard; The failure mechanism of nano-sized Si-based negative electrodes for lithium ion batteries, J. Mater. Chem., 2011, 21, 6201.

188- Y. Yamada, Y. Iriyama, T. Abe, Z. Ogumi; Kinetics of Electrochemical Insertion and Extraction of Lithium Ion at SiO, J. Electrochem. Soc., 2010, 157, A26.

189- M. Thomas, P. G. Bruce, J. B. Goodenough; AC Impedance Analysis of Polycrystalline Insertion Electrodes: Application to $Li_{1-x}CoO_2$, J. Electrochem. Soc., 1985, 132, 1521.

190- R. Dedryvere, D. Foix, S. Franger, S. Patoux, L. Daniel, D. Gonbeau; Electrode/Electrolyte Interface Reactivity in High-Voltage Spinel $LiMn_{1.6}Ni_{0.4}O_4/Li_4Ti_5O_{12}$ Lithium-Ion Battery, J. Phys. Chem. C, 2010, 114 (24) 10999.

191- M. Gaberscek, J. Jamnik; Impact of electrochemical wiring topology on the kinetics of insertion electrodes, Solid State Ionics, 2006, 177, 2647.

192- R. H. Nilson, M. T. Brumbach, B. C. Bunker; Modeling the Electrochemical Impedance Spectra of Electroactive Pseudocapacitive Materials, J. Electrochem. Soc., 2011, 158 (6) A678-A688.

193- P. Verma, P. Maire, P. Novák; A review of the features and analyses of the solid electrolyte interphase in Li-ion batteries, Electrochimica Acta, 2010, 55, 6332–6341.

194- D. Aurbach, M.D. Levi, E. Levi, A. Schechter; Failure and Stabilization Mechanisms of Graphite Electrodes, J. Phys. Chem. B, 197, 101, 2195.

195- B. S. Parimalam, A. D. MacIntosh, R. Kadam, B. L. Lucht; Decomposition Reactions of Anode Solid Electrolyte Interphase (SEI) Components with $LiPF_6$, J. Phys. Chem. C, 2017, 121, 22733−22738.

196- J. Zhang, R. Wang, X. Yang, W. Lu, X. Wu, X. Wang, H. Li, L. Chen; Direct Observation of Inhomogeneous Solid Electrolyte Interphase on MnO Anode with Atomic Force Microscopy and Spectroscopy, Nano Lett., 2012, 12, 2153-2157.

197- J. Zheng, H. Zheng, R. Wang, L. Ben, W. Lu, L. Chen, L. Chen, H. Li; 3d Visualization of Inhomogeneous Multi-Layered Structure and Young's Modulus of the Solid Electrolyte Interphase (SEI) on Silicon Anodes for Lithium Ion Batteries, Phys. Chem. Chem. Phys., 2014, 16, 13229-13238.

198- P. Guan, L. Liu, X. Lin, Simulation and Experiment on Solid Electrolyte Interphase (SEI) Morphology Evolution and Lithium-Ion Diffusion, J. Electrochem. Soc., 2015, 162, A1798-A1808.

199- C. C. Nguyen, S.-W. Song; Characterization of SEI layer formed on high performance Si–Cu anode in ionic liquid battery electrolyte, Electrochem. Commun., 2012, 12, 1593–1595.

200- M. Miyachi, H. Yamamoto, H. Kawai, T. Ohta, M. Shirakata; Analysis of SiO Anodes for Lithium-Ion Batteries, J. Electrochem. Soc., 2005, 152 (10) A2089-A2091.

201- J. Maibach, F. Lindgren, H. Eriksson, K. Edström, M. Hahlin; Electric Potential Gradient at the Buried Interface between Lithium Ion Battery Electrodes and the SEI Observed Using Photoelectron Spectroscopy, J. Phys. Chem. Lett., 2016, 7, 1775-1780.

202- M. Miyachi, H. Yamamoto, H. Kawai, T. Ohta, M. Shirakata; Analysis of SiO Anodes for Lithium-Ion Batteries, J. Electrochem. Soc., 2005, 152, A2089-A2091.

203- P. C. Howlett, N. Brack, A. F. Hollenkamp, M. Forsyth, D. R. MacFarlane; Characterization of the Lithium Surface in N-Methyl-N-alkylpyrrolidinium Bis(trifluoromethanesulfonyl) amide Room-Temperature Ionic Liquid Electrolytes, J. Electrochem. Soc., 2006, 153 (3) A595-A606.

204- J. Zheng, M. Gu, H. Chen, P. Meduri, M. H. Engelhard, J.-G. Zhang, J. Liu, J. Xiao; Ionic liquid-enhanced solid state electrolyte interface (SEI) for lithium–sulfur batteries, J. Mater. Chem. A, 2013, 1, 8464–8470.

205- E. Markevich, R. Sharabi, V. Borgel, H. Gottlieb, G. Salitra, D. Aurbach, Guenter Semrau, Michael A. Schmidt; In situ FTIR study of the decomposition of N-butyl-N-methylpyrrolidinium bis(trifluoromethanesulfonyl)amide ionic liquid during cathodic polarization of lithium and graphite electrodes, Electrochim. Acta, 2010, 55, 2687–2696.

206- G. A. Giffin, A. Moretti, S. Jeong, S. Passerini; Complex Nature of Ionic Coordination in Magnesium Ionic Liquid-Based Electrolytes: Solvates with Mobile Mg^{2+} Cations, J. Phys. Chem. C, 2014, 118, 9966–9973.

207- A. Balducci; Ionic Liquids in Lithium-Ion Batteries. Topics in Current Chemistry, 2017, 375, 20, DOI 10.1007/s41061-017-0109-8.

208- T. Shimanouchi, in: P.J. Linstrom, W. G. Mallard (Eds.); NIST Chemistry WebBook, NIST Standard Reference Database Number 69 (2005).

209- K. R. Seddon, A. Stark M.-J. Torres; Influence of chloride, water, and organic solvents on the physical properties of ionic liquids, Pure Appl. Chem., 2002, 72 (12) 2275–2287.

210- X. Dou, Y. Zhu, X. Huang, L. Li, G. Li; Effective Deposition Potential Induced Size-Dependent Orientation Growth of Bi-Sb Alloy Nanowire Arrays, J. Phys. Chem. B, 2006, 110, 21572-21575.

211- D. Pullini, D. Busquets-Mataix; Electrodeposition Efficiency of Co and Cu in the Fabrication of Multilayer Nanowires by Polymeric Track-Etched Templates, ACS Appl. Mater. Interfaces, 2011, 3, 759–764.

212- M. A. Mughal, M. J. Newell, J. Vangilder, S. Thapa, K. Wood, R. Engelken, B. R. Carroll, J. B. Johnson; Optimization of the Electrodeposition Parameters to Improve the Stoichiometry of In_2S_3 Films for Solar Applications Using the Taguchi Method, J. of Nanomaterials, 2014, Article ID 302159.

213- Va. Kuryliuk, A. Nadtochiy, O. Korotchenkov, C.-C. Wang, P.-W. Li; A model for predicting the thermal conductivity of SiO_2–Ge nanoparticle composites, Phys. Chem. Chem. Phys., 2015, 17, 13429-13441.

214- N. S. Rao, S. Dhamodaran, A. P. Pathak, P. K. Kulriya, Y. K. Mishra, F. Singh, D. Kabiraj, J. C. Pivin, D. K. Avasthi; Structural studies of Ge nanocrystals embedded in SiO_2 matrix, Nucl. Instrum. Methods Phys. Res., Sect. B, 2007, 264, 249.

215- M. I. Ortiz, A. Rodriguez, J. Sangrador, T. Rodriguez, M. Avella, J. Jimenez, C. Ballesteros; Luminescent nanostructures based on Ge nanoparticles embedded in an oxide matrix, Nanotechnology, 2005, 16, S197.

216- E. W. H. Kan, W. K. Choi, W. K. Chim, E. A. Fitzgerald, D. A. Antoniadis; Origin of charge trapping in germanium nanocrystal embedded system: Role of interfacial traps, J. Appl. Phys., 2004, 95, 3148.

217- R. Wibowo, S. Jones, R. Compton; Investigating the electrode kinetics of the Li/Li^+ in a wide range of room temperature ionic liquids at 298 K. J. Chem. Eng. Data, 2010, 55, 1374-1376.

218- L. H. S. Gasparotto, N. Borisenko, N. Bocchi, S. Zein El-Abedin, F. Endres; In situ STM investigation of the lithium underpotential deposition on Au(111) in the air- and water-stable ionic liquid 1 – butyl – 1 - methylpyrrolidinium bis (trifluoromethylsulfonyl)amide, Phys. Chem. Chem. Phys. 2009, 11, 11140-11145.

219- H. Nakai, T. Kubota, A. Kita, A. Kawashima; Investigation of the Solid Electrolyte Interphase Formed by Fluoroethylene Carbonate on Si Electrodes, J. Electrochem. Soc., 2011, 158, A798–A801.

220- J. Shin, E. Cho; Agglomeration Mechanism and a Protective Role of Al_2O_3 for Prolonged Cycle Life of Si Anode in Lithium-Ion Batteries, Chem. Mater. 2018, 30, 3233-3243.

221- S. Zein El-Abedin, E. M. Moustafa, R. Hempelmann, H. Natter, F. Endres; Additive free electrodeposition of nanocrystalline aluminium in a water and air stable ionic liquid; Electrochem. Commun., 2005, 7, 1111-1116.

222- S. Zein El-Abedin, E. M. Moustafa, R. Hempelmann, H. Natter, F. Endres; Electrodeposition of Nano- and Microcrystalline Aluminium in Three Different Air and Water Stable Ionic Liquids, ChemPhysChem, 2006, 7, 1535–1543.

223- J. Y. Xiang, X. L. Wang, X. H. Xia, L. Zhang, Y. Zhou, S. J. Shi, J. P. Tu; Enhanced high rate properties of ordered porous Cu_2O film as anode for lithium ion batteries, Electrochim. Acta, 2010, 55, 4921–4925.

224- L. B. Chen, J. Y. Xie, H. C. Yu, T. H. Wang; Si–Al thin film anode material with superior cycle performance and rate capability for lithium ion batteries, Electrochimica Acta, 2008, 53, 8149–8153.

225- G. Hwang, H. Park, T. Bok, S. Choi, S. Lee, I. Hwang, N.-S. Choi, K. Seo , S. Park; A high-performance nanoporous Si/Al_2O_3 foam lithium-ion battery anode fabricated by selective chemical etching of the Al–Si alloy and subsequent thermal oxidation, Chem. Commun., 2015, 51, 4429.

226- J. Ping, Y. Wang, K. Fan, J. Wu, Y. Ying; Direct electrochemical reduction of graphene oxide on ionic liquid doped screen-printed electrode and its electrochemical biosensing application, Biosensors and Bioelectronics, 2011, 28, 204–209.

227- X. Zhou, Y. Zhang, Z. Huang, D. Lu, A. Zhu, G. Shi; Ionic liquids modified graphene oxide composites: a high efficient adsorbent for phthalates from aqueous solution, Sci. Rep.2016, 6:38417. DOI: 10.1038/srep38417.

228- A. M. Chockla, M. G. Panthani, V. C. Holmberg, C. M. Hessel, D. K. Reid, T. D. Bogart, J. T. Harris, C. B. Mullins, B. A. Korgel; Electrochemical Lithiation of Graphene-Supported Silicon and Germanium for Rechargeable Batteries, J. Phys. Chem. C, 2012, 116, 11917-11923.

229- Y. Chen, N. Du, H. Zhang, D. Yang; Firmly bonded graphene-silicon nanocomposites as high-performance anode materials for lithium-ion batteries, RSC Adv., 2015, 5, 46173.

230- H. Mi, F. Li, S. Xu, Z. Li, X. Chai, C. He, Y. Li, J. Liu; A tremella-like nanostructure of silicon@void@ graphene-like nanosheets composite as an anode for lithium-ion batteries, Nanoscale Research Lett., 2016, 11, 204.

231- V. Z. Mordkovich; Synthesis and XPS investigation of super dense lithium-graphite intercalation compound, LiC_2, Synthetic Metals, 1996, 80, 243-247.

232- R. Zhao, S. Bobev, L. Krishna, T. Yang, J. M. Weller, H. Jing, C. K. Chan; Anodes for Lithium-Ion Batteries Based on Type I Silicon Clathrate $Ba_8Al_{16}Si_{30}$- Role of Processing on Surface Properties and Electrochemical Behavior, ACS. Appl. Mater. Interfaces, 2017, 9 (47) 41246-41257.

233- D. Wang, F. Li, H. T. Fang, M. Liu G. Q., G. Q. Lu, H. M. Cheng; Effect of pore packing defects in 2D ordered mesoporous carbons on ionic transport. J. Phys. Chem. B, 2006, 110 (17) 8570–8575.

234- Z. C. Chang, H. J. Sohn; Electrochemical Impedance Analysis for Lithium Ion Intercalation into Graphitized Carbons. J. Electrochem. Soc., 2000, 147 (1) 50-58.

235- S. Perumbilavil, P. Sankar, T. P. Rose, R. Philip; White light Z-scan measurements of ultrafast optical nonlinearity in reduced graphene oxide nanosheets in the 400–700 nm region, App. Phys. Lett., 2015, 107, 051104.

236- K. Krishnamoorthy, M. Veerapandian, R. Mohan, and S. Kim; Investigation of Raman and photoluminescence studies of reduced graphene oxide sheets, Appl. Phys. A, 2012, 106, 501.

237- M. S. Dresselhaus, A. Jorio, M. Hofmann, G. Dresselhaus, R. Saito; Perspectives on Carbon Nanotubes and Graphene Raman Spectroscopy, Nano Lett., 2010, 10, 751.

8. List of figures

9. List of tables

Curriculum vitae

Name:	Adel Elsayed
Date of birth:	09.05.1983
Place of birth:	Fayoum, Egypt.
Current address:	Leibnizstraße 22, 38678 Clausthal-Zellerfeld, Germany.
Permanent address:	33 Al-Behouth st., Dokki, 12622 Cairo, Egypt.
E-mails:	amae16@tu-clausthal.de, adel_chemphysics@yahoo.com

Education

05/2016 - 5/2019:	Clausthal University of Technology, Institute of Electrochemistry, PhD student.
04/2011 - 03/2016:	University of Cologne, Institute of Inorganic chemistry, PhD student.
02/2010 - 06/2012:	National Research Centre (NRC) / Al-Azhar University, Faculty of Science, Cairo, Egypt, M.Sc. in inorganic chemistry.
09/2000 - 07/2005:	Fayoum University, Faculty of Science, Egypt, B.Sc. in chemistry.

Professional Experience

05.2016 - 5.2019:	Doctoral candidate, Institute of Electrochemistry, Clausthal University of Technology.
04.2015 - 04.2016:	Doctoral candidate, Institute of Inorganic chemistry, University of Cologne.
08.2013 - 10.2014:	Researcher assistant (PhD student), National Research Centre (NRC), Cairo, Egypt.
08.2008 - 12.2013:	Assistant researcher (M.Sc. student), National Research Centre (NRC), Cairo, Egypt.

Scholarships/Awards

2014:	DAAD / GERLS Scholarship.
2013:	The National Research Centre Prize for the best M.Sc. thesis in applied chemistry in 2012.